Mineralogical and Geochemical Changes Associated with Sulfide and Silicate Weathering in Natural Alteration Scars, Taos County, New Mexico

By

Gabriel James Graf

Submitted in partial fulfillment of the requirements
for the Degree of Master of Science in Geology at
New Mexico Institute of Mining and Technology

Earth and Environmental Science Department
Socorro, New Mexico
May, 2008

ABSTRACT

Natural alteration scars occur along the Red River valley, NM and were studied as mineralogical analogs to future weathering in rock piles created by Chevron Mining Inc, (formerly Molycorp, Inc.) during open pit mining from the Questa mine. These natural alteration scars provide a glimpse into weathering that may affect these rock piles in the long term (up to 4.5 million years) (Lueth et al., 2006). The alteration scars provided excellent analogues to the rock piles because they are located within close proximity (~2 miles) from the Questa mining operation and contain similar lithologies and hydrothermal alteration mineral suites. The weathering processes (sulfide and silicates) and overall architecture of these systems (open) appear very similar.

Three distinct weathering profiles were collected in the Hansen and Southwest Hansen alteration scars to document chemical and mineralogical changes that occur related to sulfide and silicate weathering. These weathering profiles are different from classic weathering profiles since they were profoundly influenced by hydrothermal alteration, and commonly contain multiple lithologies.

Within each profile particle size decreases upward, which suggests physical weathering processes are active. The mineralogical changes associated with grain size reduction include pyrite oxidation with the precipitation of gypsum, jarosite and Fe-oxides. Acid base accounting has documented limited acid consuming minerals (i.e. calcite) to buffer the acid created during pyrite oxidation. Stable isotope analysis of pyrite and gypsum indicate $\delta^{34}S$ pyrite range from -1.0 to -6.6 ‰. $\delta^{34}S$ of gypsum range from -2.1 to -5.1 ‰ and gypsum $\delta^{18}O_{SO4}$ range from -7.0 to 5.2 ‰. This data

provides convincing evidence that sulfates within the alteration scars are formed only in the weathering environment.

Silicate mineralogical changes through the weathering profiles include, decreasing feldspar and increasing clay upwards. The working hypothesis was silicate mineral changes result from feldspar weathering to form secondary clay minerals. Clay mineral analysis, however, indicates the clay minerals are similar to hydrothermal alteration minerals. Much of the fining upward character may be due to hydrothermal alteration. Clay mineral stable isotope analysis, $\delta^{18}O$ (-0.3 to 4.6‰) and δD (-65 to
-95‰), documents the clays analyzed are hydrothermal in origin and provide no evidence for weathering clays. Review of USGS (Nordstrom et al., 2005) ground and surface water geochemistry, along with silicate mineral observations, indicate congruent dissolution of silicate minerals is active in the alteration scars.

The major active chemical weathering system in the alteration scars is the oxidation of pyrite. The soil pH of 2 to 3 is compatible with silicate minerals dissolution, and the chemical conditions do not favor precipitation of new clay minerals. Physical weathering in the alteration scars continues by freeze-thaw and precipitation of gypsum that causes a volume increase; providing pathways for fluid and oxygen for the further oxidation of pyrite. This acidic environment is responsible for the precipitation of jarosite, gypsum and dissolution of silicate minerals. Sulfide weathering will continue to occur in the alteration scars until the remaining pyrite has oxidized.

ACKNOWLEDGEMENTS

The funding for this study was provided by Chevron Mining, Inc. (formerly Molycorp, Inc.) in the form of a research assistantship. I express my sincere appreciation to Chevron for providing me the opportunity to further enhance my education in geology through this funding. I would like to thank Bruce Walker and Dave Jacobs, Chevron Geologists, for providing insight and guidance to the geology of the alteration scar areas and also for the safe and hard work put forth in mapping and collection of samples.

I would especially like to thank my advisors, Dr. Andrew Campbell and Dr. Virgil Lueth for the discovery and thorough insight into this thesis project. Their guidance, insight, and support during this research project were outstanding and the projects success relied on their expertise in the research area. Appreciation is also extended to Dr. Virginia McLemore for her guidance in the field. I would also like to thank Dr. David Norman and Dr. Virginia McLemore for serving on the thesis committee and for the thorough input on this thesis document to improve the final manuscript.

Members of the Questa Weathering Rock Pile and Stability Weathering Index Committee provided constant encouragement and insight to this study. Members of the committee that I would especially like to thank include: Andrew Campbell, Virgil Lueth, Virginia McLemore, Mark Logsdon, Dave Jacobs, Dirk van Zyl and Bruce Walker. A special thanks also to the members of the Acid Drainage Technology Institute (ADTI) committee of the Questa Weathering Rock Pile and Stability Project for their thorough review and common suggestions on project improvements.

Laboratory work for this project would not have been possible without the guidance and help of many friends and coworkers on the project. Kelly Donahue provided guidance and help during the project, including but not limited to, enormous work on preparing and analyzing clay minerals. Dawn Sweeney located the mineralogical modeling program, ModAn, and provided documentation on how to use the program. Kwaku Boayke provide assistance in geotechnical lab procedures and Jon Morkeh aided in geochemical lab procedures. Leann Giese aided in other lab procedures.

This thesis is dedicated to my family, especially Jim and Teri Graf, for without their encouragement and support, none of my higher education studies would have been possible. I finally like to thank my girlfriend, Leann Giese, for all the support and assistance she provided me over the past two years while completing my thesis. She spent many hours editing versions of my thesis and providing suggestions on how to greatly improve the manuscript. The encouraging and insightful environment she provided for me greatly helped to fulfill my master's degree.

TABLE OF CONTENTS

LIST OF FIGURES

LIST OF TABLES

1. INTRODUCTION

1.1 Background

The Hansen and Southwest Hansen alteration scars are located between the villages of Questa and Red River, Taos County, New Mexico (Figure 1). Alteration scars occur along the Red River valley in pyrite rich-rocks and are characterized by steep slopes, a lack of soil, iron oxide staining, rapid erosion and common slumping and landsliding following major rainfall events (Meyer and Leonardson, 1990). A number of geologic factors control the formation of scars including slope angle, tectonic fracturing, pyrite content, and vegetation cover (Meyer and Leonardson, 1990).

This study of alteration scars documents an example of long-term physical and chemical weathering of pyrite-bearing rocks. These alteration scars are being used as mineralogical analogs for rock piles constructed by Chevron Mining Inc, (formerly Molycorp, Inc.) during a period of open pit mining from 1964 to 1983. The rock types and hydrothermal alteration types in the alteration scars and rock piles are similar. This thesis will focus on the mineralogical changes in the alteration scar due to weathering, which provides a basis for predicting mineralogical changes that could occur in the rock piles.

This thesis documents mineralogical and geochemical changes through three weathering profiles from the Hansen and Southwest Hansen alteration scars. Methods utilized in this study include geological mapping, whole rock geochemistry, particle-size geochemistry, petrography, acid base accounting, stable isotope analysis of sulfates, sulfides and clay minerals, quantitative X-Ray diffraction (QXRD), particle

size distribution, and sulfide-sulfate ratios. The ability to differentiate supergene weathering minerals from hydrothermal alteration minerals is critical to this study.

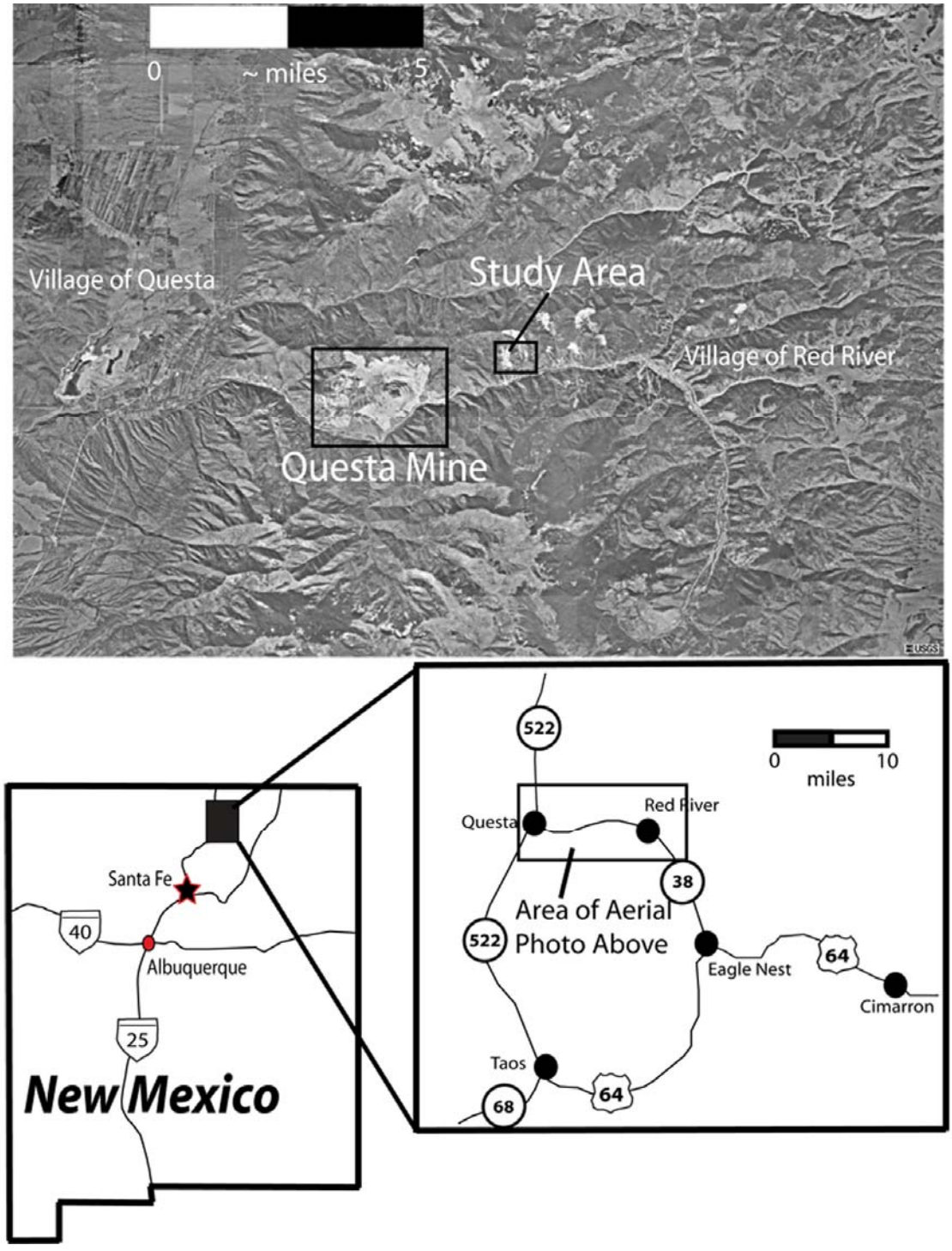

Figure 1. Location map of study area. Aerial photo courtesy of USGS.

1.2 Natural Alteration Scars

Numerous naturally formed, colorful (yellow to red to orange to brown) alteration scars are located throughout the Red River valley, NM and are characterized by badlands-type topography, a lack of soil, steep unstable slopes, sulfide content >1%, little to no vegetation, and extensively fractured bedrock (Figure 2) (McLemore et al. 2004; Ludington et al., 2004; Meyer and Leonardson, 1990). The scars in the area range in size from 100 acres to less than 1 acre in size (Shaw et al., 2003). Public and scientific interest in these scars has increased during the last decade because of sporadic, but destructive, mudslides or debris flows that emanate from the scar areas during wet periods (McLemore et al., 2004).

The first interpretation proposed for scar formation was by low-temperature fumerolic alteration related to breccia pipes and/or tectonic pipes formed during the end processes of volcanism (Schilling, 1956; Ishirara, 1967; Clark and Read, 1972). However, after an extensive mapping study by Meyer and Leonardson (1990) was completed, a new interpretation was proposed that these scars were not volcanic features, but rather resulted from sulfide oxidation, acid weathering, and erosion of altered rock. Four major controls that are now thought to induce scar formation: 1) steep slope angle; 2) strong tectonic shearing; 3) high-sulfide content (mostly pyrite, >1%); and 4) low vegetation cover (Meyer and Leonardson, 1990).

Geological relationships indicate the scars are associated with Tertiary andesitic rocks that have been extensively altered by hydrothermal fluids, and are developed locally in the base of the Amalia Tuff. The Amalia Tuff is physically more competent than the underlying andesitic rocks, resulting in the formation of near-

vertical spires or hoodoos at the highest ridges of the scars. Recent studies by Lueth and others (2006), suggest that these scars initiated near the contact of the Amalia Tuff (rhyolite tuff) and older andesitic rocks as hydrothermal fluids ponded at the base of the more competent rhyolitic rocks, causing intense alteration.

The combination of this intense QSP alteration coupled with zones of conjugate fractures over intrusions was critical in localization of modern scars with respect to deposition of pyrite and the establishment of pathways for modern

Figure 2. Example of natural occurring alteration scar located throughout the Red River valley, NM. Photograph taken on knife ridge located between Upper Southwest Hansen and Lower Southwest Hansen alteration scars. Photograph courtesy of Leann Giese.

groundwater penetration (Lueth et al., 2006). Fracturing in these areas is pervasive down to the microscopic level (Caine, 2003; Ludington et al. 2004), which enhances the physical weathering in the scar areas (Lueth et al. 2006). Recent dating of

supergene jarosite indicates weathering of the scar material may have begun as early as 4.5 million years ago and continues to the present (Lueth et al., 2006).

The main geologic factor that affects the mineralogy of the alteration scars is the oxidation of pyrite. This oxidation process creates sulfuric acid that dissolves hypogene minerals forming sulfates and precipitation of Fe-oxides and Fe-oxyhydroxide minerals (McLemore et al., 2004). The production of sulfuric acid from pyrite oxidation has the potential to dissolve silicate minerals; however, the precipitation of secondary clay minerals is dependent on pH and fluid chemistry.

The chemical weathering to form sulfates can cause the rock to become incompetent, causing landsliding, slumpage and erosion of the interior of the scar, causing physical weathering of the material. However, this weathering also can form a ferricrete, an iron oxide-cemented conglomerate. Ferricrete formation occurs at the base of scars where iron-rich solutions mix with local groundwater under highly oxidizing conditions and precipitates hematite and goethite (Lueth et al., 2006).

1.3 Weathering Systems

Physical and chemical weathering occurs within the alteration scars. Chemical weathering enhances physical removal of material by disaggregating the rock and physical weathering enhances chemical dissolution by increasing access of fluids to rock material, increasing the exposed mineral surface area (White and Brantley, 1995). These two types of weathering co-exist in nature and influence one another.

Two types of chemical weathering are proposed to exist in the alterations scars and include: 1) sulfide weathering (pyrite-calcite to gypsum) and 2) silicate

weathering. The general concepts of these two different types of chemical weathering are discussed below.

1.3.1 *Sulfide weathering*

The reaction of pyrite with aqueous solutions containing ferric iron or oxygen ultimately produces sulfuric acid and dissolved ferric iron (McKibben and Barnes, 1986). The two reactions listed below are thought to control the oxidation of pyrite to aqueous sulfate (Garrels and Thompson, 1960).

$$FeS_2 + 7/2O_2 + H_2O \longrightarrow Fe^{2+} + 2\ SO_4^{2-} + 2H^+ \quad (1)$$

$$FeS_2 + 14\ Fe^{3+} + 8\ H_2O \longrightarrow 14\ Fe^{2+} + 2\ SO_4^{2-} + 14H^+ \quad (2)$$

The oxidation of pyrite, in the first equation, is controlled by the oxidant oxygen, which is supplied by the atmosphere and water. This oxidant produces aqueous sulfate, dissolved iron and an acidic environment. Reaction (2) oxidizes pyrite by ferric iron in water. The products from reaction (2) are ferrous iron, sulfate, and even more acid.

For reaction (2) to continue, the supply of ferric iron needs to be rejuvenated through the oxidation of ferrous iron as described by the reaction:

$$Fe^{2+} + ¼\ O_2 + H^+ \longrightarrow Fe^{3+} + ½\ H_2O \quad (3)$$

The rate of reaction (3) is greatly enhanced by the bacterium *Acidothiobacillus ferrooxidans*, which can accelerate the rate of aqueous ferrous iron oxidation by a factor of at least 10^5 relative to the abiotic rate (Singer & Stumm, 1968, 1970). The bacteria feed on sulfur from pyrite, and ferrous iron is released and oxidized by atmospheric oxygen. The resulting equation for the oxidation of ferric iron to continue is:

$$FeS_2 + 10\ Fe^{3+} + 6\ H_2O + O_2 \longrightarrow 11\ Fe^{2+} + 2\ SO_4^{2-} + 12\ H^+ \quad (4)$$

As ferrous iron begins to leach out of the crystal sites, the sulfur-rich surface will become unstable and either disrupt and reorganize into elemental sulfur or dissolve into solution, which would be highly unstable and would form sulfate rapidly in the presence of a strong reacting agent (Nordstrom, 1982).

1.3.2 *Silicate Weathering*

The chemical weathering of feldspar minerals results from the differences in the thermodynamic conditions that existed at the time of mineral formation and that of ambient conditions at the earths surface (White and Brantley, 1995). Surfical processes that mostly affect silicate weathering are the flow and chemistry of water at the earth's surface (White and Brantley, 1995).

The alteration of feldspars generally involves initial dissolution of feldspar into solution, and the subsequent precipitation of kaolinite and other secondary phases from solution (Blum and Stillings, 1995). The dissolution and growth of secondary

white phyllosilicates occurs mainly on the base and edges of feldspar grains, and along cleavage planes (White and Brantley, 1995). Reaction (5) represents the weathering

$$\underset{\textbf{\textit{Feldspar}}}{2\ NaAlSi_3O_8} + 2\ H^+ + 9\ H_2O \longrightarrow \underset{\textbf{\textit{Kaolinite}}}{Al_2Si_2O_5(OH)_4} + 4\ H_4SiO_4 + 2\ Na^+ \quad (5)$$

of feldspar minerals. The equation can vary in both products and reactants depending on the type of feldspar dissolving. The dissolution of silicate minerals will not always precipitate clay minerals as the environmental conditions (pH) and fluid chemistry will influence if secondary clay minerals will precipitate.

Increasing concentrations of secondary mineral phases (i.e. clays and Fe-oxides) in soils with time exerts a negative impact on the dissolution rates by effectively shielding chemical interaction between the physical mineral surface and soil water (White, 1995). High solute concentrations may promote the effects of aluminum and other species (Fe) in fluids that have been experimentally shown to inhibit feldspar dissolution (White, 1995). Low pH fluids tend to dissolve clay minerals and prevent the precipitation of kaolinite or other secondary clay minerals (Krauskopf and Bird, 1995; Lawson et al., 2005).

2. GEOLOGIC BACKGROUND

2.1 Geologic Setting

The Questa mining district, located in the Sangre de Cristo range of northern New Mexico, has had a long and complex volcanic, plutonic, tectonic and hydrothermal geological history (Meyer, 1990). It is situated on the southern margin of the Oligocene Questa caldera of the late-Oligocene Latir volcanic field and on the eastern flank of the modern Rio Grande rift valley (Lipman, 1983; Meyer, 1990). The Latir volcanic field covers about 1200 km^2 and is composed primarily of alkaline rocks of intermediate composition that range from basaltic andesite volcanic and volcaniclastic rocks to peralkaline rhyolite flows and ash-flow tuffs (Figure 3) (Lipman, 1983). Mid-Miocene to present day uplift of the Sangre de Cristo range has exposed a complex geologic history of the volcanic field (Meyer, 1990).

Pre-volcanic rocks located in the Questa mining district are composed of Proterozoic metasedimetary and metaigneous rocks overlain by lower Tertiary fluvial sedimentary rocks (Meyer and Foland, 1991). These sedimentary Tertiary rocks were produced from Paleocene to Eocene erosion of Laramide highlands of Precambrian provenance (Lipman, 1983). This upward-fining sequence of sedimentary rocks range from 0-180 meters in thickness and is an excellent stratigraphic marker, when exposed, between pre-and syn-volcanic rocks (Meyer and Foland, 1991).

Volcanism initiated during the development of early rift extension of the modern Rio Grande rift, approximately 29 Ma (Meyer and Foland, 1991). During this period of volcanic activity, a thick sequence of intermediate composition (mostly andesitic) rocks was erupted. During the waning stages, a change in volcanism

occurred and rhyolitic rocks were erupted on top of the intermediate composition rocks. The final stages of volcanism were associated with the eruption of the Amalia Tuff and the formation of the Questa caldera (Meyer 1990).

Pre- and syn-volcanic intrusions are found within the Latir volcanic field and range in composition from felsic to intermediate (Meyer, 1990). After the formation of the Questa Caldera, volcanic rocks were intruded by a series of highly evolved silica granites and subvolcanic porphyries that are the apparent source of hydrothermal fluids that formed a series of molybdenum deposits in the mining district (Ludington et al., 2004). These intrusions were emplaced after 25 Ma and occur as small dikes and stocks along a N 75°E trend that extends about 20 km from the Bear Canyon Pluton, on the western range front, and extend to at least the reaches of Bitter Creek, northeast of the village of Red River (Ludington et al., 2004). Lueth et al. (2006) presented one of the first successful $^{40}Ar/^{39}Ar$ ages (alunite) of hydrothermal alteration in the Red River area (24.86 ± 0.15 Ma), which is similar in age to numerous intrusions.

Approximately 15 Ma, modern Rio Grande rifting began and is characterized by north-south-striking axial grabens and rift-flanking uplifts (Chapin, 1979; Tweto, 1979; Morgan et al., 1986; Meyer and Foland, 1991, Ludington et al., 2004). This Miocene to recent tectonic event is responsible for the uplift and erosion of the present day Sangre de Cristo range, which exposes the batholiths and the lower reaches of the Questa Caldera (Meyer and Foland, 1991). The western flank of the Rio Grande rift block is down dropped and covered with rift-fill sediments, covering the western side of the Questa Caldera (Meyer and Foland, 1991).

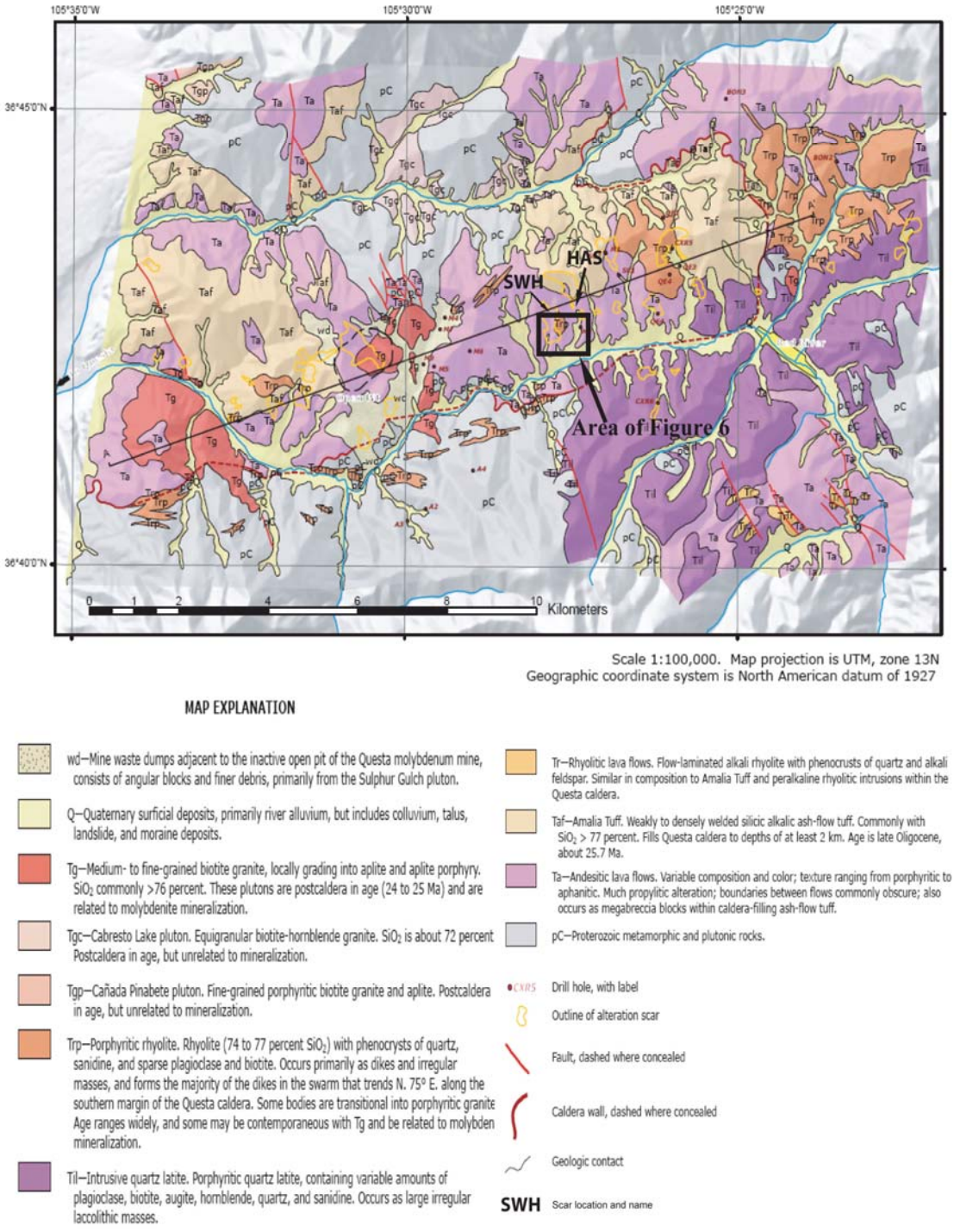

Figure 3. Generalized geologic map of the Questa Mining District. Modified from Lipman and Reed (1989) and Ludington et al., (2004). (SWH = Southwest Hansen alteration scar and HAS = Hansen alteration scar)

2.2 Regional Alteration

Extensive hydrothermal alteration of volcanic rocks, resulting from hydrothermal fluids evolved from numerous intrusions, occurs along a N 75°E trend along the lower Red River Valley; an area of about 18 km long by 4 km wide (Ludington et al., 2004). Economically important mineralization occurs in the Questa deposits as molybdenite (MoS_2) and has been mined from a horseshoe shaped ore body from 1919 to the present. The ore deposit formed from magmatic-hydrothermal fluids that were expelled from magma as it crystallized to form intrusive rocks (Ludington et al., 2004). The magmatic-hydrothermal fluids deposited quartz, molybdenite, pyrite, fluorite, carbonates and associated minerals in veins, stockwork vein systems, and breccia ore bodies (Ross et al., 2002). This mineralization event created an alteration shell around the ore deposit, which is composed of the following alteration suites: potassic, magnetite-hematite veining, QSP, propylitic, and advanced argillic.

2.2.1 *Potassic Alteration*

Potassic alteration is directly associated with the molybdenite mineralization. This altered the rocks, regardless of their type or composition, to a mixture of biotite, potassium feldspar, quartz, fluorite and molybdenite. Potassic alteration occurs closest to the intruding porphyry stock, so it is interpreted to be the highest temperature alteration of the deposit. Locating an unrecognized potassic alteration zone in the Questa area could be used as an exploration tool for locating economically important ore bodies.

2.2.2 *Magnetite-Hematite Veining*

Stockwork veining of magnetite-hematite occurs in a shell overlapping the outer portions of the potassic zone in the Molycorp open pit (Ludington et al., 2004). Also associated with this magnetite-hematite veining is hydrothermal anhydrite with intergrown secondary gypsum that occurs in the stockworks around the periphery of the potassically-altered rocks (Martineau et al., 1977). Similarly, limited occurrences of gypsum and anhydrite have been noted in drill core beneath the alteration scars (Loucks et al., 1977).

2.2.3 *Quartz-Sericite-Pyrite (QSP) Alteration*

QSP alteration occurs above and outwards from the main potassic alteration zone (Ludington et al., 2004). This alteration is characterized by the extensive development of quartz, pyrite, and white phyllosilicates. In addition to altering the host rock, crosscutting veinlets of quartz and pyrite as well as crosscutting veinlets of dominantly sericite, with lesser abundances of quartz and pyrite, are present in this alteration stage (Figure 4) (Ludington et al., 2004). The most pyrite-rich QSP alteration in the Questa area occurs in andesitic rocks and apparently resulted from the reaction of abundant iron-bearing silicates and iron-titanium oxides with sulfur rich hydrothermal fluids (Ludington et al., 2004). Alternatively, in the silicic host rocks, rhyolite porphyries and the Amalia Tuff, QSP alteration is not well developed because of the lack of iron-bearing silicate minerals to react with hydrothermal sulfur (Ludington et al., 2004).

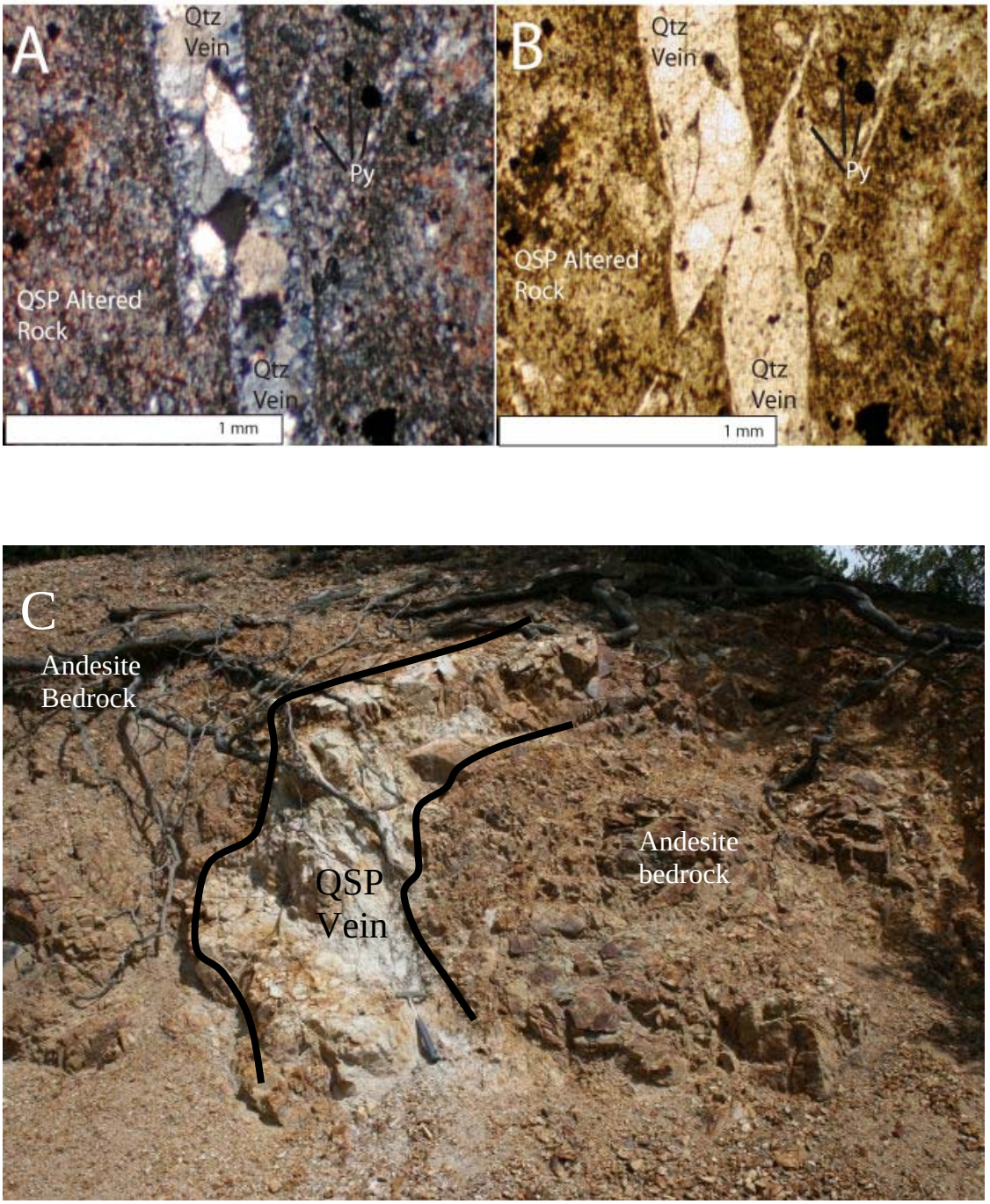

Figure 4. Photomicrographs of quartz and pyrite stockwork veinlets crosscutting QSP altered rocks, as described by Ludington et al., 2004. Samples are from upper Southwest Hansen alteration scar. A) SWH-GJG-0022, Cross Polarized Light (XPL); B) SWH-GJG-0022, Plane Polarized Light, (PPL), (Qtz= quartz, Py = pyrite); C) Hydrothermal QSP vein in andesite bedrock, located east of lower Southwest Hansen alteration scar. Note hammer for scale

Clay mineralogical analysis in the current study has documented the presence of dominantly illite in gray clay zones (described below), while smectite occurs around these intense QSP zones (gray clays). These mineralogical variations are suggestive that the dominant mineral assemblage classified as QSP is more representative of an intermediate argillic alteration. These two alteration types appear to be complexly interrelated. The remainder of this thesis will use the term QSP when describing either alteration, to be consistent with geological and alteration studies from previous authors.

2.2.4 *Propylitic Alteration*

Propylitic alteration associated with the magmatic-hydrothermal fluids partially overlaps and in part occurs peripherally to the QSP alteration (Ludington et al., 2004). These altered rocks contain chlorite, epidote, albite and some calcite and are usually green in color. This alteration is also associated with andesitic rocks as there was high Ca, Mg, and Fe to form abundant chlorite and epidote (Ludington et al., 2004). This alteration is associated with the main mineralizing event; however, there was an earlier regional propylitic alteration event that affected the rocks of the Latir volcanic field (Ludington et al, 2004).

It is difficult to differentiate between propylitic alteration from the mineralizing event and pre-mineralizing alteration. The older propylitic alteration event has been altered, in places, to a QSP-overprinting propylitic alteration from the mineralizing event. Depending on the extent of the QSP alteration, a mix of quartz,

pyrite and white phyllosilicates are observed in thin section replacing feldspars, chlorite, carbonates and epidote (Figure 5)(Ludington, et al., 2004).

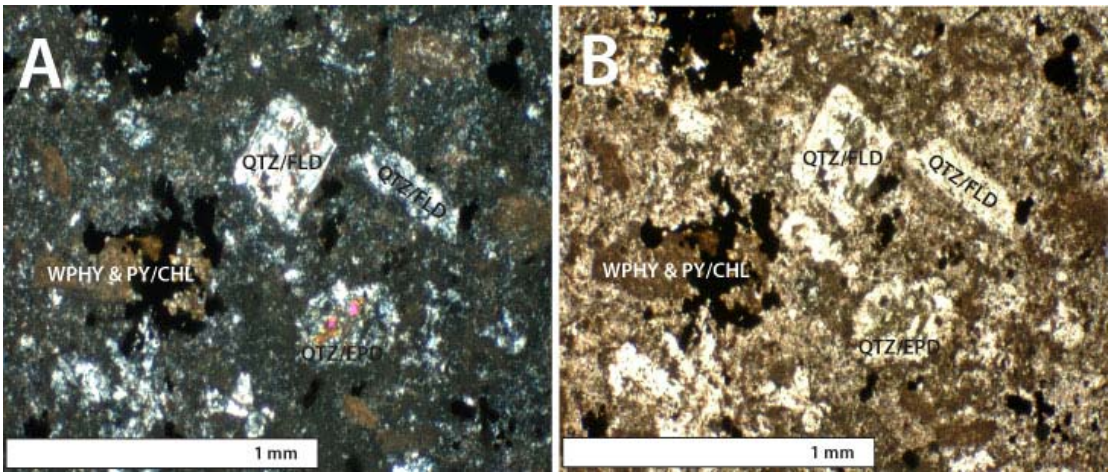

Figure 5. Photomicrographs of QSP alteration overprinting older propylitic alteration, as described by Ludington et al., 2004. Samples are from Hansen alteration scar. A) HAS-GJG-0006 XPL; B) HAS-GJG-0006-PPL, (XPL= Cross Polarized Light), (PPL = Plane Polarized Light), (QTZ/FLD= quartz replacing feldspar, QTZ/EPD = quartz replacing epidote, WPHY & PY/CHL = white phyllosilicates and pyrite replacing chlorite)

2.2.5 *Advanced Argillic*

Advanced argillic alteration occurs as an outer halo of the magmatic-hydrothermal system at Questa. The advanced argillic zone is characterized by well-crystallized kaolinite, poorly crystallized kaolinite, alunite, and sericite alteration (Livo and Clark, 2002). This alteration zone occurs in the highest elevation alteration scars and is generally associated with the Amalia Tuff (rhyolite).

2.3 Local Geology and Alteration

Geologic mapping of the study area was completed on a scale of 1:5700 (Figure 6). The area is located approximately 2.5 miles from the Questa Molybdenum

Mine and encompasses the ridge west of the Southwest Hansen alteration scar to the ridge east of the Hansen alteration scar. Geologic mapping was completed to determine the lithologic units and geologic features common to both of the alterations scars.

The rocks in the area (oldest to youngest) include: Tertiary porphyritic andesite (Tpa), Tertiary dacite flow (Td), Tertiary quartz latite porphyry (Tap), Quaternary debris flow (Qdf), and Quaternary alluvium and colluvium (Qac). The porphyritic andesite erupted during the early stages of the Oligocene Latir volcanic field. This unit is dark green to gray, massive and very thick (~2500 ft, Martineau et al., 1977). The andesite contains abundant plagioclase phenocrysts (5-20%) that range in size from 1-4 mm. Other identifiable minerals in hand specimen include chlorite, epidote, pyrite, quartz and goethite/hematite (Figure 7). The mineralogy varies locally depending on the intensity of propylitic and QSP alteration.

Tertiary dacite flows lie stratigraphically below the Amalia Tuff unit and directly above the Tertiary andesitic units. This dacite (Td) unit may represent the onset of felsic volcanism, erupted before the Amalia Tuff and the collapse of the Questa caldera. The Amalia Tuff is not located with in the mapping area, but lies directly to the north at the head of both alteration scars. Dacite is porphyritic to aphanitic and contains potassium and plagioclase feldspar phenocrysts (5-10%) ranging in size from 1-4 mm. Pumice fragments are located within the groundmass, suggesting an extrusive origin of the rock. Orbicular quartz and white phyllosilicates are abundant in hand sample (Figure 8).

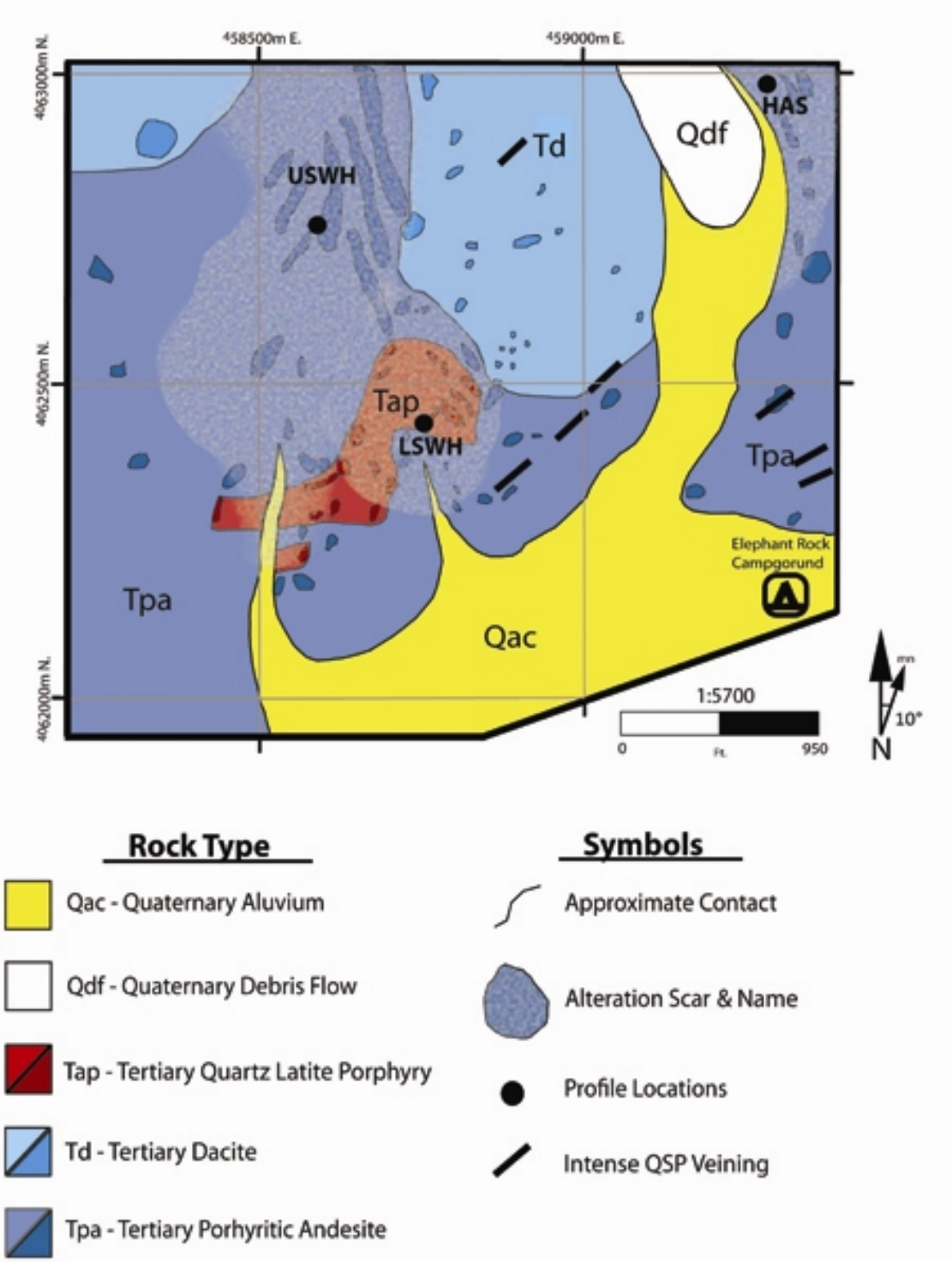

Figure 6. Generalized geologic outcrop map of the Southwest Hansen and Hansen alteration scars. Dark color variations represent outcrops mapped in the area. Area mapped by Gabriel Graf, Leann Giese and Virginia McLemore (September 2007)

Figure 7. Tertiary andesite rocks from the alteration scars. Notice the dark green to brown color, which is remnant of propylitic alteration.

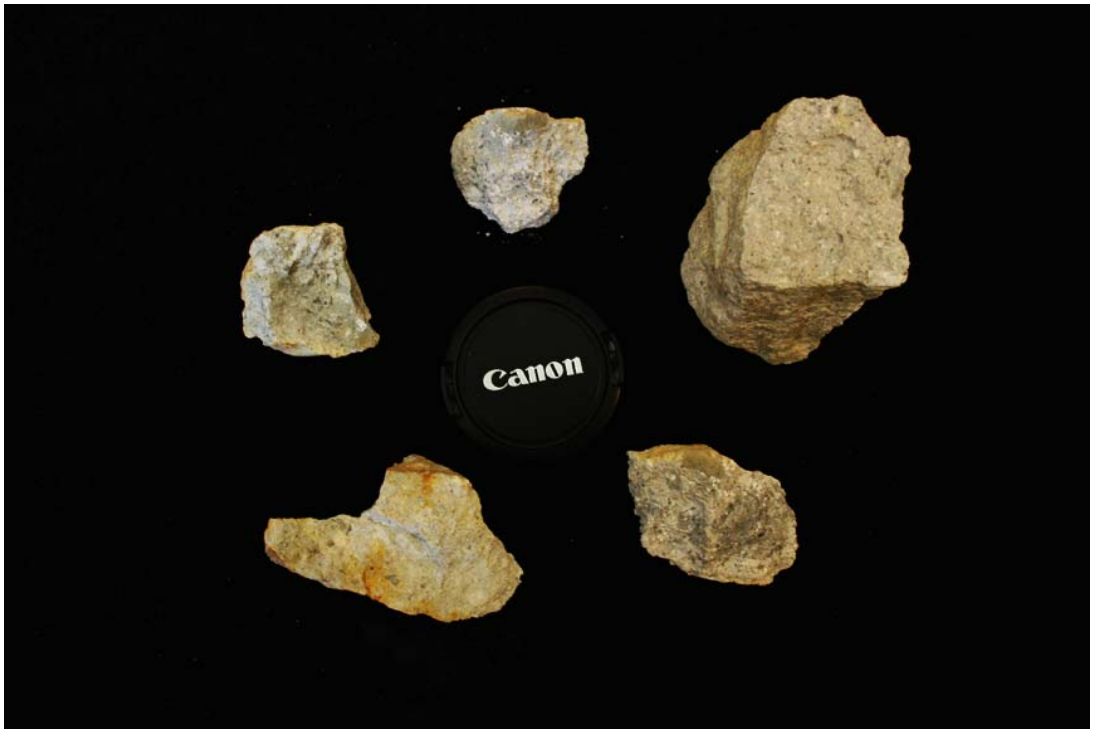

Figure 8. Tertiary dacite rocks from the alteration scars.

A post volcanic intrusive rock has been identified in the lower reaches of the Southwest Hansen drainage. This intrusive rock has been identified as a hypabassal quartz latite porphyry sill (Figure 9). The rock intruded into the porphyritic andesite and contains large xenoliths (meter-size) of andesite within the intrusive unit. The quartz latite porphyry is white-gray in color and contains abundant plagioclase (15-30%) and potassium feldspar (5-10%) phenocrysts that range in size from 4-10 mm. The rock also contains identifiable quartz, white phyllosilicates and pyrite.

Figure 9. Tertiary quartz latite porphyry rocks from the alteration scars.

Alteration in the study area is restricted to propylitic alteration, QSP alteration, and QSP overprinting of propylitic alteration in the study area. The ridge to the west of the Southwest Hansen scar is the only area containing dominantly propylitic alteration, with minimal evidence of QSP alteration. Andesitic rocks outside of the alteration scars still contain abundant chlorite and epidote in hand specimen and are a

dark green color. Minimal pyrite is present in the rocks mapped to the west of the Southwest Hansen Drainage.

Andesite and quartz latite porphyry located within the Southwest Hansen and Hansen drainage are intensely QSP altered. These rocks are pyrite rich (2-5%) and contain abundant clay minerals. These areas of intensely QSP alteration contain “gray clay” layers or veins (Figure 10), which occur in 1-3 meter bands or 1-2 mm veins within the bedrock.

Figure 10. Gray clay layers located throughout the alteration scars. Note: gypsum crystal in bottom right corner

The dacite flow located at the top of the central ridge of the study area appears to have experienced less QSP and propylitic alteration. Pyrite is present but in small components (<1%). These rocks are more competent and have experienced less chemical and physical weathering.

A large debris flow (probably Quaternary in age) emanated from the Upper Hansen alteration scar. The debris flow caused the drainage to shift further to the east and incised a channel (~10 ft.) deep within the present Hansen drainage. Debris aprons of alluvium and colluvium developed on both the Hansen and Southwest Hansen drainages. Mudslides and/or debris flows transport large amounts of material into the drainages and onto the debris aprons during extremely wet periods.

3. METHODS

3.1 Sampling

Sampling was conducted in November 2006 during which samples were collected from three distinct profiles. These samples were collected to determine the mineralogical changes through each profile. Two weathering profiles were collected in Southwest Hansen alteration scar and one weathering profile was collected in the Hansen alteration scar.

Eight samples were collected from the lower amphitheater of Southwest Hansen (LSWH) (UTM Coordinates 458732 E., 4062439 N.) (Figure 6), which spanned thirty-seven feet (Figure 11). Sample locations were selected based on interpreted changes in lithology or mineralogy (color changes). Samples were collected using a rock hammer, shovel and a ladder to access the higher reaches of the profile. The lithologies encountered included unweathered quartz latite porphyry, weathered quartz latite porphyry, gray clay segregations (QSP veins), and residual soils with rock fragments, near the top of the profile.

Five samples were collected from the Hansen alteration scar profile (HAS) (UTM Coordinate 459288 E., 4062957 N.) (Figure 6) that spanned twenty-two feet (Figure 12). These samples were collected where, by observation, it appears that the lithology and/or mineralogy changes. Samples were collected with a rock hammer and shovel, from andesite bedrock, to weathered andesite bedrock, and finally residual soils.

The final weathering profile was collected in the upper amphitheater of Southwest Hansen alteration scar (USWH) (UTM Coordinates 458592 E., 4062741

N.) (Figure 6). This was the shortest profile with four samples that spanned seven feet (Figure 13). The profile was sampled from andesite bedrock, weathered andesite bedrock and was capped by a ferricrete.

The samples collected from the weathering profiles in Southwest Hansen and Hansen alteration scars were subjected to a variety of analyses. Weathering changes can clearly be recognized in samples spanning the weathering profiles. Table 1 is a list of samples studied. In-situ sample photographs are located in Appendix E.

Table 1. List of Samples used in study

Date	Sample Number	Rock Type	Comments
11/2/2006	SWH-GJG-0008	Bedrock (porphyry)	East Arroyo of Scar
11/2/2006	SWH-GJG-0009	Weathered bedrock (porphyry)	East Arroyo of Scar
11/2/2006	SWH-GJG-0010	Gray Clay Vein	East Arroyo of Scar
11/2/2006	SWH-GJG-0011	Weathered rock, residual soil	East Arroyo of Scar
11/2/2006	SWH-GJG-0012	Weathered rock, residual soil	East Arroyo of Scar
11/2/2006	SWH-GJG-0013	White Clay Vein (?)	East Arroyo of Scar, similar to clay on SSW & SSS
11/2/2006	SWH-GJG-0014	Weathered rock, residual soil	East Arroyo of Scar
11/2/2006	SWH-GJG-0015	Weathered rock, residual soil	East Arroyo of Scar
11/3/2006	SWH-GJG-0020	Andesite Bedrock	Upper amphitheater on side slope above modern stream gully
11/3/2006	SWH-GJG-0021	Weathered Andesite	Upper amphitheater on side slope above modern stream gully
11/3/2006	SWH-GJG-0022	Weathered Andesite/Residual Soil	Upper amphitheater on side slope above modern stream gully
11/3/2006	SWH-GJG-0023	Ferricrete	Upper amphitheater on side slope above modern stream gully
11/2/2006	HAS-GJG-0006	Andesite Bedrock	NE Rills of Scar
11/2/2006	HAS-GJG-0007	Weathered Andesite	NE Rills of Scar
11/2/2006	HAS-GJG-0008	Weathered Andesite/residual soil	NE Rills of Scar
11/2/2006	HAS-GJG-0009	Weathered Andesite/residual soil	NE Rills of Scar
11/2/2006	HAS-GJG-0010	Weathered Andesite/residual soil	NE Rills of Scar

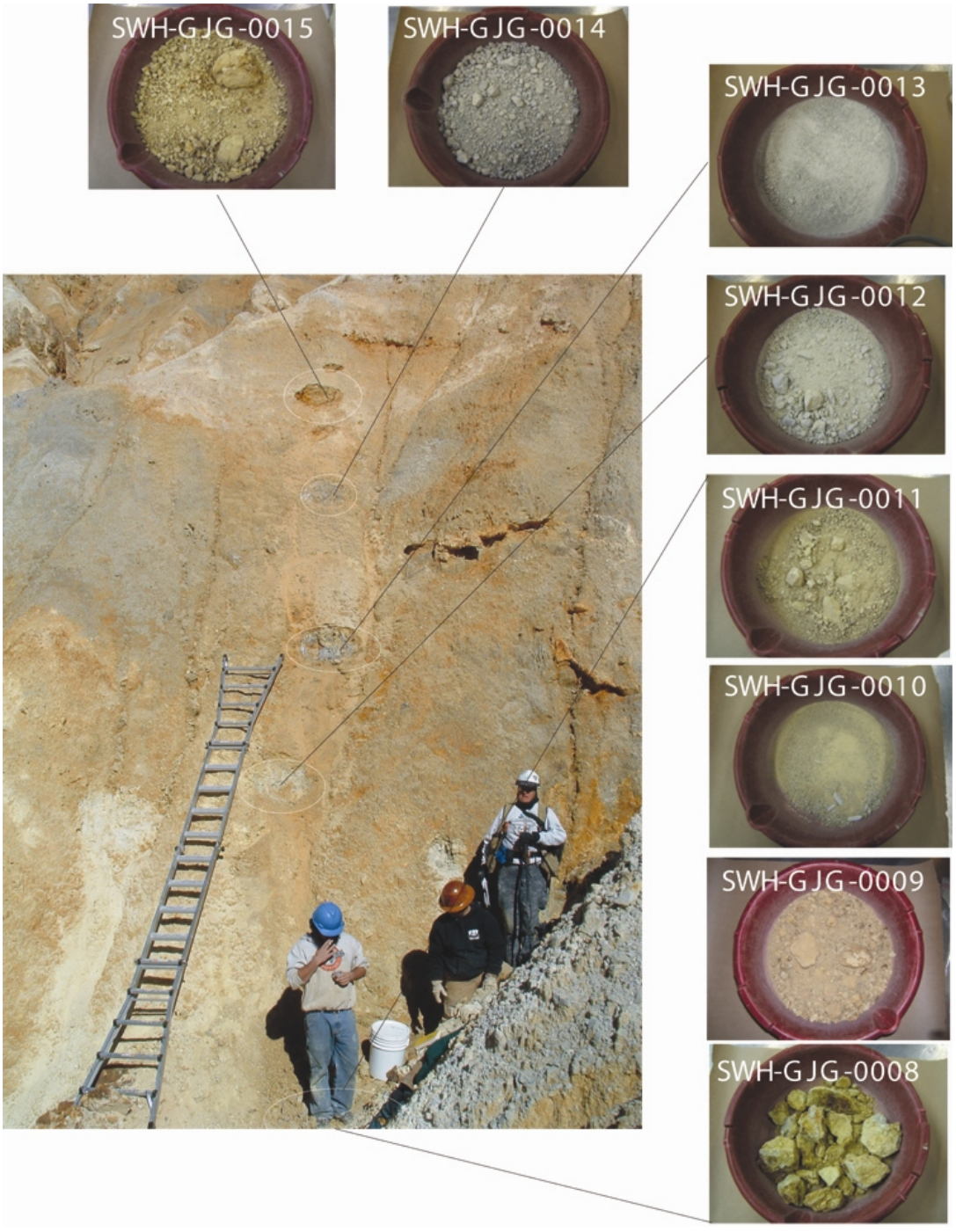

Figure 11. Photo showing locations and sample numbers of profile samples in lower amphitheater Southwest Hansen alteration scar.

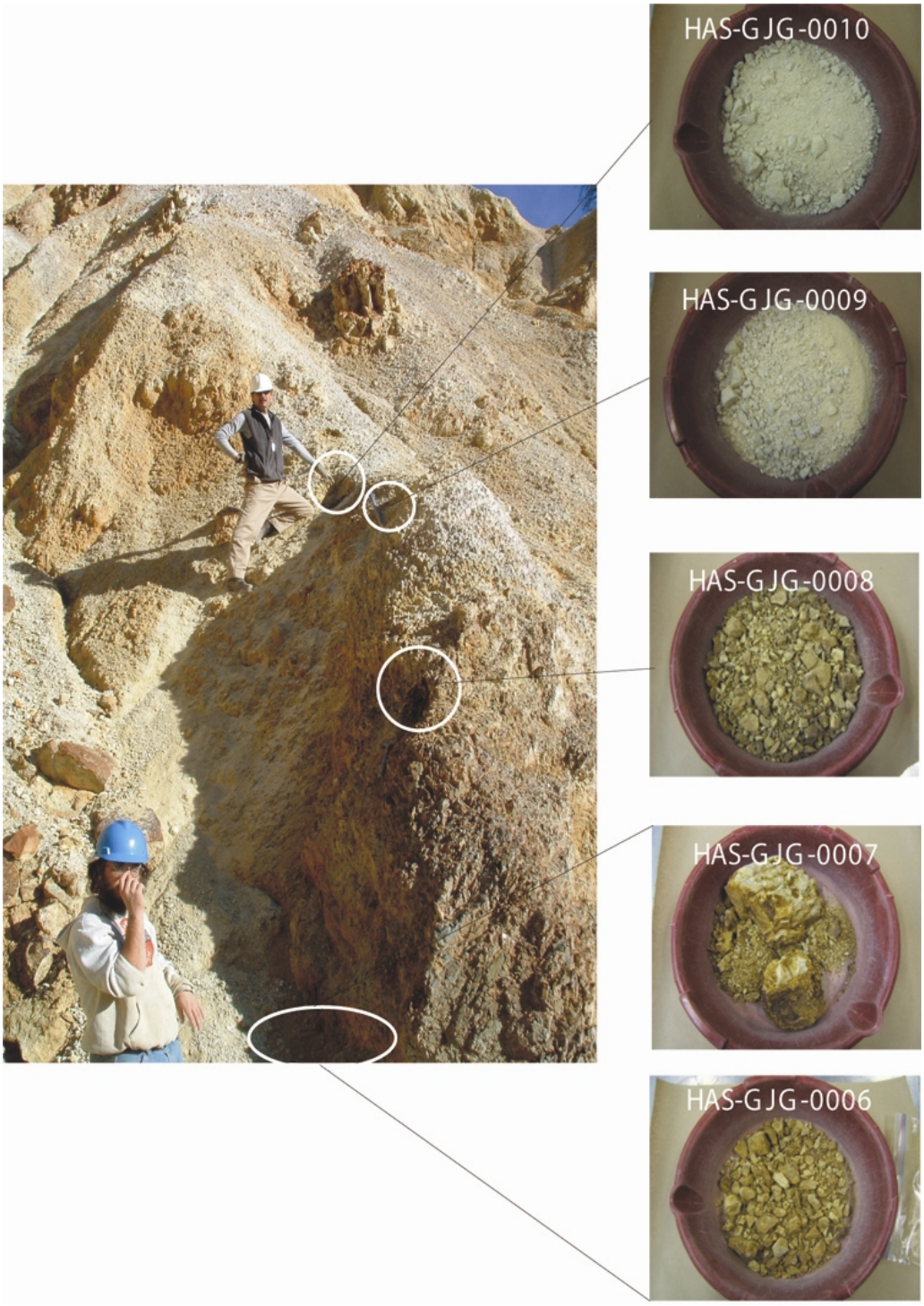

Figure 12. Photo showing locations and sample numbers of profile samples in the Hansen alteration scar.

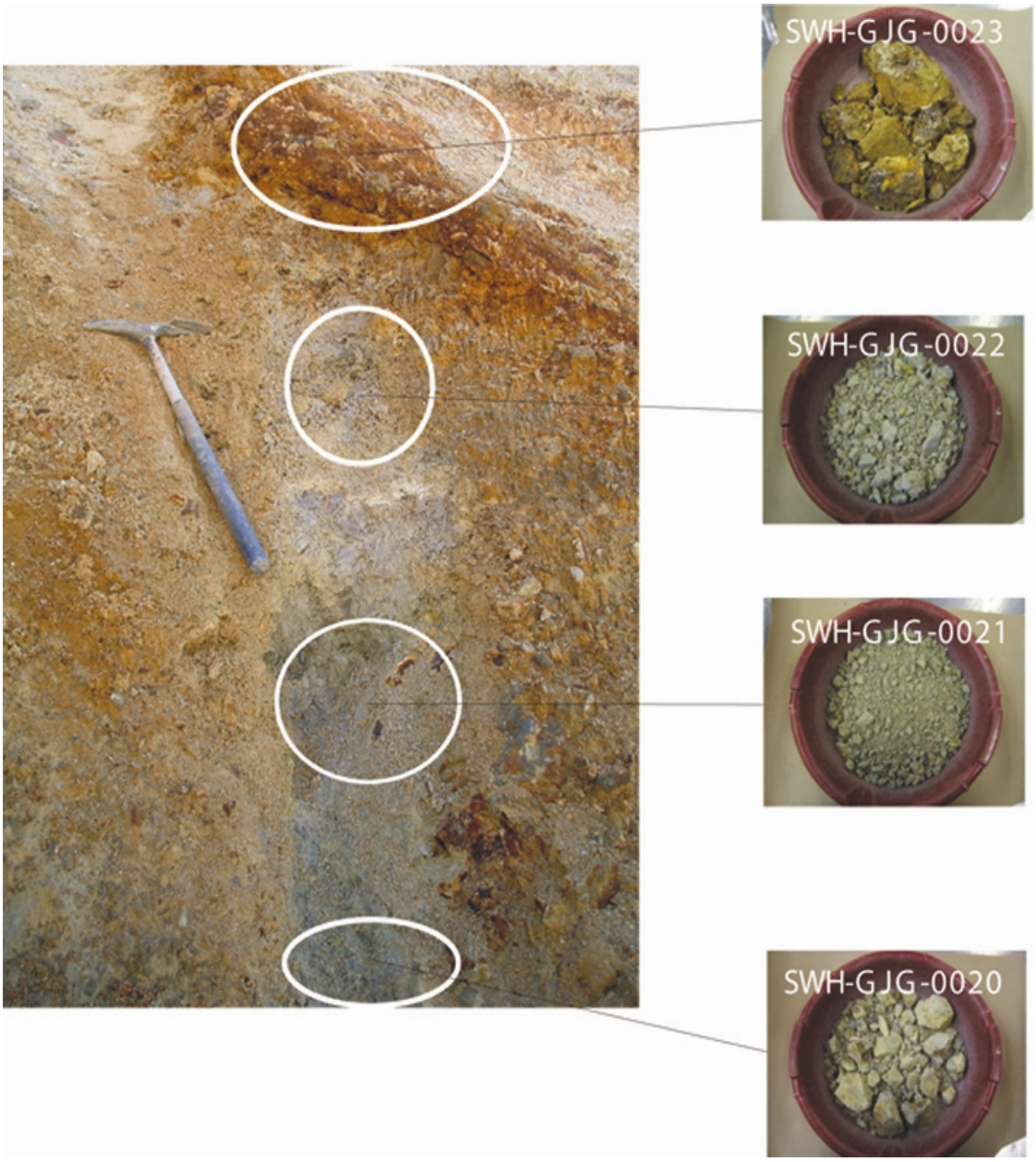

Figure 13. Photo showing locations and sample numbers of andesite profile samples in the upper amphitheater of Southwest Hansen alteration scar.

3.2 Particle Size Analysis

Particle size analysis was performed on samples, based on ASTM standards, from the three profiles to determine the amount of gravel, sand, and fine particles. Using the assumption that the top of any given profile has experienced a longer period of weathering than the samples at the bottom of a profile, a prediction was made that the samples should decrease in grain size from the bottom to the top of the profiles.

Two methods were used because of the misrepresentation of the total amount of fines in the samples due to the agglomeration of clay particles. For each method, the total amount of sample was weighed, and the resulting gravel, sands and fines were weighed to determine the percentage of each size fraction. All samples were performed using U.S. Standard Sieves.

Method 1, "Dry Sieving" consisted of mechanically dry sieving particles that were larger than 75 μm. The samples were shaken in a W.S. Tyler, Inc. Sieve Shaker Rx-86 for approximately 30 minutes and weighed. Particles that were smaller than 75 μm were not analyzed using the hydrometer test, as the total amount of fines was more important in this study than the distribution of silt to clay.

Method 2, "Wet Sieving Equivalent" consisted of mechanically sieving particles larger than 75 μm in the sieve shaker for approximately 30 minutes. After this, the agglomerated particles were physically removed and were broken by a physically induced technique using a mortar and pestle. The broken agglomerated particles were then returned to the sieves and shaken for another 30 minutes. The samples were then weighed to determine the percentage of gravel, sand and fines

present in each sample. Even though this method was termed "Wet Sieving Equivalent," water was never used in the preparation and analysis.

The two methods were completed on all of the profile samples. The results were then compared to determine which procedure provided a more representative analysis of the fines present in the samples. It was determined that Method 2, "Wet Sieve Equivalent" provided more representative results of the percentage of fines present in the samples because of the known agglomeration of clay particles. The remainder of this thesis will focus on particle size results from Method 2 "Wet Sieve Equivalent." Table 2 provides a summary of the results of the two different methods preformed for particle size analysis for sample SWH-GJG-0011. Figure 14 is a plot showing the comparison of the two methods used in the particle size analysis.

Table 2. Table summarizing the differences in results between the two methods of particle size analysis (SWH-GJG-0011).

	Method 1, "Dry Sieving"	Method 2, "Wet Sieve Equivalent"
Fines (%)	0.35	2.87
Sand (%)	41.29	58.71
Gravel (%)	58.37	38.42

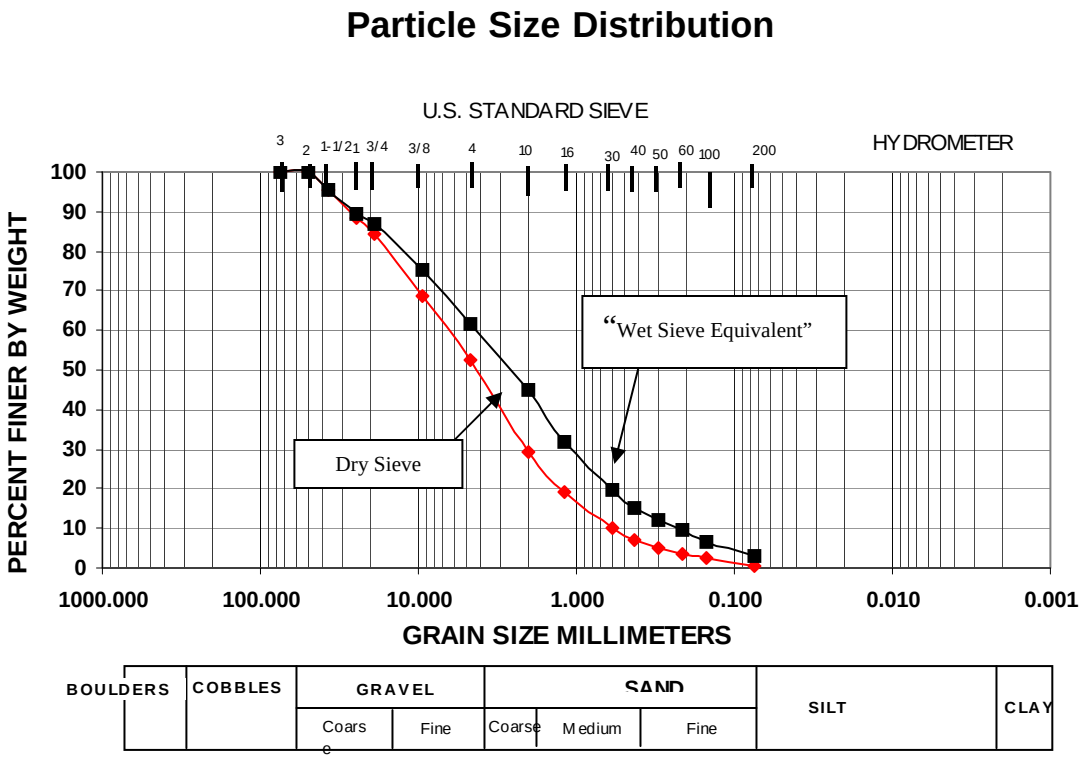

Figure 14. Comparison graph showing the results from the two different methods used in particle size analysis

3.3 Whole Rock and Particle Size Split Geochemistry

Geochemical analysis was completed on whole rock samples and on particle size splits from the three weathering profiles. The particle size splits included both coarse (>25 mm) material and fine grain (<0.2 mm) material. Whole rock analyzes were completed on all the profile samples and particle size splits were completed on one profile (HAS). These analyses were completed to determine the effect of both chemical and physical weathering that may occur in the weathering profiles. Any chemical changes between the coarse and fine grain particle sizes could indicate chemical weathering occurring as the particle size of the material decreases.

Sample preparation for the whole rock and coarse particle size split samples involved using a jaw crusher to break up the rock. These broken rocks were then crushed to roughly pea size gravel using a smaller jaw crusher. The finer grained particle size splits were not crushed in the jaw crushers because of their already fine grain nature.

Samples crushed in the jaw crushers and fine-grained particle size samples were crushed to a fine powder using a tungsten-carbide crushing disk. The tungsten-carbide disk was used to prevent any chemical contamination into the samples. Two to four tablespoons, 75-100 grams, of material were placed into the tungsten-carbide crushing disk and were shaken on a Bico, Inc. pulverizer for 90 seconds. The fine powder was removed from the puck with a rubber spatula and placed on a clean sheet of paper. Once this crushing procedure had been replicated for a total of four times, the sample was "cone-cut-and-quartered" to rehomogenize the sample. They were then split into four separate envelopes, 75-100 grams each, for the different analyzes to be preformed on the samples.

Following the completion of the sample crushing, one envelope of each sample was sent to the Washington State Chemistry Laboratory. The samples were analyzed using standard X-Ray Fluorescence (XRF). Duplicate and triplicate analyses were completed to check the precision of the machine.

3.3.1 *Isocon Calculations*

The isocon method (Grant, 1986) was originally developed for metasomatically altered rocks, but has been modified to document changes through

these weathering profiles. The final results from the isocon calculations document changes in the gains or losses of elemental oxide compositions relative to the least altered sample. "By careful considerations of the field relationships and petrology of the area, one may be able to determine a "least-altered equivalent" (Grant, 1986)".

In this study, the bottom samples of the each weathering profile were selected as the "least altered equivalent" based on the previous assumption that the bottoms of the profiles have undergone the shortest period of weathering. Major elemental oxides from XRF results for each sample in a profile were compared to the least altered rock (bottom profile). This chemical data was then scaled to ensure all chemical elemental oxides plot within the same scale for each sample. This scale is arbitrary and any value can be assigned to each individual element.

Another assumption needs to be made for plotting the results. A choice of constant volume, constant mass, or a constant element oxide is needed to determine the percent gains and losses for each individual element. The most constant of the elemental oxides in the alteration scar profiles was TiO_2. The scaled chemical data for TiO_2 can be used to determine the slope of a line for constant TiO_2 (6). The scaled data is plotted with least altered on the x-axis and altered on the y-axis (Figure 15). This diagram provides the relative gains and losses relative to constant TiO_2. The exact gains and losses can then be calculated using an equation from Grant, 1986 (7).

$$\text{Constant } TiO_2 = TiO_2 \text{ altered rock} / TiO_2 \text{ least altered rock} \quad (6)$$

$$\%\text{ gain or loss} = (((\text{oxide altered}/\text{ oxide least altered})/\text{Constant } TiO_2)-1) \times 100 \quad (7)$$

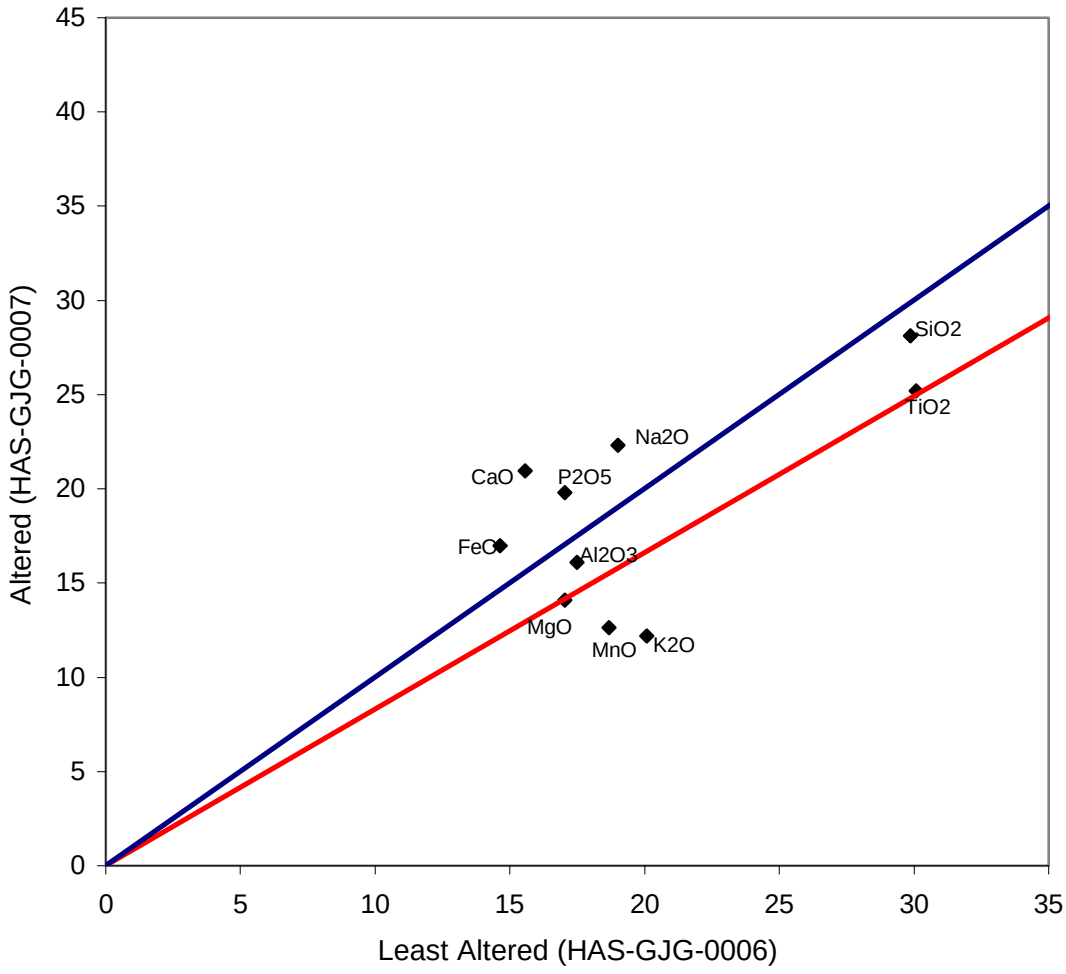

Figure 15. Example of an Isocon diagram for samples in weathering profile. Red line represents constant TiO_2 and blue line represents constant mass. Elemental oxides plotting above red line are enriched and oxides below and depleted, with respect to the least altered sample.

3.4 Acid Base Accounting

Pyrite oxidation of the samples results in the generation of sulfuric acid in the alteration scars. Acid potential, neutralizing potential and paste pH measurement were completed on the profile samples to determine the balance between acid producing and acid consuming minerals and the relative pH of samples through a profile. The

results will help to identify the potential for any further pyrite oxidation in the samples. Acid potential and neutralization potential are from Sobek Acid Base Accounting Method (Sobek, 1978).

3.4.1 Neutralizing Potential (NP)

The amount of neutralizing bases, including carbonates, present in alteration scar material is found by treating a sample with a known excess of standardized hydrochloric acid. The sample and acid are heated to insure that the reaction between the acid and the neutralizers goes to completion. The calcium carbonate equivalent of the sample is obtained by determining the amount of unconsumed acid by titration with standardized sodium hydroxide (Questa Project, SOP 62).

The procedure begins with weighing 0.5 g of pulverized material on a watch glass to check for the presence of calcium carbonate ($CaCO_3$). One or two drops of 25% hydrochloric acid (HCl) are added to the material to determine if there is a reaction of $CaCO_3$ with the HCl acid. An observation is made on the degree of reaction that is observed (Table 3) and a "fizz rating" is assigned to each individual sample based on the observations.

Following the observation of the "fizz rating," 2.00 g of pulverized sample was weighed and added to a wide mouth conical flask. Then HCl acid was added to the flask, amount and normality dependent of the "fizz rating." The flask was placed on a hot plate and heated until the sample begins to boil. The flask was swirled every 5 minutes until the reaction goes to completion; when no gas evolution is visible and the particles settle evenly over the bottom of the flask. Distilled water (125 mL) was

Table 3. Observation, fizz rating and amount and normality of acid required for NP analysis (from SOP 62).

Observation	Fizz Rating	HCl	
		(ml)	(Normality)
Not audible nor visible	None	20	0.1
Audible but not visible	Slight	40	0.1
Audible and visible	Moderate	40	0.5
Very audible and visible	Strong	80	0.5

added to the flask and the material was placed on the hot plate and boiled for one minute. The samples are then removed from the hot plate and set aside to cool to slightly above room temperature. Parafilm was placed over the flask and the material was allowed to cool to room temperature. The samples are set aside until analysis can be completed.

The analysis begins with titrating the sample using standardized NaOH, either 0.1 or 0.5 N depending on fizz rating assigned, to a pH of 7.0. The total volume of NaOH used to titrate the sample to pH 7.0 is recorded for NP calculations (below). A blank sample is analyzed for each of the different "fizz ratings" used in that batch of samples. This blank is comprised of only HCl and is titrated to a pH of 7.0. The blank allows for a calculation of a constant that is used in calculating the total NP. The following calculations are used to complete the NP analysis:

$$\text{Constant } \{C\} = (\text{mL of acid in blank} - \text{mL of base in blank})$$

$$\text{mL of acid consumed} = (\text{ml of acid added} - (\text{mL of based added} \times C))$$

$$\text{NP (kg } CaCO_3\text{/ton)} = (\text{mL of acid consumed}) \times (25) \times (\text{N of acid})$$

A simple calculation of the NP can also be completed if the amount of carbon in each sample is known and assumed to only be from $CaCO_3$:

1 weight % C = 83.33 tons $CaCO_3$ equivalent / 1000 tons of rock

NP = weight % C x 83.33

3.4.2 *Acid Potential (AP)*

Acid Potential (AP) tests were completed on the pulverized sample material to determine the amount of potential (kg $CaCO_3$ /ton) need to neutralize the acid produced. The principle behind the method is that reduced sulfur in a soil sample is directly oxidized to acid with hydrogen peroxide and titrated with a standard base to evaluate the acid potential of the soil (SOP 62). By completing both AP and NP tests, the potential for the rock to be acid producing or acid consuming can be determined.

The treatment and analysis began by adding 3.0 g of sample material into a funnel fitted with filter paper. Leaching of the sample was completed by adding 300 mL of 40 % hydrochloric acid (HCl) in funnel filled increments, followed by distilled water rinsing of the material using funnel filled increments. This was done until the effluent is free from chloride. To test for presence of chloride, 10% silver nitrate solution was added in the effluent. If a white cloudy coloration did not form in the effluent, no chloride remained in the samples. The filter paper and sample were set aside to air-dry overnight.

After the material had air-dried, 2.00 g of material was scraped from the filter paper into a 150 mL tall form beaker and 24 ml of 30% H_2O_2 was added to the beakers

and heated to 40°C on a hot plate. The samples were removed from the hot plate when they reached the desired temperature and set aside for 30 minutes to allow for the reaction to go to completion. An additional 12 mL of 30% H_2O_2 was added to the flask to allow the solution and material to react for 30 minutes. The beaker was placed back onto the hot plate at approximately 90-95°C and allowed to react for 30 minutes until the unreacted H_2O_2 was completely destroyed. The sides of beaker are rinsed with distilled water, filling the beaker to 100 mL. The beaker was placed back onto the hot plate to drive off any dissolved CO_2 and then set aside to cool at room temperature.

The resulting solution is titrated using 0.1 N NaOH, which was CO_2 free and sealed off from the atmosphere. The solution is titrated to pH of 7.0 and the amount of 0.1 N NaOH needed to reach a solution with pH equal to 7.0 is recorded. Calculations can then be used to determine the AP of each sample:

$$\text{meq } (H^+)/100g = (\text{mL of NaOH}) \times (\text{Normality of NaOH}) \times (50)$$

$$\text{tons } (H^+)/\text{thousand tons of material} = \text{meq } (H^+)/100g \times 0.01$$

- one ton of H^+ requires 50 tons of $CaCO_3$ to neutralize the material

AP (kg of $CaCO_3$/ton) = (mL of NaOH) x (Normality of NaOH) x (25)

3.4.3 *Paste pH*

Paste pH analyses were completed to evaluate the geochemical behavior of alteration scar materials subject to weathering under field conditions and to estimate the pH and conductivity of the pore water resulting from dissolution of secondary mineral phases on the surfaces of oxidized rock particles (SOP 11). These analyses

will estimate the pH of the samples and help determine the acidity of the alteration scar samples. The method is based on the Sobek method (1978).

This method is completed on uncrushed samples once the samples are returned from the field. The sample is sieved through US Standard Sieve size 10 to obtain both sand, silt and clay sized material for the test. After sieving the material, 25 g of the material is placed in a decontaminated beaker. Approximately 25 mL of deionized water is added to the beaker and the material and solution is stirred with a glass rod until it forms a paste. The beaker is set-aside for 10 minutes.

The pH and conductivity meters are calibrated during this 10-minute period. The probes are calibrated using standard solutions of known pH and conductivities. Once calibrated, the paste pH, paste conductivity and total dissolved solids (TDS) of the samples can be analyzed. The beakers are tipped to one side to allow a pool of water or slurry to collect on that side. The probe is then inserted into this slurry to measure the pH, conductivity, and TDS. The measurements are recorded and the probes are decontaminated between each sample.

3.5 Sulfide-Sulfate Ratios

Sulfide and sulfate ratios were determined to document the degree of pyrite oxidation to form sulfates (i.e. gypsum). The results from these ratios may help to determine the reaction progress in the sulfide weathering system in the weathering profiles. One packet of the finely powdered and homogenized sample from whole rock and particle size split geochemistry preparation was sent to the ALS Chemex laboratory in Reno, NV for analysis.

Geochemical analysis of total sulfur and sulfate was completed using the standard Leco furnace method. This procedure analyzes the samples, at low temperature, for total sulfate from S_2 gas. The samples are reanalyzed at higher temperature for the total sulfur as S_2 gas. The amount of total sulfide can be determined from the subtraction the two reported results (total sulfur – sulfur from sulfate = sulfur from sulfide). Total carbon is also analyzed and reported as CO_2 from the method.

3.6 Mineralogical Analyses

The weathering profile samples have been analyzed using petrographic analysis, clay XRD analysis, standard quantitative X-Ray diffraction (QXRD) and a mineralogical modeling software program (ModAn) that uses Gaussian elimination and multiple linear regression techniques to solve simultaneous mass balance equations (Paktunc, 2001). By using the four unique methods, best estimates of mineralogy can be determined for the three profiles.

QXRD was only performed on the Hansen profile so an alternate method was needed to establish semi-quantitative mineralogy for the remaining two profiles. The results of the ModAn modeling simulations are compared to the QXRD from the Hansen profile to determine if the ModAn modeling program can be used to determine the best estimate of mineralogy through the weathering profile and then be applied to the other profiles.

3.6.1 *Petrography*

Large and small rock fragments from the bulk composite samples were selected to make thin section billets and fabricated into polished thin sections for mineralogical analysis. The thin sections were analyzed by standard petrographic analysis (mineralogy, percentages, and textures) using both reflected and polarized light on a Nikon Optiphot Pol research petrographic microscope.

3.6.2 *Clay Mineralogy*

The mineralogy of the clay material may potentially help determine the origin of clay minerals and to see possible weathering effects occurring in the silicate weathering system. The clays analyzed were from both the weathered matrix and the core of rock clasts.

Preparation of matrix clay minerals was completed by grab sampling of the fine-grained material. The preparation of the rock clays was completed by grab sampling crushed rock fragments used for the geochemical preparations. Both types of samples were placed in a beaker of water to allow for any clay-sized minerals to stay in suspension longer than silt-sized minerals. The clay minerals were then carefully removed from the beaker with a dropper and placed onto a thin section slide and set aside to dry. The samples were analyzed at New Mexico State University in Las Cruses, NM using standard X-Ray Diffraction techniques (XRD).

3.6.3 *Quantitative X-Ray Diffraction (QXRD)*

QXRD sample preparation for the whole rock, coarse particle size (>25 mm) and fine grained material (<0.2 mm) was completed using the same procedure for whole rock geochemistry described in section 3.3. One envelope of each sample packet from the Hansen weathering profile was analyzed using standard QXRD analysis. The analysis provided mineralogical weight percentages for each of the mineral phases identified using the XRD Topaz computer program. The values are reported in weight percentage and the reported standard error is ± 2-weight % for this procedure. QXRD analysis was completed at the Nicolet National Laboratories, Madison, WI.

3.6.4 *ModAn Mineralogy Modeling*

The ModAn modeling program (Paktunc, 2001) is used to estimate mineral quantities in sulfide-rich rocks using whole rock geochemical analysis. Geochemistry of the weathering profile samples was completed using standard XRF procedures at the Washington State Chemistry Laboratories. The percentage of elemental oxides is input to the model to calculate the mineral abundances of each sample.

A few parameters constrain the use of this program and must be considered before attempting to model mineralogy with ModAn. These parameters include the presence of sulfide minerals, in addition to the presence of sulfate minerals. The program is only useful when one sulfide mineral is present. If pyrite and chalcopyrite are both present, the program can only model one of the sulfide minerals and will not accurately report the sulfide mineral abundances. In the case of the alteration scar weathering profiles, pyrite is the dominant sulfide mineral phase. Chalcopyrite has

been observed in the profile samples but only in small abundances (<0.1%), and was ignored in the calculations.

ModAn simulations were not design to calculate the amount of sulfate in samples. Gypsum and jarosite are sulfate minerals that have been documented to exist in each of the weathering profiles sampled. Gypsum is more abundant than jarosite, so a simplification was employed accounting all sulfate in the sample as gypsum. This assumption allows for simplified mathematical calculations to determine the total weight percentage of sulfate utilizing the following algorithm:

Weight percentage sulfate = (amount of sulfur in sulfate x 96) / 32

Weight percentage gypsum = (weight percentage sulfate / 0.557)

Ca in gypsum = (amount of gypsum / 0.233)

CaO in Gypsum = (56.078 x amount of Ca) / 40.078

CaO from each sample containing sulfate can be subtracted from the XRF CaO to account for amount of gypsum. By correcting for the amount of CaO in gypsum from the geochemical analysis, the program can be used to model mineralogy with a calculated amount of gypsum removed.

The ModAn mineralogy program may be used to model all of the weathering profiles to determine a semi-quantitative mineralogy. Before using this program, the different minerals selected for the model were based on thin section petrography and clay mineralogy studies. The minerals used in the ModAn simulation contain mineral compositions from Questa area minerals, which where determined by electron

microprobe analysis (D. Sweeney, personal comm.). The minerals used in the ModAn program include: Moly Na-spar 1, Moly ksp 2, avg. Moly clay, Moly epidote 1, Moly chlorite 1, Fe-oxides 1, calcite, quartz and pyrite (Table 4). Quartz and calcite are from the ModAn database of ninety-two general mineral compositions. The Avg. Moly clay is the average composition of Questa composition illite, smectite, kaolinite and mixed layer clays. Parts in ten calculations completed from clay mineralogy studies, (Hall, 2004; Donahue, et al., 2007) were used to determine the weight percentages of each of these simulated clay minerals.

Table 4. Mineral compositions from the Questa Area

Mineral	**Composition**
Moly Na-Spar 1	$(K_{0.03}, Na_{0.78}, Ca_{0.18})Al_{1.22}Si_{2.8}O_8$
Moly ksp 2	$(K_{0.99}, Na_{0.04})Al_{1.03}Si_{2.97}O_8$
Avg. Moly clay	$(K_{0.33}, Na_{0.05}, Ca_{0.07})(Fe_{0.29}, Mn_{0.01,} Mg_{0.61}) Al_{2.56}Si_{3.85}O_{13}$
Moly Epidote 1	$Ca_{1.82}(Fe_{1.47}Al_{1.82})Si_{2.74}O_{13}$
Moly Chlorite 1	$(K_{0.03}, Na_{0..17}, Ca_{0.02})(Fe_{1.83}, Mn_{0.24,} Mg_{6.16}) Al_{1.67}Si_{2.67}O_{18}$
Fe-Oxides	$(Fe_{0.9}, Ti_{0.05,} Mg_{0.08})O_2$

To run a simulation for each individual sample, geochemical data was imported into the ModAn program, and corrected for gypsum CaO. The petrographic mineral assemblages were entered into the simulation to estimate the abundance of each mineral. If a mineral contained a negative mode, it was suppressed from the

simulation and the process restarted. This was completed until all negative mineral modes were removed from the simulation. Only the minerals noted in individual sample petrography were allowed for the ModAn simulations.

3.7 Stable Isotope Geochemistry

Stable isotopes from a variety of minerals were completed in this study to determine the origin of these minerals. The minerals and isotopes analyzed include: 1) pyrite ($\delta^{34}S$); 2) gypsum ($\delta^{34}S$ & $\delta^{18}O_{SO4}$); and 3) clays (mixture of illite, smectite, chlorite, and kaolinite) ($\delta^{18}O$ & δD). The results from these analyzes will help determine the origin of the minerals (i.e. hydrothermal or weathering).

3.7.1. *Sulfide and sulfate minerals*

Sulfur were completed on both pyrite and gypsum and oxygen isotopes completed on gypsum. By completing both the $\delta^{34}S$ and $\delta^{18}O_{SO4}$ it may be possible to discriminate supergene gypsum from hydrothermal gypsum. The following preparation methods were used prior to stable isotope analysis.

3.7.1.1 Gypsum preparation

Gypsum crystals were hand-picked using a tweezers under a Wild M8 variable magnification binocular microscope. The gypsum was picked from the fine-grained sample material, fracture fillings, gypsum coatings on rock fragments, and large crystals found in the field near sample locations.

Gypsum contains two oxygen sites within its chemical structure ($CaSO_4 \cdot 2H_2O$), however, the oxygen in the sulfate (SO_4) is the desired oxygen to be analyzed. This oxygen will provide insights into the origin of the sulfate minerals (ancient supergene, modern supergene, or magmatic). A method was developed by Wasserman et al., (1998) to dissolve alunite and reprecipitate the dissolve sulfate as barite ($BaSO_4$). This method was modified at the New Mexico Institute of Mining and Technology Stable Isotope Laboratory for gypsum (Campbell and Lueth, 2008).

The procedure began by adding 120 mg of 0.5 N NaOH to a 150-200 mL beaker. Then 60 mg of gypsum was weighed and added to the solution in the beaker. The beaker was heated on a stirring hot plate at 80°C for 3 hours and periodically checked to see that the gypsum was being dissolved. After 3 hours of heating, the samples were set aside to cool until filtering can be performed.

Once the samples have cooled sufficiently, the solution was filtered through a 1.0μm cellulose nitrate membrane Whatman filtering device. This filtering ensures that any solid residue that was not dissolved will remain on the filter. The solution was then reheated to 80°C on the stirring hot plate and quickly acidified using 10 N HCl to a pH of < 2. One 2 ml squirt of 0.5 N $BaCl_2$ was added to the solution. The sample was heated for 2-3 hours and periodically checked for the presence of precipitating white material (barite). The sample was removed from the heating plate and set aside to cool overnight. The material was then filtered with a 0.45μm cellulose nitrate membrane Whatman filtering device, dried in the oven at 30°C, weighed and stored until analysis could be completed.

3.7.1.2 Pyrite Preparation

Selected rock fragments containing pyrite from the bottom samples of the three weathering profiles were prepared for $\delta^{34}S$ analysis. These samples were selected because of the abundance of pyrite towards the bottom of the profiles. Because of the fine-grained nature of the pyrite grains in the rock fragments, the samples were crushed in a disk grinder to a fine powder.

Pyrite grains were separated using sodium metatungstate heavy liquid with a density of three. This allows for the pyrite grains to sink to the bottom of the device and the lighter minerals (i.e. quartz, feldspars, and clays) to float to the top of the device. The pyrite crystals were placed into a funnel fitted with filter paper to remove the heavy liquids and leave the remaining pyrite crystals. The samples were rinsed with distilled water until the heavy liquids were completely removed and then dried in an oven.

The resulting material was examined under a binocular microscope to determine if there were any other minerals besides pyrite. Some quartz and clay minerals were observed, so the material was run through a Franz magnetic separator to try to concentrate as much of the pyrite as possible. Pyrite crystals were then hand picked from the material and placed in sample vials until the material could be analyzed.

3.7.1.3 $\delta^{18}O$ Analysis of Sulfate Isotopes

Gypsum crystals that were chemically converted to barite were analyzed to determine the $\delta^{18}O$ of sulfate. This method uses the continuous flow method on the

FinniganMAT Delta Plus XP Gas Mass Spectrometer using a CO reference gas. Reference samples analyzed include NBS127 (National Bureau of Standards isotope standard) and benzoic acid (HEKA isotopic standard). The known reference values are used to make a correction curve to correct the unknown samples isotopic values.

The procedure involved weighing 0.1 milligrams of barite into 3 x 5 mm silver cups (Costech # 041072). These cups were placed into a turret that drops the samples into a Thermo Finnigan TC/EA Elemental Analyzer furnace set to 1450ºC. The furnace contains a reactor of glassy carbon granules, which converts the oxygen from sulfate into carbon monoxide gas. The gas is carried through a gas chromatograph, and into the mass spectrometer through a continuous flow of helium. The gas samples were measured against the carbon monoxide reference gas to determine the oxygen isotopic value and then corrected to the known mineral standards. Reproducibility of $\delta^{18}O$ isotopic values measured on the mass spectrometer is 0.1 ‰.

3.7.1.4 $\delta^{34}S$ Analysis of Sulfur Isotopes

Pyrite crystals that were separated using the heavy liquid separation method were analyzed to determine the $\delta^{34}S$ of pyrite. This method uses the continuous flow method on the FinniganMAT Delta Plus XP Gas Mass Spectrometer using a SO_2 reference gas. Reference samples analyzed include AJC (barite) (NMT SI Laboratory in house standard), FeS (pyrrhotite) (NMT SI Laboratory in house standard), NBS123 (sphalerite)(National Bureau of Standards isotope standard) and NBS127 (barite) (National Bureau of Standards isotope standard). The known reference values are used to make a correction curve to correct the unknown samples isotopic values.

The procedure involved weighing, depending on amount of sulfur in the mineral, 0.7 mg of pyrite or 2.8 mg of barite into 3 x 5 mm pressed tin cups (Costech #041077). An additional 6.0 mg of Vanadium Pentaoxide (V_2O_5) is added to the barite samples to aid in combustion of the material. These cups are placed into a turret that dropped the samples into a Costech Elemental Combustion System CHNS-O (ECS 4010) set to a temperature of 1020°C. A sample is dropped automatically into a combustion reactor and a pulse of high purity oxygen (purity = 99.99%) is injected into the reactor. The samples combust with the addition of the oxygen and create SO_2 gas; the sulfur in the SO_2 gas is derived directly from the mineral analyzed. The gas is carried through a gas chromatograph, and into the mass spectrometer through a continuous flow of helium. The gas samples are measured against the sulfur dioxide reference gas to determine the sulfur isotopic value and then corrected to the known mineral standards. Reproducibility of $\delta^{34}S$ isotopic values measured on the mass spectrometer is ± 0.1 ‰.

3.7.2 *Clay Isotopes*

The preparation methods involved in this study were modeled after a flow chart from Gilg et al. (2004), but were modified to meet specific needs, based on the mineralogy of clay-sized material (Figure 16). Sample selection was based in part on X-Ray Diffraction (XRD) patterns from clay mineralogy studies of the Questa area (Donahue et al., 2007). Samples selected for isotope analysis from the alteration scars include, 1) “gray clay” layers, 2) HAS-GJG-0009 (pure illite), and 3) various samples from the Southwest Hansen and Hansen alteration scar profiles. The pure illite sample

is a potential end-member for determining the isotopic composition of hydrothermally produced clay. The Southwest Hansen and Hansen profile samples were selected to see the variations of clay compositions through a weathering profile. Rock pile clays from the clay leach study of Goat Hill North were also analyzed to determine the isotopic similarities and/or differences between rock pile and alteration scar clay origin.

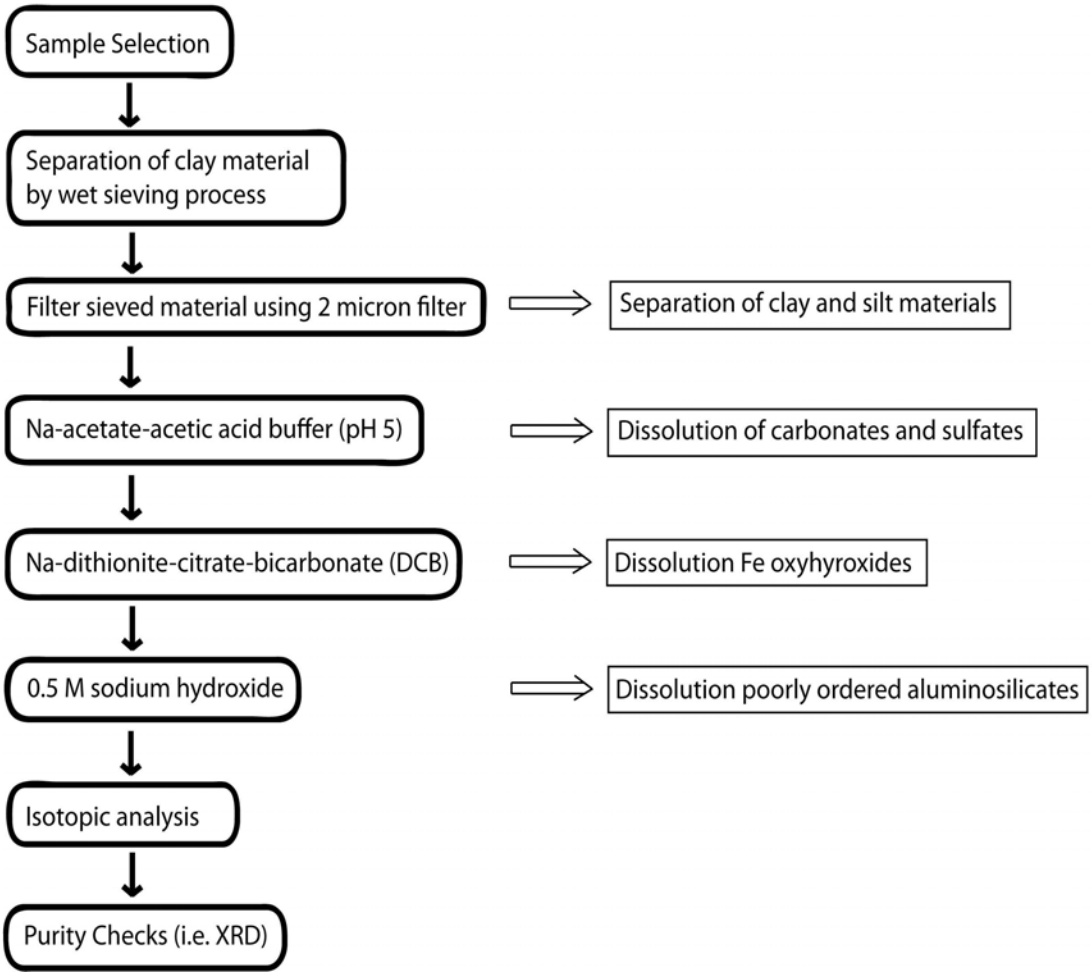

Figure 16. Flow chart of sample preparation procedures used prior to stable isotope analysis (modified from Gilg et al., 2004).

The diversity of clay-sized oxygen and hydrogen bearing minerals, identified by XRD, within the rock piles and alteration scars necessitated sample purification procedures before isotopic analysis. Clay purification treatments used in this study include a sequential treatment of the clay-sized samples in the following order: 1) 1N acetic acid buffered to pH 5; 2) Na-dithionite-citratre-bicarbonte (DCB) and 3) 0.5 M Sodium Hydroxide. These methods are described in detail below.

3.7.2.1 *Physical Separation*

The physical separation of clay-sized minerals was completed using a sedimentation process. A split of each sample was wet sieved through US Standard size sieves 10 (2 mm), 50 (0.3 mm), and 200 (0.075 mm). Clay and silt-sized material passing the 200 sieve was screened through a 2μ filter using a Millipore vacuum system. This material was then transfer to 500mL beakers and dried in an oven at 30ºC until the water evaporated. The remaining clay was pulverized using a mortar and pestle and transferred into sample bottles for storage.

3.7.2.2 *Acetic Acid Treatment*

The abundance of gypsum and calcite (both hydrothermal and supergene) in the samples could affect the final $\delta^{18}O$ of the clays. No gypsum or calcite was detected in the XRD scans of the clay-sized material; however, because of their common occurrence in local rocks, this treatment was performed.

This treatment involves treating 1.5 grams of clay-sized sample with 1N acetic acid, adjusted to a pH =5 using 1M Na-acetate (Gilg et al, 2004) and heating at 25-50ºC for 2-3 hours. Following the treatment, the sample was rinsed with distilled water and filtered through a 1.0μm cellulose nitrate membrane Whatman filtering device. The sample was weighed and stored in sample vials.

3.7.2.3 *Na-Dithionite-Citrate-Bicarbonate Treatment*

Sulfide weathering (pyrite and calcite to gypsum) of the rock piles and alteration scars precipitates goethite, hematite, and jarosite. These minerals contain oxygen, which will affect the bulk $\delta^{18}O$. Samples that were treated to remove carbonates and sulfates were subsequently treated using the Na-dithionite-citrate-bicarbonate (DCB) method (Mehra and Jackson, 1960). This treatment was completed to remove any iron oxides and hydroxides.

This treatment involves adding 1g of clay-sized sample to a mixture of 40mL of 0.3 M Na-citrate and 5mL of 1 M Na-bicarbonate into a 50mL centrifuge tube and heating in a water bath to 60ºC. After the solution reaches the desired temperature, 2 grams of Na-dithionite are added to the centrifuge tube. The sample is then stirred continuously for 1 minute and stirred for 15 seconds after every 5 minutes, for duration of fifteen minutes. The time to complete a set of ten samples was 30-45 minutes. The samples, independent of starting color, should turn gray upon completion of the test. If the sample stayed the original color, the treatment was repeated a second time.

The samples are then set aside to cool. Upon cooling of the solution, the tubes are centrifuged for 15 minutes to separate the solution and the clay material. The solution is discarded (using hazardous waste protocols because of its strong oxidizing potential) and the clay samples are rinsed with distilled water, filtered through 1.0μm cellulose nitrate membrane Whatman filtering device, and dried in an oven at 30ºC. The sample is weighed and stored in sample vials.

3.7.2.4 *0.5 M Sodium Hydroxide Treatment*

The presence of amorphous or poorly ordered aluminosilicate minerals (i.e. amorphous silica) that could affect the final $\delta^{18}O$ of the samples cannot be ruled out because these amorphous minerals are not readily detected in XRD scans. The sodium hydroxide treatment (Hashimoto and Jackson, 1960) was used to remove any amorphous minerals from the sample before isotopic analysis.

This treatment involves adding 100-150 mg of the clay sample to 100 mL of 0.5 M solution of NaOH. The addition of larger amounts of clay sample to the solution will result in the supersaturation of the solution, which will prevent the dissolution of amorphous materials (Hashimoto and Jackson, 1960). The mixture of sample and solution is brought to a rapid boil and boiled for two and a half minutes. The samples are removed from the heat and placed in a water bath at room temperature to cool.

They are washed with distilled water, filtered with a 0.45μm cellulose nitrate membrane Whatman filtering device, dried in an oven at 30ºC, weighed and stored in sample vials until isotopic analysis could be completed. The amount of treated sample

recovered ranged from 45mg to 145mg because of the sticky nature of the clay material, which made it difficult to remove all of the treated material from the Whatman filtering paper.

3.7.2.5 *XRD Analysis*

Clay mineralogy of the samples was determined by X-Ray Diffraction analysis at New Mexico State University, Las Cruces, New Mexico. These analyzes were completed prior to the chemical treatments and after the chemical treatments to check for sample purity (Figure 17). It is evident that non-clay minerals containing oxygen were removed from the clay-sized fraction before isotopic analysis. This specific sample (SWH-GJG-0022) contains jarosite as an oxygen-bearing sulfate before chemical treatments, and the post-treat XRD pattern indicate jarosite was removed from the sample prior to analysis. Comparison of all the samples pre- and post-treatment XRD patterns indicates that non-clay oxygen-bearing minerals (i.e. jarosite) were removed from the samples, with the exception of quartz.

The chemically treated clays were prepared for isotopic analysis using a technique created by Taylor and Epstein, (1962) and modified by Borthwick and Harmon, (1982). This method uses a fluorinating agent to break the silica-oxygen bond and release the oxygen as O_2 gas. The O_2 gas is converted to carbon dioxide by heating with a hot carbon rod. The CO_2 gas is measured using the dual inlet method on a FinniganMAT Delta Plus XP Gas Mass Spectrometer. $\delta^{18}O$ isotopic values are measured on the mass spectrometer with a precision of 0.1 ‰.

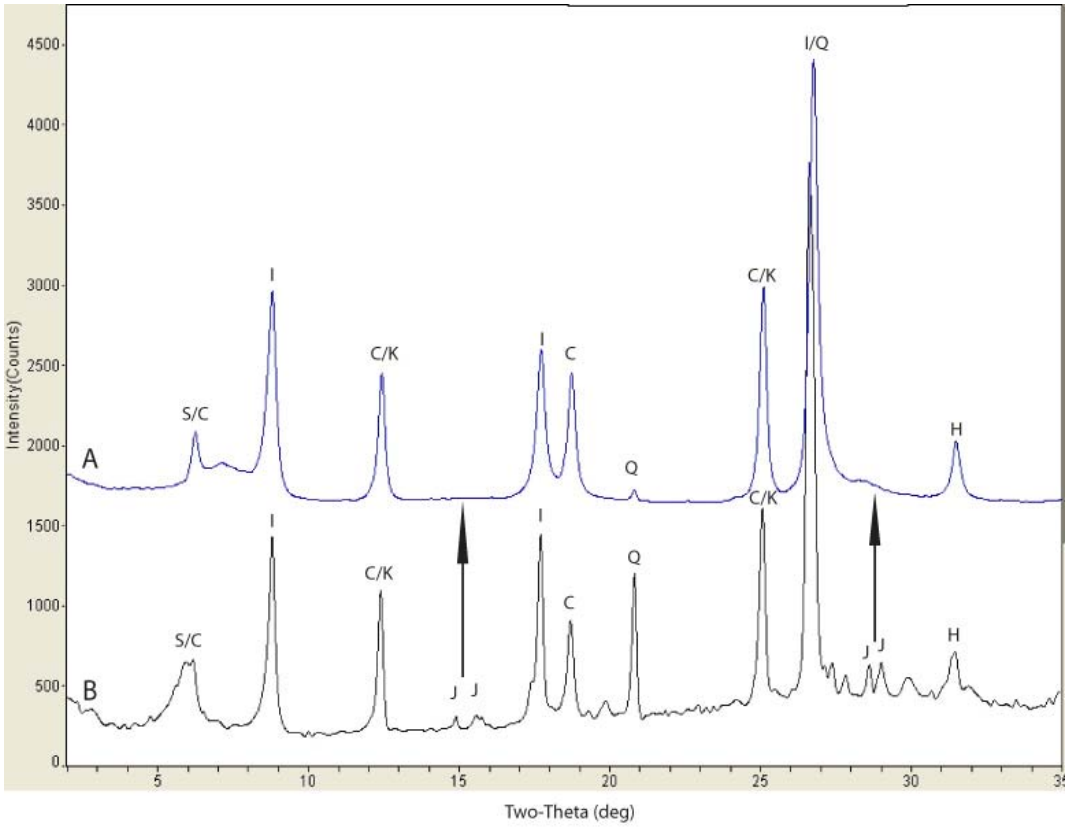

Figure 17. Comparison of XRD patterns pre-and post-chemical treatments to check for sample purity (SWH-GJG-0022). A) post-treatment XRD pattern, B) pre-treatment pattern. Notice that jarosite (J) was removed from the sample by performing chemical treatments. (Minerals – S/C = smectite & chlorite; I = illite; C/K = chlorite & kaolinite; J = jarosite; C = chlorite; Q = quartz, H = halite)

3.7.2.6 *$\delta^{18}O$ Analysis*

15 mg of chemically treated clay-sized sample were loaded into stainless steel vials for transfer into vacuum-sealed heating nickel reaction vessels. A fluorinating agent (ClF_3) is introduced into the reaction vessels and heated at 550ºC for 8 hours. The O_2 gas is expanded into a cold trap containing an electrically heated carbon rod. The carbon rod, using platinum wire as a catalyst, converts O_2 gas to carbon dioxide. The carbon dioxide is frozen in the cold trap containing the carbon rod by liquid nitrogen. The trap is heated, using a heat gun, transferring the carbon dioxide to the cold finger to measure the converted carbon dioxide gas. Liquid nitrogen is placed on

a sample vial and the cold finger is heated to transfer the carbon dioxide gas to the sample vial.

The carbon dioxide gas is measured using the dual inlet system on a FinniganMAT Delta Plus XP Gas Mass Spectrometer using an Oztech certified stable isotope gas standard. Quartz reference samples (NBS-28 from NIST) were analyzed to determine the accuracy and precision of the extraction procedure. NBS-28 reference samples known $\delta^{18}O$ isotopic composition is 9.64 ‰. The NBS-28 reference samples analyzed during this experiment were 9.0 ± 0.1 ‰.

3.7.2.7 *δD Analysis*

Chemically treated samples were analyzed to determine the hydrogen isotope composition of the clay minerals. This method uses the continuous flow method on the FinniganMAT Delta Plus XP Gas Mass Spectrometer using an Oztech certified stable isotope gas standard. Reference samples analyzed include CH7 (IAEA isotopic standard) and benzoic acid (Costech isotopic standard). The known reference values are used to make a correction curve to correct the unknown samples isotopic values.

The procedure involves weighing 1-1.5 grams of treated clay-sized sample into a 3 x 5 mm silver cup (Costech # 041072). These cups are placed into a turret that drops the samples into a Thermo Finnigan TC/EA Elemental Analyzer furnace set to 1450ºC. This furnace contains a reactor of glassy carbon granules, which converts oxygen to carbon monoxide gas and hydrogen to hydrogen gas. The gas is carried through a gas chromatograph, and into the mass spectrometer through a continuous flow of helium. The gas samples are measured against the hydrogen reference gas to

determine the hydrogen isotopic value and then corrected to the mineral standards. Reproducibility of δD isotopic values measured on the mass spectrometer is ±1 ‰.

4. RESULTS

4.1 Particle Size

A summary of the particle size results is presented in Table 5. These results illustrate how grain size changes with respect to the height in each sample profile. Each individual sample particle size analysis is located in Appendix A.

Table 5. Summary of particle size analysis

Sample #	Height from Bottom of Profile (Ft.)	%Gravel	%Sand	%Fines
HAS-GJG-0010	22	50.07	47.53	2.40
HAS-GJG-0009	17	33.78	62.71	3.51
HAS-GJG-0008	10	75.94	22.94	1.12
HAS-GJG-0007	1	94.40	5.48	0.11
HAS-GJG-0006	0	78.01	21.64	0.35
SWH-GJG-0015	37.1	36.61	62.52	0.86
SWH-GJG-0014	28.9	34.94	64.05	1.01
SWH-GJG-0013	18.8	2.37	85.87	11.76
SWH-GJG-0012	11.3	44.38	54.53	1.09
SWH-GJG-0011	1.5	38.42	58.71	2.87
SWH-GJG-0010	1.3	0.00	87.40	12.60
SWH-GJG-0009	1.1	44.28	53.80	1.92
SWH-GJG-0008	0	59.41	39.28	1.30
SWH-GJG-0023	7	85.35	13.91	0.74
SWH-GJG-0022	5	50.65	48.22	1.13
SWH-GJG-0021	3	37.33	59.26	3.41
SWH-GJG-0020	0	92.44	7.15	0.42

Figure 18 A-C depicts the location of each sample in a weathering profile versus the resulting percent finer by weight for gravel, sand, and fines (silt and clay). Generally, from the bottom to the top of each weathering profile, the percentage of gravels decrease and the percentages of sands and fines increase.

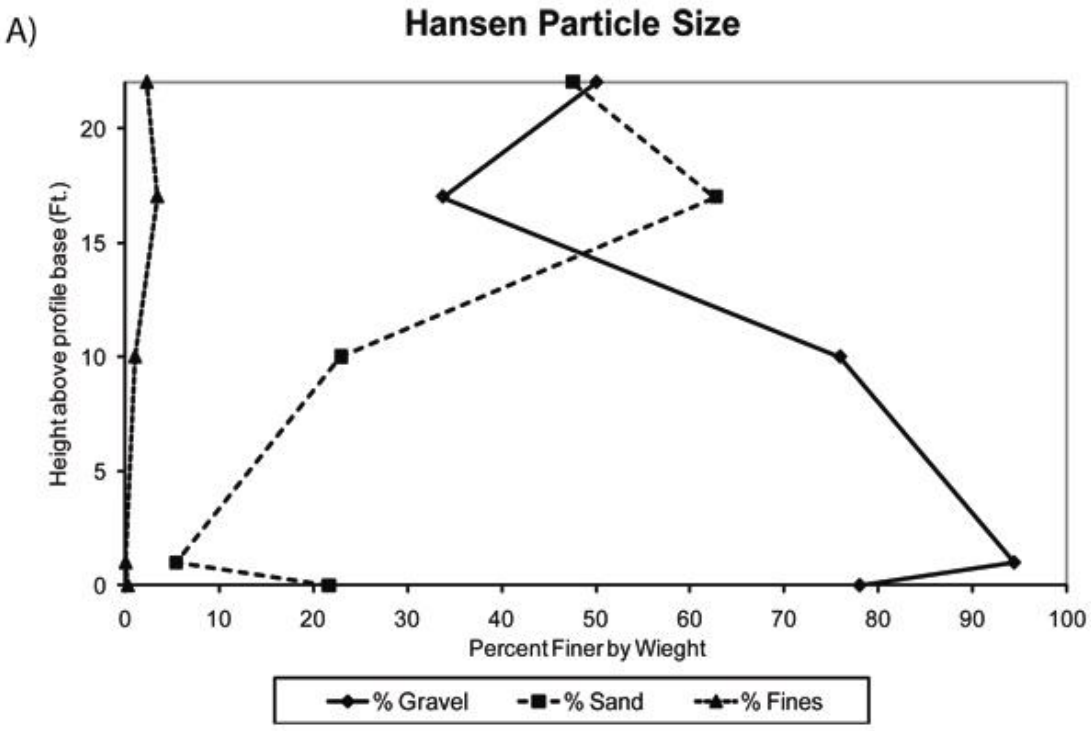

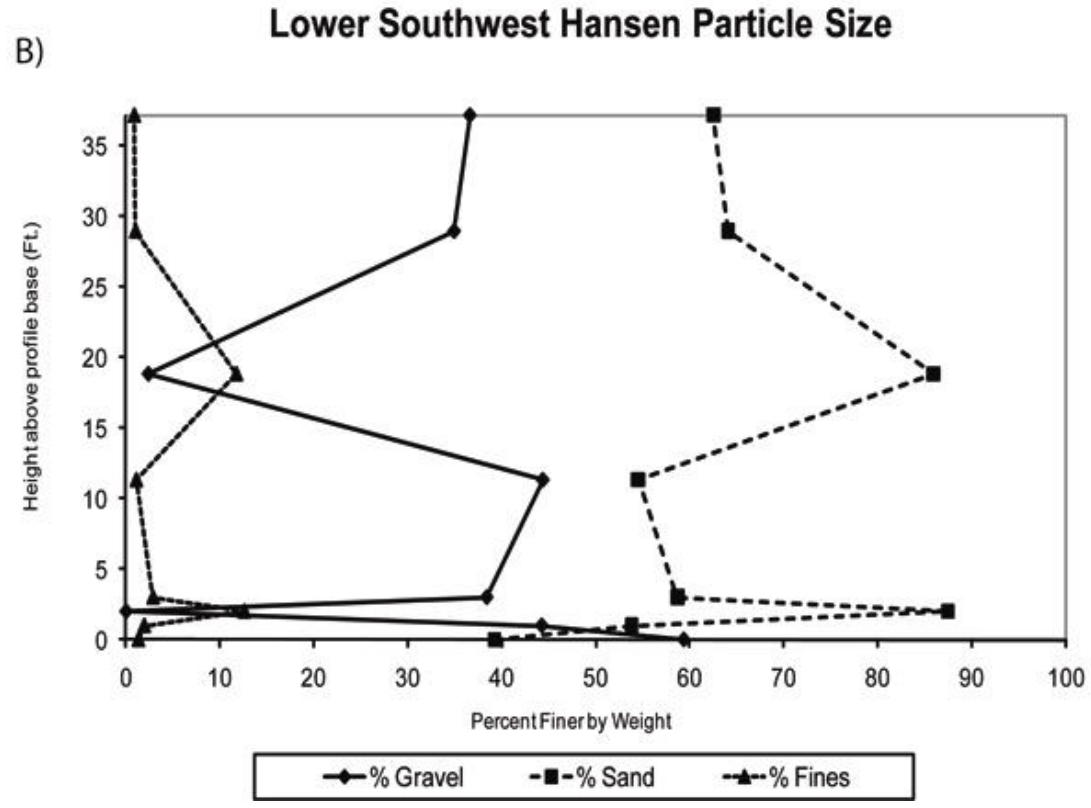

Figure 18. Caption on the following page.

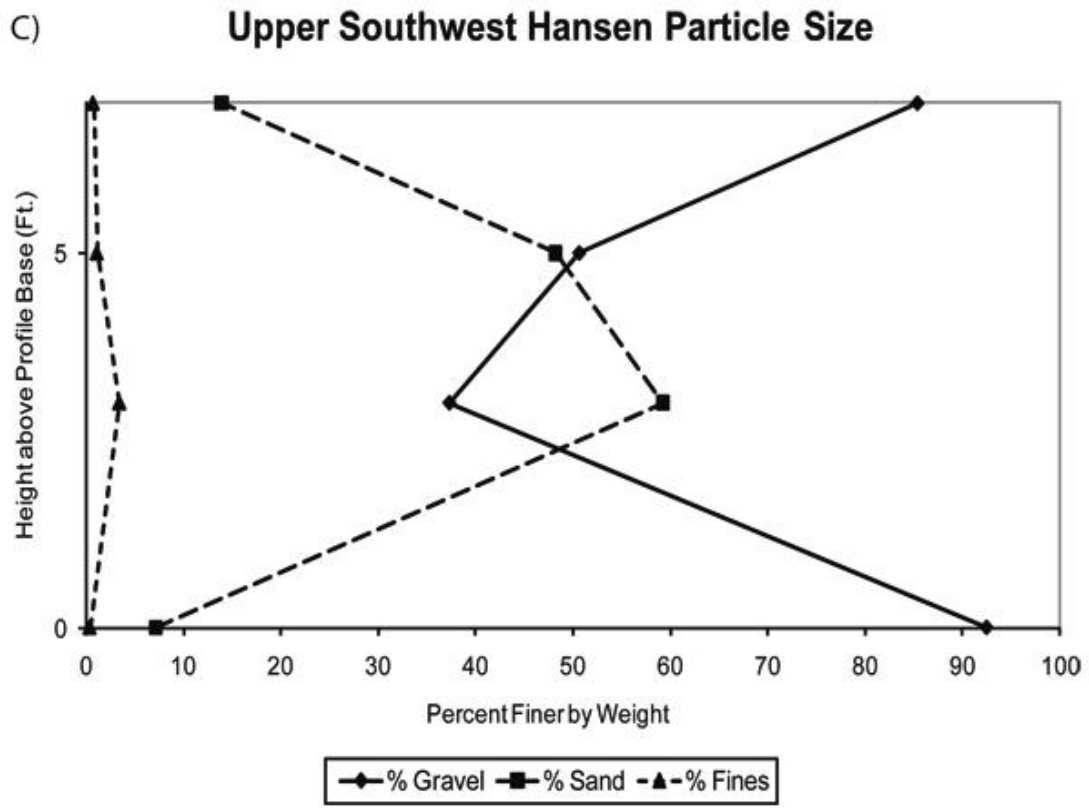

Figure 18. A) Particle size distribution for the Hansen weathering profile; **B)** Particle size distribution for the Lower Southwest Hansen weathering profile; **C)** Particle size distribution for the Upper Southwest Hansen weathering profile. (Note: y-axis is location of each sample in weathering profile; 1 = bottom).

Figure 18A represents apparent particle size trend in the Hansen profile where there is an increase in particle size at the top of the profile. The apparent increase in gravels in the top of the profile is due to the presence of a "gray clay" layer below, which contains few gravel fragments. In figure 18B, the spikes in the percentage of sands and fines correspond with other "gray clay" layers located within the profile. In contrast, the large increase in the percentage of gravel in figure 18C represents recementation by a ferricrete at the top of the profile.

4.2 Geochemistry

The results from the whole rock XRF geochemistry are located in Table 6 (major chemistry) and Table 7 (trace elements). The results from these analyzes have been employed in a variety of different methods in this study. The study was focused on the major element geochemistry to determine any geochemical signatures from mineralogical changes.

4.3 Acid Base Accounting

Acid base accounting (ABA), and paste pH results are located in Table 8. The results from these tests determine the potential for the materials to be acid producing or acid consuming and provide a pH of the composite samples. The Neutralizing Potential (NP) is the neutralizing potential given in kg of $CaCO_3$/ton and Acid Potential (AP) is the amount of $CaCO_3$ needed to buffer all the acid that will be produced from the composite samples. NP of the samples range from –20.63 to 7.54 kg of $CaCO_3$/ton. The Acid Potential (AP) of the samples range from 104.06 to 0.00 kg of $CaCO_3$/ton.

The Net Acid Producing Potential (NAPP) is the potential for the sample to be acid producing or acid consuming. Positive values are acid producing and negative values are acid consuming. Only two samples (SWH-GJG-0011 & SWH-GJG-0014) have negative NAPP, which means there is potentially enough acid consuming minerals to consume the acid produced. The remaining samples will be acid producing from the time the acid consuming minerals are consumed or until all of the

Table 6. Major oxide XRF geochemistry (weight %)

	Sample	SiO_2	TiO_2	Al_2O_3	FeO*	MnO	MgO	CaO	Na_2O	K_2O	P_2O_5	Sum	LOI (%)	Total
Hansen Profile	HAS-GJG-0006	49.79	1.00	13.46	7.32	0.12	5.68	3.11	0.63	4.02	0.57	85.71	11.35	97.06
	HAS-GJG-0007	46.86	0.84	12.39	8.49	0.08	4.70	4.19	0.74	2.44	0.66	81.41	15.63	97.04
	HAS-GJG-0008	47.31	0.94	12.43	7.25	0.12	5.29	4.39	0.45	2.54	0.44	81.17	13.58	94.75
	HAS-GJG-0009	59.18	1.05	21.37	1.12	0.01	0.61	1.07	0.11	5.96	0.17	90.64	6.33	96.97
	HAS-GJG-0010	66.89	0.78	14.32	1.82	0.05	2.29	1.11	0.07	4.04	0.16	91.52	6.27	97.79
Upper Southwest Hansen Profile	SWH-GJG-0020	57.09	1.293	14.92	6.41	0.116	4.12	1.23	3.54	2.57	0.500	91.78	6.76	98.54
	SWH-GJG-0021	57.61	1.165	13.05	3.54	0.087	3.50	2.96	1.93	2.25	0.202	86.30	9.51	95.81
	SWH-GJG-0022	62.65	1.374	16.20	1.72	0.022	1.92	2.05	0.35	4.04	0.095	90.41	6.12	96.53
	SWH-GJG-0023	49.73	0.560	11.86	14.26	0.029	1.62	0.87	0.83	2.80	0.791	83.34	12.67	96.01
Lower Southwest Hansen Profile	SWH-GJG-0008	62.52	0.402	12.69	3.53	0.035	1.02	2.32	2.72	4.36	0.213	89.81	7.64	97.45
	SWH-GJG-0009	49.71	0.423	11.99	9.54	0.085	1.79	2.73	2.23	2.82	0.671	82.00	13.98	95.98
	SWH-GJG-0010	58.30	0.517	14.22	5.59	0.081	2.43	1.50	0.95	3.21	0.365	87.17	10.08	97.25
	SWH-GJG-0011	65.46	0.423	12.72	4.00	0.049	1.08	1.35	2.99	3.87	0.206	92.16	5.72	97.88
	SWH-GJG-0012	66.11	0.567	15.49	1.25	0.036	1.61	1.13	2.94	2.96	0.048	92.14	5.47	97.61
	SWH-GJG-0013	69.11	0.536	14.16	3.39	0.005	0.24	0.96	0.10	3.06	0.185	91.74	6.38	98.12
	SWH-GJG-0014	68.91	0.884	17.46	0.44	0.002	0.23	0.53	0.86	3.43	0.316	93.06	4.58	97.64
	SWH-GJG-0015	53.13	0.492	13.12	4.73	0.064	2.35	4.26	1.26	2.35	0.394	82.15	13.90	96.05

* = Total Iron

Table 7. Trace element geochemistry (ppm)

	Sample	Ni	Cr	Sc	V	Ba	Rb	Sr	Zr	Y	Nb	Ga	Cu	Zn	Pb	La	Ce	Th	Nd	U
Hansen Profile	HAS-GJG-0006	92.1	213.3	15.8	152.6	2983	79.8	1106	161.3	19	21.4	18	64.6	172.7	23.8	29.8	64.4	7.3	31.7	1.9
	HAS-GJG-0007	81.6	190.9	15.4	135.5	1730	53.1	364.1	137.7	12	17.2	14.2	53.1	173.1	23.1	14.3	37	9.7	17	3
	HAS-GJG-0008	59.3	199.1	14.8	140.8	1863	72.8	433.6	148.6	14.4	20	16.2	44.7	165.5	39.7	38.5	70.4	6.3	29.2	2.4
	HAS-GJG-0009	4.5	109.1	6.5	105	1136	188.3	66.3	231.5	10.3	14.5	12.5	7	18.9	18.5	16.6	30.8	8	10.9	2.4
	HAS-GJG-0010	8.9	92.8	10.1	116.1	1257	126.4	127.5	168.2	14.9	13.5	19	9.2	46.9	27.9	36	63.9	8.3	25.2	1.9
Upper Southwest Hansen Profile	SWH-GJG-0020	66	97.5	15.3	174.7	1615	50	436.8	219.8	16.1	25.6	20.1	127.6	101.3	17	18.1	42.2	4.5	21.8	3.1
	SWH-GJG-0021	37.2	84.2	13.9	120.9	1624	60	316.6	187.7	13.4	22.3	19.9	20.1	81.5	43.8	18.3	36.4	5.2	18.9	1.5
	SWH-GJG-0022	13.4	101.4	17.2	154.4	1417	95.7	160.6	223.3	19.5	27.3	21.8	10.5	27.8	39.5	48	101.4	6	45.4	2.1
	SWH-GJG-0023	10.4	84	9.3	91.2	1434	66.1	410.1	142.2	11.4	10.7	15	16.6	32.4	58	32	62.9	7.4	24.4	2.6
Lower Southwest Hansen Profile	SWH-GJG-0008	10.5	14.2	4.1	38.2	883.1	112.6	372.2	165.2	8.4	22.5	15.2	8.7	37.6	15.5	18.4	31.8	10.5	11.9	3.2
	SWH-GJG-0009	10.3	30	7.3	74.7	1306	69.6	577.7	106.6	8.3	6.2	15.4	9.4	28.8	30.6	20.3	39.5	4.5	15.9	0.3
	SWH-GJG-0010	18.3	28.6	8.9	78.4	1037	128.3	275.4	131.6	9.4	8.3	18.1	11.1	52.4	44.5	16.9	31.9	5.5	14.1	3.6
	SWH-GJG-0011	11.1	11.7	4.2	37.8	754	102.1	385.2	183.6	8.7	24.8	16.8	6.8	45.6	28.1	13.4	24	10.6	7	4
	SWH-GJG-0012	6.5	23.7	10.1	84.3	694.6	86.6	530.8	135.8	17.3	7.8	18.4	15.2	22	49.1	33.6	60.5	8.3	28.1	1.1
	SWH-GJG-0013	26.1	43.9	5.5	78.3	730.6	69.7	384.8	161.2	9	8.7	17	18.5	9.6	132.9	24.1	45.8	4.8	19.1	0
	SWH-GJG-0014	4.7	93.4	12.1	113.7	1377	77	860.5	199.9	18.9	15.2	23.8	27	15.1	82.8	44.3	87.3	10.8	35.5	4.5
	SWH-GJG-0015	10	65	7.8	67.8	1035	86.1	361.5	146.4	11.6	7.9	16.4	19.3	50.8	28.3	34.7	63.6	8.8	24.6	0.7

acid-producing minerals (pyrite) are oxidized. Paste pH results indicate a very acidic environment with pH's ranging from 2.05-2.98.

Table 8. Acid Base Accounting and Paste pH results

Sample #	Wt % Sulfide	AP	NP	NAPP	Paste pH
HAS-GJG-0010	0.09	2.81	-0.80	3.61	2.60
HAS-GJG-0009	0.17	5.31	-4.04	9.35	2.05
HAS-GJG-0008	0.25	7.81	-0.39	8.21	2.80
HAS-GJG-0007	3.33	104.06	-7.26	111.32	2.98
HAS-GJG-0006	2.55	79.69	7.50	72.18	2.52
SWH-GJG-0015	0.08	2.50	0.08	2.42	2.64
SWH-GJG-0014	0.15	4.69	5.34	-0.65	2.17
SWH-GJG-0013	2.34	73.13	4.45	68.67	2.65
SWH-GJG-0012	0.4	12.50	4.47	8.03	2.59
SWH-GJG-0011	0.09	2.81	5.39	-2.58	2.46
SWH-GJG-0010	1.76	55.00	-14.89	69.89	2.42
SWH-GJG-0009	0.59	18.44	-20.63	39.06	2.37
SWH-GJG-0008	0.32	10.00	-6.49	16.49	2.36
SWH-GJG-0023	0	0.00	-13.68	13.68	2.36
SWH-GJG-0022	0.68	21.25	-0.88	22.13	2.56
SWH-GJG-0021	0.41	12.81	3.39	9.42	2.39
SWH-GJG-0020	2.33	72.81	7.54	65.27	2.49

4.4 Sulfide to Sulfate Ratios

The ratio of sulfur in sulfide to sulfur in sulfate tends to decrease as a function of height in each profile (Figure 19 A-C). The highest S/SO_4 ratios correspond with "gray clay" layers and the base of two profiles. The S/SO_4 ratios in the Hansen and

upper Southwest Hansen profile document the increasing sulfate content, coupled with the decrease in sulfide, which is the expected weathering scenario within a profile. The lower Southwest Hansen profile does not follow the expected weathering scenario as the S/SO_4 ratio varies within the profile.

Table 9. Sulfide-Sulfate ratio results

Sample #	Sulfur in Sulfide	Sulfur in SO4	Sulfide/Sulfate	Wt % Carbon
HAS-GJG-0010	0.09	0.89	0.10	0.02
HAS-GJG-0009	0.17	0.97	0.18	0.01
HAS-GJG-0008	0.25	2.98	0.08	0.05
HAS-GJG-0007	3.33	2.68	1.24	0.02
HAS-GJG-0006	2.55	1.70	1.50	0.03
SWH-GJG-0015	0.08	3.41	0.02	0.02
SWH-GJG-0014	0.15	0.45	0.33	0.02
SWH-GJG-0013	2.34	0.66	3.55	0.01
SWH-GJG-0012	0.40	0.75	0.53	0.02
SWH-GJG-0011	0.09	1.05	0.09	0.02
SWH-GJG-0010	1.76	1.33	1.32	0.05
SWH-GJG-0009	0.59	2.59	0.23	0.05
SWH-GJG-0008	0.32	1.49	0.21	0.03
SWH-GJG-0023	0.00	2.11	0.00	0.10
SWH-GJG-0022	0.68	1.39	0.49	0.04
SWH-GJG-0021	0.41	1.78	0.23	0.04
SWH-GJG-0020	2.33	0.43	5.42	0.03

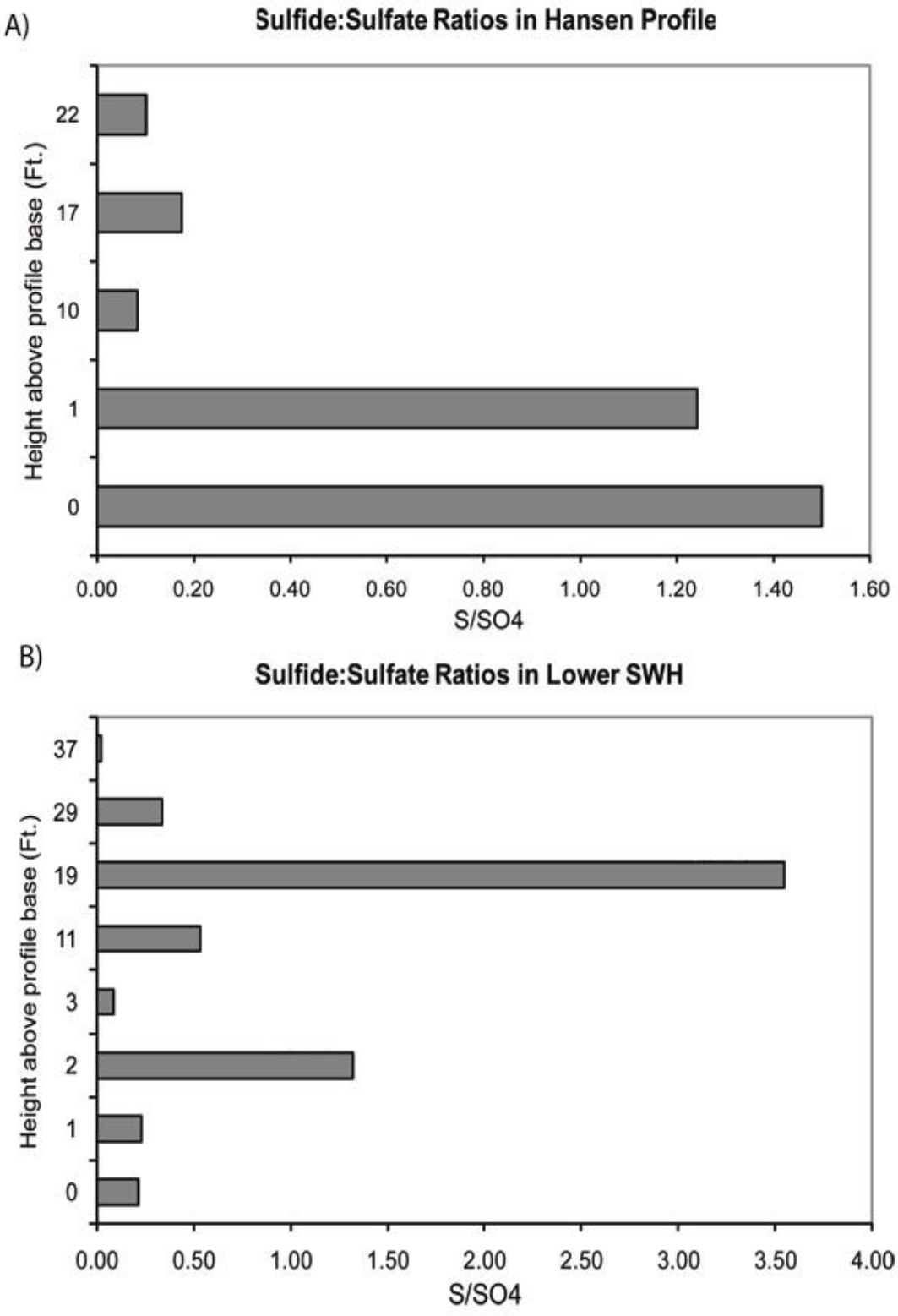

Figure 19. Caption on the following page.

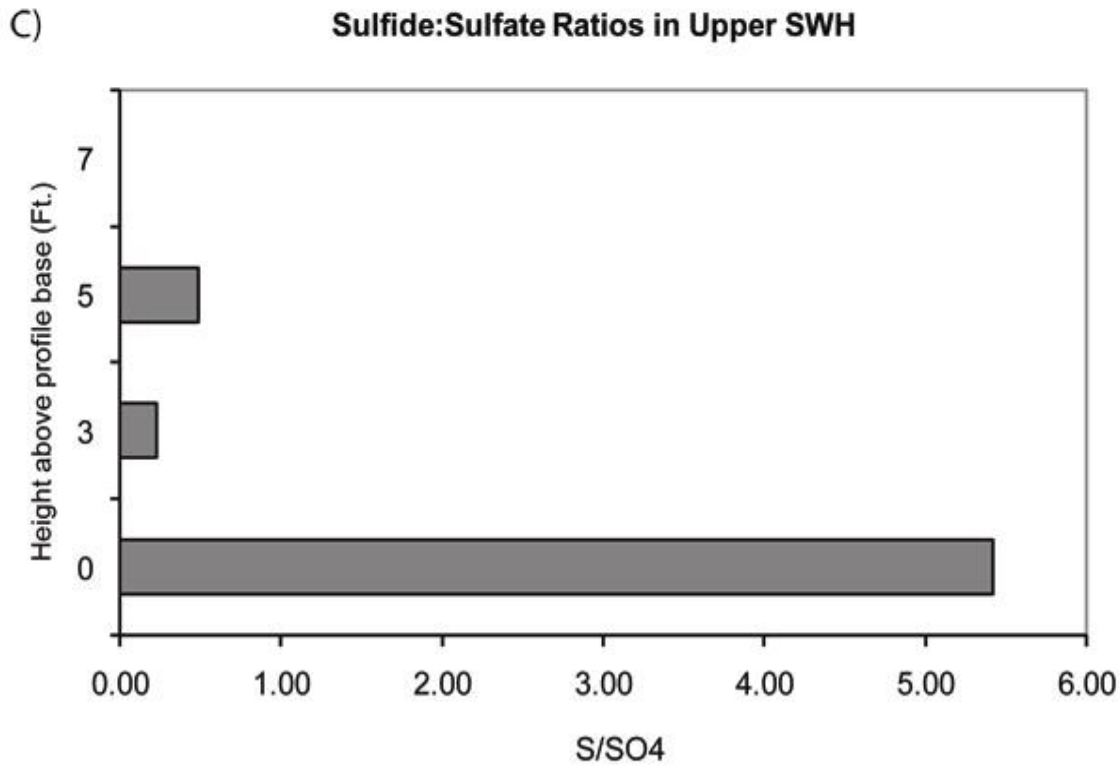

Figure 19. Graphical representation of the ratio of sulfur from sulfide divided by sulfur from sulfate versus location in weathering profile. A) Hansen Profile; B) Lower Southwest Hansen Profile; C) Upper Southwest Hansen Profile

4.5 Mineralogical Results

4.5.1 *Petrography*

Thin section petrography was completed on all samples where rock fragments were large enough to cut and make a thin section. The results from each individual petrographic analysis are located in Appendix B. These analyses provide semi-quantitative results on mineral abundances and textures and provide a method to determine the alteration type of each sample (Figure 20 A-B).

A)

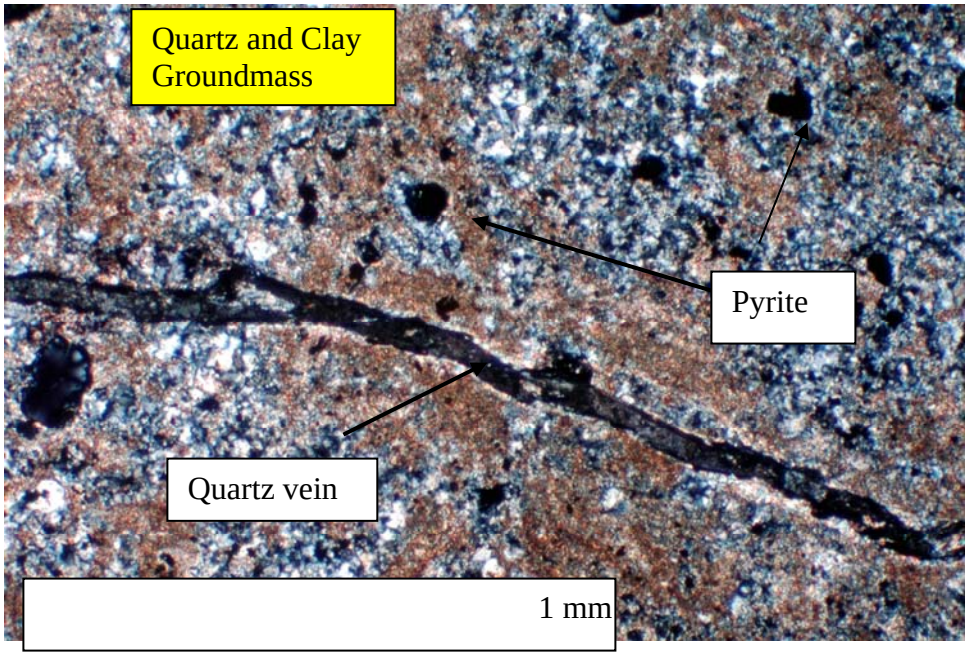

B)

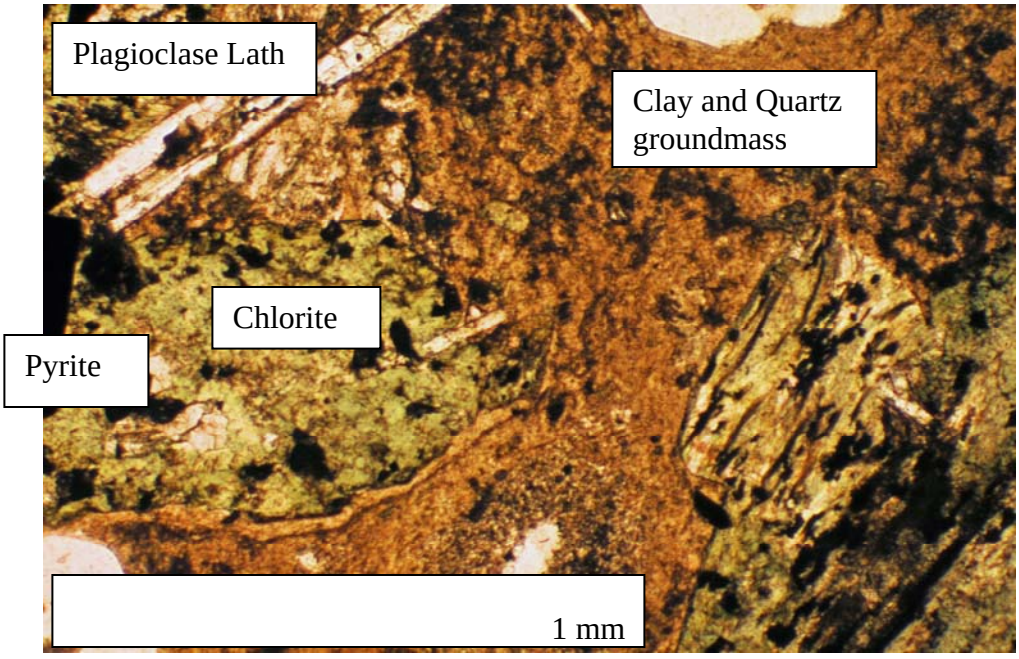

Figure 20. Thin section photomicrographs of samples of different hydrothermal alteration. **A)** Intense QSP hydrothermal alteration (HAS-GJG-0009) (Crossed Polarized Light); **B)** QSP overprinting propylitic alteration (SWH-GJG-0008) (Plane Polarized Light).

Figure 20A represents an intense QSP altered rock that has been hydrothermally altered to quartz, pyrite and clay. The fine-grained groundmass of the sample makes it difficult to distinguish the types of clay minerals, but the abundance of total clay can be estimated. Quartz is easily recognized in phenocrysts, groundmass and as crosscutting veinlets. The black minerals are pyrite grains and are most easily recognized using reflected light. This intense QSP alteration typically occurs near the tops of the profiles, but also has been noted to occur near the bottom of the profiles in bedrock samples, were it is associated with gray clay veinlets.

Figure 20B illustrates QSP overprinting propylitic alteration. In this alteration we see propylitic minerals, epidote and chlorite, being replaced by quartz, clay and pyrite. Pyrite and other oxides minerals replace chlorite in the samples. A small, fresh plagioclase crystal still remains and appears to have been unaffected by the hydrothermal alteration. The groundmass of the sample contains abundant quartz and clay minerals.

These two photomicrographs represent examples of the two distinct hydrothermal alteration types seen in the alteration scars. Many of the plagioclase crystals seen in other samples have a very distinct hydrothermal texture. Pyrite crystals in other samples have oxide rims and/or gypsum rims indicating that oxidation is occurring. The main purpose for the petrographic analysis is to determine the mineralogy of each sample as an input to the modeling of the mineralogy using the ModAn modeling program.

4.5.2 *Clay Mineralogy*

Clay mineralogy (reported as parts in ten) results are located in Table 10. Sample numbers that contain (–20) are clays liberated by crushing rock fragments and samples with (–06) are matrix clays. Figure 21 illustrates similarities between clays liberated from rock fragments and matrix clays. All clay documented within the rock fragments also are located within the matrix clays. Each individual clay XRD scan can be found in Appendix D.

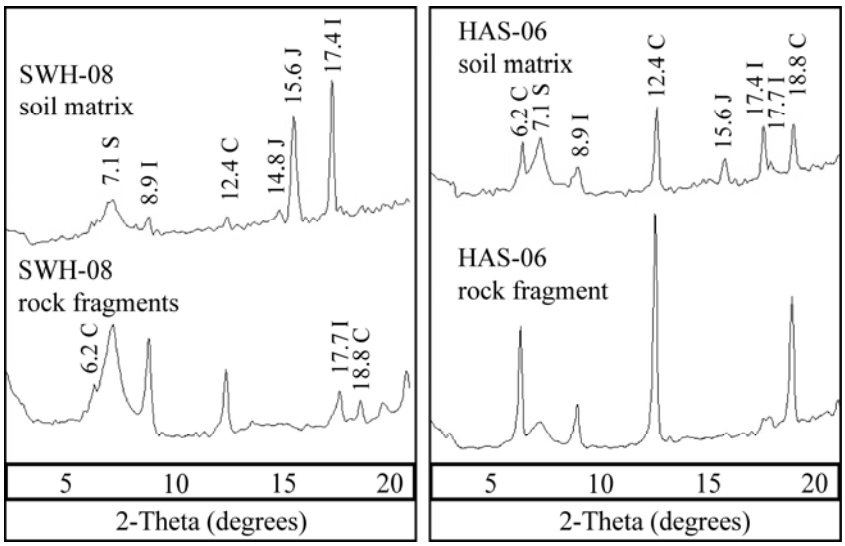

Figure 21. Clay X-Ray diffraction scans of rock fragments to soil matrix for samples SWH-GJG-0008 (SWH-08) and HAS-GJG-0006 (HAS-06) (from Donahue et al, 2008). Number above peaks corresponds to 2θ of clay minerals (abbreviated by capitalized first letter). (S = smectite, C = chlorite, I = illite, J = jarosite).

The results from the XRD clay mineralogy indicate there is no systematic variation with the types and abundances of clays upwards in each profile. However, in the intense QSP alteration, illite is the dominant clay mineral phases (i.e. HAS-GJG-0009 & SWH-GJG-0013). Where QSP overprints propylitic alteration, clay phases

that are present include kaolinite, chlorite, illite, smectite, and mixed layer clays, with illite and chlorite being the dominant clay phases.

Table 10. Parts in ten clay results

Sample	Kaolinite	Chlorite	Illite	Smectite	Mixed Layer
HAS-GJG-0010-06	0	2	5	1	2
HAS-GJG-0009-06	0	0	10	0	0
HAS-GJG-0007-06	0	6	2	1	1
HAS-GJG-0006-06	1	4	1	2	2
SWH-GJG-0015-06	1	3	2	2	2
SWH-GJG-0014-06	0	0	6	1	3
SWH-GJG-0013-06	1	0	7	0	2
SWH-GJG-0012-06	0	3	3	2	2
SWH-GJG-0011-06	0	1	1	5	3
SWH-GJG-0010-06	1	2	3	2	2
SWH-GJG-0009-06	1	2	2	3	2
SWH-GJG-0008-20	1	2	3	3	1
SWH-GJG-0008-06	2	1	2	3	2
SWH-GJG-0023-06	1	2	4	1	2
SWH-GJG-0022-06	0	3	5	1	1
SWH-GJG-0021-06	0	2	2	2	4
SWH-GJG-0020-20	1	2	1	2	4
SWH-GJG-0020-06	1	2	0	3	4

4.5.3 *Comparison of Mineralogical Methods*

Quantitative X-Ray diffraction was completed on only the Hansen weathering profile samples. The QXRD results from the Hansen profile were then used to verify the ModAn mineralogical models in the Hansen profile (Table 11). ModAn, constrained with petrographic analysis, is used to refine mineralogical percentages from all three profiles. This is possible in all profiles because petrographic analysis, whole rock geochemistry and sulfide-sulfate measurements had been completed on all samples.

Mineral abundances vary slightly from the QXRD and petrographic analysis but are within ranges of error in these reported values. Silicate mineral abundances

(Table 11) simulated with ModAn and constrained with petrography, generally agree within ± 5 % of the reported values from the QXRD. This close agreement between QXRD and ModAn analysis provide confidence that the ModAn simulations, when coupled with petrographic data, are reliable for estimating semi-quantitative mineralogy of the other two profiles.

Several discrepancies in Table 11 are the amount of gypsum, illite and chlorite determined by QXRD and ModAn. The majority of gypsum in the samples is contained within the fine-grained fraction of the sample. No gypsum is detected in petrography because the petrography was completed on the larger rock fragments, which contain little to no gypsum, unless noted in fracture filling veinlets.

The discrepancy in illite and chlorite are attributed to the fine-grained nature of these minerals. Biotite also is rarely seen in thin section but is reported in QXRD. The biotite in QXRD could represent illite or chlorite, because it is documented that there is chloritization of biotite in propylitic alteration. The QXRD does not account for the extremely high amounts of illite that were identified in thin section because those peaks may have been assigned to different minerals in the XRD Topaz modeling program.

Chlorite is apparently overestimated in the reported QXRD results, while chlorite from petrography and ModAn are nearly equal in abundances. This discrepancy is attributed to using a generalized clay composition of Questa clay (Avg. Moly Clay) in the ModAn simulation. Accordingly, it appears as the ModAn models remove iron from the chlorite composition and add iron to the general clay composition, resulting in a misrepresentation of the true total chlorite in each sample.

Table 11 illustrates data that suggests ModAn, when coupled with petrography, is an acceptable way to refine the mineralogy seen in thin section petrography. By using only the minerals identified in petrography, it is possible to accurately model sample mineralogy by suppressing minerals not observed in thin section.

4.5.4 *Bulk Mineralogy*

The bulk mineralogy, determined by ModAn, is based on petrography and whole rock geochemistry. A set of locally important minerals (with average composition determined by microprobe analysis) (Table 4) forms the basis for the ModAn calculations. However, if ModAn predicts a mineral not noted in petrographic analysis, it is suppressed and ModAn rerun. In this way, the minerals in the bulk mineralogy are determined petrographically, with the refined percentages coming from ModAn.

The results from the ModAn simulations for individual profile samples are provided in Table 12. Using mineralogy (weight %) vs. location in weathering profile figures, the mineralogical changes can be identified in each weathering profile. The profiles presented in Figures 22, 23 and 24 represent the results for the mineralogical changes in each weathering profile.

Whole rock, coarse-grained (>25mm), and fine-grained (<0.2 mm) material was analyzed from the Hansen profile to determine any mineralogical changes between coarse and fine-grained material (Figure 21). These particle size split samples are from the bottom of the profile and the two samples near the top of the

Table 11. Comparison of QXRD, Petrography and ModAn Modeling results from the Hansen profile

Sample	HAS-GJG-0006 (Q)	HAS-GJG-0006 (M)		HAS-GJG-0006 (P)	HAS-GJG-0007 (Q)	HAS-GJG-0007 (M)		HAS-GJG-0007 (P)	HAS-GJG-0008 (Q)	HAS-GJG-0008 (M)		HAS-GJG-0008 (P)
Albite	5	3.7		5-10%	8	5.0		2-5%	3	3.0		2-5%
Biotite	1	0.0	*	--	2	0.0	*	--	4	0.0	*	--
Calcite	--	0.0	*	2-3%	--	0.0	*	--	--	0.0	*	--
Chlorite	25	12.1		15-20%	24	9.0		10-15%	28	16.0		25-30%
Epidote	--	0.0	*	--	--	0.0	*	--	--	0.0	*	--
Fe-Oxides	--	1.7		--	--	2.8		10-15%	--	0.0	*	--
Gypsum	9	7.5		--	16	11.5		5-10%	15	15.0		--
Orthoclase	25	20.5		18-25%	11	9.2		7-10%	6	6.0		4-8%
Pyrite	2	4.2		2-3%	3	5.1		--	0	0.4		1-2%
Quartz	28	21.4		25-30%	29	24.2		20-30%	36	28.0		30-35%
Total Clay	--	28.9		15-20%	--	33.2		20-25%	--	32.0		20-25%
TOTAL	95	100.0				100.0			22	100.0		
Smectite		9.6				8.3				0.0		
Kaolinite		4.8				0.0				0.0		
Mixed Layer		9.6				6.9				0.0		
Illite		4.8				16.6				32.0		

Sample	HAS-GJG-0009 (Q)	HAS-GJG-0009 (M)		HAS-GJG-0009 (P)	HAS-GJG-0010 (Q)	HAS-GJG-0010 (M)		HAS-GJG-0010 (P)
Albite	--	0.0	*	--	--	0.0	*	--
Biotite	--	0.0	*	--	--	0.0	*	--
Calcite	--	0.0	*	--	--	0.0	*	--
Chlorite	--	0.0	*	--	8	6.0		10-15%
Epidote	--	0.0	*	--	--	0.0	*	--
Fe-Oxides	--	1.0		2-3%	--	1.0		2-3%
Gypsum	3	5.0		--	6	5.0		--
Orthoclase	--	0.0	*	--	--	0.0	*	--
Pyrite	--	0.0		<1%	--	0.2		Tr
Quartz	17	25.0		15-20%	41	45.0		35-40%
Total Clay	80	69.0		75-80%	40	43.0		40-45%
TOTAL		100.3			97	100.0		
Smectite		0.0				5.4		
Kaolinite		0.0				0.0		
Mixed Layer		0.0				10.8		
Illite		69.0				26.9		

(Q) = QXRD
(M) = ModAn
(P) = Petrography
(*) = suppressed in ModAn simulation

Table 12. Mineralogy of weathering profiles (ModAn)

Sample	SWH-GJG-0008	SWH-GJG-0009	SWH-GJG-0010	SWH-GJG-0011	SWH-GJG-0012	SWH-GJG-0013	SWH-GJG-0014	SWH-GJG-0015
Albite	22.2	19.5	7.0	26.1	28.3	0*	0*	0*
Calcite	0*	0*	0*	0*	0*	0*	0*	0*
Chlorite	4.1	0*	1.1	9.3	0.6	0*	0*	0*
Epidote	0*	0*	0*	0*	0*	0*	0*	0*
Fe-Oxides	0*	11.7	2.6	0*	0*	1.1	0*	3.7
Gypsum	7.4	12.3	6.7	5.3	3.9	3.4	2.4	15.5
Orthoclase	23.9	13.1	12.6	21.6	13.1	0*	0*	0*
Pyrite	0.6	1.0	2.9	0.2	0.7	3.9	0.3	0.1
Quartz	30.3	22.5	30.2	32.4	30.4	45.5	40.4	32.7
Total Clay	11.5	20.0	36.9	5.1	23.2	46.0	56.9	48.0
Total	100.0	100.0	100.0	100.0	100.0	100.0	100.0	100.0
Smectite	3.8	7.5	9.2	2.8	6.6	0.0	5.7	13.7
Kaolinite	2.6	2.5	4.6	0.0	0.0	4.6	0.0	6.9
Mixed Layer	2.6	5.0	9.2	1.7	6.6	9.2	17.1	13.7
Illite	2.6	5.0	13.8	0.6	9.9	32.2	34.2	13.7

Sample	HAS-GJG-0006	HAS-GJG-0007	HAS-GJG-0008	HAS-GJG-0009	HAS-GJG-0010
Albite	3.7	5.0	3.0	0*	0*
Orthoclase	20.5	9.2	6.0	0*	0*
Quartz	21.4	24.2	28.0	25.0	45.0
Chlorite	12.1	9.0	16.0	0*	6.0
Total Clay	28.9	33.2	32.0	69.0	43.0
Epidote	0*	0*	0*	0*	0*
Fe-oxides	1.7	2.8	0*	1.0	1.0
Calcite	0*	0*	0*	0*	0*
Pyrite	4.2	5.1	0.4	0.0	0.2
Gypsum	7.5	11.5	15.0	5.0	5.0
Total	100.0	100.0	100.4	100.0	100.2
Smectite	9.6	8.3	0.0	0.0	5.4
Kaolinite	4.8	0.0	0.0	0.0	0.0
Mixed Layer	9.6	6.9	0.0	0.0	10.8
Illite	4.8	16.6	32.0	69.0	26.9

Samples	SWH-GJG-0020	SWH-GJG-0021	SWH-GJG-0022	SWH-GJG-0023
Albite	33.8	16.6	0*	8.6
Calcite	0*	0*	0*	0*
Chlorite	11.3	7.4	7.0	0*
Epidote	0*	0*	0*	0*
Fe-Oxides	0*	0*	0*	18.1
Gypsum	2.3	8.7	5.3	10.4
Orthoclase	11.7	8.3	0*	12.2
Pyrite	4.1	0.7	1.2	0.0
Quartz	21.7	31.6	37.2	24.5
Total Clay	15.1	26.6	49.3	26.3
Total	100.0	100.0	100.0	100.0
Smectite	5.6	6.7	7.0	3.3
Kaolinite	1.9	0.0	0.0	3.3
Mixed	7.5	13.3	7.0	6.6
Illite	0.0	6.7	35.2	13.1

(*) = suppressed in ModAn simulation

Table 12 (continued). Mineralogy of weathering profiles (particle size fractions)

Coarse Fraction

Sample	HAS-GJG-0006-57	HAS-GJG-0009-56	HAS-GJG-0010-57
Albite	5	0*	0*
Orthoclase	22	0*	0*
Quartz	25	55	50
Chlorite	12	0*	4
Total Clay	28	42	43
Epidote	0*	0*	0*
Fe-oxides	0*	0*	0*
Calcite	0*	0*	0*
Pyrite	5	0*	1
Gypsum	2	1	2

(*) = suppressed in ModAn simulation

Fine Fraction[1]

Sample	HAS-GJG-0006-74	HAS-GJG-0009-74	HAS-GJG-0010-74
Albite	3	0	0
Orthoclase	9	0	0
Quartz	21	7	35
Chlorite	28	0	7
Total Clay	4	90	47
Epidote	0	0	0
Fe-oxides	0	0	0
Calcite	0	0	0
Pyrite	2	0	0
Gypsum	28	0	5
Jarosite	5	3	6

1 - Fine fraction is QXRD results

profile. The results for the mineralogy of coarse grained and fine grained fractions are provided in table 12.

The green line represents fine-grain material from QXRD results because no petrography was completed on the fine grain material. Without fine-grained petrography, ModAn simulations could not be constrained. The blue line represents whole rock mineralogy and the red line represents coarse grain mineralogy from the ModAn simulations. Whole rock XRF chemistry from the Upper and Lower Southwest Hansen profiles were the only chemistry used in the ModAn simulation because no fine-grained petrography or QXRD were available to compare to the modeling results.

4.5.4.1 *Hansen "Weathering Profile"*

The changes in mineralogy through the Hansen weathering profile are illustrated in Figure 22. For whole rock samples, quartz is the only mineral that remains relatively unchanged, except in the top sample, in the profile. Chlorite and

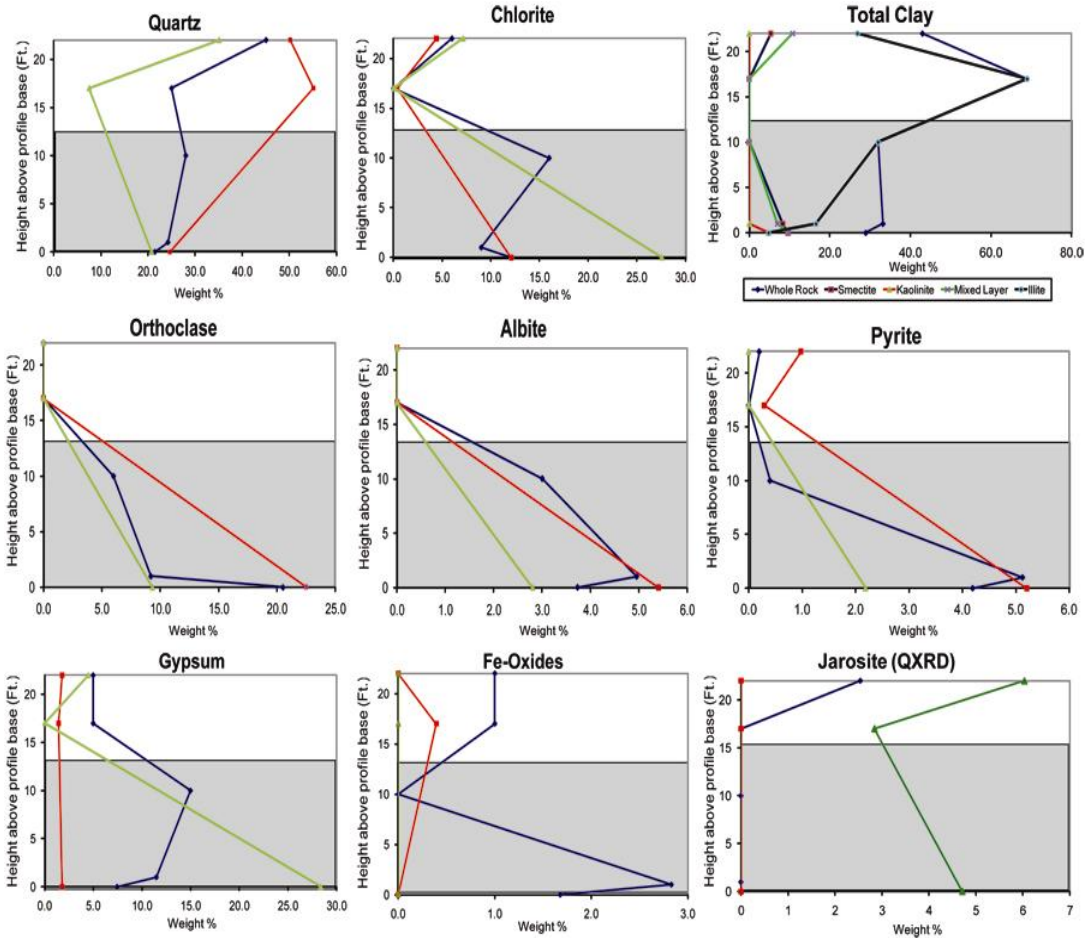

Figure 22. Mineralogical changes of identified minerals vs. sample locations in the Hansen weathering profile. Shaded gray area represents QSP overprinting propylitic alteration and white area represents intense QSP alteration. Blue line = whole rock, Red line = >25 mm, Green line = <0.2 mm. Note: jarosite plot is from QXRD results; not all plots have same scale.

illite are inversely correlated and relate to hydrothermal alteration type. Other clay minerals are relatively unchanged throughout the profile. Both of the feldspars, albite and orthoclase, also decrease as the samples get closer to the intense QSP alteration

zones (“gray clay”). Pyrite decreases and gypsum, Fe-oxides, and jarosite increase towards the top of the profile.

Comparison between the coarse and fine-grained material shows all minerals are located in both size fractions, except jarosite. Silicate minerals and pyrite are generally more abundant in the coarse grained material. The minerals associated with sulfide oxidation (gypsum and jarosite) are more abundant in the finer-grained material.

4.5.4.2 *Upper Southwest Hansen “Weathering Profile”*

The changes in mineralogy through the Upper Southwest Hansen weathering profile are shown in Figure 23. Quartz increases upwards in the profile, except in the ferricrete at the top of the profile. Chlorite decreases and illite increase towards the top of the profile. Both chlorite and illite decrease in the top of the profile, which is a ferricrete. Other clay minerals are relatively unchanged upwards in the profile. Orthoclase and albite decrease towards the top of the alteration profile. Pyrite decreases upwards in the profile, whereas gypsum and Fe-oxides increase towards the top of the profile.

4.5.4.3 *Lower Southwest Hansen “Weathering Profile”*

The changes in mineralogy through the Upper Southwest Hansen weathering profile are presented in Figure 24. This profile has a more complex alteration zonation because there are two areas that display intense QSP alteration zones. Abundant quartz, illite and pyrite are characteristic in these “gray clay” zones of intense QSP

alteration. Propylitic alteration zones are characterized by chlorite, with significantly lesser amounts of quartz and illite. The feldspars decrease in the intensely altered QSP zones and increase in the QSP overprinting propylitic zones. Pyrite decreases towards the top, while gypsum and Fe-oxides generally increase towards the top.

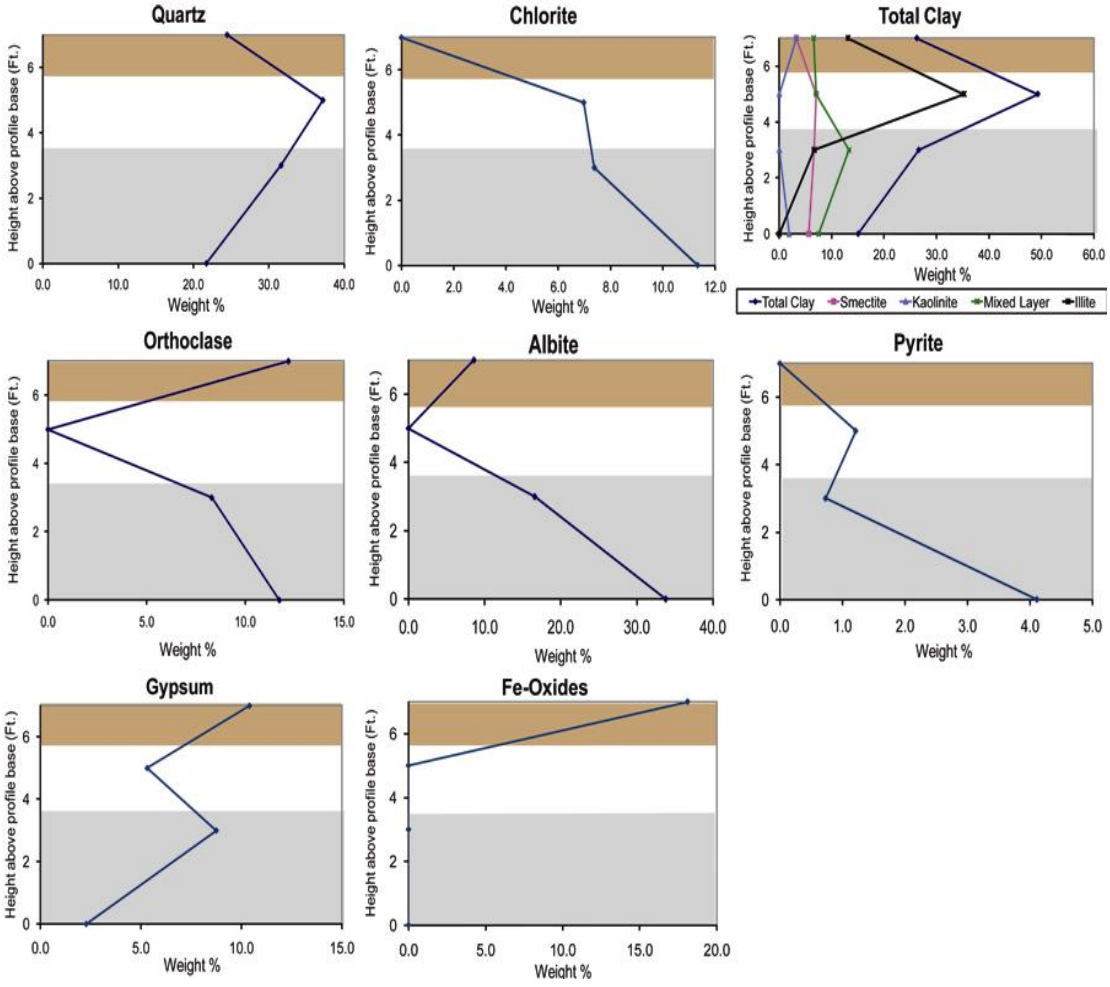

Figure 23. Mineralogical changes of identified minerals vs. sample locations in the Upper Southwest Hansen weathering profile. Shaded gray area represents QSP overprinting propylitic alteration, white area represents intense QSP alteration, and brown area represents ferricrete material. Note: not all plots have same scale

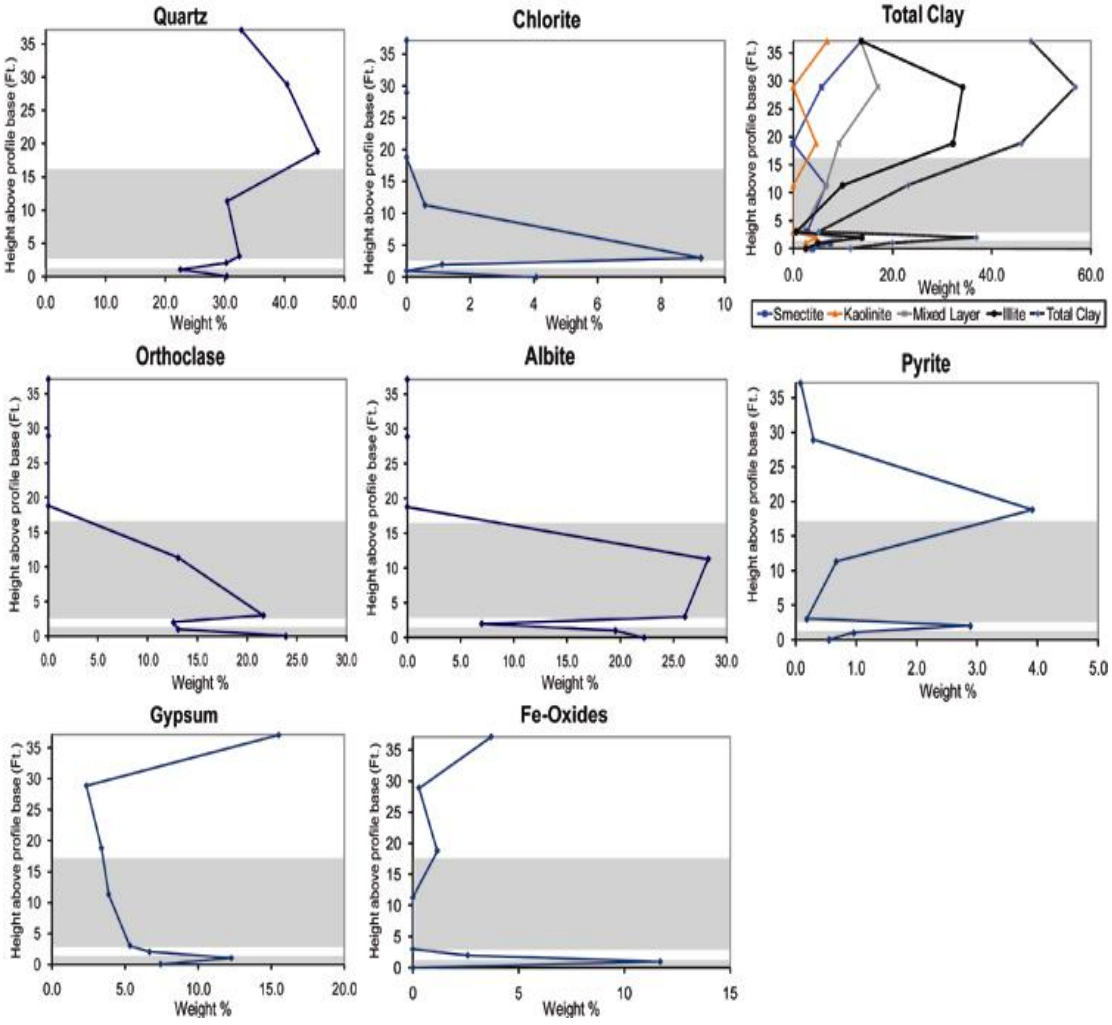

Figure 24. Mineralogical changes of identified minerals vs. sample locations in the Lower Southwest Hansen weathering profile. Shaded gray area represents QSP overprinting propylitic alteration and white area represents intense QSP alteration. Note: not all plots have same scale for weight percents.

4.6 Stable Isotopes

4.6.1 *Sulfides and sulfates*

The overall reproducibility of $\delta^{18}O_{SO4}$ values from this study range from 0.1 to 0.5‰, with the average difference in duplicates of ±0.18‰. Reproducibility of $\delta^{34}S$ isotopic values measured in this study differs by 0 to 0.5 ‰, with an average value of ±0.3‰. The $\delta^{34}S$ (pyrite and gypsum) and $\delta^{18}O_{SO4}$ values and errors from the stable

isotopic analyses are presented in Table 13. The final values are plotted on a $\delta^{34}S$ vs. $\delta^{18}O_{SO4}$ diagram (Figure 25). The range of measured $\delta^{34}S$ values for sulfate is -1.1 to -5.7 ‰ and the range of $\delta^{18}O_{SO4}$ of sulfate is -7.0 to 0.9 ‰. The range in measured $\delta^{34}S$ for pyrite is -6.6 to -1.0 ‰.

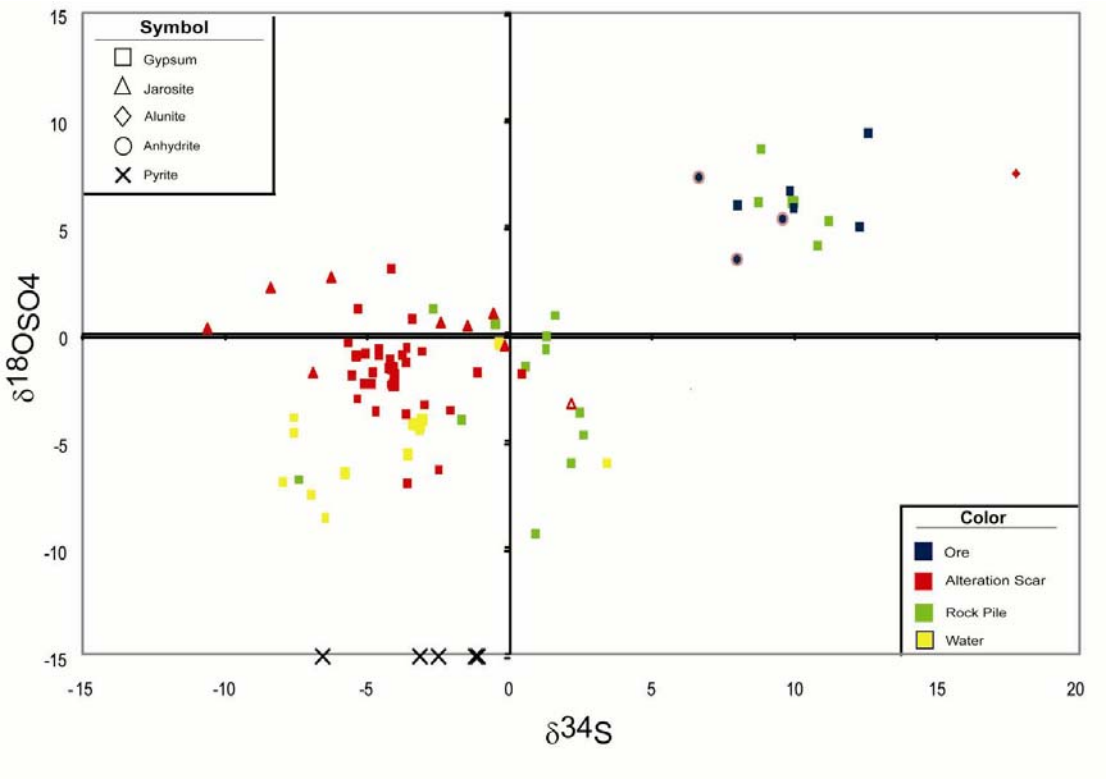

Figure 25. $\delta^{34}S$ and $\delta^{18}O_{SO4}$ diagram of sulfates and sulfides analyzed. Red squares and black X's are from this study and the remaining data is from Campbell and Lueth (2008) (Appendix C).

4.6.2 *Clays*

The overall (sample preparation plus analysis) reproducibility of $\delta^{18}O$ values from this study range from 0.1 to 0.5‰, with the average difference in duplicates of ±0.13‰. Reproducibility of δD isotopic values of individual samples measured in this study vary from 0 to 3 ‰, with an average value of ±1‰. The range of measured values for clay $\delta^{18}O$ is -0.3 to 4.6 ‰ and the range for δD is -65 to -95 ‰. The $\delta^{18}O$

and δD values and errors from the stable isotopic analyses are presented in Table 14. The final values are plotted on a $\delta^{18}O$ vs. δD diagram (figure 26).

Table 13. $\delta^{34}S$ and $\delta^{18}O_{SO4}$ results of sulfides and sulfates

Sample	δ18O	δ18O Duplicates	Final δ18O	δ18O Precision (±)	δ34S	δ34S Duplicates	Final δ34S	δ34S Precision (±)	Final δ34S (Pyrites)
HAS-GJG-0006	-1.8		**-1.8**		-4.8		**-4.8**		**-1.1**
HAS-GJG-0007	-3.8		**-3.8**		-3.6	-4.7	**-4.2**	0.5	**-1.5**
HAS-GJG-0008	-0.7	-0.3	**-0.5**	0.2	-3.6		**-3.6**		
HAS-GJG-0008-R	-1.8	-2.3	**-2.1**	0.2	-1.1		**-1.1**		
HAS-GJG-0009	-3.3	-3.2	**-3.3**	0.1	-3.0		**-3.0**		
HAS-GJG-0009-R	0.7	1.1	**0.9**	0.2	-3.4		**-3.4**		
HAS-GJG-0009-RS	-0.8		**-0.8**		-3.1	-3.0	**-3.0**	0.1	
HAS-GJG-0010	-1.0	-1.1	**-1.1**	0.1	-3.8		**-3.8**		
HAS-GJG-0010-R	-1.3	-0.5	**-0.9**	0.4	-3.6		**-3.6**		
SWH-GJG-0008	-1.9		**-1.9**		-4.1		**-4.1**		**-6.6**
SWH-GJG-0008-R	-2.3		**-2.3**		-4.8		**-4.8**		
SWH-GJG-0009	-1.6		**-1.6**		-4.1	-3.9	**-4.0**	0.1	
SWH-GJG-0009-C	-1	-1.3	**-1.2**	0.2	-5.4		**-5.4**		
SWH-GJG-0009-R	-1.6		**-1.6**		-4.2		**-4.2**		
SWH-GJG-0010	-1.9	-2.1	**-2.0**	0.1	-5.5		**-5.5**		
SWH-GJG-0011	**-3.6**	-2.7	**-3.2**	0.5	-4.7		**-4.7**		
SWH-GJG-0011-R	-2.4		**-2.4**		-4.1		**-4.1**		
SWH-GJG-0012	-6.4		**-6.4**		-2.5		**-2.5**		
SWH-GJG-0013	-0.9	-1.7	**-1.3**	0.4	-5.1		**-5.1**		
SWH-GJG-0013-F	-3.0	-3.0	**-3.0**		-5.4		**-5.4**		
SWH-GJG-0013-FLOAT	-0.4		**-0.4**		-5.7		**-5.7**		
SWH-GJG-0014	-7.0		**-7.0**		-3.6	-4.3	**-4.0**	0.3	
SWH-GJG-0015	-3.6	-3.5	**-3.6**	0.1	-2.1		**-2.1**		
SWH-GJG-0020	-0.7	-0.2	**-0.5**	0.1	-4.6		**-4.6**		**-1.8**
SWH-GJG-0021	-1.8	-1.7	**-1.8**	0.2	-4.0		**-4.0**		**-1.0**
SWH-GJG-0021-F	-2.4	0.8	**-0.8**	0.1	-4.2	-5.1	**-4.6**	0.4	
SWH-GJG-0021-L	-1.6	-1.7	**-1.6**	0.1	-4.1		**-4.1**		
SWH-GJG-0022	-1.0		**-1.0**		-4.6		**-4.6**		
SWH-GJG-0022-L	-1.1		**-1.1**		-4.2		**-4.2**		
SWH-GJG-0023	-2.3	-2.0	**-2.2**	0.2	-5.1		**-5.1**		
SWH-GJG-0023-F	1.2		**1.2**		-5.3		**-5.3**		

R = Rock Fracture
RS = Rock Surface
C = in "gray clay" matrix
F = Fine -grained crystals
L = Large grained crystals
Float = picked in field

Table 14. $\delta^{18}O$ and δD isotopic values of clay minerals

Sample	Mineralogy	δ18O	δ18O Duplicates	Final δ18O*	δ18O Precision (±)	δD	δD Duplicates	Final δD*	δD Precision (±)
GHN-KMD-0014	Various	3.3		3.3		-93	-93	-93	0.0
GHN-KMD-0017	Various	2.4	2.4	2.4	0.00	-85	-92	-89	3.0
GHN-KMD-0018	Various	4.8	4.1	4.4	0.15	-87	-86	-87	0.5
GHN-KMD-0026	Various	3.7	3.5	3.7	0.10	-94	-92	-93	1.0
GHN-KMD-0062	Various	4.3	4.2	4.3	0.10	-83	-84	-83	0.5
GHN-KMD-0079	Various	3.9	3.9	3.9	0.00	-68	-74	-71	3.0
GHN-KMD-0080	Various	3.5	4.3	3.9	0.20	-87	-87	-87	0.0
GHN-KMD-0100	Illite & Kaolinite	4.8	4.4	4.6	0.10	-95	-95	-95	0.0
HAS-GJG-0008	Various	1.2	1.0	1.1	0.10	-80	-82	-81	1.0
HAS-GJG-0009	Illite	-0.1	-0.6	-0.3	0.15	-83	-81	-82	1.5
HAS-GJG-0010	Various	3.3	2.9	3.1	0.20	-84		-84	
SWH-GJG-0010	Various	0.7	0.5	0.6	0.10	-95	-89	-92	3.0
SWH-GJG-0013	Illite	0.2	0.4	0.6	0.20	-83	-77	-80	2.0
SWH-GJG-0014	Illite	0.5	0.7	0.6	0.10	-84	-84	-84	0.0
SWH-GJG-0022	Various	2.0	2.1	2.0	0.05	-85	-85	-85	0.0
SWH-GJG-0023	Various	3.8	2.9	3.3	0.45	-68	-62	-65	3.0

* - Final values used to plot δ18O & δD diagram

Several global meteoric features are plotted on Figure 26 for reference and are described below. The meteoric water line depicts the interdependence of H- and O-isotope ratios in meteoric waters on a global scale (Hoefs, 2004), which was first described by Craig (1961). Local meteoric waters may vary locally, but generally fall on or near the meteoric water line.

The kaolinite line describes the isotopic composition of kaolinite forming at 20ºC in equilibrium with meteoric waters. This line is plotted using the fractionation factors from equation 8 and 9 (below) (Sheppard and Gilg, 1996).

$$\text{Hydrogen } 1000 \ln \alpha_{\text{kaolinite-water}} = -2.2 \times 10^{-6} \times T^{-2} - 7.7 \quad (8)$$

$$\text{Oxygen } 1000 \ln \alpha_{\text{kaolinite-water}} = 2.76 \times 10^{-6} \times T^{-2} - 6.75 \quad (9)$$

The supergene/hypogene line describes the isotopic composition of kaolinite forming in equilibrium with meteoric water at 35ºC. This line is termed the supergene/hypogene line because 35ºC is the maximum temperature for kaolinite forming at the earth's surface. Samples plotting to the left of this line are termed hypogene because these temperatures are representative of hydrothermal alteration temperatures and not supergene weathering temperatures. The lines showing T=70°C, 100°C and 200°C describe the isotopic composition of a kaolinite forming at these temperatures in equilibrium with meteoric waters.

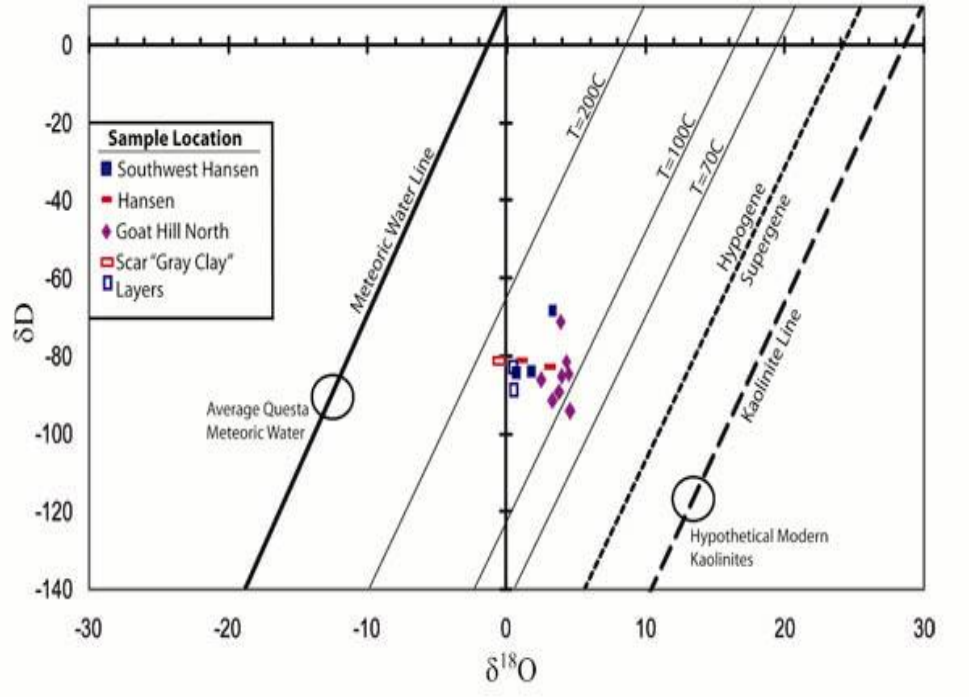

Figure 26. $\delta^{18}O$ vs. δD diagram of Questa clays. Sample points are larger than measured error.

5. DISSCUSION

5.1 Weathering profiles

A weathering profile consists of differentiated identifiable horizons that have been chemically changed, with assistance from the physical disintegration of the bedrock (Summerfield, 1991). There are typically four distinct zones recognized in a classic weathering profile and include fresh bedrock, weathered material with unweathered bedrock, a clay-rich horizon, and capped by soil (Summerfield, 1991). These classic weathering profiles essentially consist of one original lithology and are best developed in wet and humid climates with low erosional rates.

Weathering profiles collected within the alteration scars at Questa are more complex than classic weathering profiles. They may represent multiple lithologies overprinted by hydrothermal alteration, suggesting the mineralogy of each sample in the weathering profile could have had different original mineral abundances. The area is also rich in mineralization with abundant dikes and stocks that have intruded the volcanic rocks. In addition, the rocks are pyrite rich, which when oxidized, create an acidic environment. This acid environment can enhance the rates at which the rocks chemically weather. However, the climate of the area is presently semi-arid and the low annual precipitation would tend to inhibit chemical weathering. The mountainous terrain allows for high erosion rates, which may quickly remove much of the chemical weathering product.

The changes that are expected to occur upward as a consequence of weathering within the alteration scar profiles included a particle size decrease, decreasing pyrite concentrations, increasing sulfate concentrations, decreasing feldspar concentrations, and increasing clay concentrations. These main features are seen within the alteration

scar profiles. However, the reasons for these changes are more complex than the classic weathering model. The primary purpose of this study was to document any mineralogical and geochemical changes in alteration scar profiles due to the effects of physical and chemical weathering. The results can be used by the Questa Weathering and Rock Pile Stability Project to predict future mineralogical changes in mined rock piles.

5.2 Physical Weathering

Physical weathering appears active in the alteration scars with particle size generally decreasing upward in each profile. Exceptions of particle size increases are attributed to secondary Fe-oxide mineral formation (ferricrete). Mid-profile particle size decreases appear related to the presence of hydrothermal "gray clay" layers. The general decrease in particle size upwards would be expected from the physical weathering of the material. However, particle size decrease could also be a function of hydrothermal alteration, based on the presence of hydrothermal clay layers in the profiles.

Figure 12 provides an example of how particle size decreases upwards in the Hansen alteration scar profile. In this figure, the bottom three samples (HAS-GJG-0006, HAS-GJG-0007, & HAS-GJG-0008) have a similar particle size and color. The sample HAS-GJG-0007 has a larger particle size than the other two samples because it has been recemented by gypsum filling fractures (Figure 27). The two samples at the top (HAS-GJG-0009 & HAS-GJG-0010) are a finer particle size and grayish-white color. This grain size decrease can be attributed to the present of an intense QSP

altered vein, which originally consisted of finer particle sizes because of the hydrothermal alteration of various silicate minerals to clay minerals (Figure 20A).

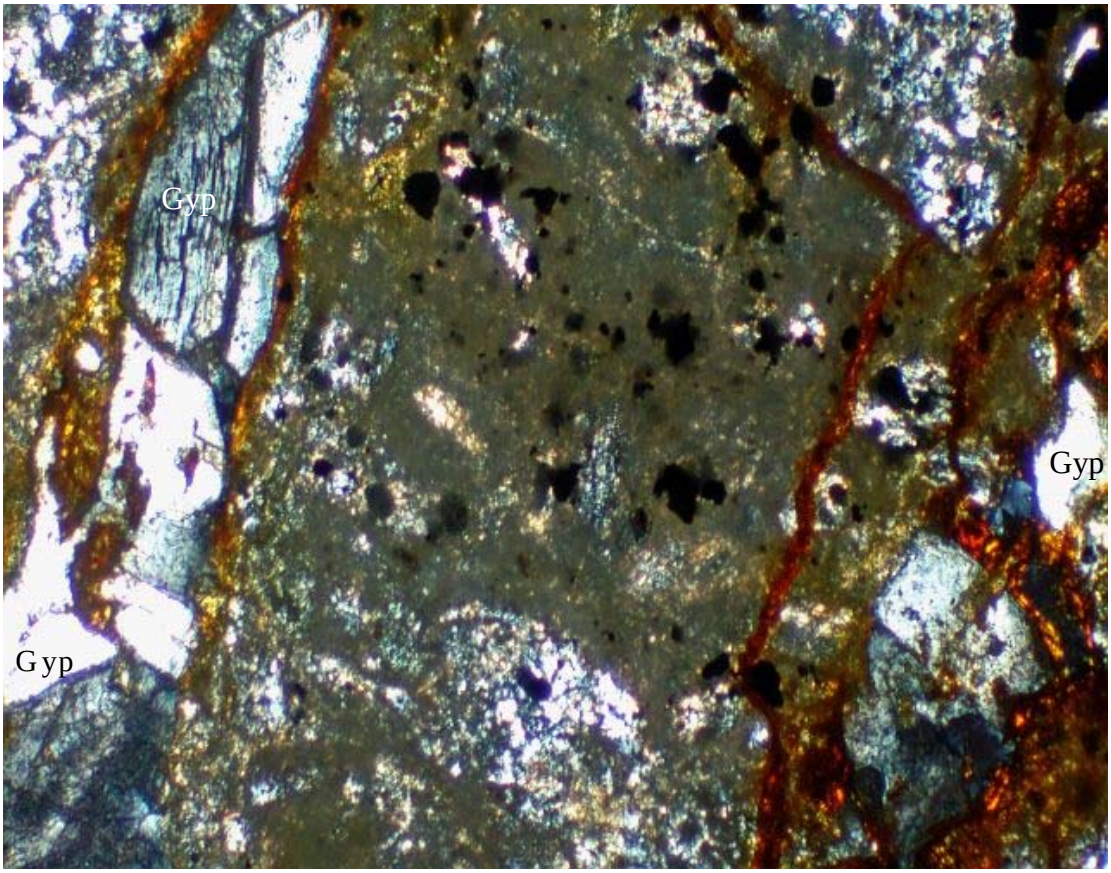

Figure 27. Photomicrograph of HAS-GJG-0007 illustrating gypsum and Fe-oxide filled fractures at the base of the Hansen Profile. (Gyp = gypsum, Red Staining = Fe-oxides)

Figure 11 illustrates a similar trend of decreasing particle size, however, the lower Southwest Hansen alteration scar profile is more complex. In this figure there are "gray clay" layers located near the bottom (SWH-GJG-0010) and top of the profile (SWH-GJG-0013). The samples that occur above and beneath SWH-GJG-0013 are stained a whitish-gray color, indicating these samples have experienced partial QSP alteration of the "gray clays", also noted in thin section. This characteristic color above and below SWH-GJG-0010 is not as apparent, possibly because this sample is a

vein in the bedrock. However, the decrease in particle size can readily be seen. This is an indication that the particle size decrease in these portions of the alteration scar profile may be due to the hydrothermal alteration of feldspar to clay minerals.

Figure 13 illustrates the upper Southwest Hansen alteration scar profile with a more subtle particle size decrease. SWH-GJG-0022 is another sample that has experienced the influence of QSP alteration; however, it appears that the intensity of alteration may have been less because of the remnant brownish color and a larger particle size compared to other "gray clay" layers. There is an accumulation of gypsum at the top of the profile and veinlets of quartz (noted in petrography, Figure 20A), which could act as cements to hold the rock fragments together. The top sample of this profile (SWH-GJG-0023) is a ferricrete, leading to the large particle sizes associated with this sample. This profile appears to follow the expected simplified weathering profile model of decreasing particle size towards the top (Figure 18A), without much influence from hydrothermal alteration.

There are three possible causes of particle size decrease within the alteration scar profiles: 1) As hydrothermal solutions were circulating through the rocks (~ 25 Ma), primary fracturing occurred and silicate minerals in the intense QSP altered zones were altered to clay minerals, decreasing the particle size; 2) Fracturing in the alteration scars is pervasive down to the microscopic level (Caine, 2003; Ludington et al. 2004), allowing for fluids to be introduced and oxidize pyrite. The fluids entering these fractures can create freeze thaw action and further disintegrate the rocks, therefore, allowing more fluids to be introduced and oxidize pyrite; and 3) The oxidation of pyrite, and subsequent reaction with calcite or Ca-bearing clays, can

cause the precipitation of gypsum in fractures, creating an accompanying volume increase, resulting in further fragmentation. These different processes appear to have worked together in the alteration scars to physically decrease grain size.

5.3 Chemical Weathering

Mineralogical analysis of the three alteration profiles has documented variations in the concentrations of silicate minerals, pyrite, sulfates and clay minerals (Figures 28-34). In general, pyrite decreases, while gypsum and jarosite increase towards the top of each profile. Changes in the silicate mineralogy in the profiles include, illite and total clay abundances increasing in and near the intense QSP alteration, while chlorite, orthoclase and albite abundances decrease in and near the zones of intense QSP alteration (Figures 32, 33, 34). Chlorite is found in higher concentrations in the QSP overprinting propylitic alteration, while illite is more dominant in the intense QSP altered zones. No systematic variation with other clays minerals (kaolinite, smectite, and mixed-layer) is apparent upwards in the profiles. All clay minerals present within the fine-grained fractions are also noted in the coarse grained fractions (Figure 21). Feldspars and pyrite are more concentrated within the coarse-grained fraction and sulfates and Fe-oxides are more abundant within the fine-grained fraction.

5.3.1 *Sulfide weathering*

The oxidation of pyrite and precipitation of sulfate minerals appears to be the predominant chemical weathering process active within the alteration scars. Figure 28

illustrates the mineralogical and geochemical changes, with respect to sulfide mineralogy for the Hansen alteration scar profile. From the base to the top of the profile, pyrite decreases, with increasing gypsum and jarosite. Gypsum concentrations vary and are attributed to the potential open nature of the system, which allows sulfate rich waters to percolate down through the profile and precipitate gypsum at the bottom of the profile. This was documented in the field from abundant gypsum filled fractures near the base of the profile (Figure 27).

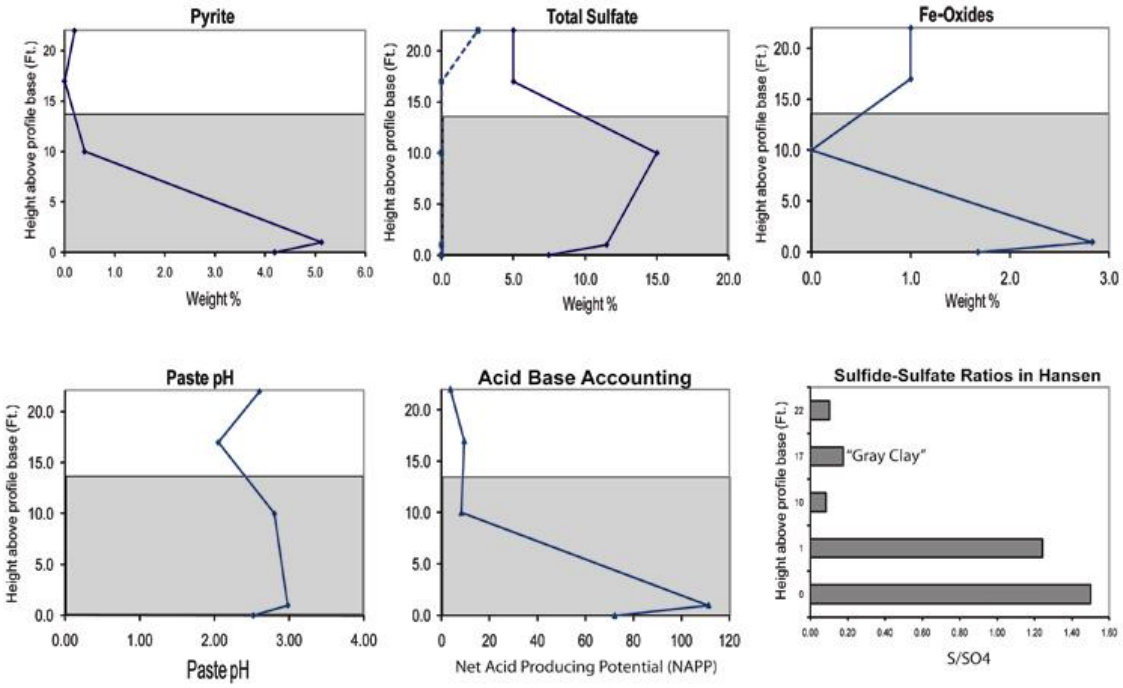

Figure 28. Geochemical and mineralogical changes associated with sulfide weathering in the Hansen alteration scar profile. Gray shades = QSP overprinting propylitic, White shades = intense QSP

Fe-oxides have no systematic variation within the profile, but indicate that oxidation of pyrite is occurring in or near the Hansen alteration scar profile. Paste pH range from 2 to 3 upward in the profile, and documents the extremely low pH of the environment. Acid Base Accounting from the profile indicates all samples in the

profile are net acid producing. The samples at the base of the profile have more acid producing potential because they have seen less sulfide oxidation. This is reflected by higher sulfide-sulfate ratios and more abundant sulfide at the base of the profile (Figure 28).

Figure 29 illustrates the changes related to sulfide weathering within the lower Southwest Hansen alteration scar profile. Pyrite generally decreases upwards in the profile, however, the high pyrite concentration zones correspond with "gray clay" layers. These layers are the finest grained of the samples in the profiles, so the lower permeability of these zones may inhibit the oxidation of pyrite. Gypsum slowly

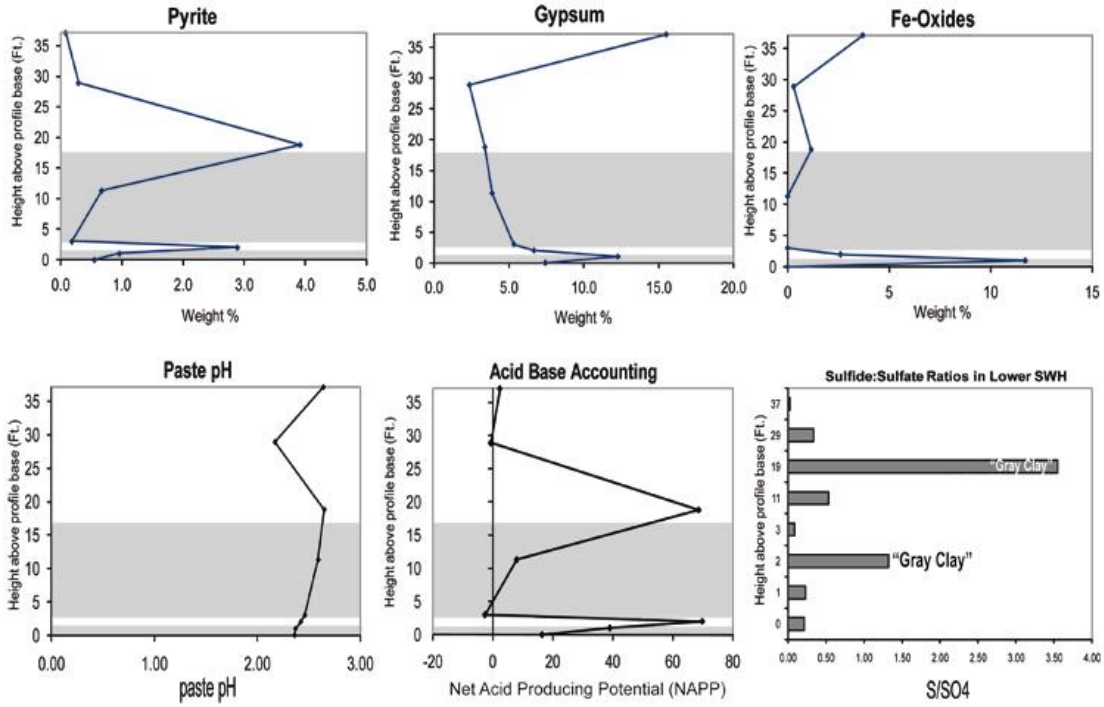

Figure 29. Geochemical and mineralogical changes associated with sulfide weathering in the lower Southwest Hansen alteration scar profile. Gray shades = QSP overprinting propylitic, White shades = intense QSP

decreases upwards in the profile, except near the base and at the top of the profile. The base of the profile consists of a ferricrete like material, where the precipitation of gypsum probably occurred from mixing of acidic runoff with Ca-bearing neutral meteoric waters. Sulfide-sulfate ratios provide less convincing evidence of sulfide oxidation upwards, but indicate that “gray clay” layers have abundant pyrite (Figure 29).

Acid Base Accounting provides documentation that most samples are acid producing, however samples 4 (SWH-GJG-0011) and 7 (SWH-GJG-0014) contain enough acid consuming minerals to buffer the acid created from pyrite oxidation. Petrographic analysis of these samples indicates calcite in these samples, but they are the only two samples noted from the entire study containing calcite. The paste pH of these samples is low (2.17 & 2.46) indicating the calcite is not available for buffering because of calcite occurring inside the rock fragments. These samples occur above the “gray clay” layers in the profile. There is generally no change within the paste pH upwards in the profile, but all samples document the low pH environment.

The geochemical and mineralogical changes associated with sulfide weathering in the upper Southwest Hansen alteration scar profile are illustrated in Figure 30. This profile represents the closest case to the expected mineralogical changes of a classic weathering profile. Pyrite decreases, while gypsum and Fe-oxides increases toward the top of the profile. The top sample of the profile is a ferricrete, with high concentrations of Fe-oxides. Perhaps this ferricrete acts as a barrier for fluid percolation through the profile, apparently preserving the gypsum near the top. Sulfide-sulfate ratios agree with the mineralogical observations that there is more

abundant pyrite within the base of this profile (Figure 30). Acid Base Accounting documents all samples are acid producing, with the bottom samples having the largest

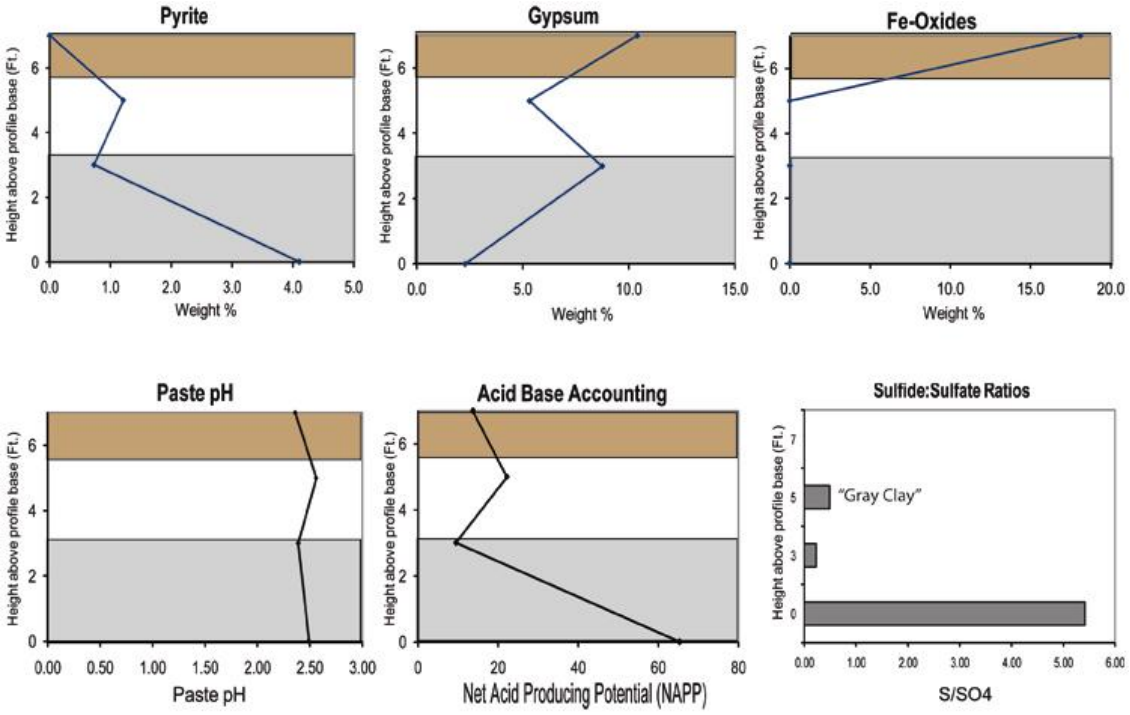

Figure 30. Geochemical and mineralogical changes associated with sulfide weathering in the upper Southwest Hansen alteration scar profile. Gray shades = QSP overprinting propylitic, White shades = intense QSP, Brown Shades = ferricrete

potential to create acid. This also correlates with the mineralogical observations of abundant pyrite in the base of the profile (Figure 30). Paste pH is essentially constant upwards in the profile and is similar to other profiles reflecting the low pH environment.

Variations in pyrite abundance through the profiles may be attributed to the intensity of hydrothermal alteration or the oxidation of pyrite. However, the abundance of pyrite appears less important than the weathering of pyrite from oxidation. Based on petrographic analysis, pyrites near the base of the profiles appear

less weathered (i.e. euhedral, no oxide rims), while pyrite near the tops of the profiles has experienced weathering (i.e. anhedral, oxide rims and trails, and gypsum rims).

5.3.2 *$\delta^{34}S$ & $\delta^{18}O_{SO4}$ isotopes of sulfide weathering*

The oxidation of pyrite to sulfate at low temperature seems to be a unidirectional process with little to no fractionation. This often results in $\delta^{34}S_{SO4}$ values being indistinguishable from those of the parent sulfide (Gavelin et al., 1960; Field, 1966; Rye et al., 1992; and Seal et al., 2000). Stable isotope analysis ($\delta^{34}S$ & $\delta^{18}O_{SO4}$) of pyrite and gypsum document sulfates formed within the alteration scars under conditions consistent with a supergene environment (Figure 31).

On Figure 31, samples plotting in the upper right formed during a hydrothermal event (Campbell and Lueth, 2008), probably in equilibrium with magmatic water. The $\delta^{34}S$ of sulfate minerals in equilibrium with magmatic sulfide (ore sulfide box), at high temperatures, are heavier than that of the precipitating sulfide. $\delta^{18}O_{SO4}$ values in this quadrant are consistent with magmatic values of oxygen-forming minerals (6-9‰).

The yellow squares represent modern values for sulfate from groundwater from the Questa area. Samples plotting to the left of $\delta^{34}S = 0$ and $\delta^{18}O_{SO4} < 0$, also form in the supergene environment. The $\delta^{18}O_{SO4}$ of these samples are closer in value to modern sulfate oxygen values, so they are interpreted to have formed in the modern weathering environment.

The analyses that plot to the left of $\delta^{34}S = 0$ and $\delta^{18}O_{SO4} > 0$ are ancient supergene in origin. These values reflect $\delta^{34}S$ of related hydrothermal pyrites and

$\delta^{18}O_{SO4}$ values reflect ancient climatic and environmental conditions during the time of mineral formation.

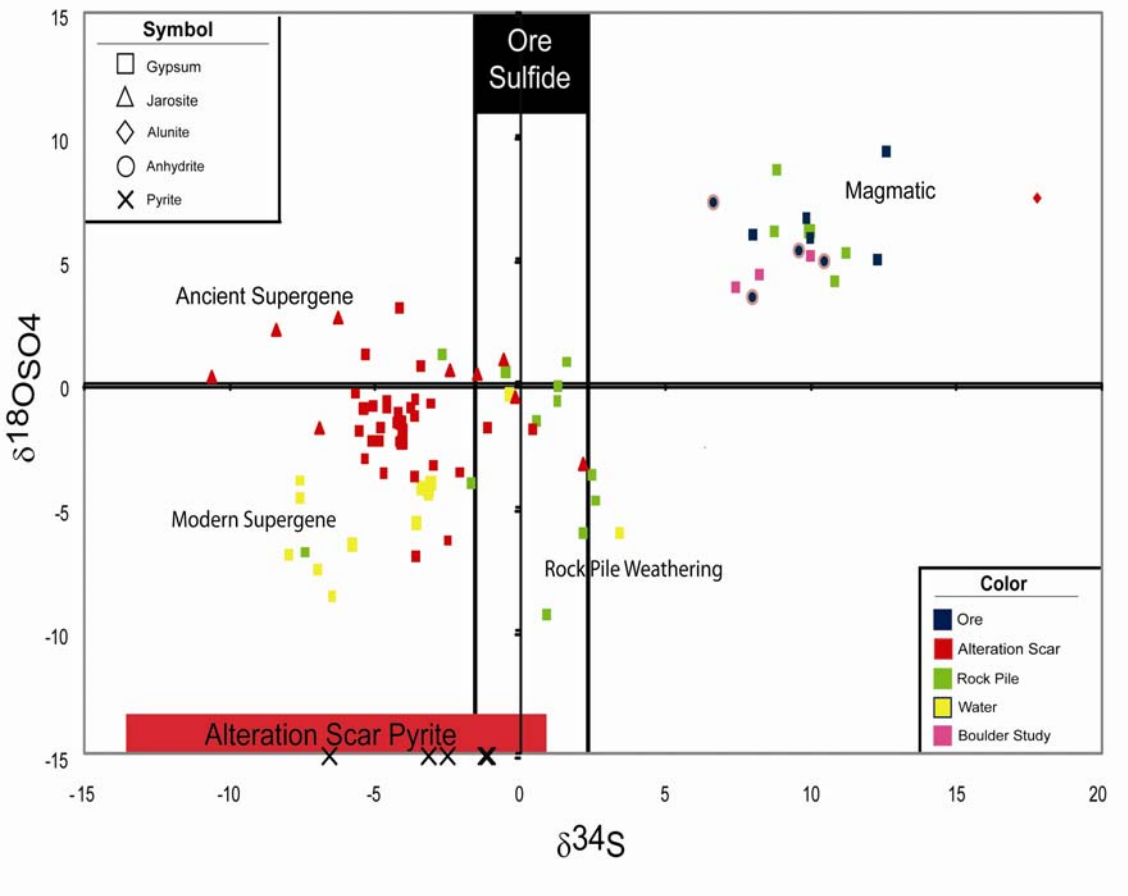

Figure 31. $\delta^{34}S$ and $\delta^{18}O_{SO4}$ diagram of sulfates and sulfides analyzed. Red squares and black X's are from this study and the remaining data is from Campbell and Lueth (2008) (Appendix C).

Alternatively, the variation in oxygen values may also represent the nature of the supergene environment where the sulfates precipitated, either the vadose zone or the saturated zone. Gypsum precipitating in the vadose zone would have a higher contribution from atmospheric oxygen ($\delta^{18}O = 23.5 \pm 0.3$ ‰) (Seal et al., 2000), and water ($\delta^{18}O = -12.4$ ‰, Questa average), while samples precipitating in the saturated zone, the oxygen isotope value would be directly from water. The resulting

environment of sulfate precipitation could also account for the variation seen within the $\delta^{18}O_{SO4}$.

Either of the explanations for the $\delta^{18}O_{SO4}$ variations are plausible, however, the results from the $\delta^{34}S$ and $\delta^{18}O_{SO4}$ analyses still indicate that all gypsums analyzed from the alteration scars formed in the weathering environment, not in the hypogene environment. This provides supporting evidence, along with mineralogical and petrographic observations (Figure 28, 29, 30, & Appendix B), that the sulfide weathering system has been active in the past and continues within the alteration scars.

5.3.3 *Silicate weathering*

The effects of silicate weathering are more difficult to determine. The changes within silicate mineralogy (i.e. decreasing feldspar, increasing clay) are expected changes resulting from the incongruent dissolution of feldspars, followed by the precipitation of secondary clay minerals. However, the dominant clay types that have been documented in the weathering profiles (chlorite and illite) appear to correspond to the hydrothermal alteration types of each individual sample. Other clay minerals in the profiles include kaolinite, smectite, and mixed layer clays, which are relatively unchanged within each profile (Figures 32, 33, & 34) and between clast and matrix fractions (Table 10 & Figure 21). These features suggest that no authigenic clay formation has occurred in the profiles.

The silicate mineralogical changes in the Hansen alteration scar profile are shown in Figure 32. Feldspars (albite and orthoclase) decrease and clays increase

upwards in the profile. Chlorite and feldspar are abundant in the QSP overprinting propylitic alteration with little to no chlorite and feldspar in the intense QSP alteration

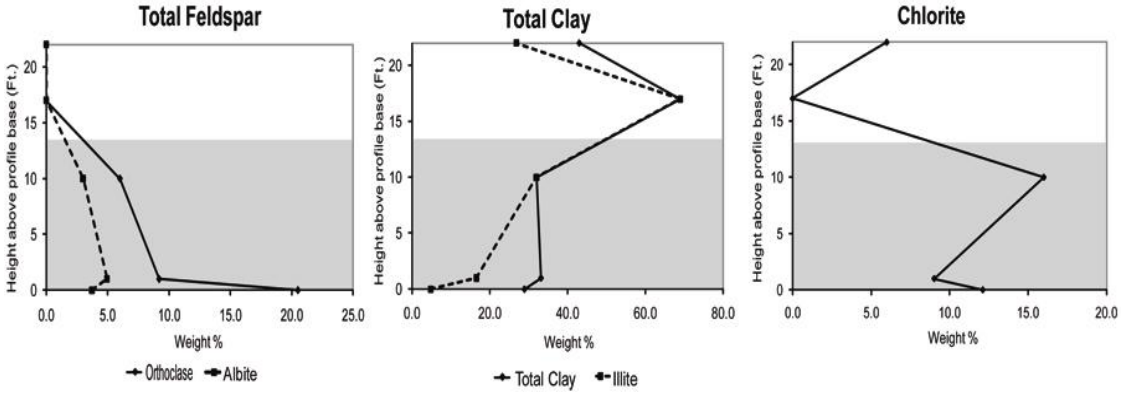

Figure 32. Silicate mineralogical changes in the Hansen alteration scar profile. Gray shades = QSP overprinting propylitic, White shades = intense QSP alteration

zones. Total clay abundances do not change in the QSP overprinting propylitic alteration, but increase substantially in the intense QSP alteration. Illite increases from the base into the intense QSP altered zone. This suggests the base of the profile has seen the effects of QSP alteration, however, the intensity of the alteration was not as great. There are no changes among other clay minerals upward in the profile (Figure 22). The presence of large amounts of orthoclase in the andesite bedrock may also represent an influence of potassic alteration near the base of the profile.

Figure 33 illustrates the changes in silicate mineralogy from the upper Southwest Hansen profile. Total feldspars decrease from the base to the top of the profile. The increase in feldspars at the top of the profile may be due to preservation by cementation of unweathered fragments into a ferricrete. Petrographic analysis has indicated both sub-angular to angular fragments in the matrix, suggesting the source was near to the place of ferricrete formation. The increased feldspar, with no chlorite, suggests that these rocks have either been QSP or advanced argillic altered.

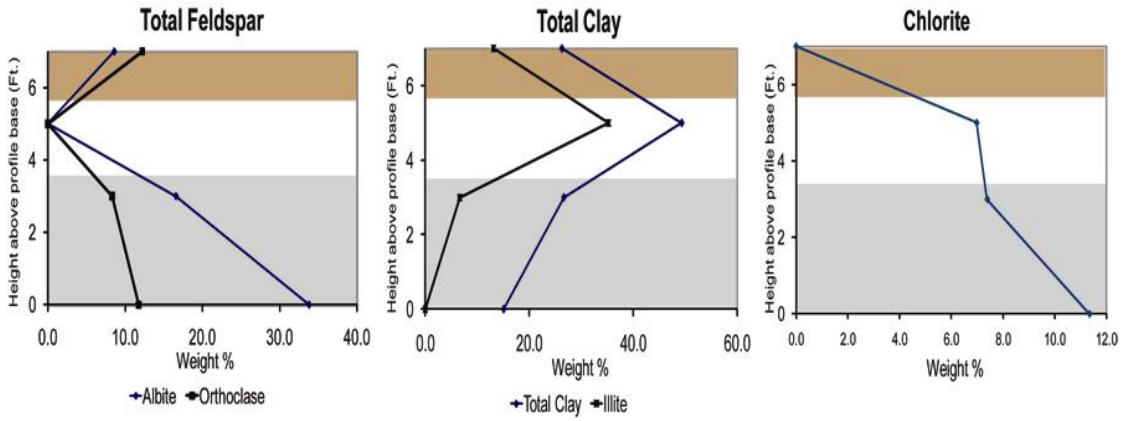

Figure 33. Silicate mineralogical changes in the upper Southwest Hansen alteration scar profile. Gray shades = QSP overprinting propylitic, White shades = intense QSP, Brown Shades = ferricrete

Total clays increase upwards in the profile, with the greatest abundance located in the QSP altered zone. The dominant clay type in this zone is illite, with little to no change in the other clay minerals (Figure 23).

The changes within silicate mineralogy from the lower Southwest Hansen profile are illustrated in Figure 34. In this profile there are two zones of intense QSP alteration. Feldspar and chlorite are less abundant in the QSP alteration and more abundant in the QSP overprinting propylitic alteration. Total clay abundances increase upwards into each individual zone of intense QSP alteration. The dominant clay mineral in these intense QSP altered zones is illite, with no systematic variation with other clay minerals upwards in the profile (Figure 24). These two distinct zones of intense QSP alteration provide convincing evidence that in these intense QSP zones, the feldspars have been altered to clay minerals through hydrothermal processes.

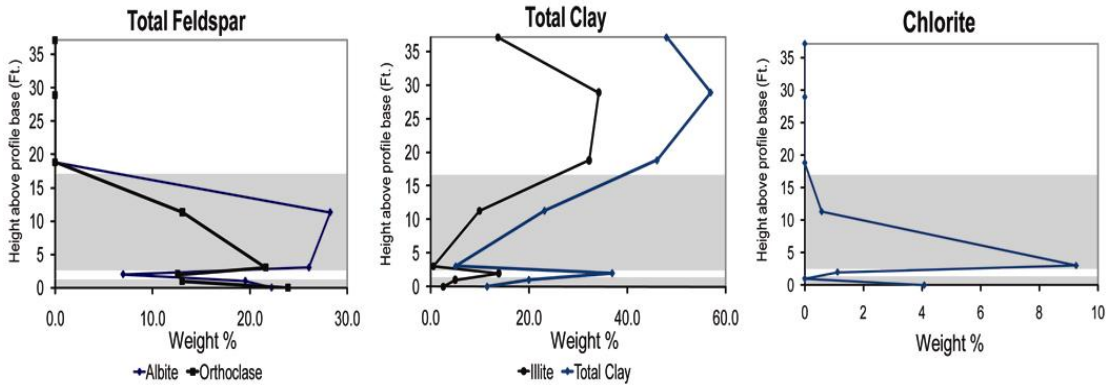

Figure 34. Silicate mineralogical changes in the lower Southwest Hansen alteration scar profile. Gray shades = QSP overprinting propylitic, White shades = intense QSP

The silicate mineralogy changes seen in the alteration scar profile are the expected chemical weathering changes through a classic weathering profile. However, because of hydrothermal alteration in the scars, the interpreted decrease in the feldspars and increase clay abundances are best reconciled as being derived from hypogene minerals during the hydrothermal alteration event.

5.3.4 *Isocon Calculations*

Using the isocon method (Grant, 1986), chemical changes between coarse and fine portions of a sample were examined. Using the coarse sample as the basis for comparison, chemical changes can be seen as the particle size decreases, keeping an oxide constant (Figure 35). Constant TiO_2 was used, as there is little change in the XRF geochemistry between the coarse to fine particle fractions with respect to this oxide. All three samples analyzed for the particle size splits show similar trends. Relative to the coarse size fraction, there is an increase of Al_2O_3, FeO, CaO and P_2O_5 in the fine-grained fraction. Elemental oxides that decrease from the coarse to fine

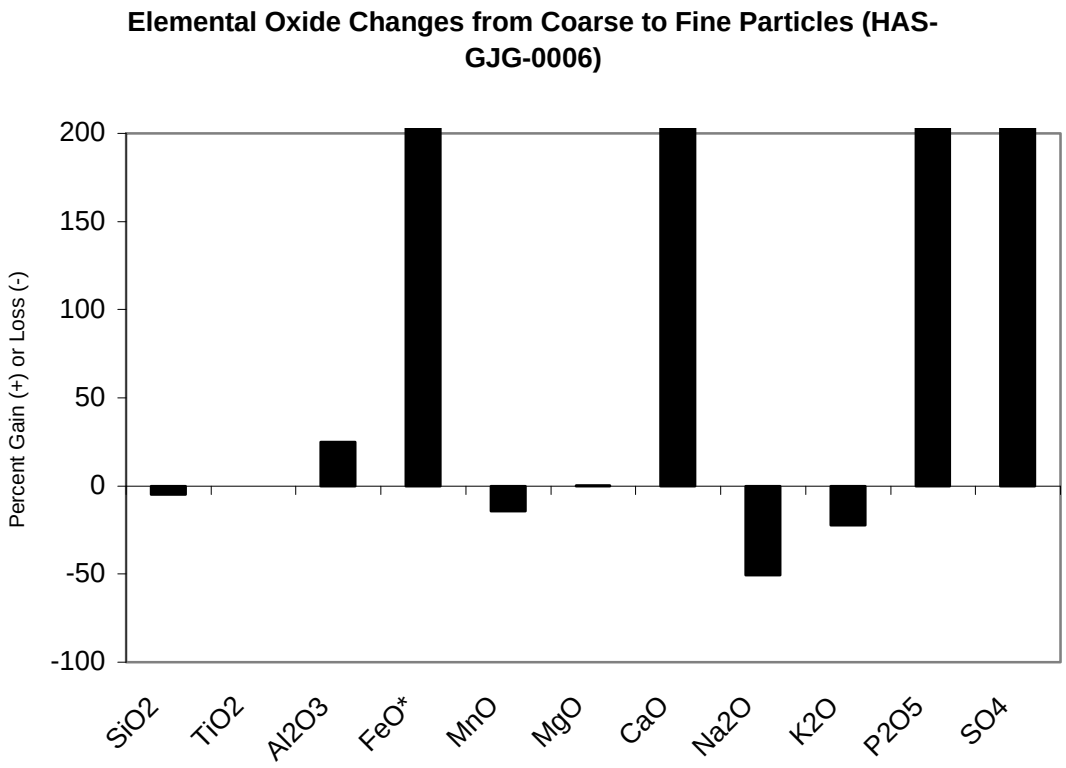

Figure 35. Chemical variation diagrams using the isocon method for coarse to fine particle. Method uses constant TiO_2 and percent gains and/or losses relative to the least weathered sample (coarse grained). Sample HAS-GJG-0006.

particles include Na_2O, K_2O, and perhaps SiO_2. Using these changes in the elemental oxides, in conjunction with mineralogy, chemical weathering can be documented during the physical break up of the rock.

The sulfide weathering system appears is apparent, as there is an increase in FeO CaO and SO_4 between the coarse and fine fractions. Even though pyrite (FeO) would be expected to decrease in the fines because of oxidation, there is an increase in FeO due to the precipitation of Fe-oxides and jarosite. P_2O_5 has been documented in microprobe analysis of goethite (N. Dunbar, personal comm.), possibly from the dissolution of apatite. Increasing P_2O_5 is attributed to higher abundances of goethite, which is consistent with increasing FeO. The increase in CaO and SO_4 is attributed

the precipitation of gypsum. The CaO for the precipitation of gypsum may be from the dissolution of calcite or epidote. The system appears to be open from the large influxes of FeO, CaO, SO_4 and P_2O_5 into the profiles and seen by sulfate precipitation in fractures (Figure 27).

Silicate dissolution may be recognized from coarse to fine particles, indicated by the decrease in Na_2O and K_2O, and the large change in total feldspar from coarse to fine fractions (Figure 36). The gains in Al_2O_3 and CaO may represent the accumulation of secondary clay minerals, however, this is unlikely since the clay mineralogy is consistent between the coarse and fine fractions (Figure 21 & Figure 36) and the extremely low pH environment of the alteration scars (Table 8). The decreases in these elemental oxides may also reflect the dilution caused by the large amounts of precipitated gypsum in the fine-grained fraction.

Bulk changes in chemistry were noted in coarse and fine-grained samples in the profiles. Because of the assumption made earlier that the tops of the profiles have experienced longer weathering, comparison of the base to top of the profiles is appropriate. The rocks within a profile should have started as a similar composition, so the chemical changes from bottom to top should mimic the results seen in the coarse to fine grained comparison.

The isocon method (Grant, 1986) was employed, in a similar fashion (constant TiO_2), to evaluate any chemical changes within each profile sample. Assuming the bottom profile samples are the least weathered rocks, chemical changes due to weathering or alteration can be observed for each profile (Figure 37, 38, and 39).

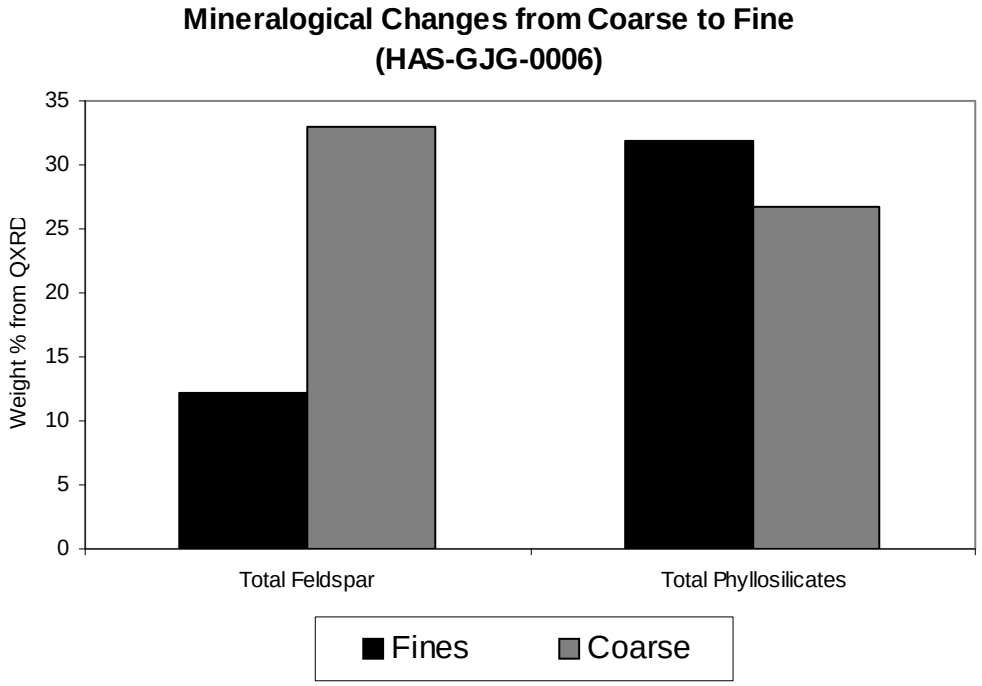

Figure 36. Histogram of QXRD mineralogy for total feldspar and total phyllosilicates between coarse and fine fractions (HAS-GJG-0006). Total feldspars have large decrease between particle sizes, while phylliosilcates have a slight to no change.

Isocon calculations for the upper Southwest Hansen alteration scar profile are illustrated in Figure 37. The two elemental oxides that show the least amount of change are Al_2O_3, and SiO_2. This indicates that there is little to no change in clay or quartz abundances through the profile. The high losses in FeO, MnO, and MgO could correspond to weathering or dissolution of epidote, chlorite and pyrite. The large decrease in Na_2O may represent the dissolution of albite upwards in the profile. The large increase in CaO correlates to the precipitation of gypsum upwards in the profile (Figure 30), while the increase in K_2O could either represent the precipitation of jarosite near the top, or an increase in illite near the QSP alteration zone. The changes within the geochemistry of this profile can readily be correlated to the changes in the

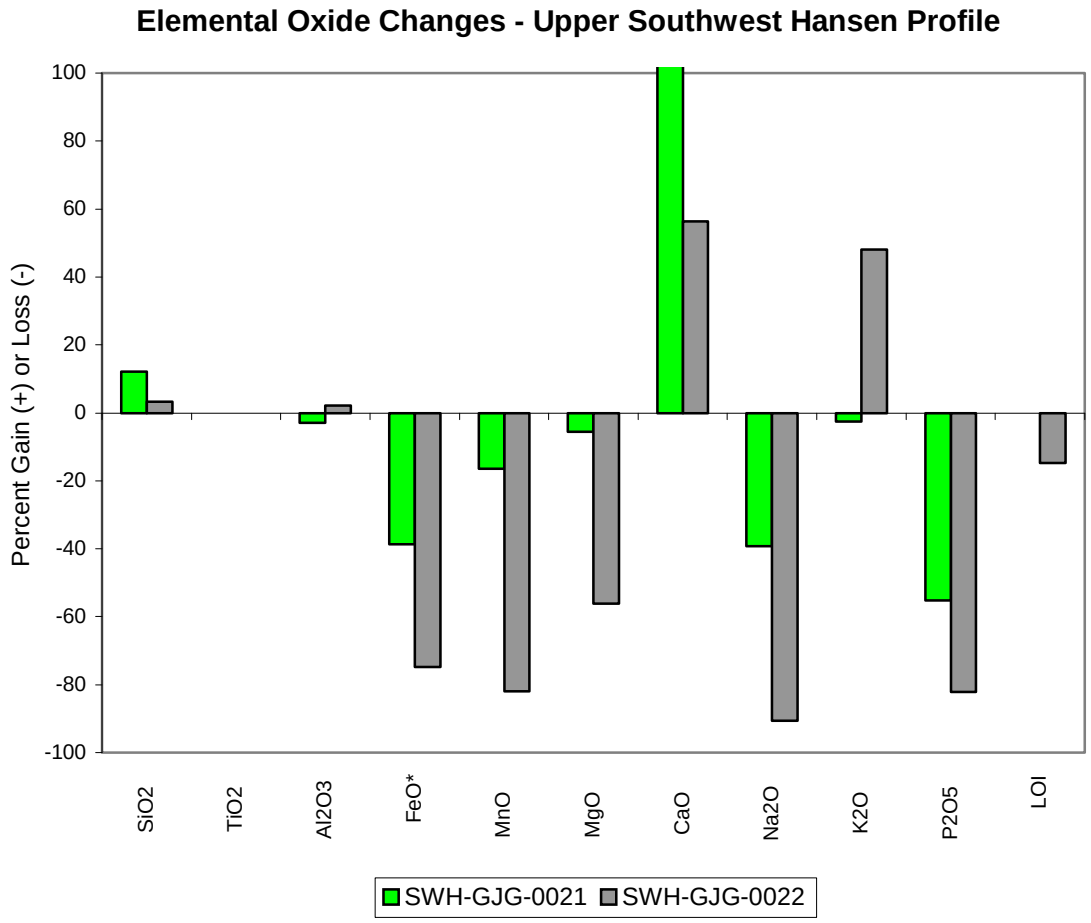

Figure 37. Chemical variation diagrams of the upper Southwest Hansen alteration scar profile using the isocon method. This method uses constant TiO_2 and percent gains and/or losses are relative to the least weathered sample (bottom of profile).

mineralogy (Figure 23). This profile is the best representative of the classic weathering model, probably because the profile appears to represent one lithology with less internal variation from hydrothermal alteration.

Figure 38 represents the geochemical changes in the Hansen alteration profile using constant TiO_2 isocon calculations. Two distinct groups of isocon variations can be recognized and appear to best correlate to hydrothermal alteration type. To illustrate, samples shaded with green represent quartz-sericite-pyrite (QSP) alteration

overprinting propylitic alteration and samples shaded in gray represent intense quartz-sericite-pyrite (QSP) alteration. Increases in SiO_2 and Al_2O_3 correlate to the intense QSP alteration within the profile (HAS-GJG-0009 and HAS-GJG-0010). The bottom of the profile has little to no change in Al_2O_3, indicating no change in clays abundances. The intense QSP alteration has large increases in both K_2O and Al_2O_3 correlating to increases in the abundance of illite.

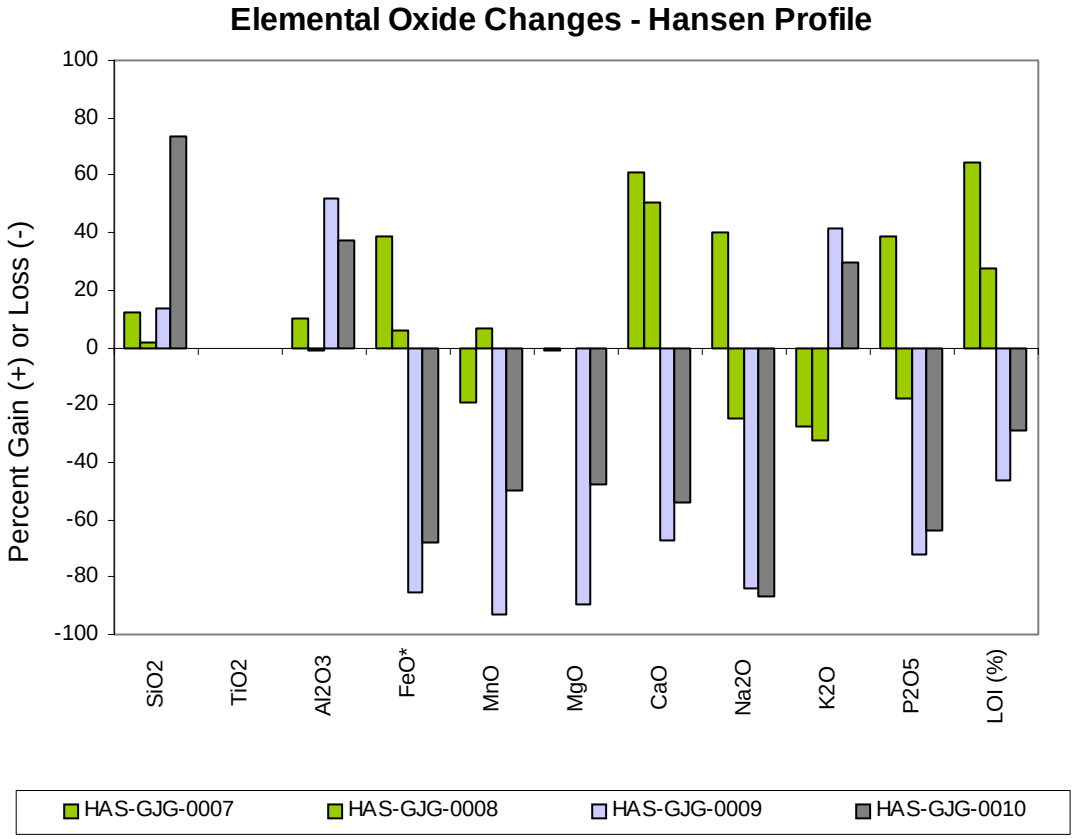

Figure 38. Chemical variation diagrams of the Hansen alteration scar profile using the isocon method. This method uses constant TiO_2 and percent gains and/or losses are relative to the least weathered sample (bottom of profile).

The increase in FeO near the base of the profile is consistent with the presence of chlorite or Fe-oxides (Figure 22). The top of the profile has a large decrease in FeO, which is attributed to the absence of chlorite or the oxidation of pyrite. Constant

MnO and MgO at the base of the profile indicates chlorite and epidote (if present) are not being dissolved, however, at the top of the profile, there are large changes in the MnO and MgO suggesting chlorite and epidote have dissolved or altered during intense QSP alteration.

The large CaO decrease at the top of the profile is attributed to sulfate being transported away from these areas (Figure 28) and precipitating in the fractures near the base (Figure 27). The decrease in Na_2O may represent the dissolution of albite. This profile provides excellent evidence for two distinct hydrothermal alteration types within one lithology and has limited application to weathering.

The isocon calculations for changes in elemental oxides from the lower Southwest Hansen profile are located in Figure 39. The elemental oxide changes within this profile are difficult to differentiate. The only elemental oxides that have identical direction changes for the QSP overprinting propylitic alteration and intense QSP alteration are Al_2O_3, and SiO_2. This would suggest there is a decrease in clays upwards in the profile, however mineralogical analysis has shown that clays do increase upwards in the profiles (Figure 24).

The isocon calculations for this profile do not reflect the changes in elemental oxides related to alteration or features noted for weathering. An explanation for this discrepancy is that this large profile has a greater variation in original lithology. Mapping of the lower Southwest Hansen alteration scar has indicated xenoliths of andesite located within the intrusive quartz latite porphyry (Figure 40). This observation suggests proximity to the roof of this sill where abundant andesite xenoliths were trapped in the magma as it cooled.

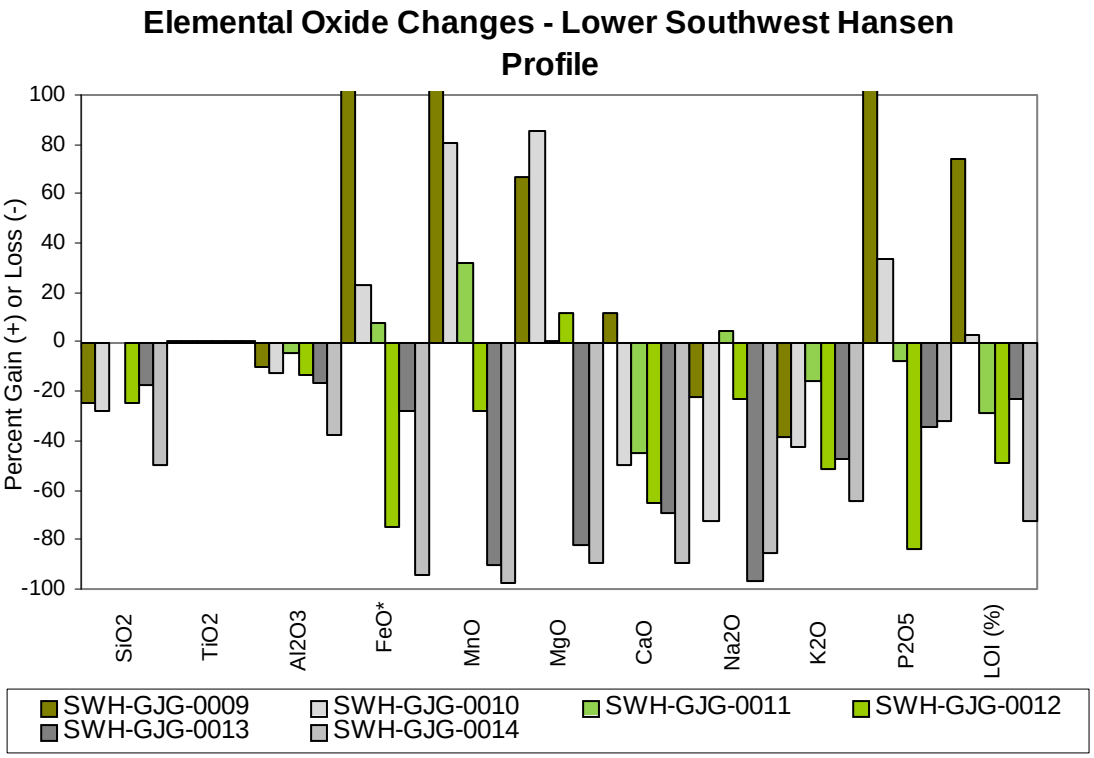

Figure 39. Chemical variation diagrams of the lower Southwest Hansen alteration scar profile using the isocon method. This method uses constant TiO_2 and percent gains and/or losses are relative to the least weathered sample (bottom of profile).

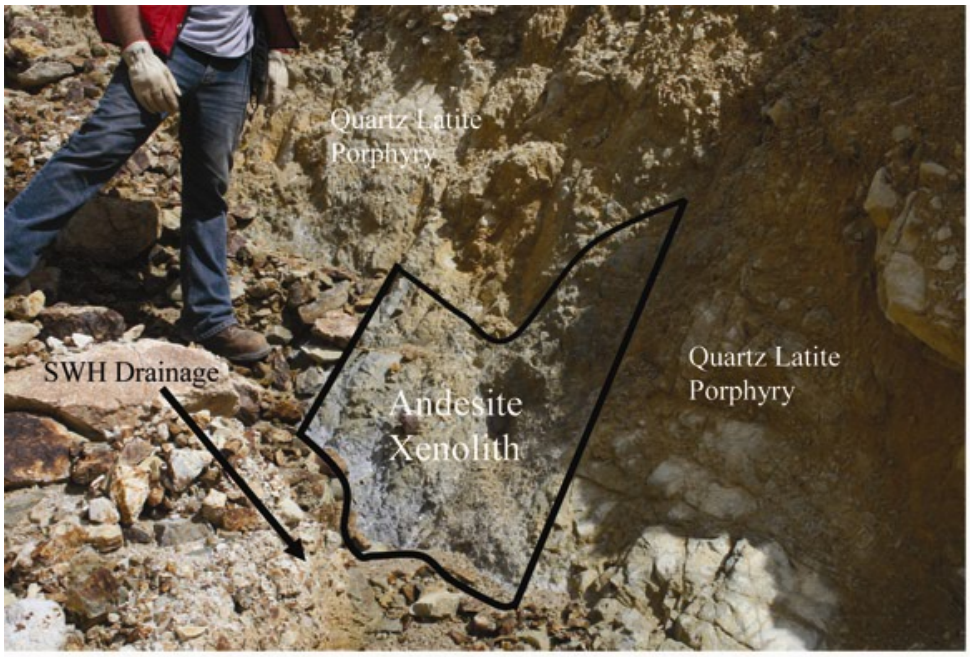

Figure 40. Observation of andesite xenolith located with the quartz latite porphyry from the lower Southwest Hansen alteration scar.

Isocon calculations provide insight into the different hydrothermal alteration assemblages and the mineralogy changes associated with elemental oxide changes in each profile. In documenting the different types of alteration within a profile, mineralogical changes associated with supergene weathering or hydrothermal alteration can be distinguished. The upper Southwest Hansen profile documents weathering features with subtle hydrothermal alterations, the Hansen profile indicates hydrothermal alteration types with subtle weathering features, and the lower Southwest Hansen profile provides alteration types and multi-lithology, with subtle weathering features.

5.3.5 *Clay Isotopes*

The origin of the clay minerals is crucial to identifying the extent of incongruent silicate weathering. The results from the stable isotope analysis of clay minerals analyzed in this study plot well within the hydrothermal field, indicating that they did not form from supergene weathering (Figure 26). The isotopic analysis results were plotted on a compilation diagram modified from Sheppard and Gilg (1996) (Figure 41). Questa clays plot firmly within the values of hydrothermal clay minerals defined by previous studies of clays from various environments.

Although the alteration scar clay samples plot firmly in the hydrothermal field, there is some minor scatted in the data, mostly in $\delta^{18}O$, with slight to no change in δD (Figure 26). This scatter could be caused by a mixture of hydrothermal and weathering clays by variable contamination with other oxygen bearing minerals and or clays formed at slightly different temperatures in the scars.

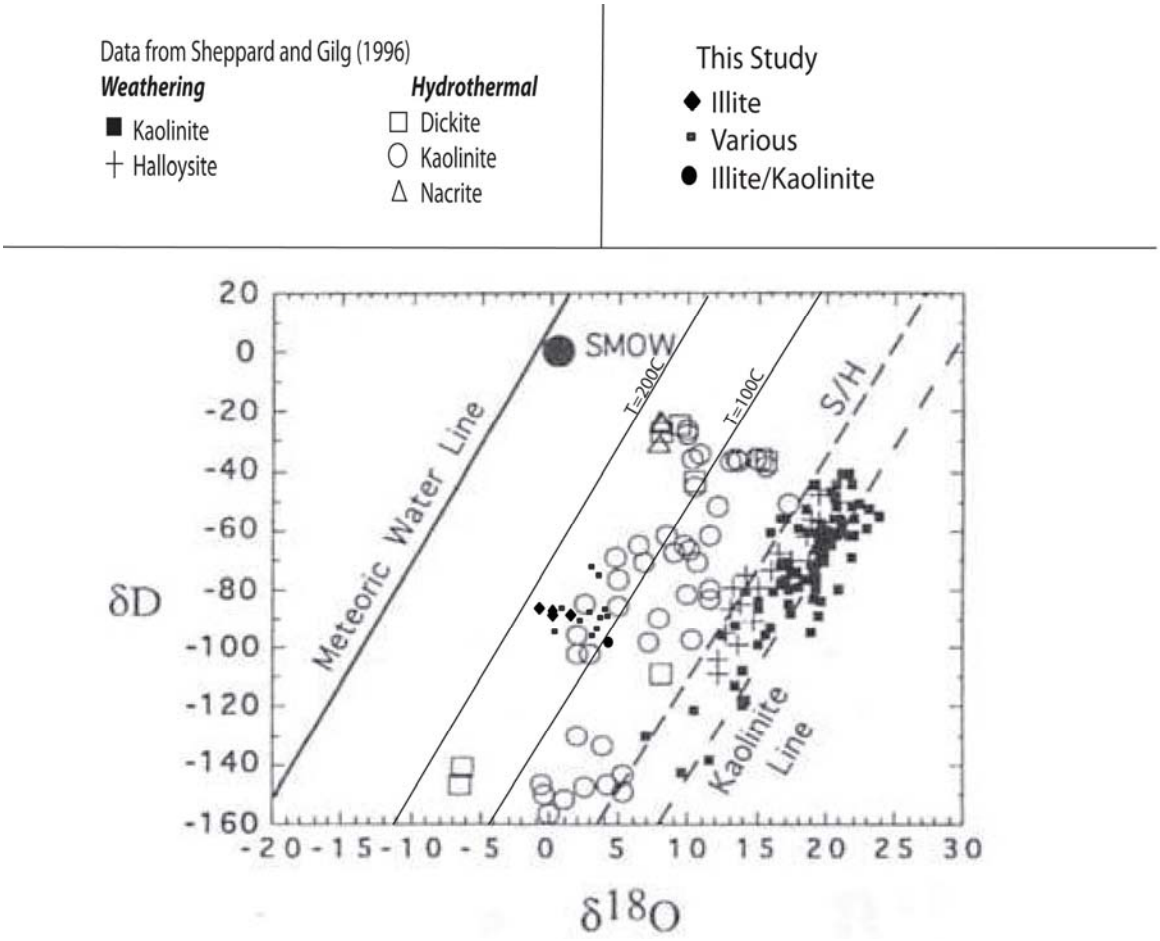

Figure 41. Compilation $\delta^{18}O$ vs. δD diagram of this study and previous clay studies. The clays from this study include kaolinite, illite, chlorite, and smectite (modified from Sheppard and Gilg, 1996).

5.3.5.1 *Quartz Contamination*

A possible cause for the weak positive variation in $\delta^{18}O$ values in the Questa clay samples is by variable contamination with quartz. Quartz was not removed from the samples by the various chemical treatments. Quartz in the sample should either be igneous magmatic values (6 to 9 ‰), or local hydrothermal quartz (7-8 ‰ for Questa mineralization (A. Rowe, personal communication).

The mineralogically most pure illite sample (HAS-GJG-0009) has the lightest $\delta^{18}O$ of the clays. Because igneous or local hydrothermal quartz is isotopically

heavier than the clays, contamination by quartz would increase the $\delta^{18}O$ of the samples, moving its composition towards the kaolinite line (Figure 26).

Using the post-chemical treatment XRD patterns, it is possible to determine the relative amount of quartz contained within each sample. Quartz X-Ray diffraction intensities ($2\theta = 20.8$) were divided by the illite intensities ($2\theta = 17.87$) to provide a ratio that is comparable between samples. These samples were plotted against the $\delta^{18}O$ values of the samples to determine the effect of quartz contamination (Figure 42).

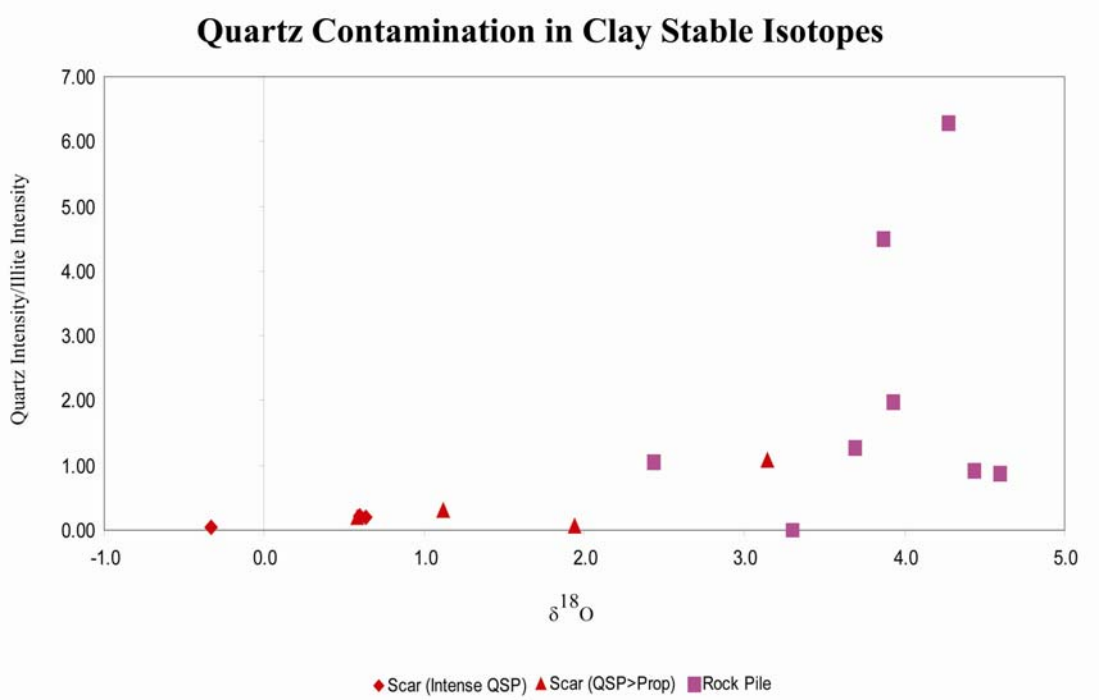

Figure 42. X-ray diffraction quartz intensity/illite intensity vs. $\delta^{18}O$ of Questa clays. Notice a slight positive correlation.

Figure 42 suggests some effect of quartz with the shift in heavier $\delta^{18}O$ (≥ 0 ‰ values) of the clays. The variation in the $\delta^{18}O$ of the clay samples appears more complex than just quartz contamination and may also be affected by the hydrothermal alteration history of each sample, discussed below.

5.3.5.2 *Propylitic vs. Quartz-Sericite-Pyrite (QSP) Alteration*

The two predominant alteration types present in the Questa mining district alteration scars that result in hypogene clay formation are propylitic and QSP. These different alteration types are thought to have formed at different temperatures and will precipitate clay minerals of differing type and isotopic composition. Although we do not have a direct geothermometer for the two types of alteration, it is likely the QSP alteration occurs at higher temperatures than propylitic because it is an interior alteration shell at Questa (Ludington et al., 2004) and at other deposits (Lowell and Gilbert, 1970; Stefanini and Williams-Jones, 1996).

Scar samples were plotted using the different alteration suites to determine any correlation between QSP (quartz contamination) and propylitic (quartz and/or chlorite contamination) alteration. Because of the different formation temperatures of these alteration suites, it may be possible that heavier $\delta^{18}O$ values are a function of the alteration type and lower temperature (greater fractionation).

5.3.5.3 *Effect of alteration type on $\delta^{18}O$*

One of the geologic factors critical to the formation of an alteration scar is the pyrite content of the rock (> 1%) (Meyer and Leonardson, 1990). Pyrite present in the Questa mining district is hydrothermal in origin, commonly associated with quartz-sericite-pyrite (QSP) alteration (Campbell and Lueth, 2008). Petrographic analysis of the rocks within the Southwest Hansen and Hansen alteration scars indicate the samples have either been intensely QSP altered or a QSP overprint on older propylitic alteration.

Carefully considering the two types of alterations present, it is possible to separate oxygen-bearing contamination minerals that would affect $\delta^{18}O$ values present in the alteration suites. Quartz is the major oxygen-bearing mineral that could affect the $\delta^{18}O$ values of the intensely QSP altered rocks, while quartz and/or chlorite may affect the $\delta^{18}O$ values of the QSP overprint on propylitic alteration.

Scatter plots of alteration minerals vs. $\delta^{18}O$ diagrams (Figure 43 & 44) indicate that when quartz and/or chlorite are present, as seen by the larger quartz and chlorite intensities, the more positive the $\delta^{18}O$ value of the sample. The contamination from quartz and chlorite shifts the $\delta^{18}O$ values of the samples to the right, closer towards the kaolinite line (Figure 26).

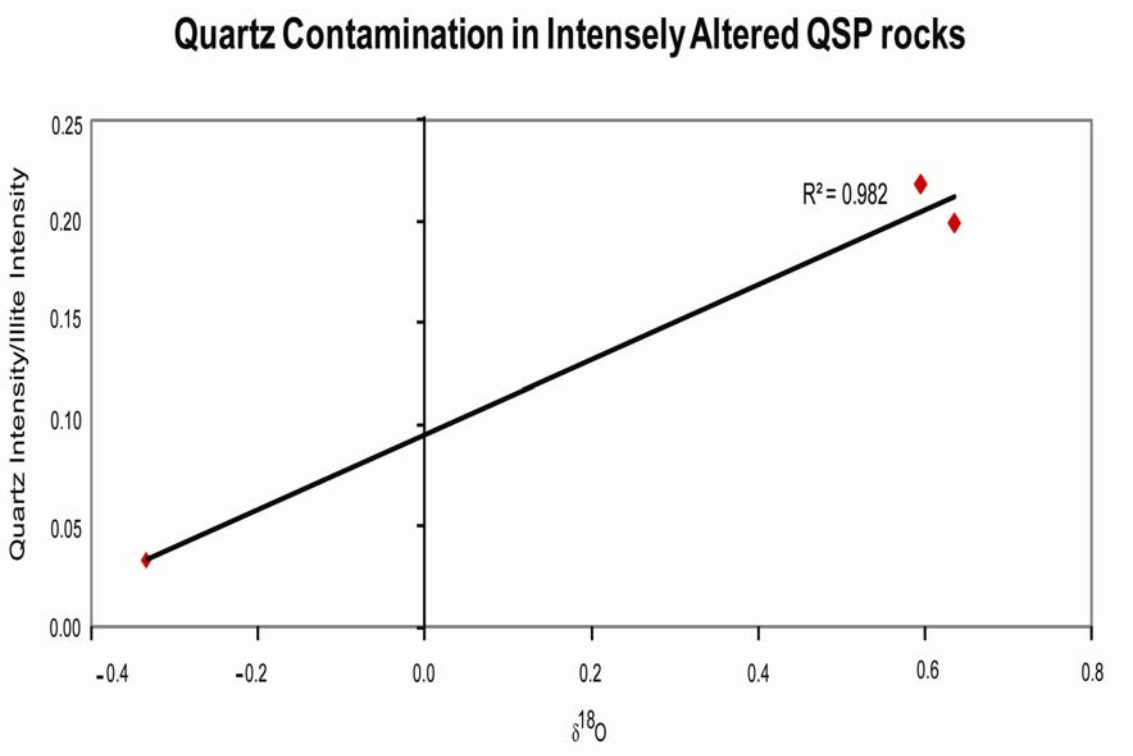

Figure 43. X-ray diffraction intensities vs. $\delta^{18}O$ of Questa clays to determine quartz contamination in intensely QSP altered scar rocks.

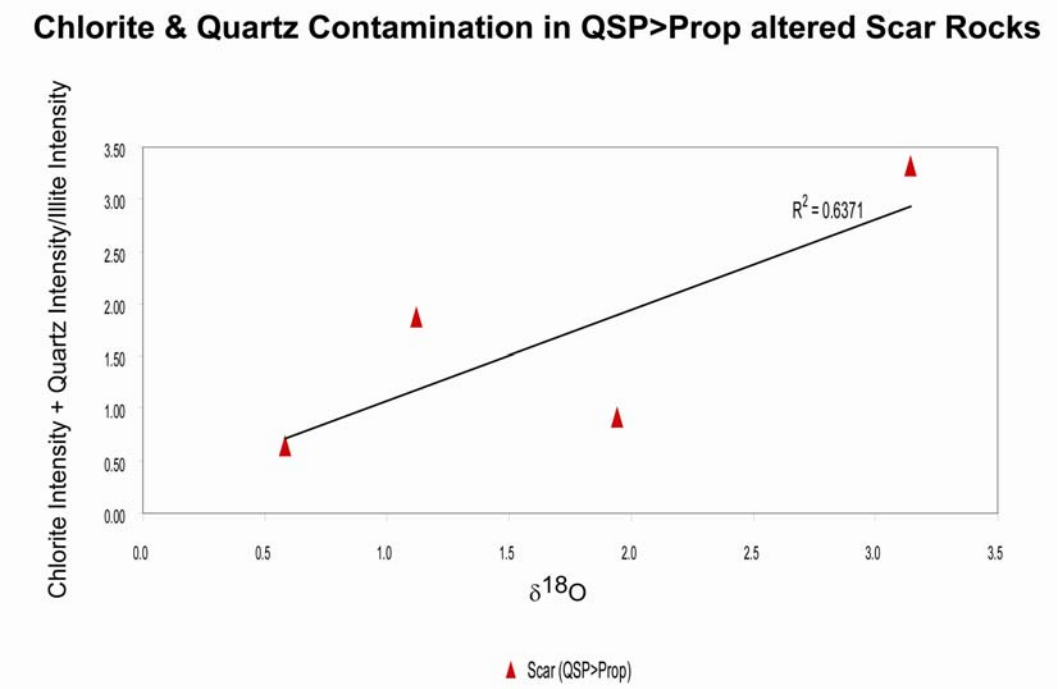

Figure 44. X-ray diffraction intensities (Chlorite & Quartz) vs. $\delta^{18}O$ of Questa clays to determine quartz and chlorite contamination in QSP>Prop altered scar rocks

Samples from the Goat Hill North rock pile were also examined in the study to determine any similarities or differences between the scars and rock piles. Half of the analyzed Goat Hill North rock pile samples correlate with the observation that quartz and chlorite contaminate the clay samples resulting in heavier $\delta^{18}O$ values (Figure 45). The other half of the Goat Hill North samples, show enrichment, with quartz and chlorite apparently having little to no affect on the $\delta^{18}O$ of the clay.

Rocks dumped in the Goat Hill North rock pile were mined from high above the ore body and could contain more variable QSP, propylitic and/or advanced argillic alteration. The alteration of the scar samples, within a single sample, is more homogeneous, where as the rock pile may potentially represent a heterogeneous mechanical mix of different alteration types. A possible explanation for the half of the rock pile samples that do show enrichment without contamination, is these samples

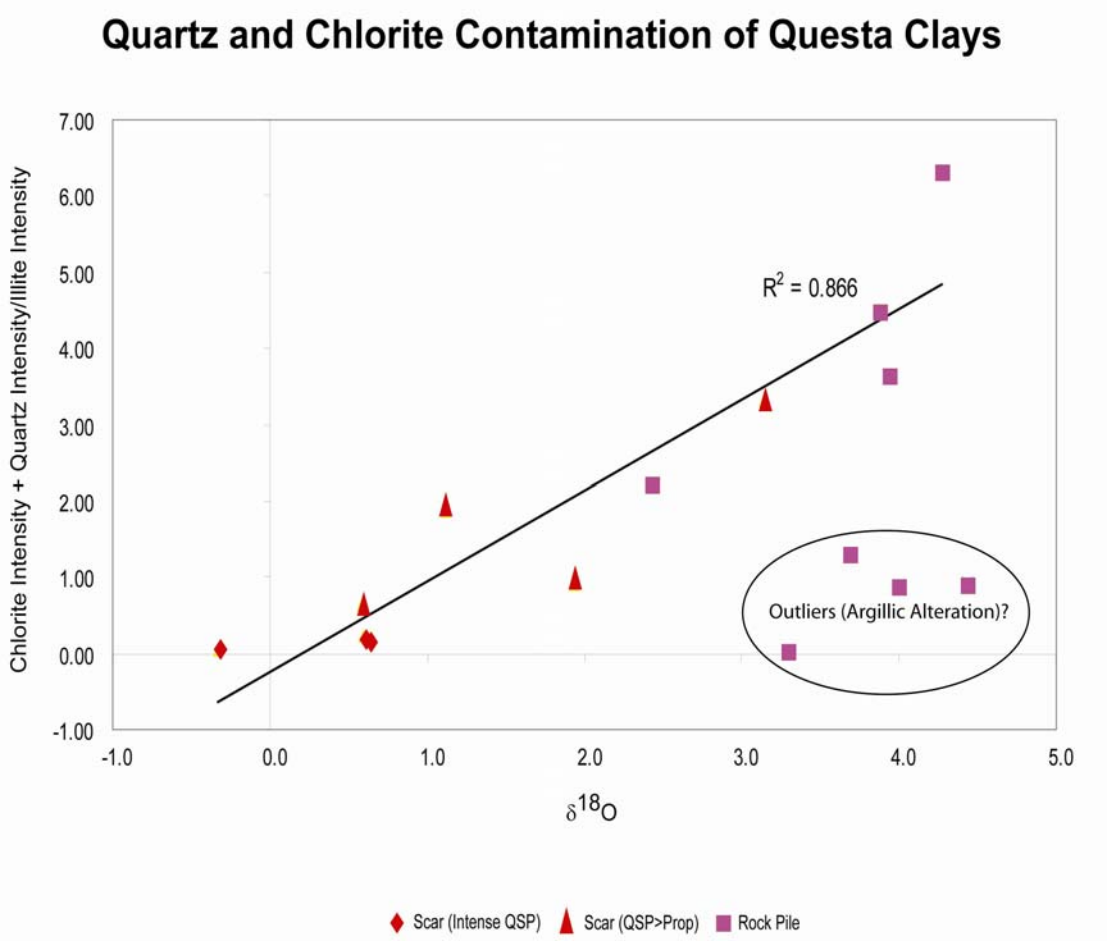

Figure 45. X-ray diffraction intensities (Chlorite & Quartz) vs. $\delta^{18}O$ of Questa clays to determine quartz and chlorite contamination in all samples.

may contain rhyolite, which was more affected by advanced argillic alteration. This alteration occurs at lower temperatures and is more distal from the magmatic hydrothermal source. An alternative explanation is that another mineral (not identified) may be contaminating the sample, causing a slightly heavier $\delta^{18}O$.

Detailed analysis of the post-chemical treatment XRD diffraction patterns resulted in the observation that the Goat Hill North rock piles have greater amounts of smectite, minimal amounts of quartz, little to no chlorite, suggesting a preponderance of a different alteration type, possibly advanced argillic alteration. On an X-Y scatter

plot of smectite intensity divided by illite intensity vs. $\delta^{18}O$ of the samples, there was no correlation between the amount of smectite and heavier $\delta^{18}O$. Therefore, it appears as though smectite is not a contaminating mineral like quartz and chlorite, but it is noted to be present in significant abundance in the rock piles.

The rock pile outliers, half of the samples without evidence of contamination, show a variation in $\delta^{18}O$ of approximately 1.3‰. The heavier $\delta^{18}O$ does not correlate with the quartz and chlorite contamination, so an alternative explanation other than contamination by isotopically heavy minerals needs to be addressed.

The samples from the Goat Hill North rock pile were located above the ore body and may contain different alteration types (propylitic, advanced argillic). The outliers have the heaviest $\delta^{18}O$ of all the samples analyzed, and based on geologic context, may have formed at the lowest temperatures, farther above the heat source. However, it may be possible for minimal amounts of weathering clay to be present, causing the shift in $\delta^{18}O$.

It is possible that these outliers have heavier $\delta^{18}O$ values based on two possible factors: 1) the temperature of clay formation, or 2) the presence of minimal weathering clays causing the $\delta^{18}O$ shift. If the cause for this variation is due to the latter hypothesis, a relative amount of weathered material can be estimated by using a lever rule with the lightest (and highest temperature) illite as one end member and a clay on the kaolinite line as the other (Figure 46).

Employing this methodology, approximately 30% of the clay in the heaviest samples could be due to weathering. The inability to recognize a discrete authigenic

clay by petrographic or XRD analysis diminishes the potential for the latter hypothesis to apply.

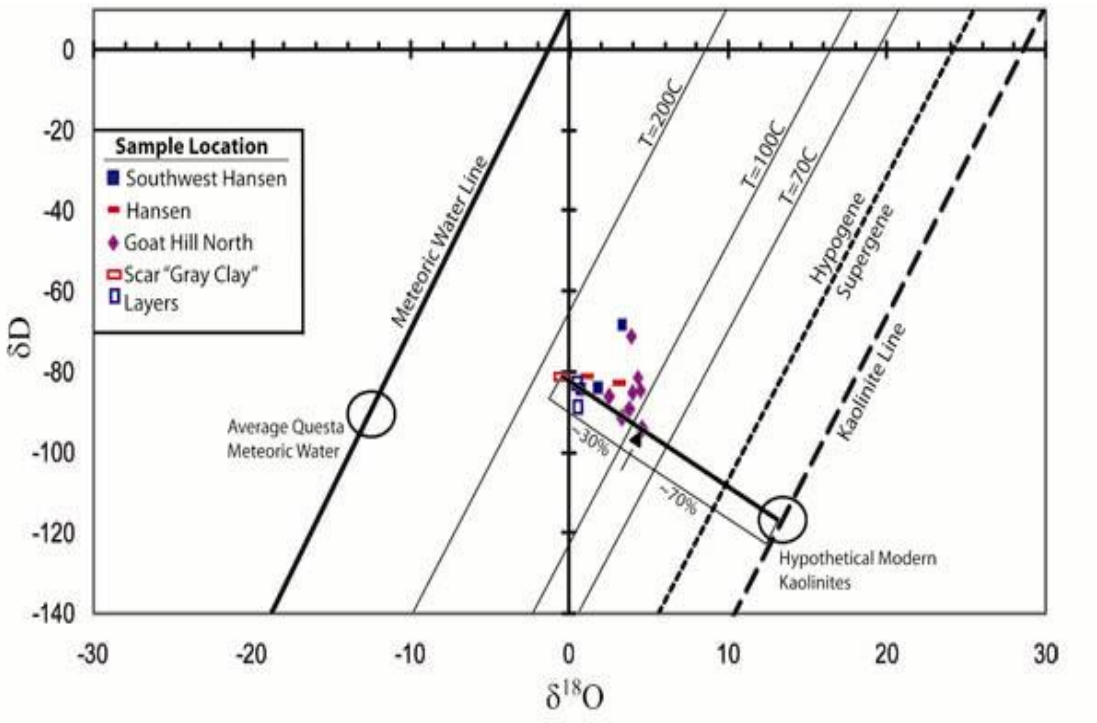

Figure 46. $\delta^{18}O$ vs. δD diagram of Questa clays showing estimation of possible amount of clay in heavy $\delta^{18}O$ samples

5.4 Relative Role of Physical and Chemical weathering

The results from this study have documented that both physical and chemical weathering of material is active in the alteration scars. The majority of the mineralogical evidence for chemical weathering is noted in the sulfide weathering system (pyrite-calcite-gypsum). However, review of surface and ground water data collected by the USGS (Nordstrom et al., 2005) shows abundant dissolved aluminum and silicon, suggesting significant dissolution of silicate minerals. This surface and

groundwater data is consistent with silicate mineralogical and geochemical changes seen within the alteration scar profiles. Thus the chemical dissolution of silicate minerals is active, but based on isotopic data, there is no supporting evidence for the formation of secondary clay minerals. The low paste pH values of soils in the profiles (< 3), coupled with groundwater data, indicate the active congruent dissolution of silicates, which precludes the precipitation of clay (Figure 47) (Krauskopf and Bird, 1995). These low pH values are independent of rock type or alteration type because the rocks in the Questa area are sulfide-rich, which will cause the drop in pH regardless of rock type.

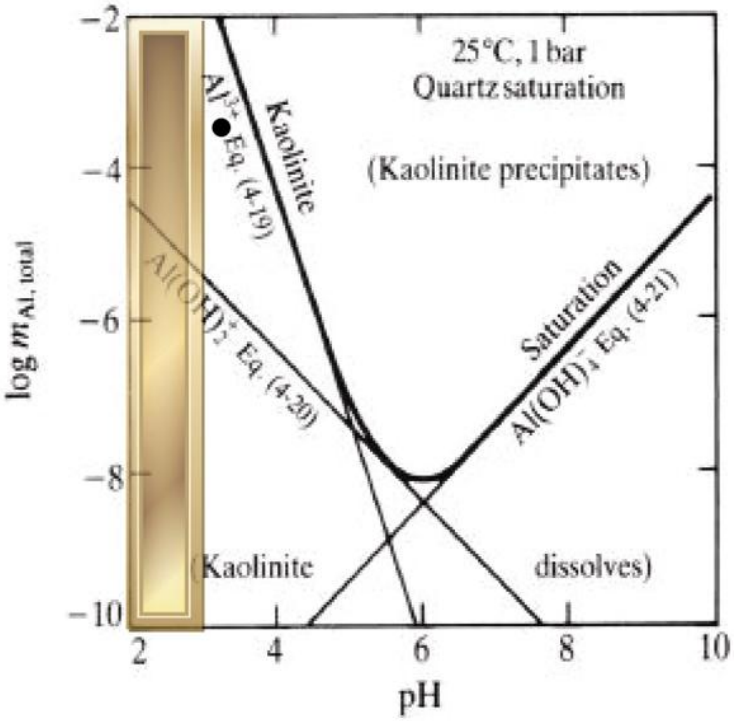

Figure 47. Phase diagram for the solubility of kaolinite. Gold bar illustrates measured paste pHs from samples in alteration scar profiles. Black circle represents calculated log $m_{\text{al total}}$ from Hansen water chemistry from Nordstrom et al., 2005. At pH's <3, kaolinite (and many other clays) dissolves (from Krauskopf and Bird, 1995).

The major implication for the dissolution of silicate minerals is the potential for a volume reduction. The resulting volume decrease could affect the overall structure of the rocks and/or rock piles. This volume change has not been quantified in this study, but could have an impact on the potential stability of the rock piles, at least on geological time scales. The active sulfide weathering system has the potential to precipitate gypsum, jarosite, and/or Fe-oxides that could potential balance the volume changes suggested by the dissolution of silicates. These minerals precipitating from the sulfide weathering system could also act as cementing agent to strengthen the rocks in the area.

Ground preparation for physical weathering of materials in the alteration scar began with hydrothermal alteration. Initial hydrothermal alteration of the rocks caused intense fracturing of the rocks at Questa. This fracturing allows for physical weathering to occur by freeze-thaw action. As the rock becomes fractured, water and air are introduced and begin the oxidation of pyrite, which creates acid and abundant sulfate in solution.

The precipitation of gypsum creates a potential volume increase and causes the rock to become even more fractured, allowing for the oxidation of more pyrite. Gypsum filled fractures has been documented in the field and are abundant in the base of the Hansen profile (Figure 26). As the pyrite becomes oxidized, Fe and O can bond to form oxides on the surfaces of mineral grains. Oxides forming on mineral grains can also inhibit the dissolution of silicate minerals as the oxides act as a barrier from water and oxygen. The formation of ferricrete material at the base and/or the tops of profiles can also inhibit the dissolution of silicate minerals.

The accumulation of gypsum at the top or bottom of the profiles gives insight into whether the system is open or closed. The upper Southwest Hansen alteration profile has an accumulation of sulfates near the top of the profile. This profile is capped by a ferricrete, which may prevent the infiltration of water at the top of the profile, inhibiting gypsum dissolution and transport of sulfate in solution. The other two profiles have an accumulation of sulfates at the bottom because waters can transport the sulfate in solution. The decrease in gypsum upwards in the profile suggests that sulfates rich solutions are percolating through the profile allowing for precipitation near the base of the profile. Precipitation of these sulfates and oxides occurs as the acid waters encounter neural pH waters from rain events and infiltrating ground waters.

Physical weathering, coupled with chemical weathering of the sulfide weathering system, are the dominant active weathering processes within the alteration scars. As the rocks are physical broken apart, water and air are introduced into the material to allow for the oxidation of pyrite, followed by the precipitation of gypsum and jarosite. With the low amounts of acid consuming minerals remaining in the alterations scars, these weathering processes will continue to work together until the remaining pyrite has been oxidized from the alteration scar material.

A weathering index was created by the Questa Weathering and Rock Pile Stability team to determine the intensity of weathering that has occurred, or will occur, in the rocks within the rock piles and the alteration scars. This weathering index has been developed largely impart due to this study, with the entire weathering index

based solely on the sulfide weathering system because there are no secondary mineral products to document the extent of weathering in the silicate weathering system.

The system uses the factors of sulfide and calcite abundance, along with sulfide to sulfate ratios to assign a weathering number between 1 and 7 (1 - unweathered & 7 - most weathered) (V. McLemore, written communication). The alteration scars have been assigned weathering index numbers, based on the criteria, between five and seven. These values indicate alteration scar rocks are near the most weathered end of the spectrum, which correlates well with the documented time the alteration scars have been weathering in place.

6. CONCLUSIONS

6.1 Conclusions

Determination of quantitative mineralogy of rocks with these extreme hydrothermal alteration assemblages can be difficult. The application of quantitative X-Ray diffraction, petrography, and the ModAn mineralogical modeling program allowed for the accurate determination of mineralogical changes. The three combined methods provided the most accurate percentage of mineralogical abundances to aid in the determination of the true mineralogical changes within the alteration scar profiles.

Isocon calculations have proven useful in this study to determine geochemical trends seen within the alteration scars profiles. The method was useful in determining weathering affects, hydrothermal alterations and lithologic variation signatures in the profiles.

Physical and chemical weathering has occurred in the natural alteration scars studied for at least the last 300,000 years (Lueth et al, 2006). For this time period, there is documented evidence for both physical and chemical weathering. The dominant chemical weathering system is the oxidation of pyrite, dissolution of calcite, leading to the precipitation of both sulfates and Fe-oxides.

The isotopic compositions of sulfates and sulfides indicate that all sulfate minerals formed in the alteration scars by weathering. The lack of calcite remaining in the alteration scars indicates that there is not enough acid consuming mineral capacity to buffer the oxidizing pyrite. The oxidation of pyrite will continue in the alteration scars until the remaining pyrite has been depleted.

In terms of silicate mineral changes, the sampled “weathering profiles” could better represent “alteration profiles.” Intense QSP alteration zones are associated with

little to no feldspars, indicating that hydrothermal solutions altered feldspars into clay minerals. These clay types, along with stable isotope analysis, show no evidence of new clays being formed in the alterations scars. Weathering of silicate minerals in this environment (acidic) was anticipated to precipitate clay minerals, however, no evidence was documented for the formation of secondary clay minerals. However, congruent dissolution of silicates is indicated in the scars based on low soil pH and drainage water geochemistry. No significant evidence for chemical weathering of silicate minerals is present in these alterations scars other than mineral dissolution under low pH conditions

Physical weathering appears active in the alteration scars. Possible mechanisms for physical weathering include: 1) initial grain size reduction by hydrothermal alteration, 2) freeze-thaw action, and 3) precipitation of gypsum. These processes can enhance the physical break and liberation of minerals from the rock; however, hydrothermal alteration is the only process that will not contribute in the future. As these processes occur, the alteration scars become finer grained and allow for the introduction of fluids to further chemically weather the sulfide weathering system.

The conclusions from this study provide important insights in to the future mineralogical changes expected in the rock pile over geological time scales. In particular, the dissolution of silicate minerals will have to be considered for particular zones or over the entire volume of the rock pile. This decrease in volume potential could be offset due to the volume increase from the precipitation of sulfates and Fe-oxides. These minerals have the potential to act as cementing agents (noted in the

scars as ferricrete or gypsum veins), which could potentially make the rock piles stronger as weathering progresses. The volume change has not been quantified in this study, but could have an impact on the geotechnical evaluation of the stability of the rock piles over the next 1,000 years.

6.2 Recommendations

This study has provided an excellent basis for predicting the possible mineralogical changes that are expected to occur within the Chevron Mining Incorporated (CMI) rock piles at the Questa mine. There is potential for future work of these alteration scars to document other mineralogical and geochemical changes not noted within this study. Potential future work includes quantifying the potential volume decrease due to weathering, documenting the dissolution of silicate minerals in these samples and QXRD of all alteration scar samples.

Density measurements within the alteration scars could provide a data set that would help to quantify the geochemical changes associated with the volume decrease using the isocon method. Using SEM (Scanning Electron Microprobe) images, documentation of silicate dissolution may be possible by looking for etch pits, dissolution along grain boundaries and dissolution along cleavage planes. These images would help verify the mineralogical and groundwater data evidence for the dissolution of silicate minerals. Completing QXRD on all the profile samples would better constrain mineralogy from the ModAn modeling for all profiles within this study.

REFERENCES

Blum, A.E. and Stillings, L.L., (1995); Feldspar dissolution rates: in Reviews in Mineralogy, v. 31, Chemical Weathering Rates of Silicate Minerals, eds. White and Brantley, p. 291-351

Borthwick, J., and Harmon, R.S., (1982); A note regarding ClF_3 as an alternative to BrF_5 for oxygen isotope analysis: Geochimica et Cosmochimica Acta, v. 46, p. 1665-1668

Caine, J.S., (2003); Questa baseline and pre-mining groundwater quality investigation 6: Preliminary brittle structural geologic data, Questa Mining District, southern Sangre de Cristo Mountains, New Mexico: USGS open-file report 03-280, 7 p.

Campbell, A.R. and Lueth, V.W., (2008); Isotopic and textural discrimination between hypogene, ancient supergene, and modern sulfates at the Questa Mine, New Mexico: Applied Geochemistry, v. 23, p. 308-319.

Chapin, C.E., (1979); Evolution of the Rio Grande Rift: A summary, *in* Riecker, R.E., ed, Rio Grande rift Tectonics and magmatism, Washington D.C., American Geophysical Union, p. 1-5

Clark, K.F., and Read, C.B., (1972); Geology and ore deposits of Eagle Nest area: New Mexico Bureau of Mines and Mineral Resources, Bulletin 94, 152 p.

Craig, H., (1961); Isotopic Variations in Meteoric Waters; Science, v. 133, p. 1702-1703

Donahue, K. M., Dunbar, N. W., and McLemore, V. T., (2007); Origins of clay minerals in the Molycorp Mine Goathill North Rock pile, Questa NM, Society of Mining, Metallurgy and Exploration Annual Convention, Denver, Feb 2007.

Donahue, K. M., Dunbar, N.W, Heizler, L.L and McLemore, V.T., (submitted, 2008); Origins of clay minerals in the Goathill North Rock Pile, Questa Mine, Taos County, New Mexico: Applied Clay Science, 13 p.

Field, Cyrus W., (1966); Sulfur isotopic method for discriminating between sulfates of hypogene and supergene origin: Economic Geology and the Bulletin of the Society of Economic Geologists 61, no. 8, p. 1428-1435

Gavelin, S., Parwel, A., Ryhage, R., (1960); Sulfur isotope fractionation in sulfide mineralization: Economic Geology and the Bulletin of the Society of Economic Geologists 55, no. 3, p. 510-530

Garrels, R.M. and Thompson, M.E., (1960); Oxidation of pyrite by iron sulfate solutions: American Journal of Science, 258-A, p. 57-67

Gilg, H.A., Girard, J.P., and Sheppard, S.M.F., (2004); Handbook of Stable Isotope Techniques, Volume 1; P.A. de Groot (editor), Elsevier B.V., New York, New York, 1248 p.

Grant, J.A., (1986); The isocon diagram---A simple solution to Gresens' equation for metasomatic alteration: Economic Geology, v. 81, n. 8, p. 1976-1982

Hall, J. S., (2004); "New Mexico Bureau of Mines and Mineral Resource's Clay Laboratory Manual". Unpublished New Mexico Bureau of Geology and Mineral Resources report.

Hashimoto, I. and Jackson, M.L., (1960); Rapid Dissolution of Allophane and Kaolinite-Halloysite after Dehydration; 7th National Conference on Clays and Clay Minerals, p. 102-113

Hoefs, J.H., (2004); Stable Isotope Geochemistry; Fifth and Updated Version, p.36, Springer, New York, New York, 206 p.

Ishihara, S., (1967); Molybdenum mineralization at the Questa mine, New Mexico, *U.S.A.*: Geological Survey of Japan, Report 218, 68 p.

Krauskopf, K. B. and Bird, D. K., (1995); Introduction to Geochemistry (3rd ed.), McGraw-Hill, Inc., New York, 647 p.

Lawson, R.T., Josick Comarmond, M.-C., Geetha Rajaratnam, and Brown, P.L., (2005); The kinetics of the dissolution of chlorite as a function of pH and at 25° C: Geochimica et Cosmochimica Acta, v. 69, p. 1687-1699.

Lipman, P.W., (1983); The Miocene Questa caldera, northern New Mexico; relation to batholith emplacement and association of molybdenum mineralization: Wheat Ridge, Colo., Proceedings of the Denver Region Exploration Geologists Society Symposium: The genesis of Rocky Mountain Ore deposits; changes with time and tectonics, p. 133-147

Lipman, P.W. and Reed, J.C., Jr., (1989); Geologic map of the Latir volcanic field and adjacent areas, Northern New Mexico: U.S. Geological Survey, Miscellaneous Investigations Map I-1907, 1:48,000

Livo, E.K and Clark, R.N, (2002); Mapped minerals at Questa, New Mexico, using Airborne Visible-Infrared Imaging Spectrometer (AVIRIS) data – Preliminary report: First quarterly report of the U.S. Geological Survey investigation of the Red River valley basin, New Mexico, November 13, 2001, Open-File report 02-0026, 13 p.

Loucks, T.A., Phillips, J.S., and Newell, R.A., (1977); Exploration potential of the Questa East area: unpublished report for the Kennecott Copper Corporation

Lowell J.D. and Gilbert, J.M., (1970); Lateral and vertical alteration mineral zoning in porphyry ore deposits; Economic Geology, v. 65, p. 373-408

Ludington, S., Plumlee, G.S., Caine, J.S., Bove, D., Halloway, J., amd Livo, E.K., (2004); Questa baseline and pre-mining groundwater quality investigation. 10. Geologic influences on ground and surface waters in the lower Red River watershed, New Mexico: U.S. Geological Survey Scientific Investigations Report 2004-5245, 45 p.

Lueth, V.W., Campbell, A.R., and Peters, L.M., (2006); Final report (Phase I) on the geochronological ($^{40}Ar/^{39}Ar$) dating of jarosite and alunite samples from the Red River area alteration scars and the Questa Mine: The timing of alteration scar formation and weathering: Questa Rock Pile Weathering and Stability Project, Unpublished report, 18 p.

Martineau, M.P., Heinemeyer, G.R., Craig, S.D. and McAndrews, K.P., (1977); Geological Report, Questa Project, 1975-1977, Questa Molybdenum Company, unpublished report, 161 p.

McKibben, M.A. and Barnes, H.L., (1986); Oxidation of pyrite in low temperature acidic solutions; rate laws and surface textures: Geochimica et Cosmochimica Acta 50, no. 7, p. 1509-1520

McLemore, V.T., Lueth, V.W. and Walker, B.M., (2004); Alteration scars in the Red River valley, Taos County, New Mexico: New Mexico Geological Society Guidebook, v. 55, p. 19

Mehra, O.P. and Jackson, M.L., (1960); Iron oxide Removal from Soils and Clays by a Dithionite-Citrate System Buffered with Sodium Bicarbonate; 7th National Conference on Clays and Clay Minerals, p. 317-337

Meyer, J.W., and Foland, K.A., (1991); Magmatic-tectonic interaction during early Rio Grande rift extension at Questa, New Mexico: Geological Society of America Bulletin, v. 103, p. 993-100

Meyer, J.W., (1990); Volcanic, plutonic, tectonic and hydrothermal history of the southern Questa caldera, New Mexico: University of California at Santa Barbara, unpub. Ph.D. dissertation, 287p.

Meyer, J. and Leonardson, R., (1990); Tectonic, Hydrothermal, and Geomorphic controls on Alteration Scar Formation near Questa, New Mexico: New Mexico Geological Society Guide Book, 41st Field Conference, Southern Sangre de Cristo Mountains, New Mexico, p. 417-422

Morgan, P., Seager, W.R., and Golombek, M.P., (1986); Cenezoic thermal, mechanical and tectonic evolution of the Rio Grande rift: Journal of Geophysical Research, v. 91, p. 6263-6276

Nordstrom, D.K., (1982); Aqueous pyrite oxidation and the consequent formation of secondary iron minerals: Acid sulfate weathering; proceedings of a symposium SSSA Special Publication 10, p. 37-56

Nordstrom, D.K., McClesky, R.B., Hunt, A.G., and Naus, C.A., (2005); Questa baseline and pre-mining groundwater quality investigation, 14. Interpretation of ground-water geochemistry in catchments other that the straight creek catchment, Red River Valley, Taos County, New Mexico, 2002-2003, USGS Scientific Investiagtions Report 2005-5050, 84 p.

Paktunc, D.A., (2001); MODAN—a computer program for estimating mineral quantities based on bulk composition: windows version: Computers & Geosciences, Vol. 27, Issue 7, p. 883-88

Robertson Geoconsultants Inc., (2000); Interim Background Characterization Study, Questa Mine, New Mexico: Questa Mine Closeout Plan Program Task A7-Subtask 1.1, 1.2 and Phase 2, Report No. 052008/6, 33 p.

Ross, P., Jebrak, M. and Walker, B.M., (2002); Discharge of hydrothermal fluids from a magma chamber and concomitant formation of a stratified breccia zone at the Questa porphyry molybdenum deposit, New Mexico: Economic Geology, v. 97, p. 1679-1700

Rye, R.O., Bethke, P.M., Wasserman, M.D., (1992); The stable isotope geochemistry of acid sulfate alteration: Economic Geology and the Bulletin of the Society of Economic Geologists 87, no. 2, p. 225-262

Schilling, J.H., (1956); Geology of the Questa molybdenum (Moly) mine area, Taos County, New Mexico: New Mexico Bureau of Mines and Mineral Resources, Bulletin 51, 87 p.

Seal, R. R., II, Alpers, C.N., Rye, R.O., (2000); Stable isotope systematics of sulfate minerals: Sulfate minerals; crystallography, geochemistry, and environmental significance, Reviews in Mineralogy and Geochemistry 40, p. 541-602

Shaw, S., Wels, C., Roberston, A., Fortin, S. and Walker, B., (2003); Background characterization study of naturally occurring acid rock drainage in the Sangre de Cristo mountains, Taos County, New Mexico: in 6th ICARD: Cairns, Queensland, Australia, July 12-18, p. 605-616

Sheppard, S.M.F. and Gilg, H.A., (1996); Stable Isotope Geochemistry of Clay Minerals; Clay Minerals, v. 31, p. 1-24

Singer, P.C. and Stumm, W., (1968); Kinetics of the oxidation of ferrous iron: in Proceedings Second Symposium on Coal Mine Drainage Research; Bituminous Coal Research Inc., Monroeville, Pennsylvania (12-34)

Singer, P.C. and Stumm, W., (1970); Acid mine drainage: the rate determining step: Science, vol. 167, p. 1121-1123

Sobek, A.A., Schuller, W.A. Freeman, J.R. and Smith, R.M., (1978); Field and laboratory methods applicable to overburden and minesoils, EPA 600/2-78-054, 203 p.

Standard Operating Procedure No. 11 (SOP 11); Paste pH and paste conductivity: Questa Rock pile weathering and stability project, unpublished report, 4 p.

Standard Operating Procedure No. 62 (SOP 62); Acid Base Accounting: Questa Rock pile weathering and stability project, unpublished report, 11 p.

Stefanini, B. and Williams-Jones, A.E., (1996); Hydrothermal evolution in the Calabona porphyry cooper system (Sardinia, Italy): The path to an uneconomic deposit; Economic Geology, v. 91, p. 774-791

Summerfield, M.A., (1991); Global Geomorphology: An introduction to the study of landforms; First Edition, Longman Group Ltd, England, p. 137-146

Taylor, H.P., Jr. and Epstein, S., (1982); Relationship between $^{18}O/^{16}O$ ratios in coexisting minerals of igneous and metamorphic rocks, Part 1: Principles and experimental results: Geological Society of America Bulletin, v. 73, p. 461-480

Tweto, O., (1979); The Rio Grande Rift system in Colorado: A summary, *in* Riecker, R.E., ed, Rio Grande rift Tectonics and magmatism, Washington D.C., American Geophysical Union, p. 35-36

Wasserman, M.D., Rye, R.O., Bethke, P.M., and Arribas, A., (1992); Methods for separation and total stable isotope analysis of alunite: US. Geological Survey, Open-file Report 92-9, 20 p.

White, A.F and Brantley, S.L., (1995); Chemical weathering rates of silicate minerals: an overview: in Reviews in Mineralogy, v. 31, Chemical Weathering Rates of Silicate Minerals, eds. White and Brantley, p. 1-22

White, A.F., (1995); Chemical weathering rates of silicate minerals in soil: in Reviews in Mineralogy, v. 31, Chemical Weathering Rates of Silicate Minerals, eds. White and Brantley, p. 407-46

Appendix A. Individual and Profile Particle Size Results

HAS-GJG-0006 Particle Size Distribution

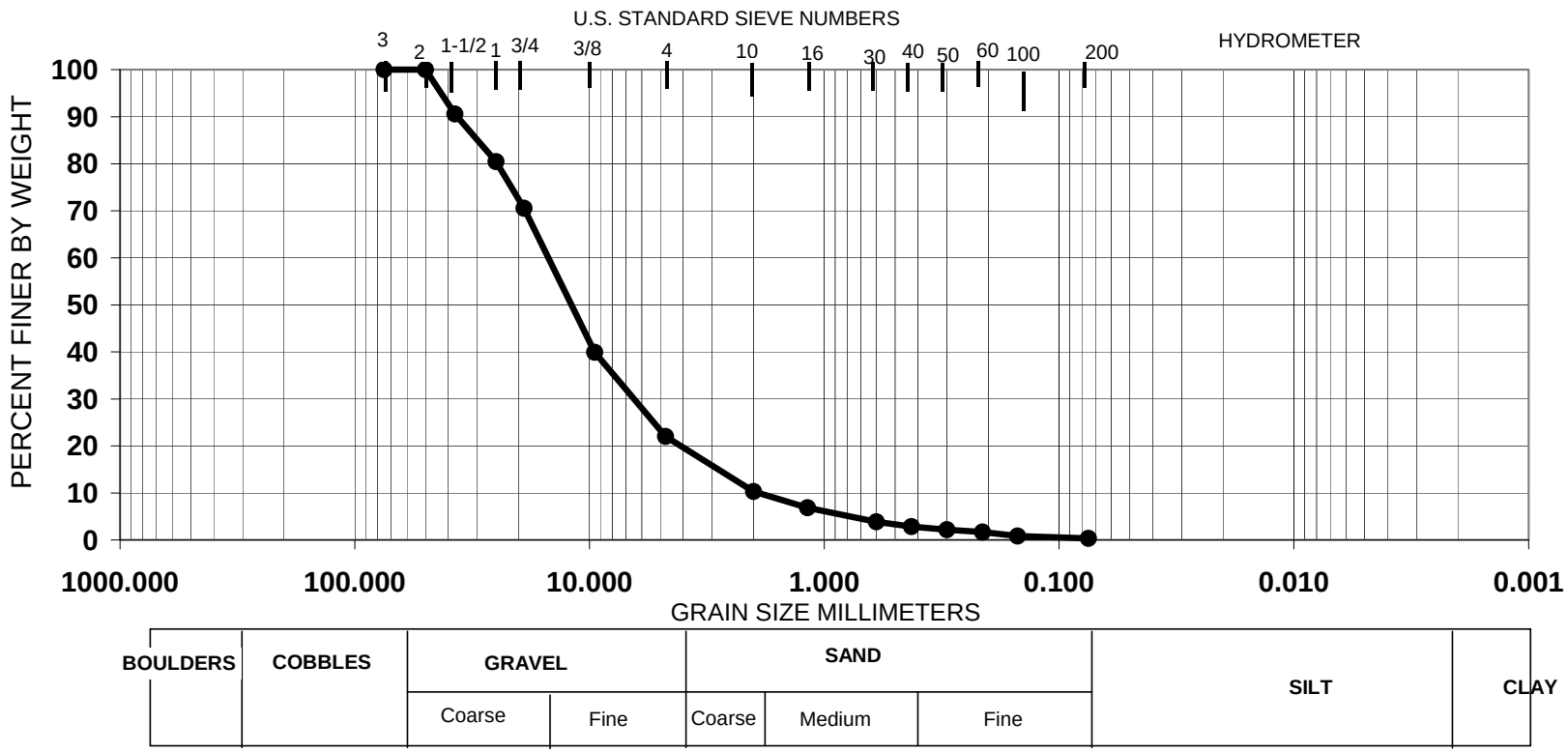

HAS-GJG-0007 Particle Size Distribution

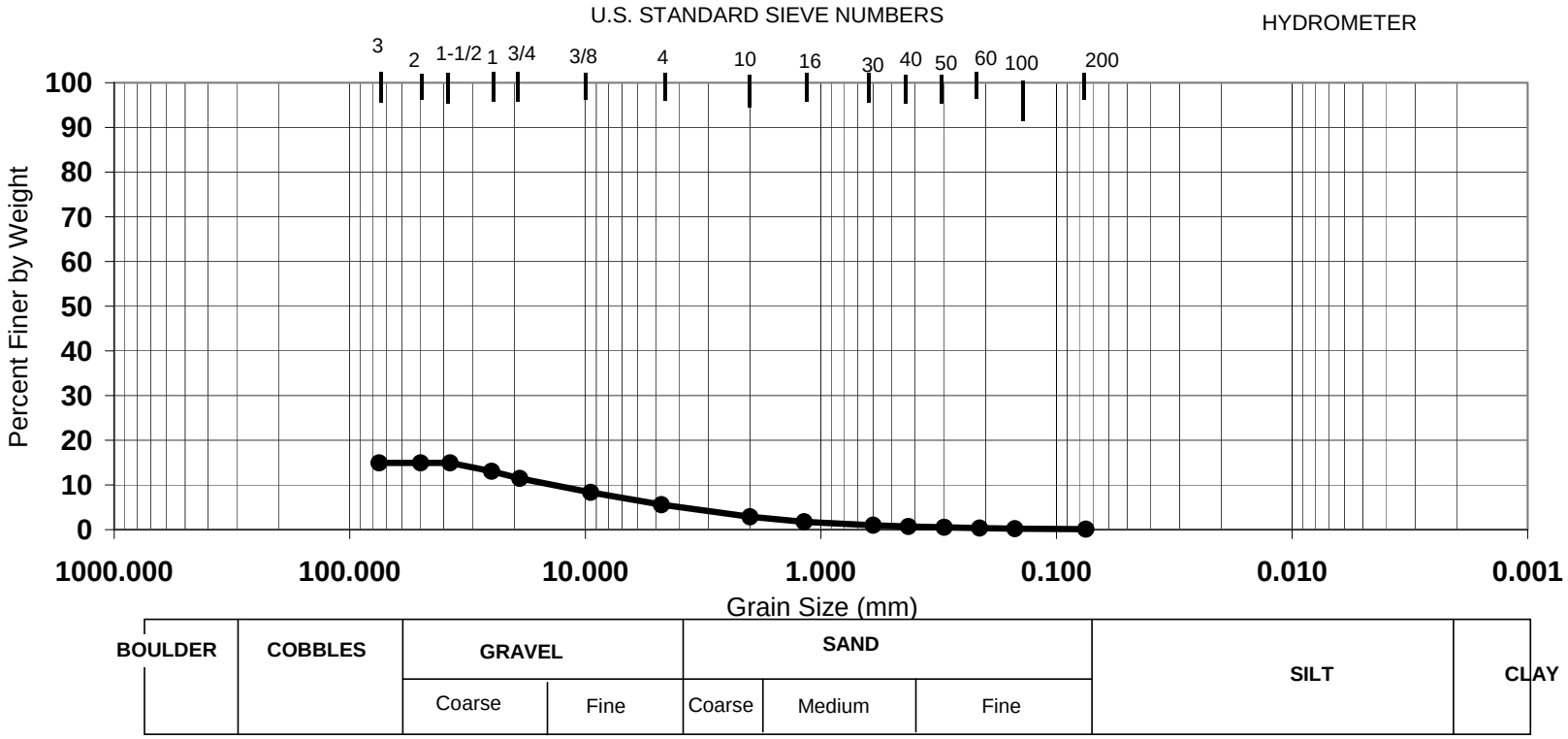

HAS-GJG-0008 - Particle Size Distribution

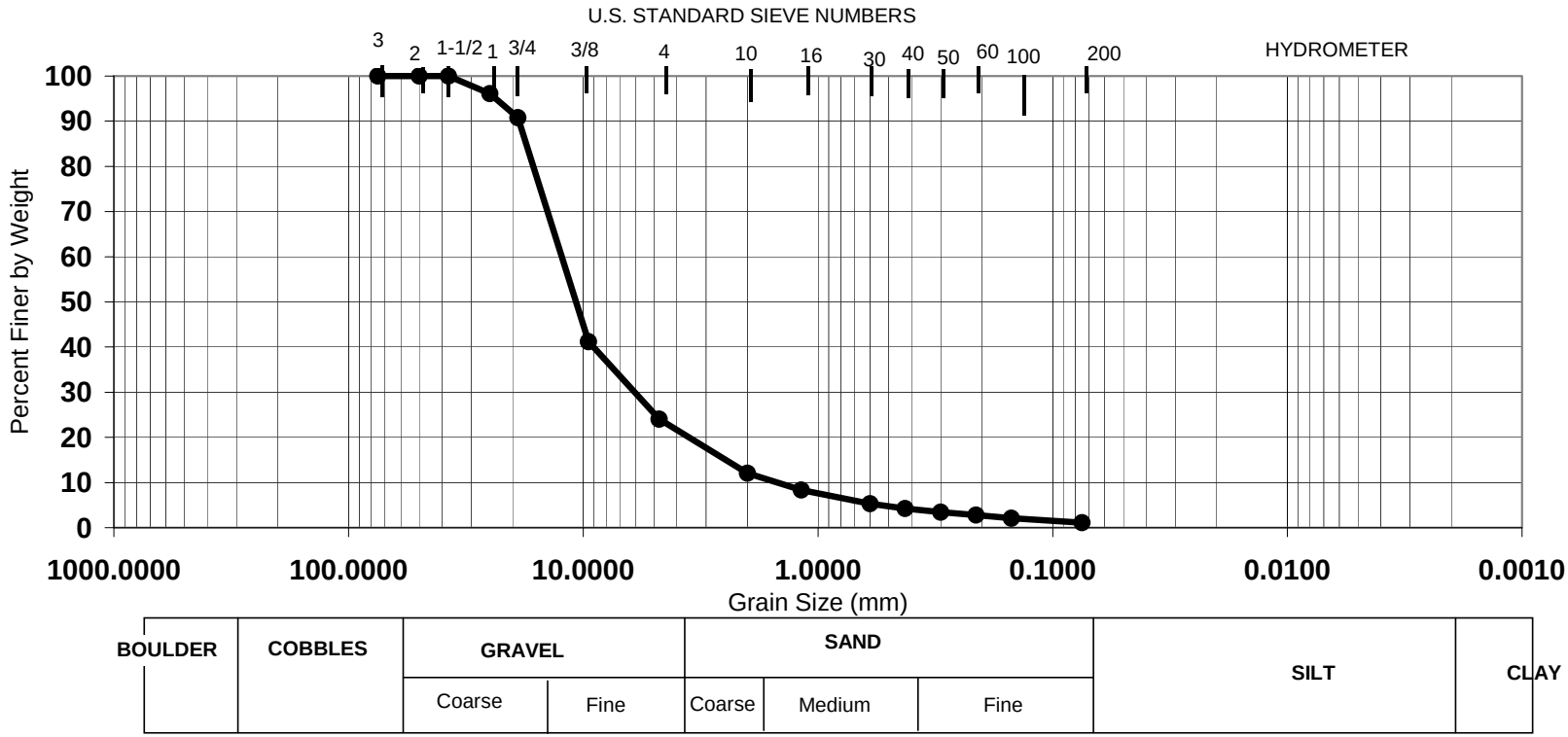

HAS-GJG-0009 - Particle Size Distribution

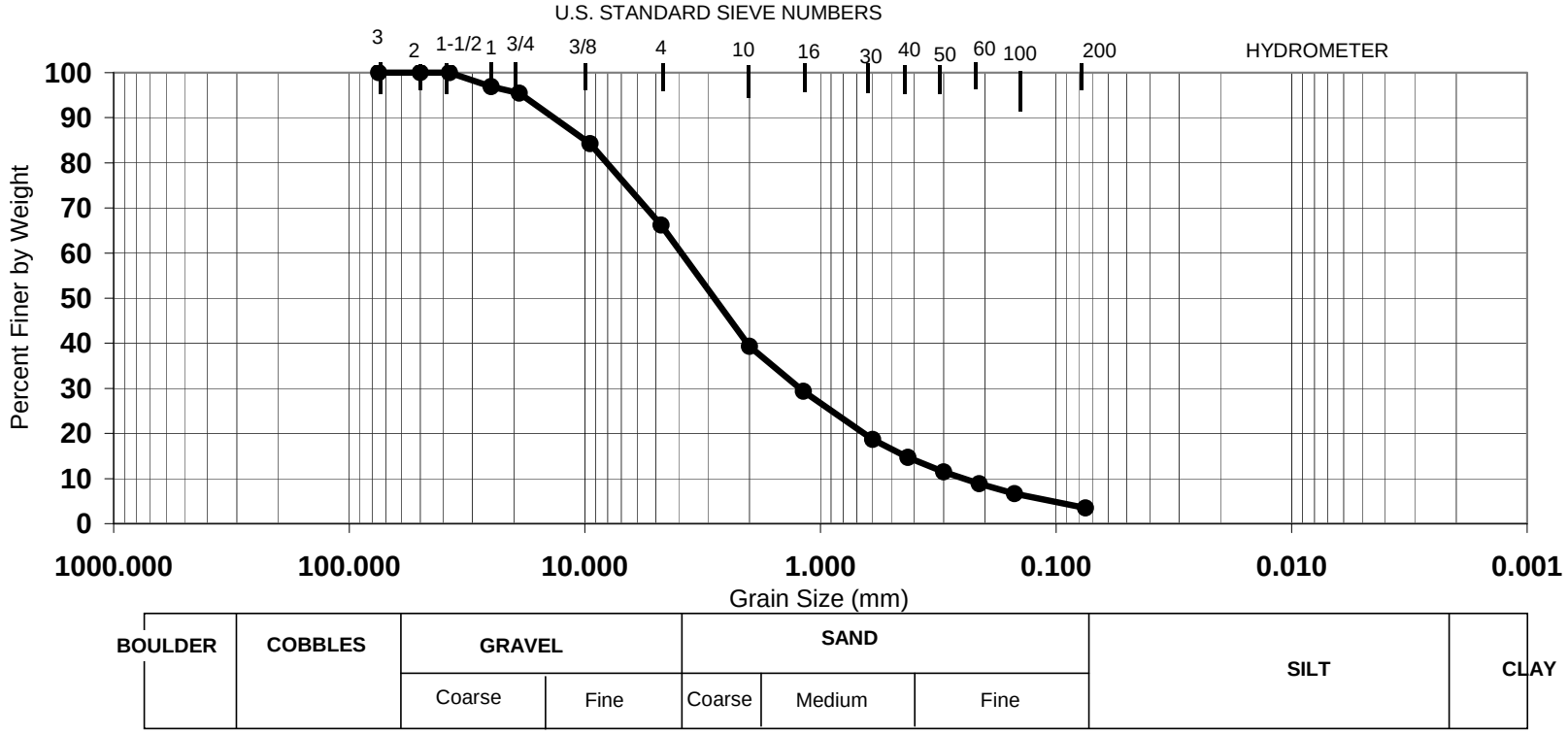

HAS-GJG-0010 - Particle Size Distribution

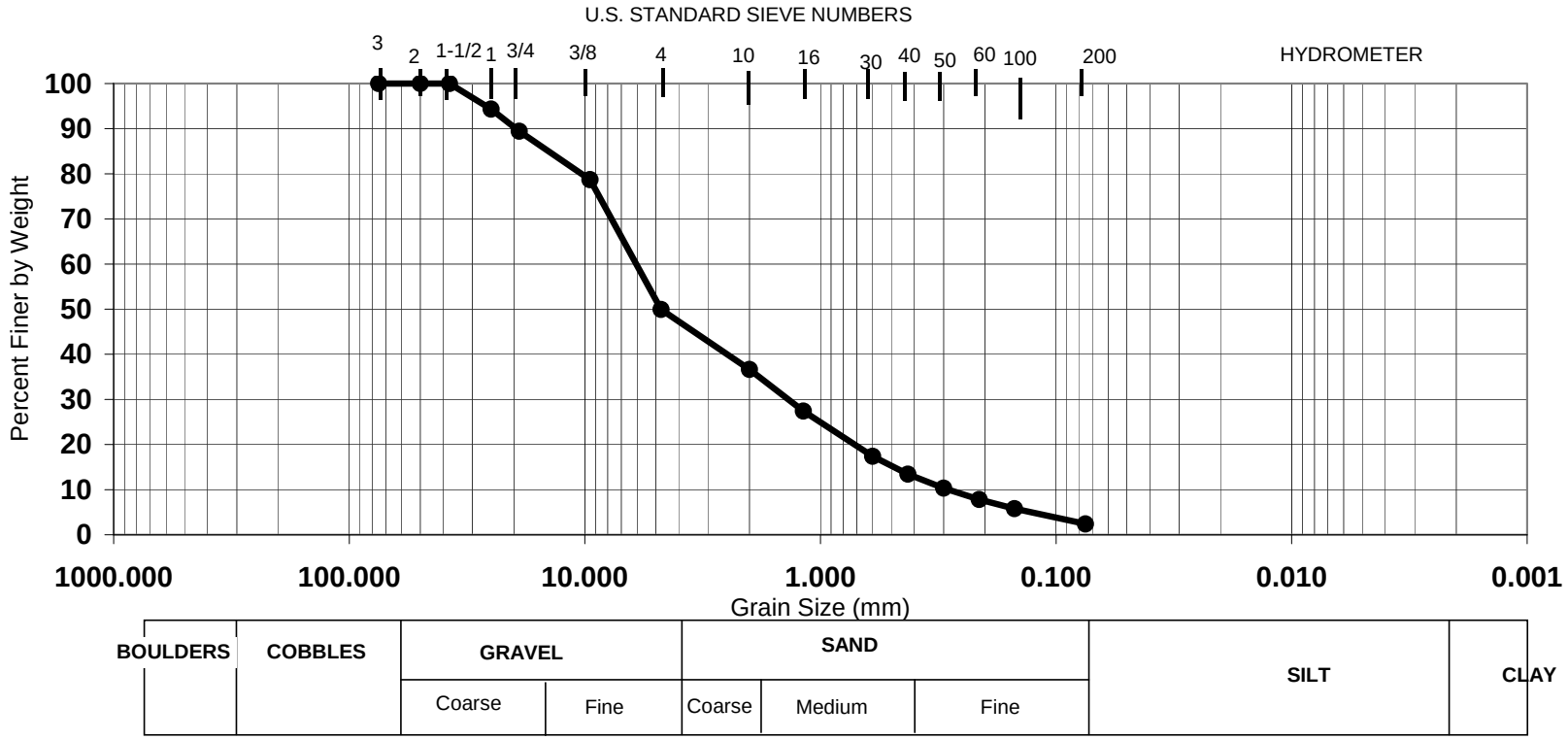

Hansen Profile (HAS) - Particle Size Distribution

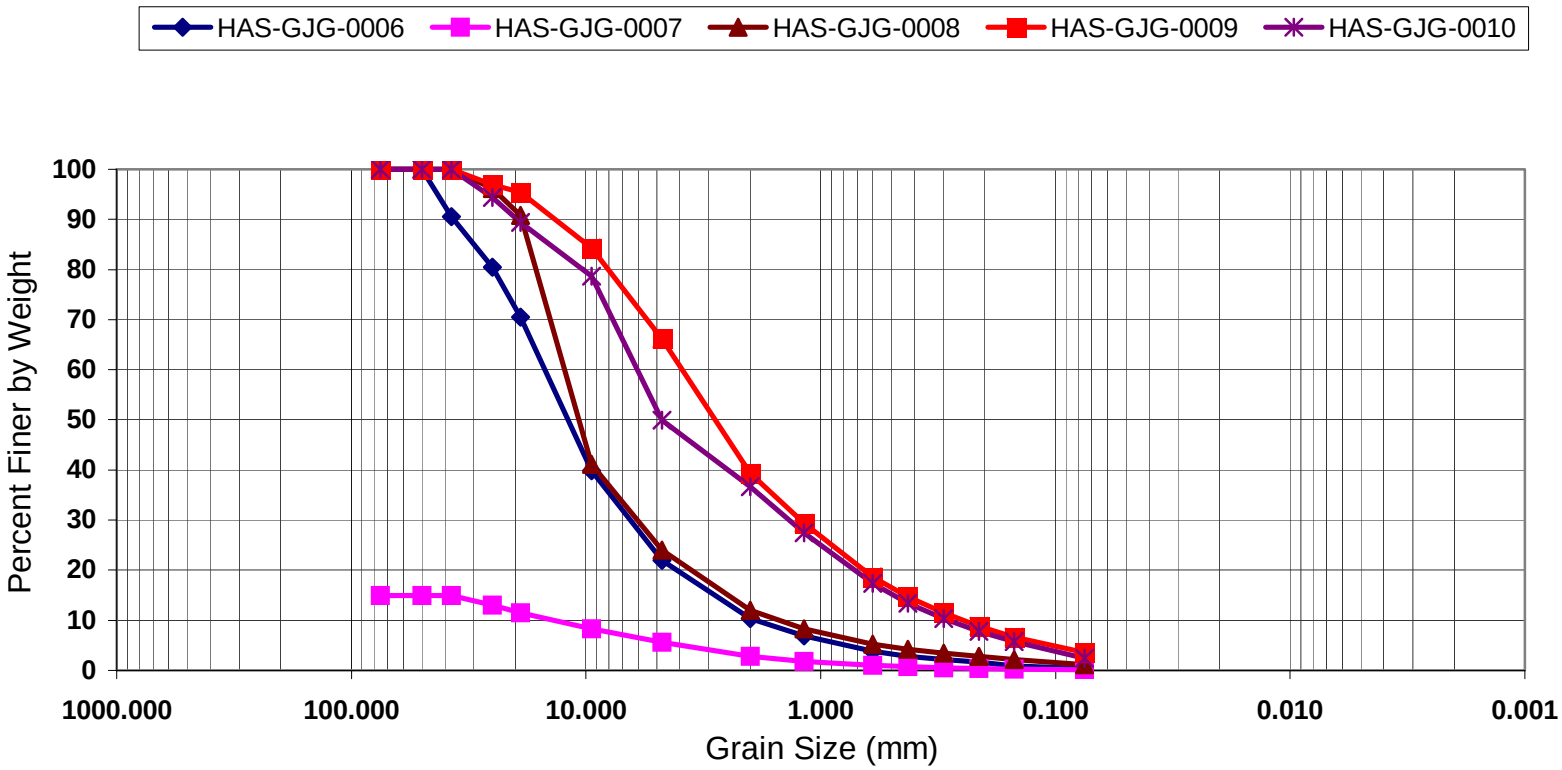

SWH-GJG-0008 - Particle Size Distribution

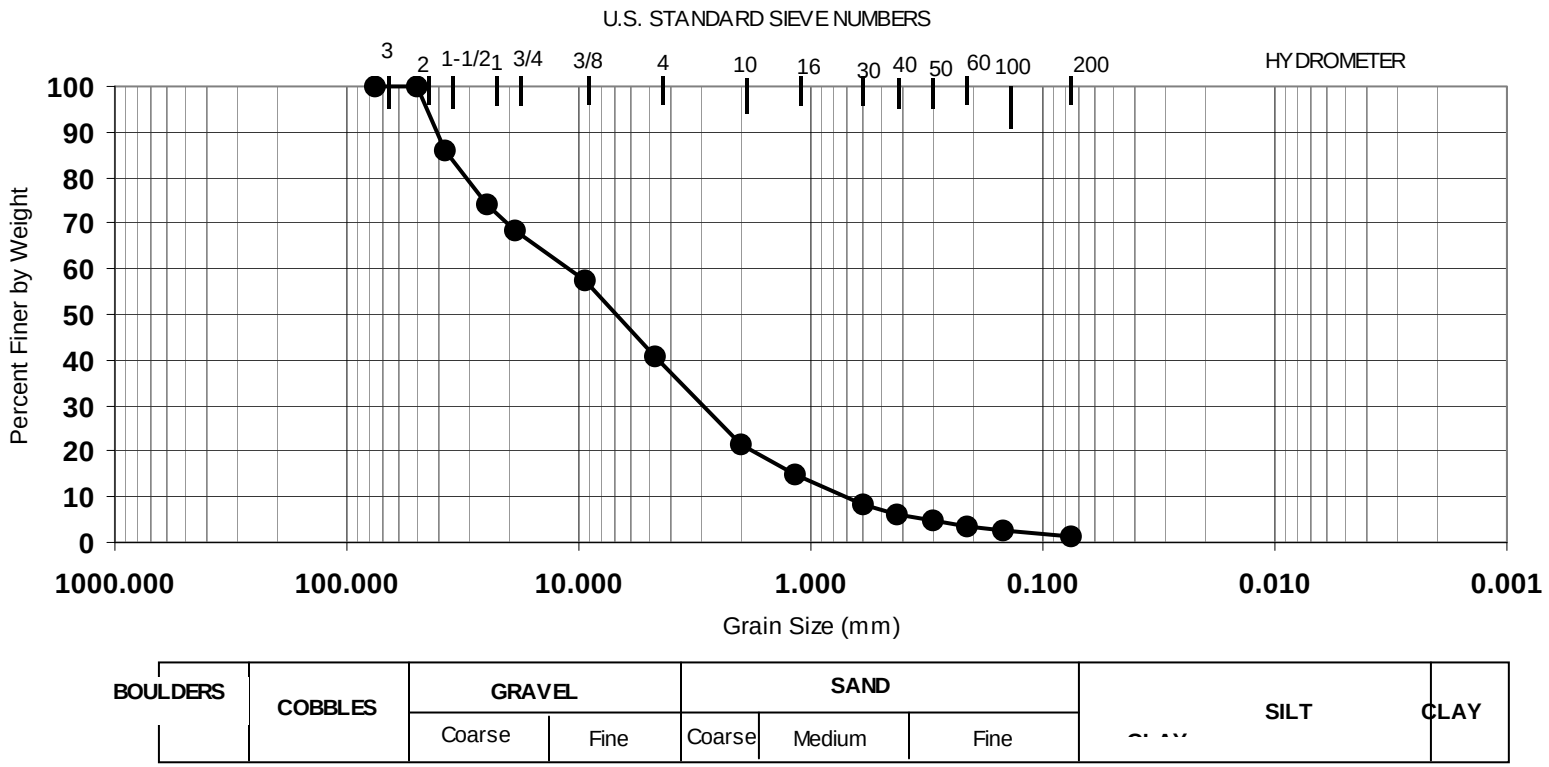

SWH-GJG-0009 - Particle Size Distribution

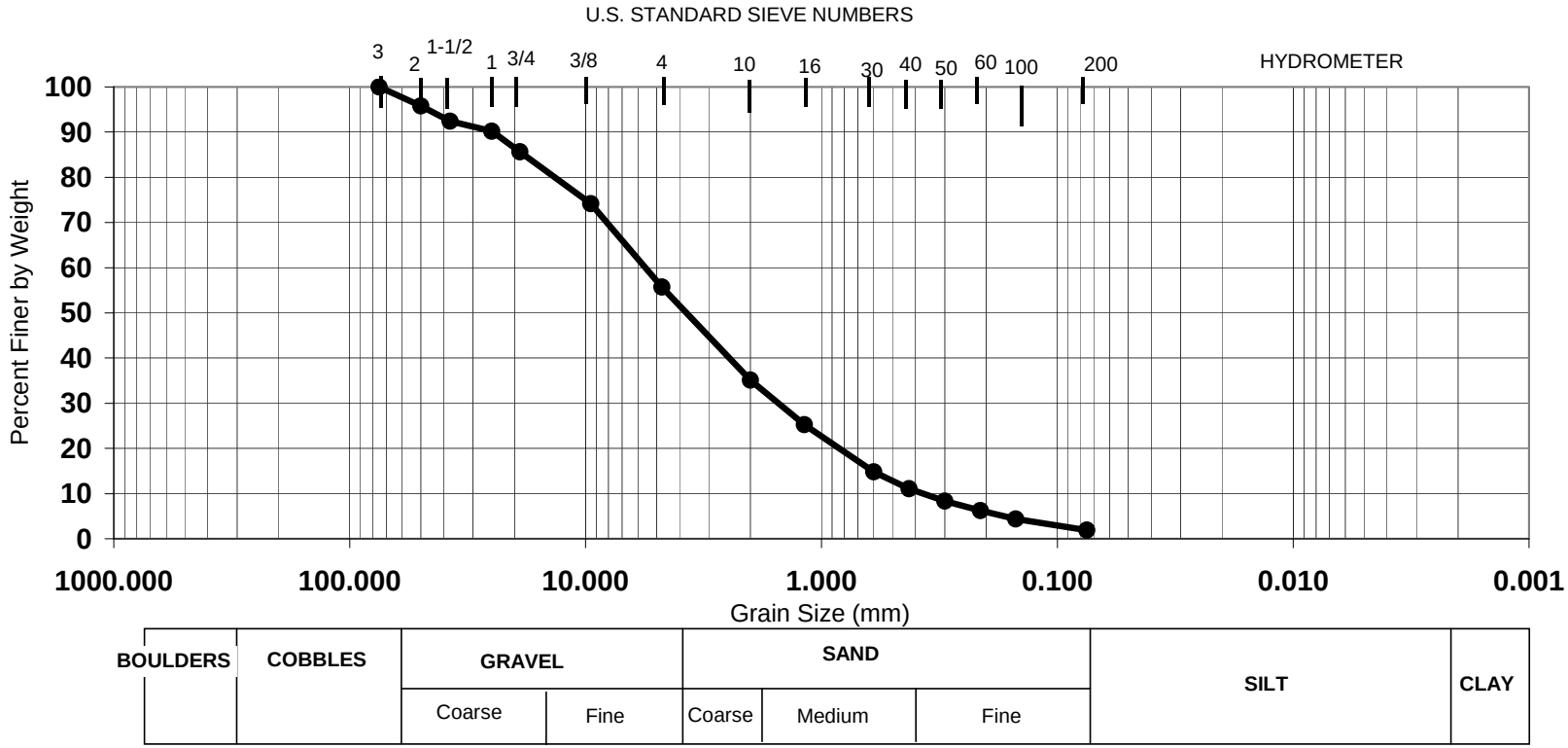

SWH-GJG-0010 - Particle Size Distribution

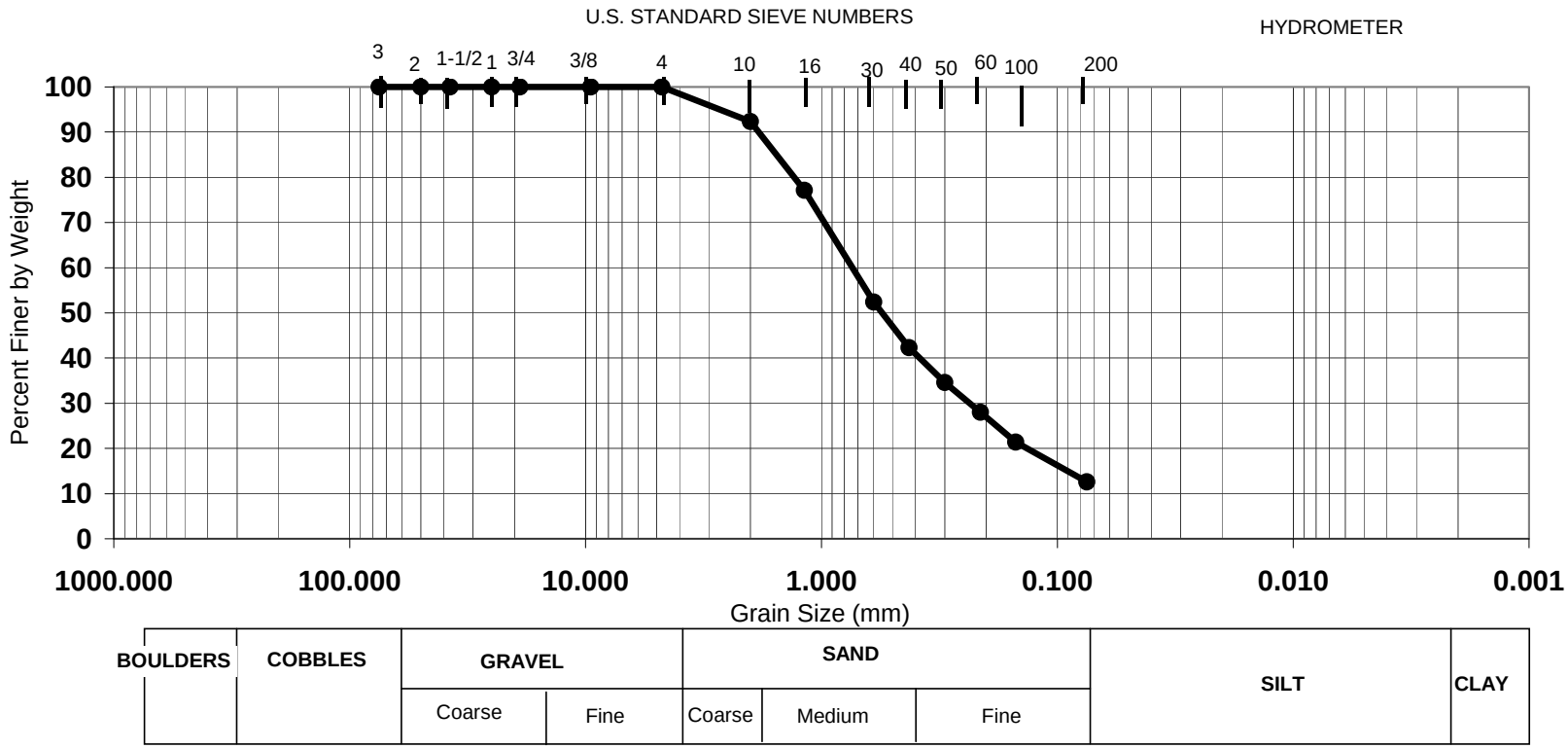

SWH-GJG-0011 - Particle Size Distribution

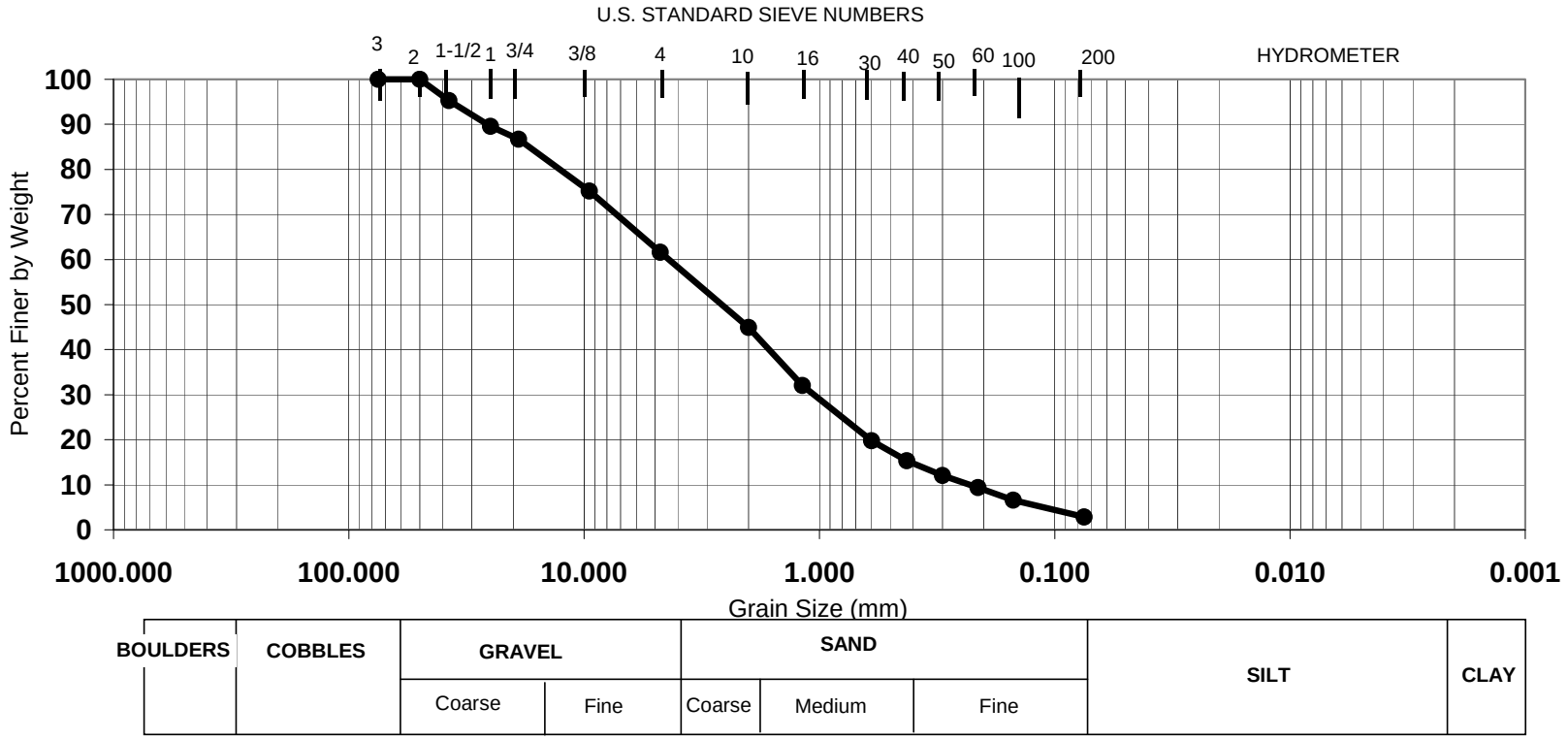

SWH-GJG-0012 - Particle Size Distribution

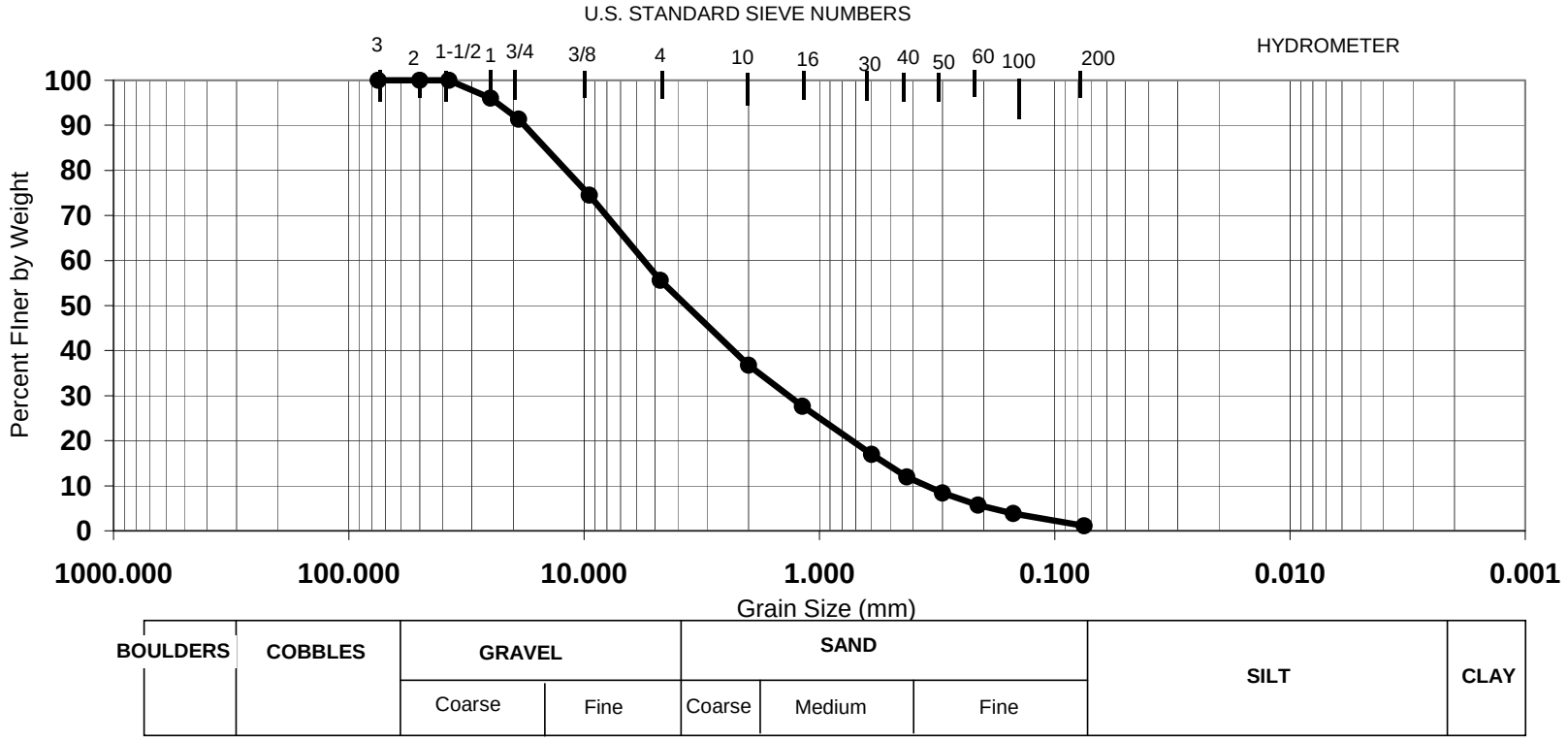

SWH-GJG-0013 - Particle Size Distribution

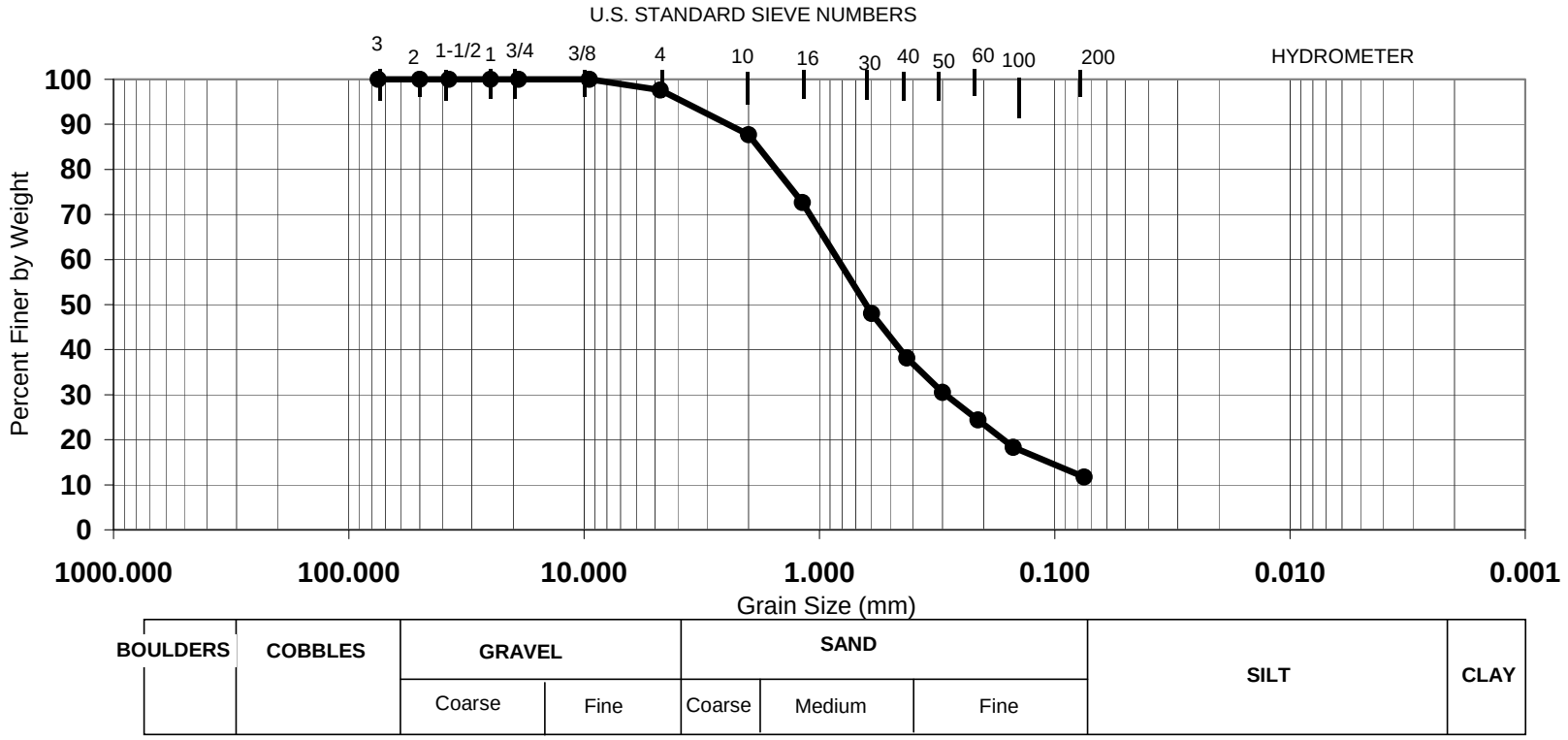

SWH-GJG-0014 - Particle Size Distribution

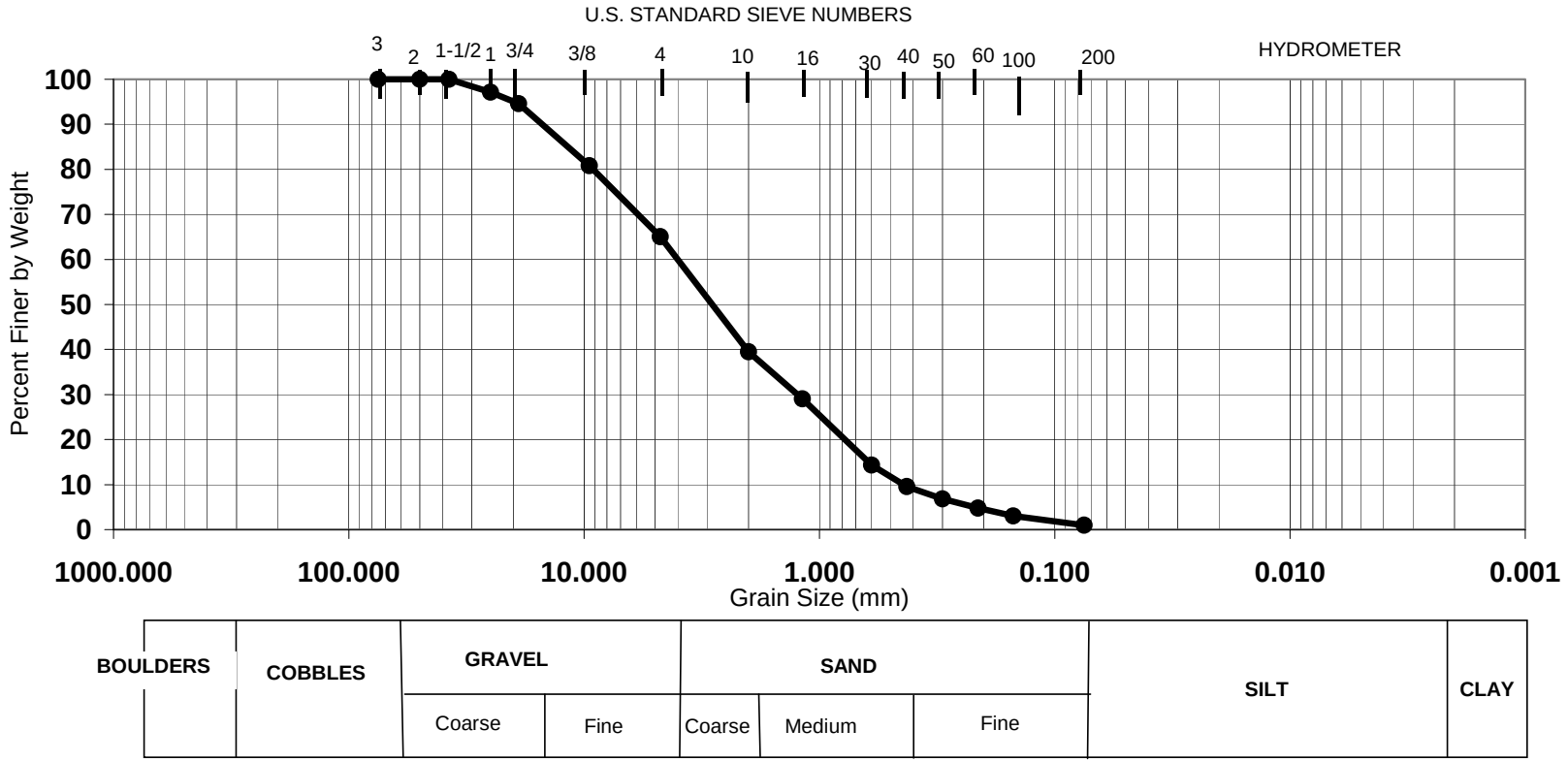

SWH-GJG-0015 - Particle Size Distribution

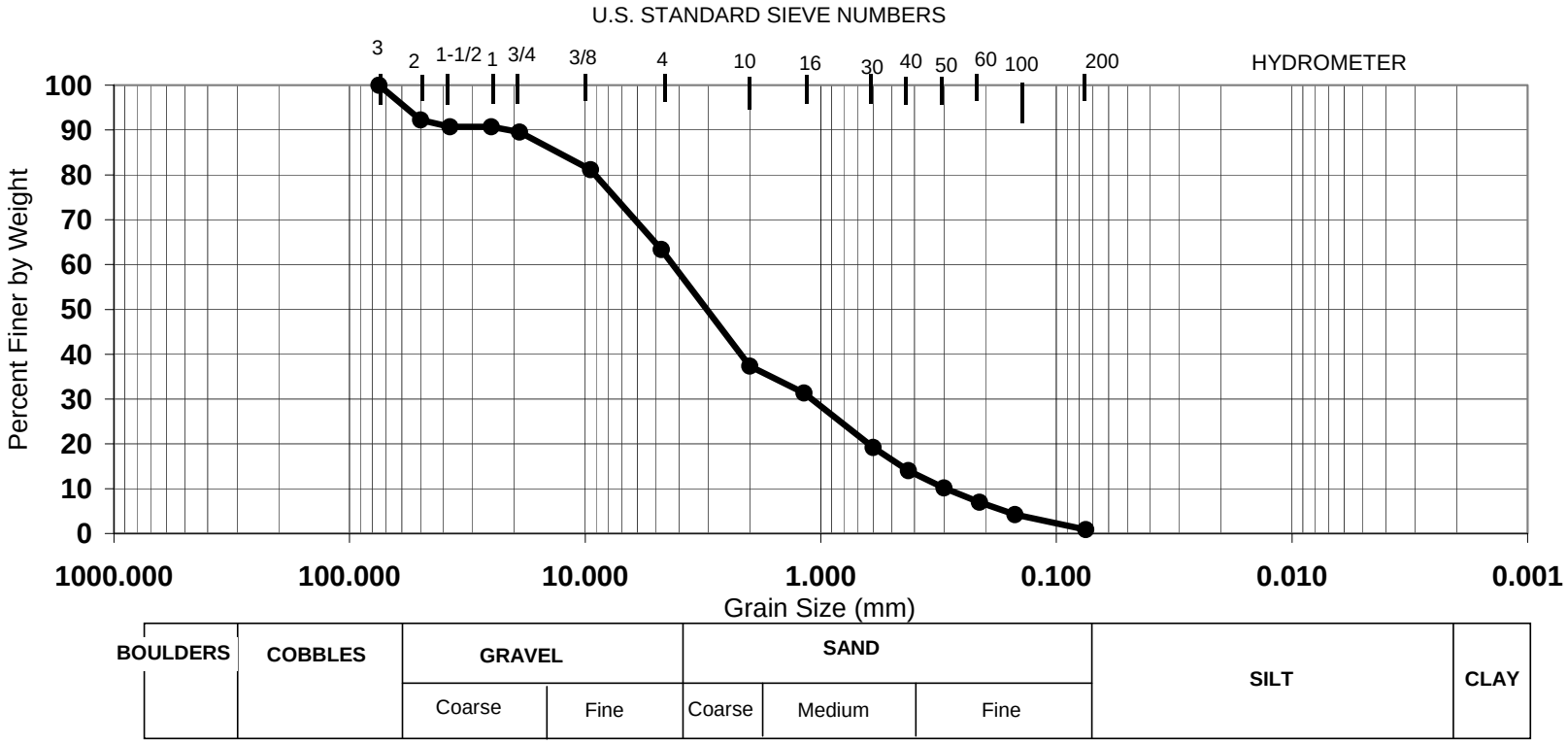

Lower Southwest Hansen Profile (SWH) - Particle Size Distribution

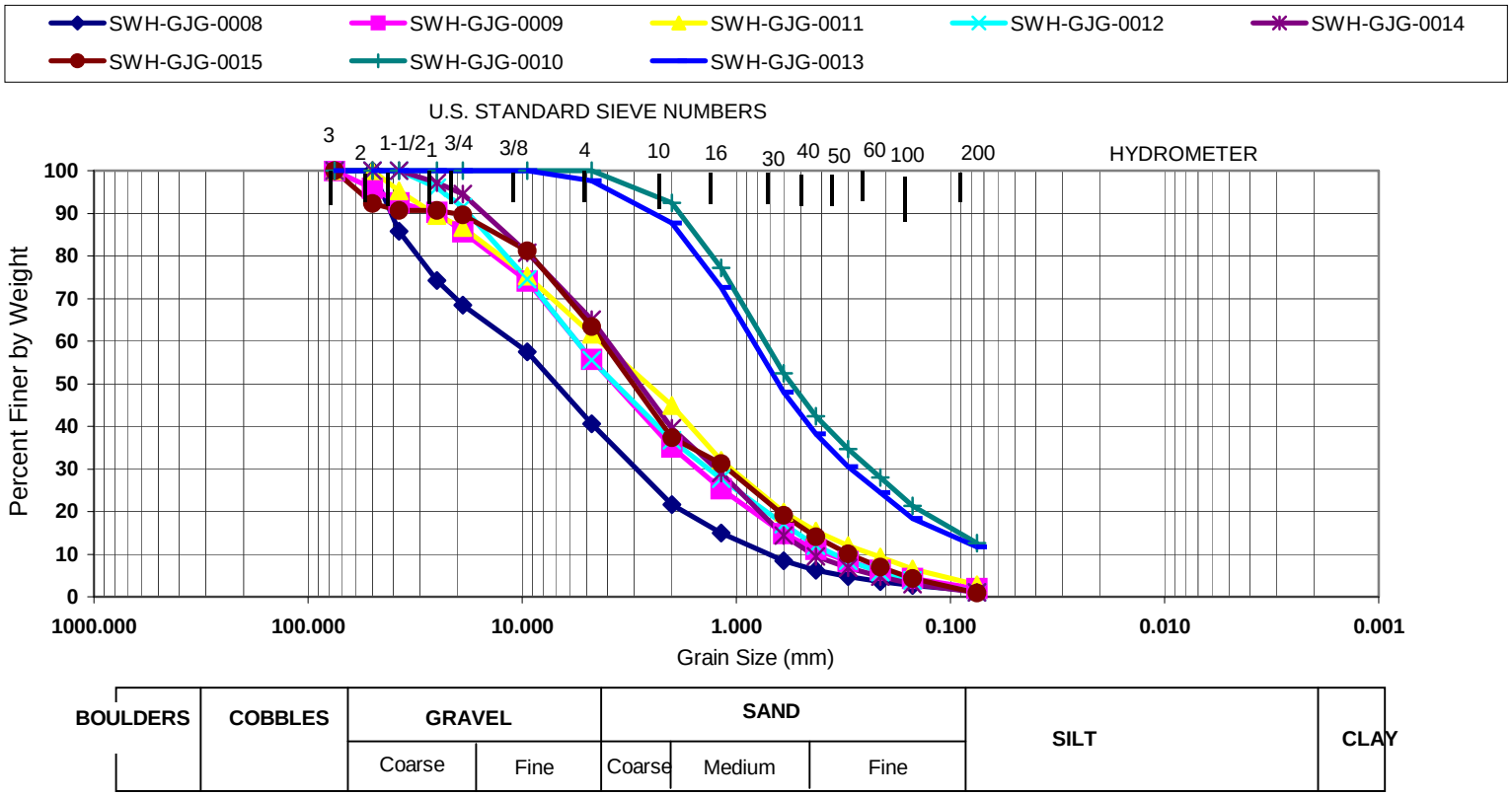

SWH-GJG-0020 - Particle Size Distribution

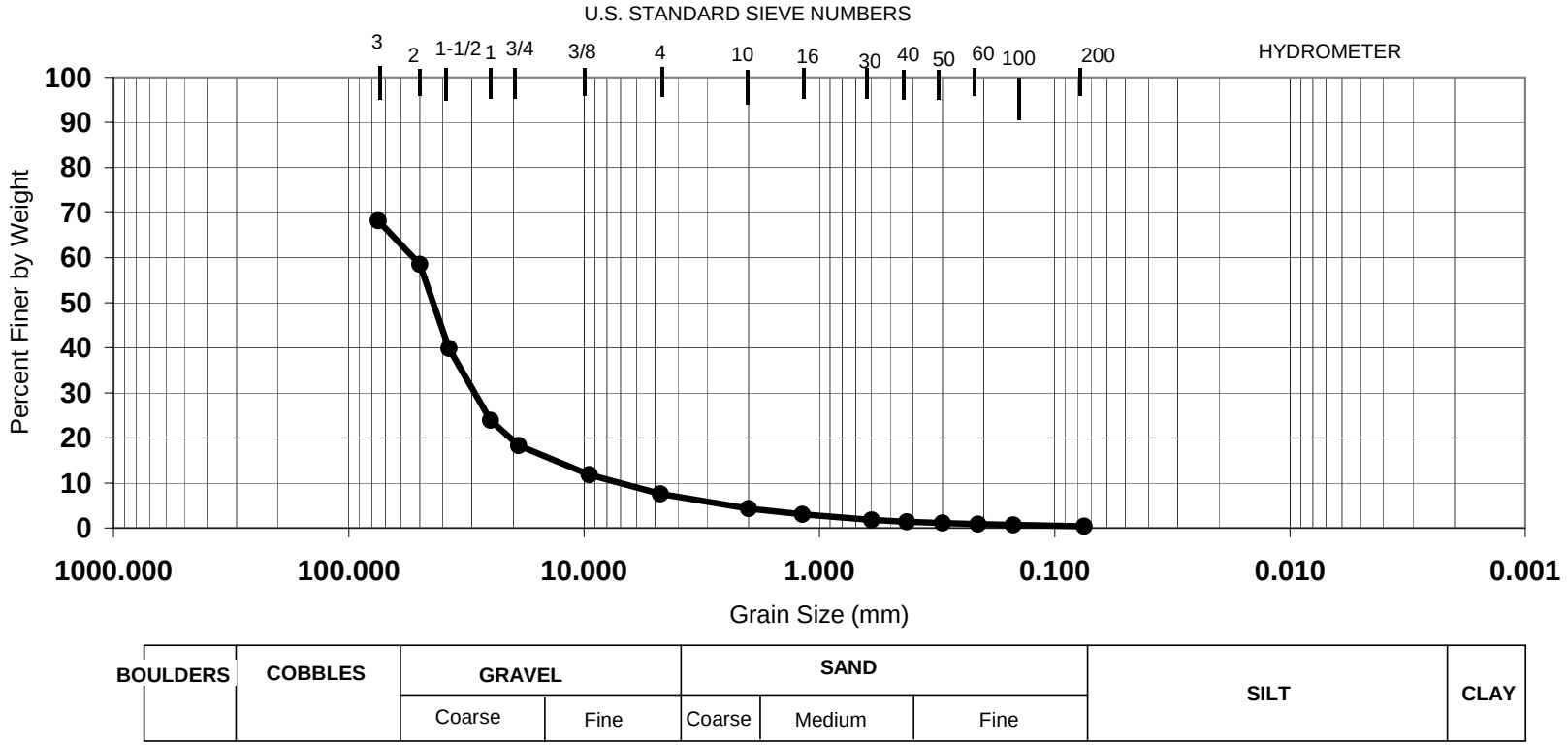

SWH-GJG-0021 - Particle Size Distribution

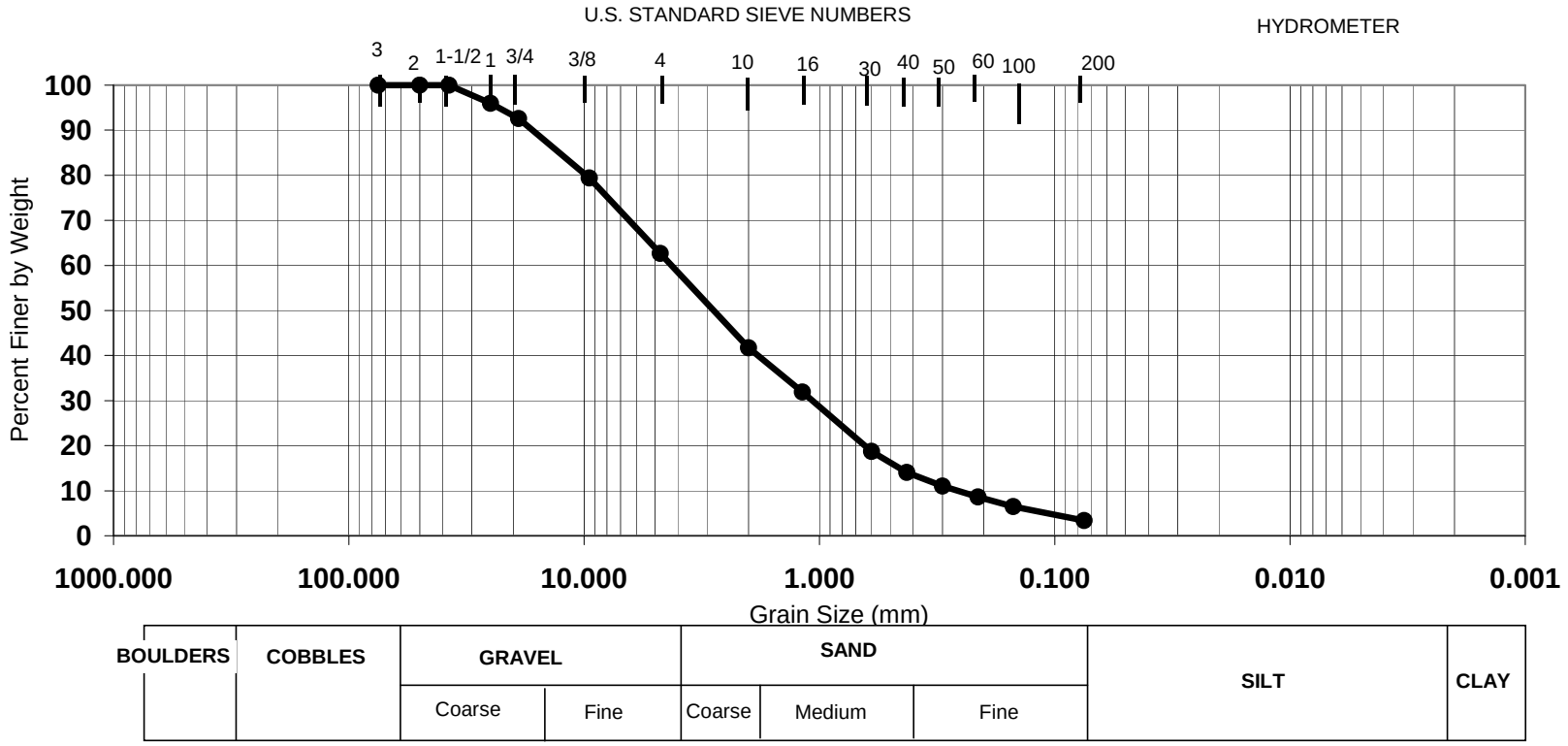

SWH-GJG-0022 - Particle Size Distribution

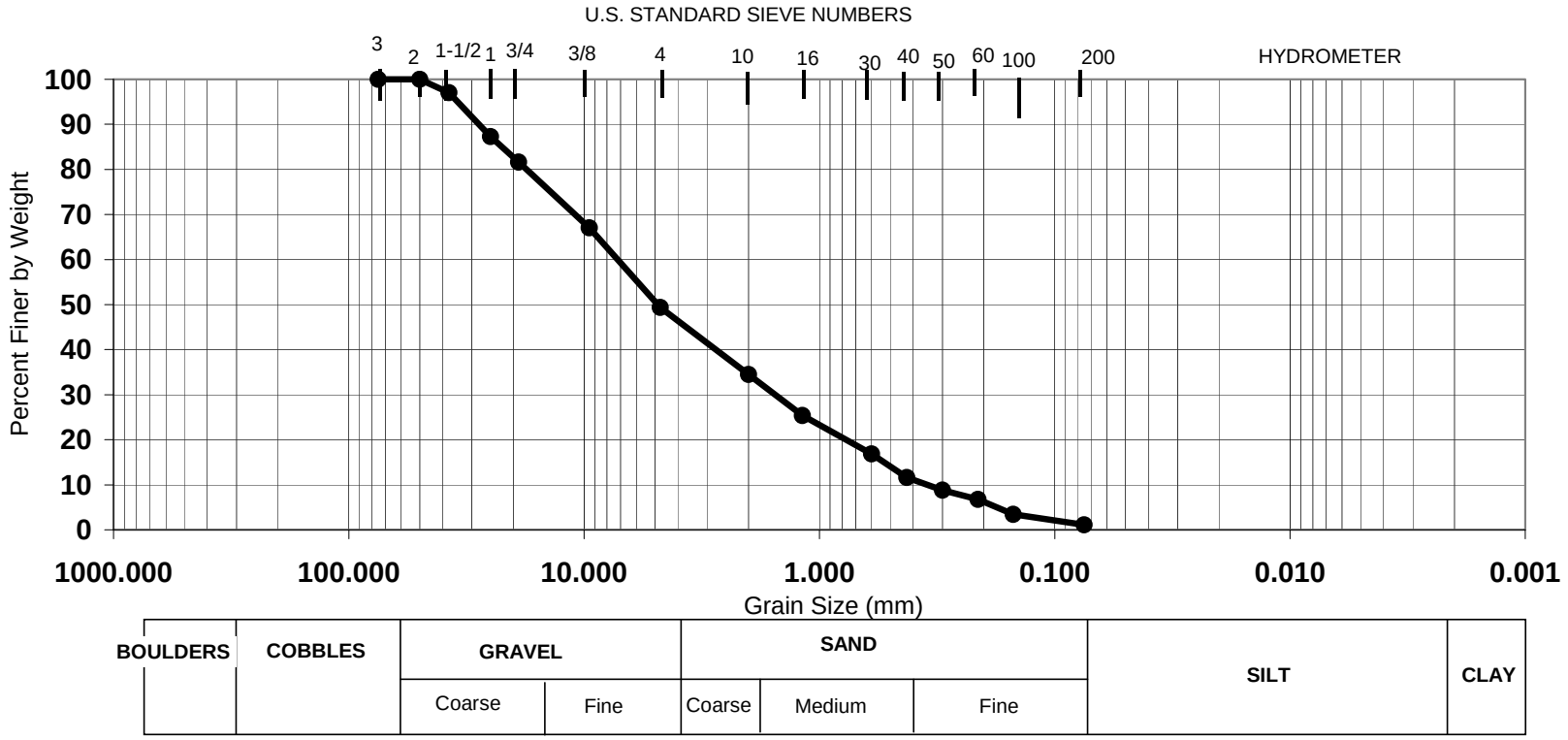

SWH-GJG-0023 - Particle Size Distribution

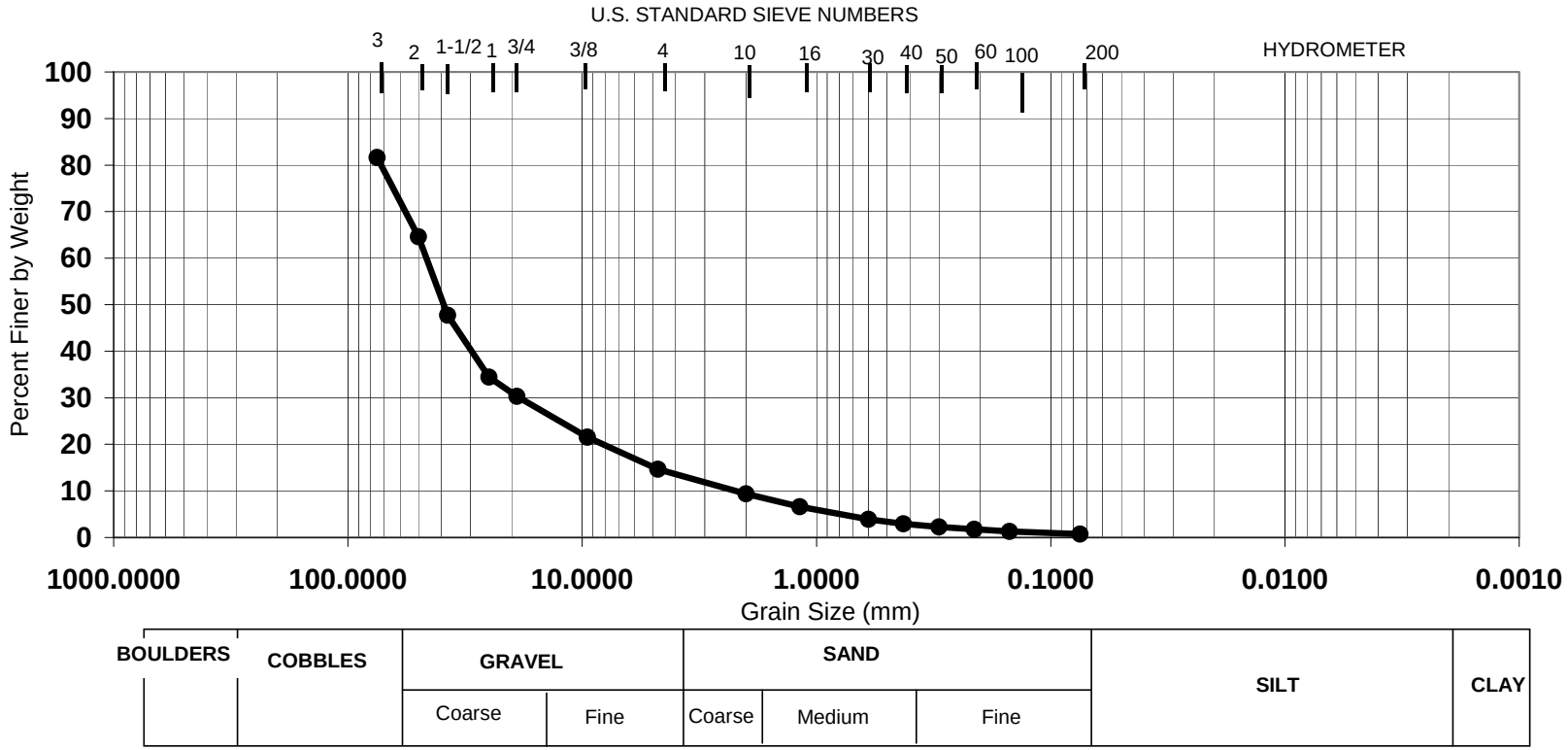

Upper Southwest Hansen Profile (SWH) - Particle Size Distribution

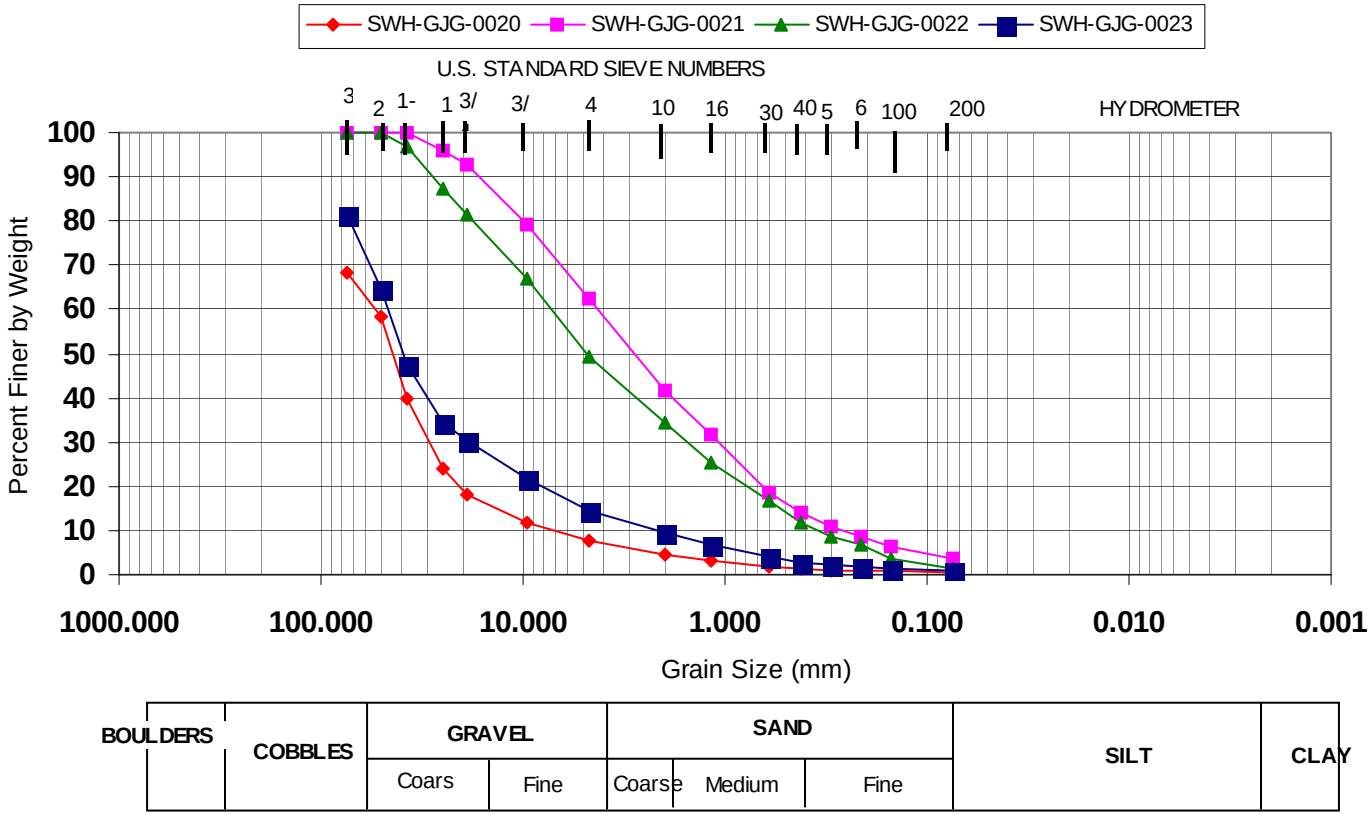

Appendix B. Petrographic Results

Hansen Profile

Silicates

Sample ID	% Plag	% K-Spar	% Quartz	% Chlorite	% Epidote	% Clay	Rock Type	Alteration	Other Comments
HAS-GJG-0010-F	0%	0%	30-35% (I or H)	5-10%% (H)	0%	40-45%% (H)	Porphyritic Andesite	QSP>>>Prop	Clays occur as groundmass and alteration of previous minerals, little survivable chlorite that hasn't turned to clay
HAS-GJG-0010-C	0%	0%	35-40% (I or H)	5-10% (H)	0%	40-45% (H)	Porphyritic Andesite	QSP>>>Prop	No evident feldspar xtals, may have been hydro alt to clays (illite), Quartz mostly as veinlets, but occurs as phenocrysts
HAS-GJG-0009	0%	0%	15-20% (I or H)	0%	0%	75-80% (H)	Porphyritic Andesite	QSP>>>>Prop	Abundant clays as groundmass and phenocrysts, No ghost feldspars, all altered to clays
HAS-GJG-0008-F	3-7% (I)	5-10% (I or H)	35-40% (I or H)	20-25% (H)	0%	25-30% (H)	Porphyritic Andesite	QSP>Prop	Clays are groundmass filling and occur around feldspars, feldspars exhibit hydrothermal texture, or clay coatings, quartz Occurs as small veinlets and phenocrysts
HAS-GJG-0008-C	2-5% (I)	4-8% (I or H)	30-35% (I or H)	25-30% (H)	0%	20-25% (H)	Porphyritic Andesite	QSP>Prop	Clays occur as mostly groundmass, occur with chlorites and feldspars, feldspars are scarce, where they do remain, crystal structure present, but clay rich
HAS-GJG-0007	2-5% (I)	7-10% (I or H)	20-30% (I or H)	10-15% (H)	0%	20-25% (H)	Porphyritic Andesite	QSP with Chemical Weathering	Crystal shapes of feldspar remain, but appear to have clay staining or replacement, Chlorite remnants replaced by clays, Quartz occurs as veinlets and phenocrysts
HAS-GJG-0006-F	2-5% (I)	10-15% (I or H)	20-25% (I or H)	15-20% (H)	3-5% (H)	20-25% (H)	Porphyritic Andesite	QSP>Prop	Clays occur as matrix fill and hydro alt textured minerals, Phenocrysts and small veinlets
HAS-GJG-0006-C	5-10% (I)	18-25% (I or H)	25-30% (I or H)	15-20% (H)	0%	15-20% (H)	Porphyritic Andesite	QSP > Prop	Clays are alteration of feldspars, veins and groundmass, remnant chlorite

(I) = Igneous Mineral
(I or H) = Igenous or Hydrothermal Mineral
(H) = Hydrothermal Mineral
(-C) = Coarse Fragment
(-F) = Finer Fragment

Sulfide Related

Sample ID	% Pyrite	% Calcite	% Gypsum	% Fe-Oxides	Rock Type	Alterations	Other Comments
HAS-GJG-0010-F	1% (H)	0%	1-2% (S)	1-2% (S)	Porphyritic Andesite	QSP>>>Prop	Small (< 1mm) pyrite grains with Fe-Oxide rims, ghost pyrites
HAS-GJG-0010-C	1% (H)	0%	0%	2-3% (S)	Porphyritic Andesite	QSP>>>Prop	Subhedral to anhedral pyrite xtals, Fe-oxide rims, ghost pyrites
HAS-GJG-0009	2-3% (H)	0%	0%	2-3% (S)	Porphyritic Andesite	QSP>>>>Prop	Pyrite very fine grained, mostly anhedral, see remnant pyrites that are now Fe-Oxides, oxide rims on ghost pyrites
HAS-GJG-0008-F	1-2% (H)	0%	0%	0%	Porphyritic Andesite	QSP>Prop	Most anhedral pyrite xstals w/ some subhedral, no oxide rims, near chlorites
HAS-GJG-0008-C	1-2% (H)	0%	0%	0%	Porphyritic Andesite	QSP>Prop	Subhedral to anhedral pyrite xtals, no oxide rims, occur near chlorites
HAS-GJG-0007	2% (H)	0%	5-10% (S)	10-15% (S)	Porphyritic Andesite	QSP with Chemical Weathering	Pyrite occurs as phenocrysts and veinlets, Abundant Fe-Oxide fracture filling, gypsum occurs in fracture fillings
HAS-GJG-0006-F	2-3% (H)	0%	3-5% (S)	0%	Porphyritic Andesite	QSP>Prop	Pyrite occurs as phenocrysts and veinlets, little fresh texture left, Needle-like gypsums occur near pyrite crystals
HAS-GJG-0006-*C*	2-3% (H)	2-3% (H)	0%	0%	Porphyritic Andesite	QSP>Prop	Pyrite occurs as veinlets and disseminations, no visible oxide rims, calcite occurs along feldspar grain boundaries

(S) = Supergene Mineral
(H) = Hydrothermal Mineral
(-C) = Coarse Fragment
(-F) = Finer Fragment

Lower Southwest Hansen Profile

Silicates

Sample ID	% Plag	% K-Spar	% Quartz	% Chlorite	% Epidote	% Clay	Rock Type	Alteration	Other Comments
SWH-GJG-0015	0%	0%	20-25% (I or H)	0%	0%	40-45% (H)	Quartz Latite Porphyry	QSP>>>>Prop	Dominant silicate mineral, occurs as phenocrysts and veinlets
SWH-GJG-0014	0%	0%	30-40% (I or H)	0%	0%	60-65% (H)	Quartz Latite Porphyry	QSP>>>>Prop	Quartz phenocrysts and veinlets. Clays replacing all other minerals
SWH-GJG-0013	0%	0%	30-35% (I or H)	0%	0%	60-65% (H)	Gray Clay	QSP>>>>Prop	Quartz and clay phenocrysts, veinlets with visible flourite
SWH-GJG-0012-F	20-25% (I or H)	5-10% (I)	12-15% (I or H)	5-10% (H)	<2% (H)	30-35% (H)	Quartz Latite Porphyry	QSP>Prop	Original biotite present, Feldspars exhibit hydrothermal texture. Clays occur in ground mass and as coarse grained illite
SWH-GJG-0012-C	25-30% (I or H)	5-10% (I)	12-15% (I or H)	7-10% (H)	<2% (H)	30-35% (H)	Quartz Latite Porphyry	QSP>Prop	Feldspars exhibit hydrothermal texture. Clays occur in ground mass and as coarse grained illite
SWH-GJG-0011-F	15-18% (I or H)	2-5% (I)	10-15% (I or H)	5-8% (H)	0%	25-30% (H)	Quartz Latite Porphyry	QSP>Prop	Clays occur in groundmass and feldspars "fresh" with calcite intergrowths
SWH-GJG-0011-C	8% (I or H)	2% (I)	10-15% (I or H)	5-10% (H)	0%	60-70% (H)	Quartz Latite Porphyry	QSP>>>Prop	Highly clay altered rock composed of coarse grained illite
SWH-GJG-0009	9-12% (I or H)	3-6% (I)	10-15% (I or H)	0% (H)	0%	10-15% (H)	Quartz Latite Porphyry	QSP with Chemical Weathering	Highly Fractured rock with clay and feldspar in clasts
SWH-GJG-0008-F	15-18% (I or H)	7-10% (I)	15-20% (I or H)	15-18% (H)	1-2% (H)	30-35% (H)	Quartz Latite Porphyry	QSP>Prop	Feldspars have both hydrothermal and fresh texture, clays occur in groundmass
SWH-GJG-0008-C	27-32% (I or H)	3-8% (I)	15-18% (I or H)	10-15% (H)	0%	25-30% (H)	Quartz Latite Porphyry	QSP > Prop	Feldspars have hydrothermal texture appearance, clays are located in groundmass

(I) = Igneous Mineral
(I or H) = Igenous or Hydrothermal Mineral
(H) = Hydrothermal Mineral
(-C) = Coarse Fragment
(-F) = Finer Fragment

Sulfide Related

Sample ID	% Pyrite	% Calcite	% Gypsum	% Fe-Oxides	Rock Type	Alterations	Other Comments
SWH-GJG-0015	Trace (H)	0%	5-8% (S)	15-20% (S)	Quartz Latite Porphyry	QSP>>>>Prop with chemical weathering	Trace amounts of anhedral (<0.2mm) pyrites. Gypsum and Fe-Oxides occur as cementaing agents for clay particles
SWH-GJG-0014	<1% (H)	<1% (H)	0%	<1% (S)	Quartz Latite Porphyry	QSP>>>>Prop	Fine grained anhedral pyrites, some oxide rims and staining, small calcite stinger vein
SWH-GJG-0013	2-3% (H)	0%	1-2% (S)	1-2% (S)	Quartz Latite Porphyry	QSP>>>>Prop	Pyrites euherdal to subhedral, thin gypsum veinlets, few oxide rims
SWH-GJG-0012-F	1-2% (H)	0%	0% (S)	<1% (S)	Quartz Latite Porphyry	QSP>Prop	Pyrites anherdal to subherdal, occur near chlorites, and few have Fe-Oxide rims
SWH-GJG-0012-C	1-2% (H)	0%	0%	<1% (S)	Quartz Latite Porphyry	QSP>Prop	Pyrites anherdal to subherdal, occur near chlorites, and few have Fe-Oxide rims
SWH-GJG-0011-F	2-3% (H)	10-15% (H)	0%	5-7% (S)	Quartz Latite Porphyry	QSP>Prop	Calcite occurs as veinlets and phenocrysts, appear intergrown w/some feldspar. Pyrites subhedral shape and oxide staining present
SWH-GJG-0011-C	1-2% (H)	0%	0%	0%	Quartz Latite Porphyry	QSP>>>Prop	Pyrite grains appear very euhedral and located in clay groundmass
SWH-GJG-0009	1-2% (H)	<1% (H)	10-15% (S)	30-35% (S)	Quartz Latite Porphyry	QSP with Chemical Weathering	Fe-oxides are cementing agent and fracture fillings, pyrites occur in rock clasts, gypsum precipitates in Fe-Oxides
SWH-GJG-0008-F	1-2% (H)	<1% (H)	2-3% (S)	0%	Quartz Latite Porphyry	QSP>Prop	Pyrites mostly euhedral, but begin to lose xtal shape. Gypsum occurs in veinlets along w/ flourite
SWH-GJG-0008-C	2% (H)	5-7% (H)	0%	0%	Quartz Latite Porphyry	QSP>Prop	Pyrites are perfect euhedral xtals, calcites occur as fracture filling

(S) = Supergene Mineral
(H) = Hydrothermal Mineral
(-C) = Coarse Fragment
(-F) = Finer Fragment

Upper Southwest Hansen Profile

Silicates

Sample ID	% Plag	% K-Spar	% Quartz	% Chlorite	% Epidote	% Clay	Rock Type	Alteration	Other Comments
SWH-GJG-0023	10-15% (I or H)	5-10% (I)	15-20% (I or H)	2-5% (H)	0%	10-15% (H)	Ferricrete	Modern Weathering	Rock clasts of different composition set in Fe-Oxide cement
SWH-GJG-0022	0% (I or H)	0%	40-45% (I or H)	1-2% (H)	0%	50-55% (H)	Porphyritic Andesite	QSP>>>Prop	Clays replacing all minerals present, all minerals destroyed by intense QSP
SWH-GJG-0021-F	30-35% (I or H)	2-5% (I)	15-20% (I or H)	15-20% (H)	0%	25-30% (H)	Porphyritic Andesite	Prop>QSP	Large and small feldspar laths, biotites still remain
SWH-GJG-0021-C	9-12% (I or H)	2-5% (I)	30-35% (I or H)	10-15% (H)	1-2% (H)	25-30% (H)	Porphyritic Andesite	QSP>Prop	Hydrothermal textured feldspars, chloritization of biotite w/small remaining biotites, clay groundmass
SWH-GJG-0020-F	30-35% (I or H)	5-10% (I)	10-15% (I or H)	15-18% (H)	3-5% (H)	20-25% (H)	Porphyritic Andesite	QSP>Prop	Small and large laths of feldspar, flow textures, chlorites present with clays
SWH-GJG-0020-C	30-35% (I or H)	5-10% (I)	15-20% (I or H)	13-17% (H)	3-6% (H)	20-25% (H)	Porphyritic Andesite	QSP>Prop	Small and large laths of plagioclase crystals that exhibit flow texture. Ground mass composed of clays and phaneritic black minerals

(I) = Igneous Mineral
(I or H) = Igenous or Hydrothermal Mineral
(H) = Hydrothermal Mineral
(-C) = Coarse Fragment
(-F) = Finer Fragment

Sulfide Related

Sample ID	% Pyrite	% Calcite	% Gypsum	% Fe-Oxides	Rock Type	Alterations*	Other Comments
SWH-GJG-0023	Trace (H)	0%	1-3% (S)	45-50% (S)	Ferricrete	Modern Weathering	Fe-Oxide cementing rock clasts, gypsum intergrown in cement, pyrite occurs in both clasts and cement
SWH-GJG-0022	2-3% (H)	0%	0%	0%	Porphyritic Andesite	QSP>>>Prop	Abundant pyrite with subhedral xtal shapes
SWH-GJG-0021-F	2-3% (H)	0%	3-5% (S)	<1% (S)	Porphyritic Andesite	Prop>QSP	Fine grained euhedral to subhedral pyrite, dendritic network of gypsum in clays, some Fe-Oxide rims on pyrite
SWH-GJG-0021-C	2-3% (H)	0%	0%	4-6% (S)	Porphyritic Andesite	QSP>Prop	Fe-oxides are cementing agent and fracture fillings, pyrites occur in rock clasts, gypsum precipitates in Fe-Oxides
SWH-GJG-0020-F	3% (H)	0%	0%	2-3% (S)	Porphyritic Andesite	QSP>Prop	Euhedral to subhedral pyrite xtals w/few Fe-Oxide rims, 1-2 Fe-Oxide veins in fractures
SWH-GJG-0020-C	3% (H)	0%	0%	0%	Porphyritic Andesite	QSP>Prop	Euhedral pyrite xtals

(S) = Supergene Mineral
(H) = Hydrothermal Mineral
(-C) = Coarse Fragment
(-F) = Finer Fragment

Appendix C. Isotopic Data from Campbell and Lueth (2008)

Sample No.	Mineral	Mineral Habit	Deposit Type	$\delta^{34}S$	$\delta^{18}O_{SO4}$	$\delta^{18}O_{OH}$	δD
AR 163*	Anhydrite	massive	Ore	8.0	3.5		
AR 89*	Anhydrite	massive	Ore	9.6	5.37		
AR 165*	Anhydrite	massive	Ore	6.6	7.34		
AR 23*	Gypsum	vein fill	Ore	12.6	9.4	-8.5	-122.9
AR 140*	Gypsum	vein fill	Ore	10.0	5.9	-5.1	-117.4
AR 165*	Gypsum	vein fill	Ore	9.9	6.7	-7	-114.7
AR 86*	Gypsum	vein fill	Ore	8.0	6	-12.8	-114
GMG PIT 0001	Gypsum	vein fill	Ore	12.3	5	-4.7	-114.9
SSS VWL 0001	Gypsum	efflorescent crust	Pile (HZ)	2.6	-4.7	-9.36	-104.7
SSW VWL 0002	Gypsum	crystal on clast	Pile	2.5	-3.65	-13.7	-104.6
SGS VWL 0003	Gypsum	crystal on clast	Pile	2.2	-6	-10.7	-115.3
SGS VWL 0002	Gypsum	crystal on clast	Pile (HZ)	0.9	-9.33	-23.9	-201.4
SGS VWL 0001	Gypsum	vein fill	Pile	10.8	4.19	-5.26	-121.9
SSS VWL 0003	Gypsum	satin spar float	Pile	11.2	5.3	-13.5	-120.7
SGS VWL 0003	Gypsum	massive	Pile	8.7	6.2	-24.1	-107.1
SGS VWL 0004	Gypsum	rounded grains	Pile	10.0	6.2	-21.2	-116.9
SGS VWL 0005	Gypsum	massive	Pile	8.8	8.7	-19.4	-92.5
SSS VWL 0002	Jarosite	surface crust	Pile (HZ)	2.2	-3.3	-6.3	-105.9
GHN VWL 0008-2	Gypsum	small euhedral xtals	Pile	1.3	-0.1		
GHN VWL 0008-1	Gypsum	xtals on clast	Pile	1.3	-0.7		
GHN KMD 0082	Gypsum	small euhedral xtals	Pile	-7.4	-6.8		
GHN VWL 0006	Gypsum	small euhedral xtals	Pile	0.6	-1.5		
GHN VWL 0007	Gypsum	small euhedral xtals	Pile	-1.7	-4		
GHN LFG 0055	Gypsum	small euhedral xtals	Pile	-2.7	1.2		
GHN VWL 0001	Gypsum	small euhedral xtals	Pile	1.6	0.9		
GHN VWL 0005	Gypsum	small euhedral xtals	Pile	-0.5	0.5		
SCS VWL 0005	Gypsum	fracture fill	Scar	0.4	-1.89	-14.3	-122.8
PIT VWL 0007	Jarosite	fracture fill	Scar	-10.6	-0.96	-6.8	-154.99
BCS VWL 0002	Jarosite	fracture fill	Scar	-0.6	2.2	-3.04	-177.5
CAS VWL 0001	Jarosite	ferricrete	Scar	-0.2	0.4	-4.48	-175
ESS VWL 0001	Jarosite	fracture fill	Scar	-2.4	2.7	-3.35	-140
SWH VWL 0001	Jarosite	ferricrete clast	Scar	-5.4	-1.8	-2.03	-163
GHR KMD 0011	Gypsum	fracture fill	Scar	-4.2	3.1		
PIT VWL 0004	Jarosite	fracture fill	Scar	-8.4	0.29		
GHR VWL 0003	Jarosite	ferricrete	Scar	-1.5	0.99		
GHS VWL 0010	Jarosite	fracture fill	Scar	-6.3	-0.54		
PIT VWL 0001	Jarosite	fracture fill	Scar	-6.9	0.55		
HTS USG 0005#	Alunite	vein fill	Scar	17.8	7.5	-2.05	-47
PIT VWL 0010	Gypsum	fracture fill	Scar	0.8			
GHR VWL 0011	Jarosite	fracture fill	Scar	-2.2			
GHR VWL 0006	Jarosite	fracture fill	Scar	-8.4			
PIT VWL 0003	Jarosite	fracture fill	Scar	-10.1			
PIT VWL 0005	Jarosite	fracture fill	Scar	-12.1			
HAS VWL 0002	sulfate crust	fracture fill	scar	-8.0			
HAS VWL 0003	Gypsum	xtal float	scar	-2.7			
HAS VWL 0004	Gypsum	fracture fill	scar	-3.3			
HTS VWL 0001	sulfate crust	fracture fill	scar	-3.6			
HTS VWL 0002	sulfate crust	fracture fill	scar	-4.1			
SWH VWL 0002	Gypsum	fracture fill	scar	-4.2			
SWH VWL 0002	Gypsum	crystal float	scar	-4.6			
SWH VWL 0002	sulfate crust	fracture fill	scar	-5.5			
SHE VWL 0001	Gypsum	fracture fill	scar	-4.3			
PIT VWL 0012	Pyrite	disseminated	Ore	-1.2			
PIT VWL 0012	Pyrite	vein fill	Ore	2.7			
GHR VWL 0011	Pyrite	disseminated	Scar	-0.2			
GHN KMD 0097	Pyrite	disseminated	Pile	-3.2			
SWH VWL 0002	Pyrite	disseminated	scar	-5.9			
SHE VWL 0001	Pyrite	disseminated	scar	-7.5			
HTS VWL 0001	Pyrite	disseminated	Scar	-2.8			
HTS VWL 0002	Pyrite	disseminated	Scar	-2.9			
HTS VWL 0003	Pyrite	disseminated	Scar	-0.7			
HTS VWL 0004	Pyrite	disseminated	Scar	-2.3			
HAS VWL 0001	Pyrite	disseminated	Scar (amalia)	-13.6			
HAS VWL 0002	Pyrite	disseminated	Scar	-8.9			
HAS VWL 0004	Pyrite	disseminated	Scar	-4.7			
GHN VWL 0003	Pyrite	disseminated	Pile	-2.4			
CC1A	2/5/2003	water	filtered	-0.4	-0.4		
CC1B	2/5/2003	water	filtered	-3.4	-4.2		
CC2A	5/14/2003	water	filtered	-3.1	-4		
CC2A	8/19/2003	water	filtered	-3.2	-4.3		
CC2A_R	8/19/2003	water	filtered	-3.2	-4.5		
Hansen	5/13/2003	water	filtered	-7.0	-7.5		
Hansen SW-L	9/11/2001	water	filtered	-8.0	-6.9		
Hansen SW-H	9/11/2001	water	filtered	-6.5	-8.6		
Hottentot	5/12/2003	water	filtered	-5.8	-6.5		
Hottentot SW-L	9/13/2001	water	filtered	-7.6	-3.9		
Hottentot SW-H	9/13/2001	water	filtered	-7.6	-4.6		
La Bobita	2/5/2003	water	filtered	-3.6	-5.6		
La Bobita	5/15/2003	water	Raw	3.4	-6		

Note:

* sample supplie by Amanda Rowe, New Mexico Institute of Mining & Technology

sample provided by Geoff Plumlee, United States Geological Survey

Appendix D. Clay X-Ray Diffraction Scans

Table of 2θ peak locations for identified clay minerals

I	1W Dismectite 2θ	2W Dismectite 2θ	Clinochlore 2θ	Chamosite 2θ	Kaolinite 2θ	Illite (Dimica) 2θ
(001)	*7.06*	*5.83*	*6.21*	*6.14*	*12.42*	*8.74*
(002)	*14.34*	*17.64*	*12.5*	*12.42*	*24.95*	*17.87*
(003)	*29.06*	*23.77*	*18.86*	*18.71*	___	*26.91*

Hansen Profile

HAS-GJG-0006

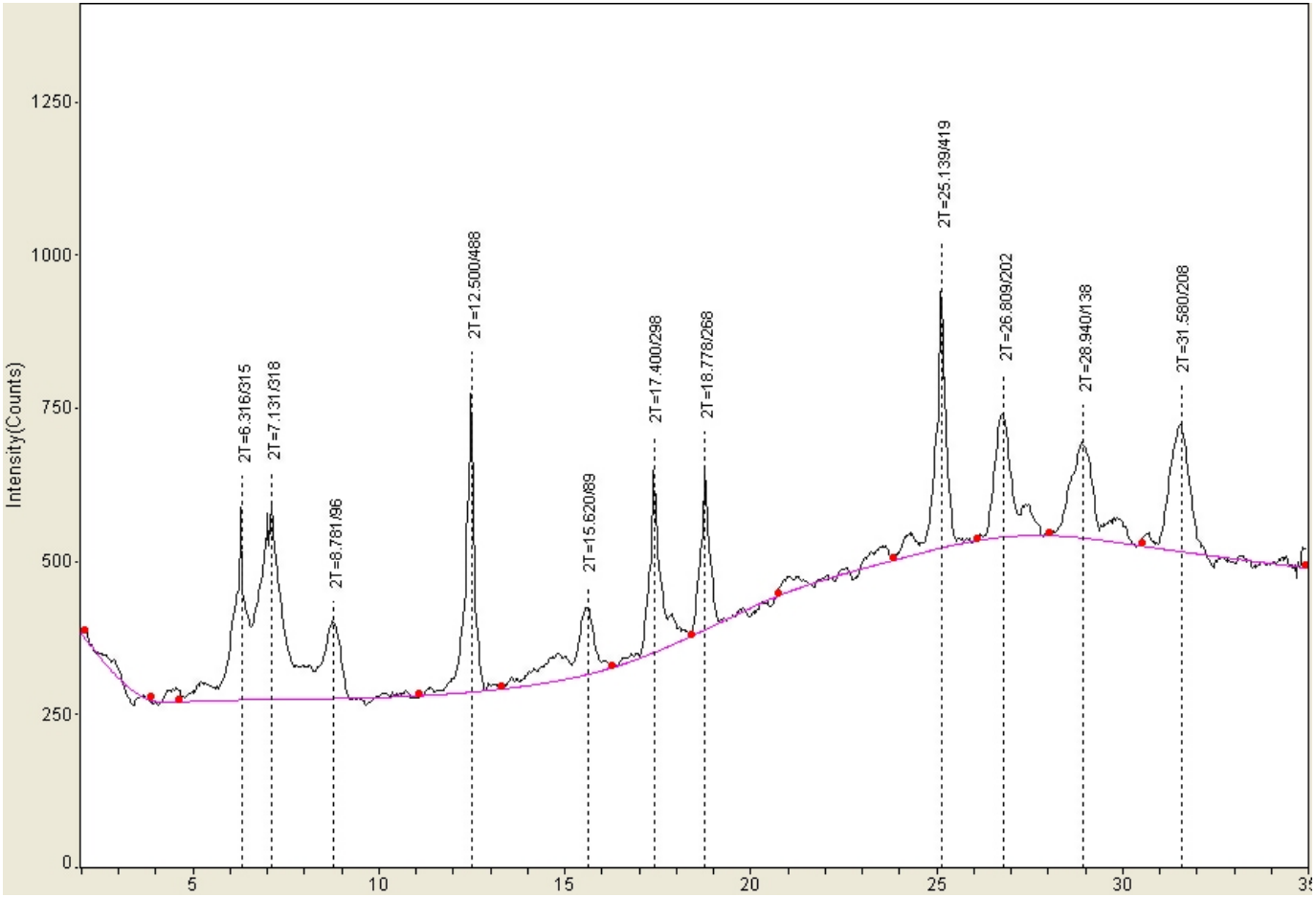

HAS-GJG-0006-20

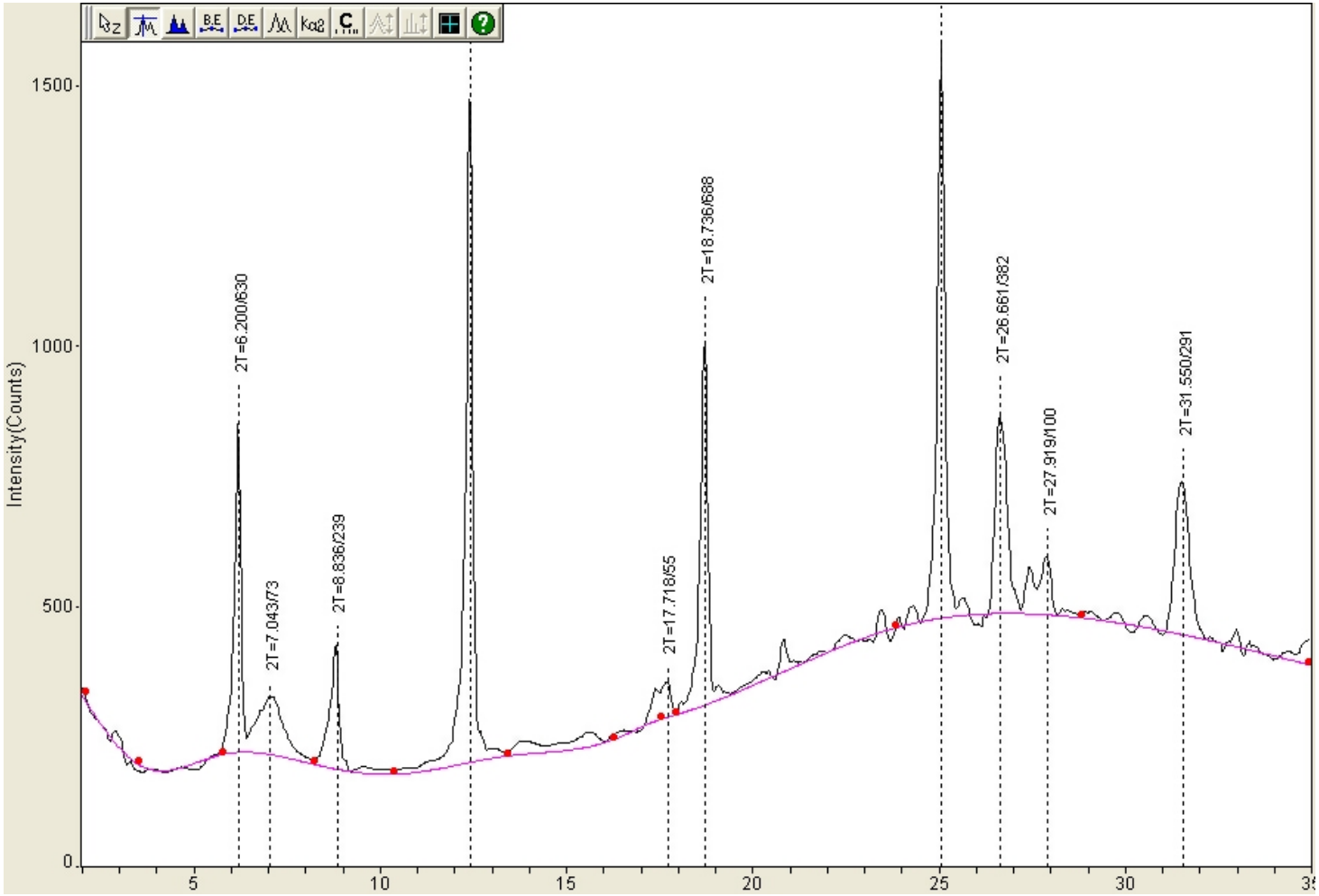

HAS-GJG-0008

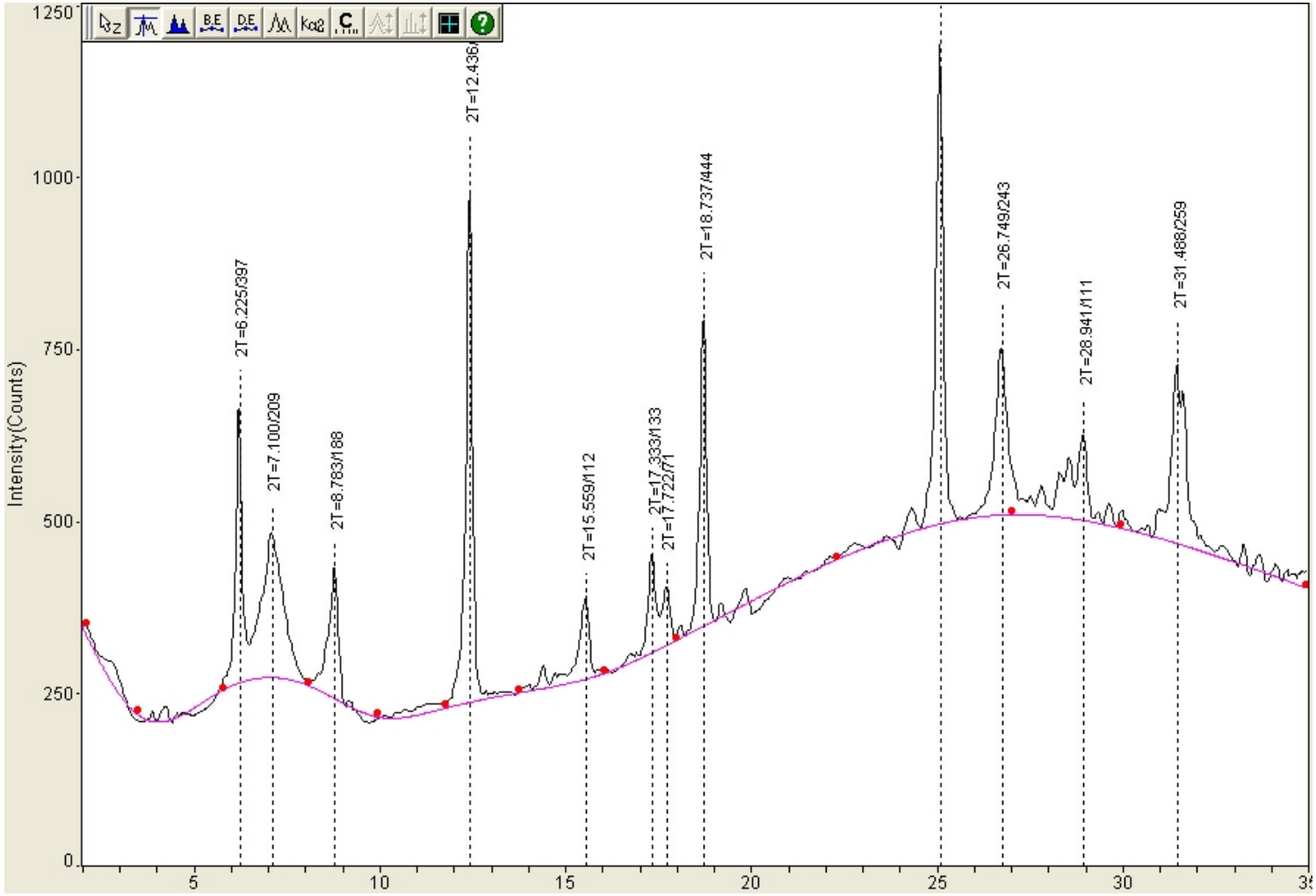
Intensity(Counts)
1250
1000
750
500
250
0
5
10
15
20
25
30
2T=6.225/397
2T=7.100/209
2T=8.783/188
2T=12.436/
2T=15.559/112
2T=17.333/133
2T=17.722/71
2T=18.737/444
2T=26.749/243
2T=28.941/111
2T=31.488/259

HAS-GJG-0009

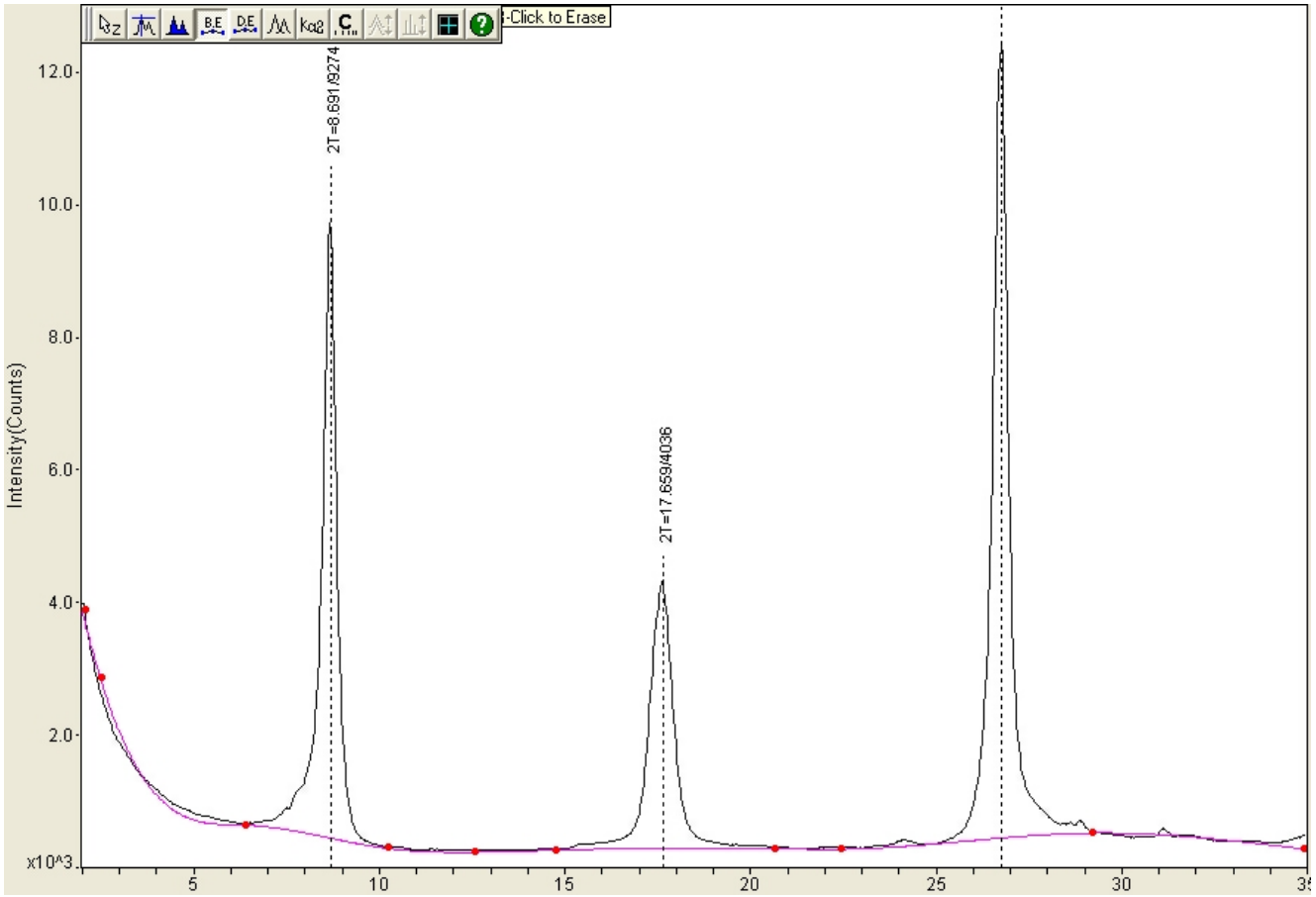
Click to Erase
2T=8.691/9274
2T=17.659/4036
Intensity(Counts)
x10^3
12.0
10.0
8.0
6.0
4.0
2.0
5
10
15
20
25
30

HAS-GJG-0010

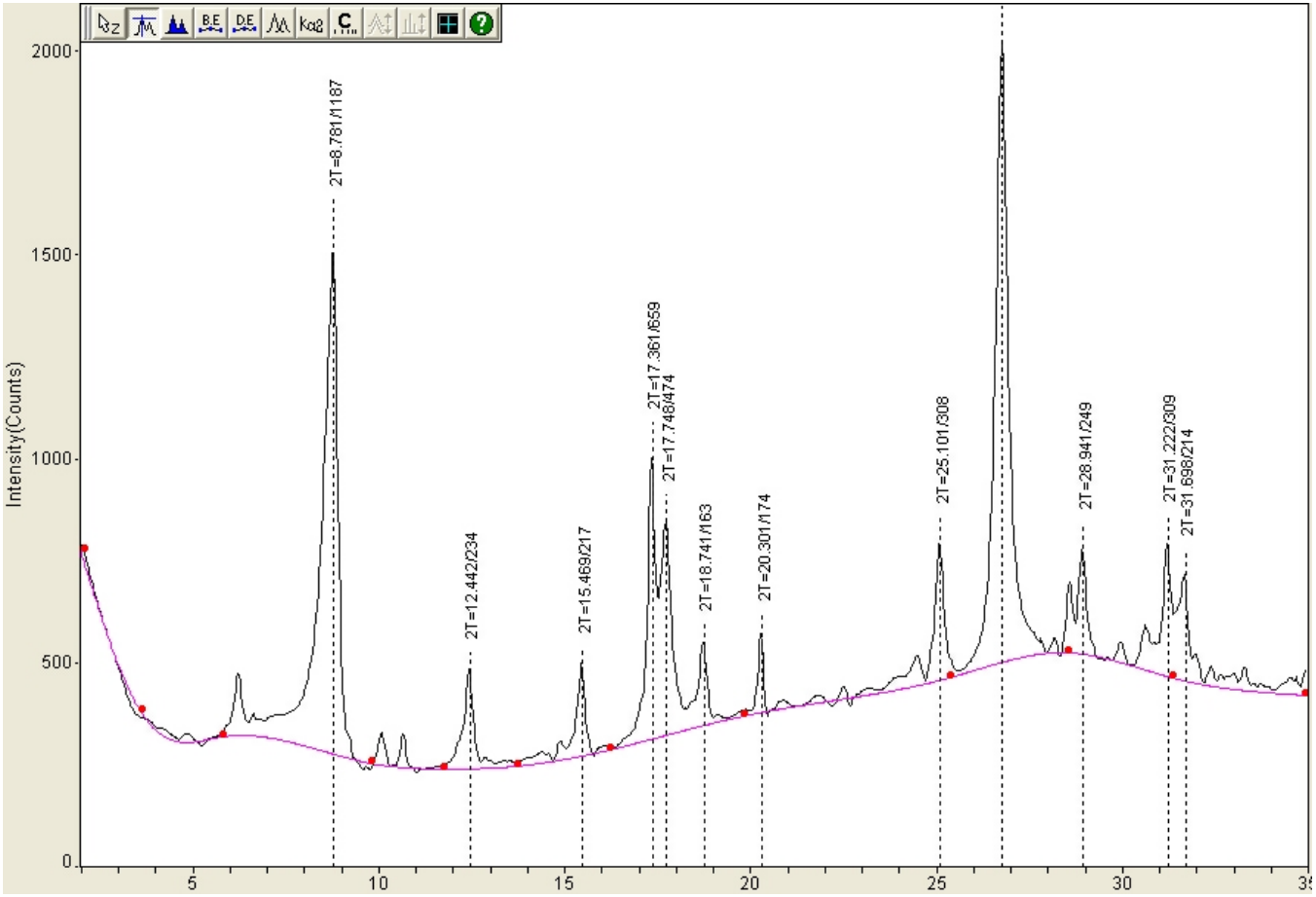
Intensity(Counts)
2000
1500
1000
500
0
5
10
15
20
25
30
2T=8.781/1187
2T=12.442/234
2T=15.469/217
2T=17.361/659
2T=17.746/474
2T=18.741/163
2T=20.301/174
2T=25.101/308
2T=28.941/249
2T=31.222/309
2T=31.698/214

Lower Southwest Hansen Profile

SWH-GJG-0008

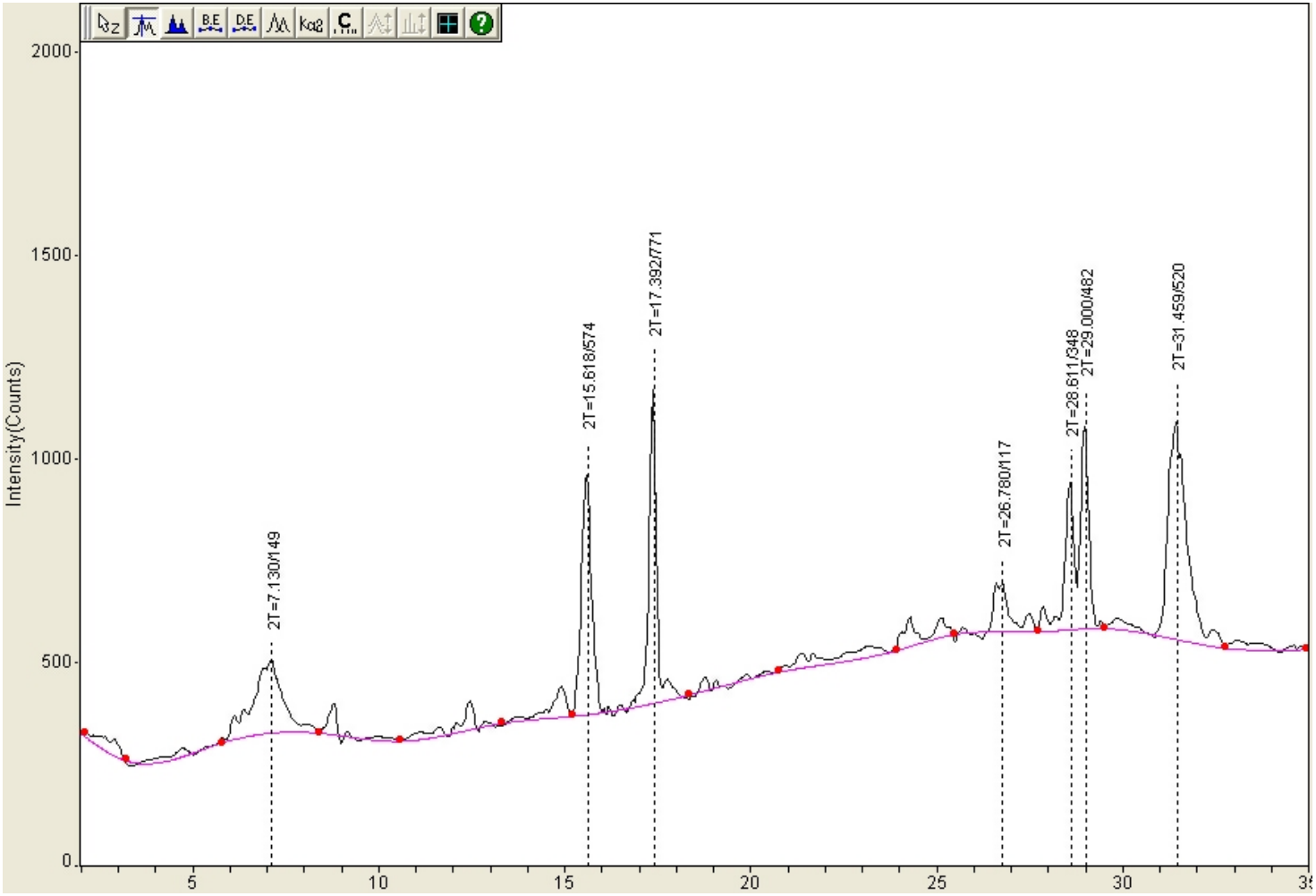

SWH-GJG-0009

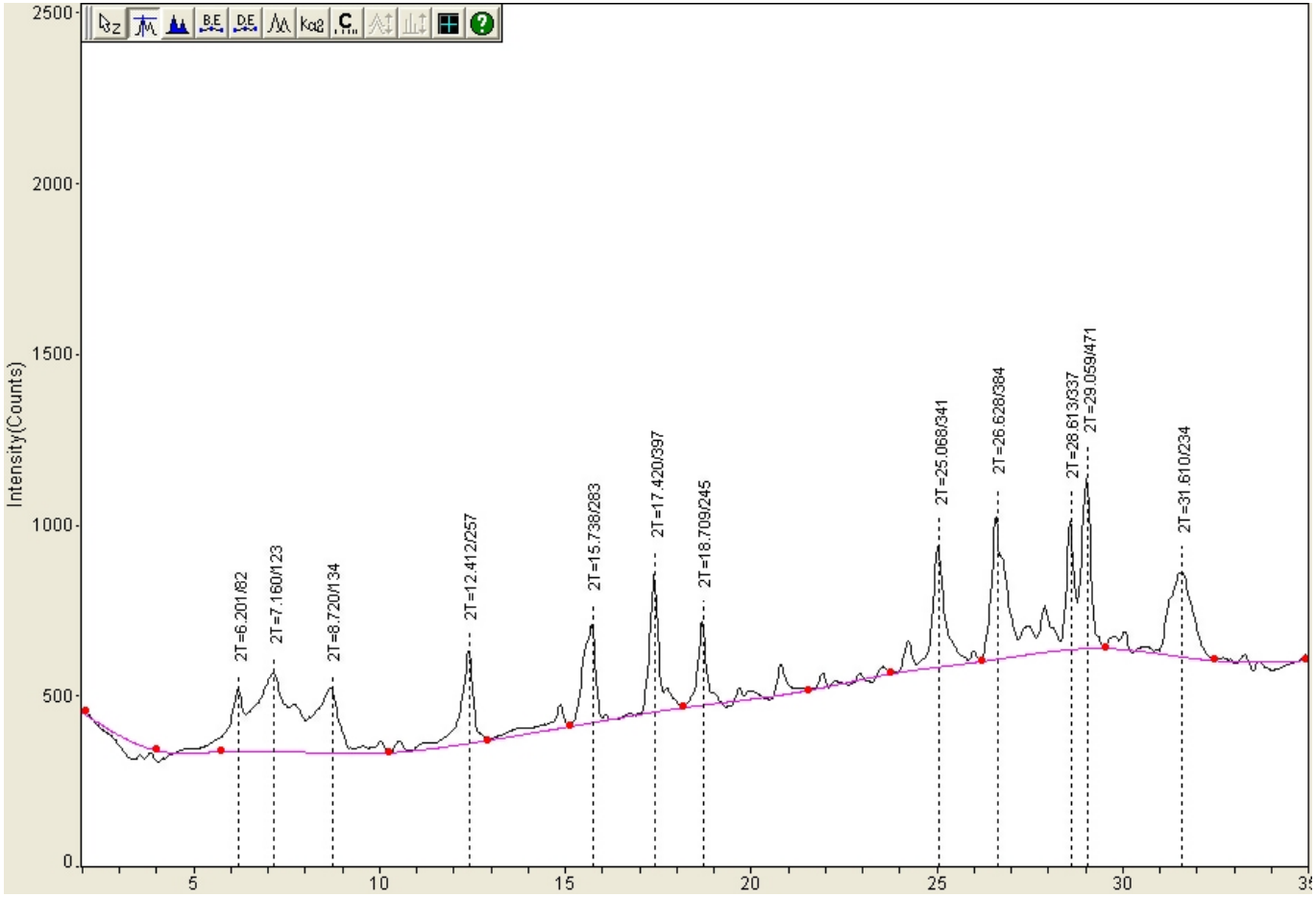
Intensity(Counts)
2500
2000
1500
1000
500
0
5
10
15
20
25
30
2T=6.201/82
2T=7.160/123
2T=8.720/134
2T=12.412/257
2T=15.738/283
2T=17.420/397
2T=18.709/245
2T=25.068/341
2T=26.628/384
2T=28.613/337
2T=29.059/471
2T=31.610/234

SWH-GJG-0010

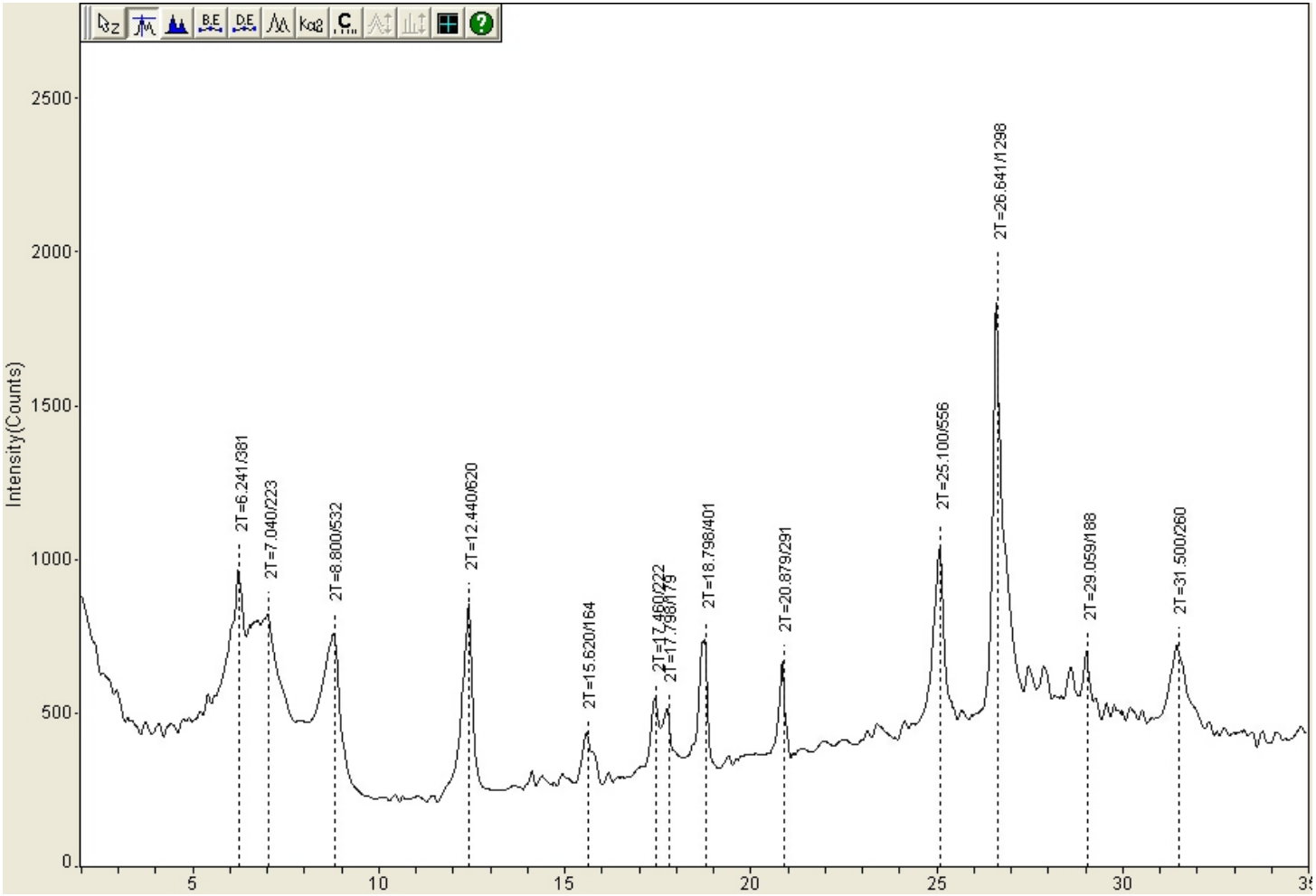
Intensity(Counts)
2500
2000
1500
1000
500
0
5
10
15
20
25
30
2T=6.241/381
2T=7.040/223
2T=8.800/532
2T=12.440/620
2T=15.620/164
2T=17.460/222
2T=17.798/179
2T=18.798/401
2T=20.879/291
2T=25.100/556
2T=26.641/1298
2T=29.059/188
2T=31.500/260

SWH-GJG-0011

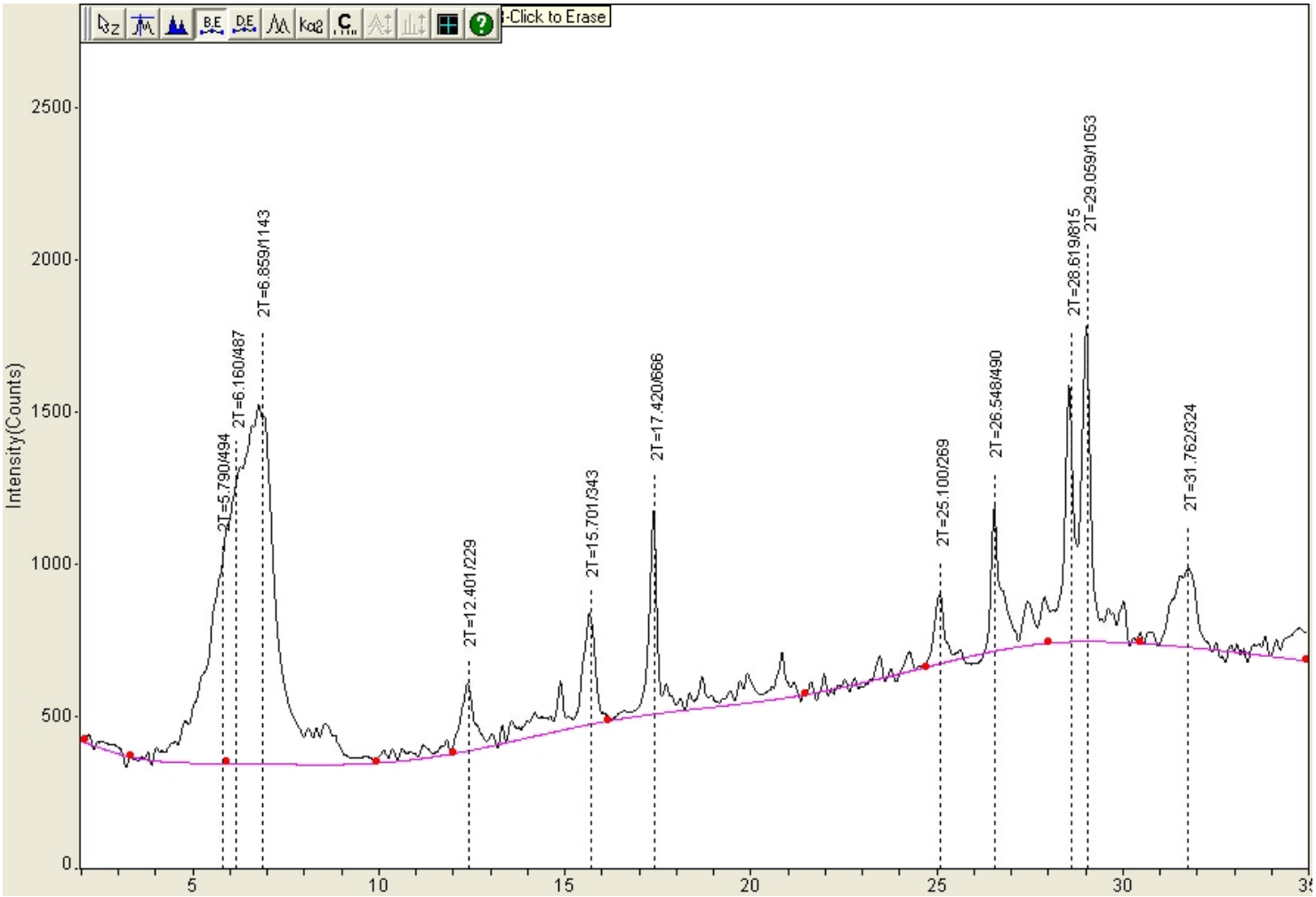
Click to Erase
Intensity(Counts)
2500
2000
1500
1000
500
0
5
10
15
20
25
30
2T=5.790/494
2T=6.160/487
2T=6.859/1143
2T=12.401/229
2T=15.701/343
2T=17.420/666
2T=25.100/269
2T=26.548/490
2T=28.619/815
2T=29.059/1053
2T=31.762/324

SWH-GJG-0012

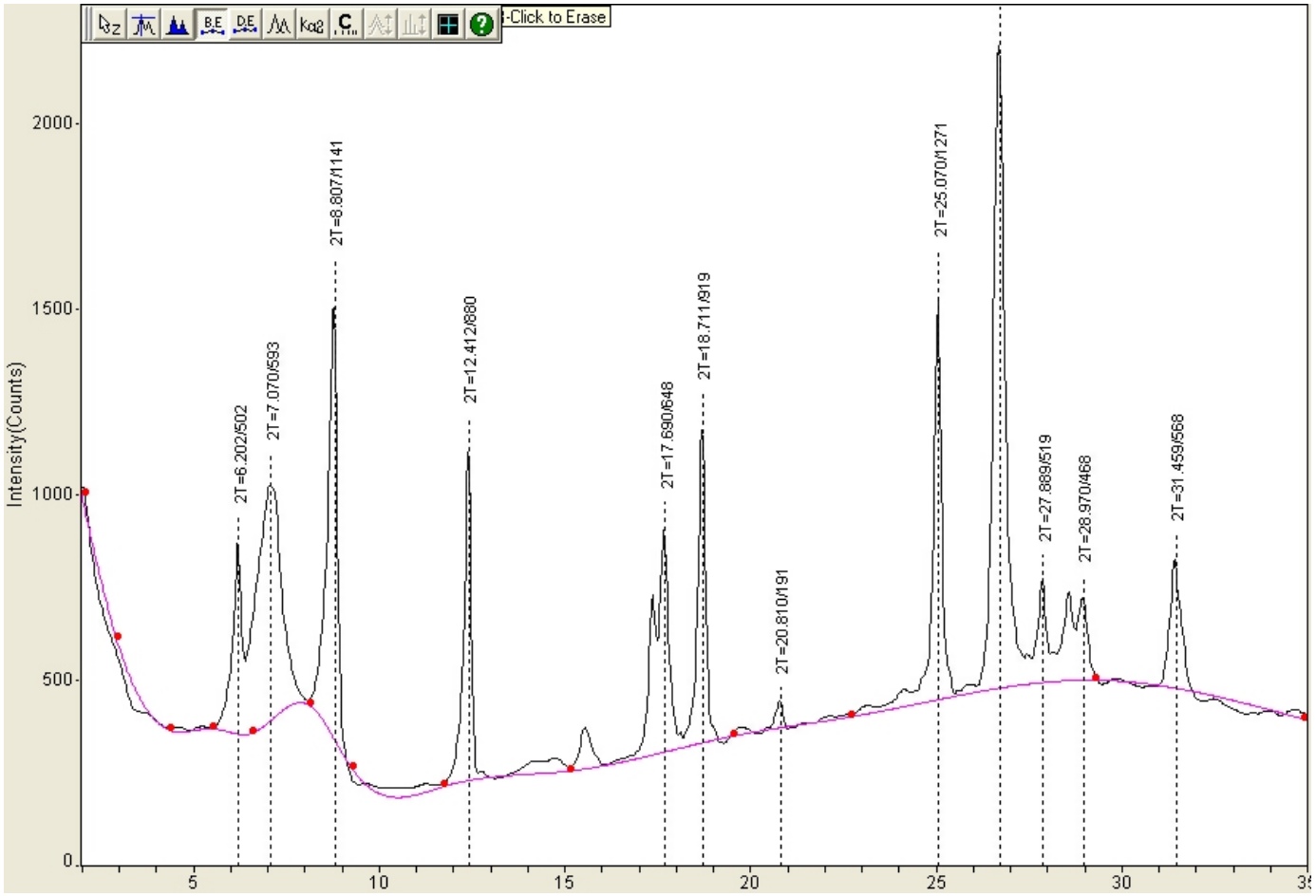
Intensity(Counts)
2000
1500
1000
500
0
5
10
15
20
25
30
2T=6.202/502
2T=7.070/593
2T=8.807/1141
2T=12.412/880
2T=17.690/648
2T=18.711/919
2T=20.810/191
2T=25.070/1271
2T=27.889/519
2T=28.970/468
2T=31.459/568

SWH-GJG-0013

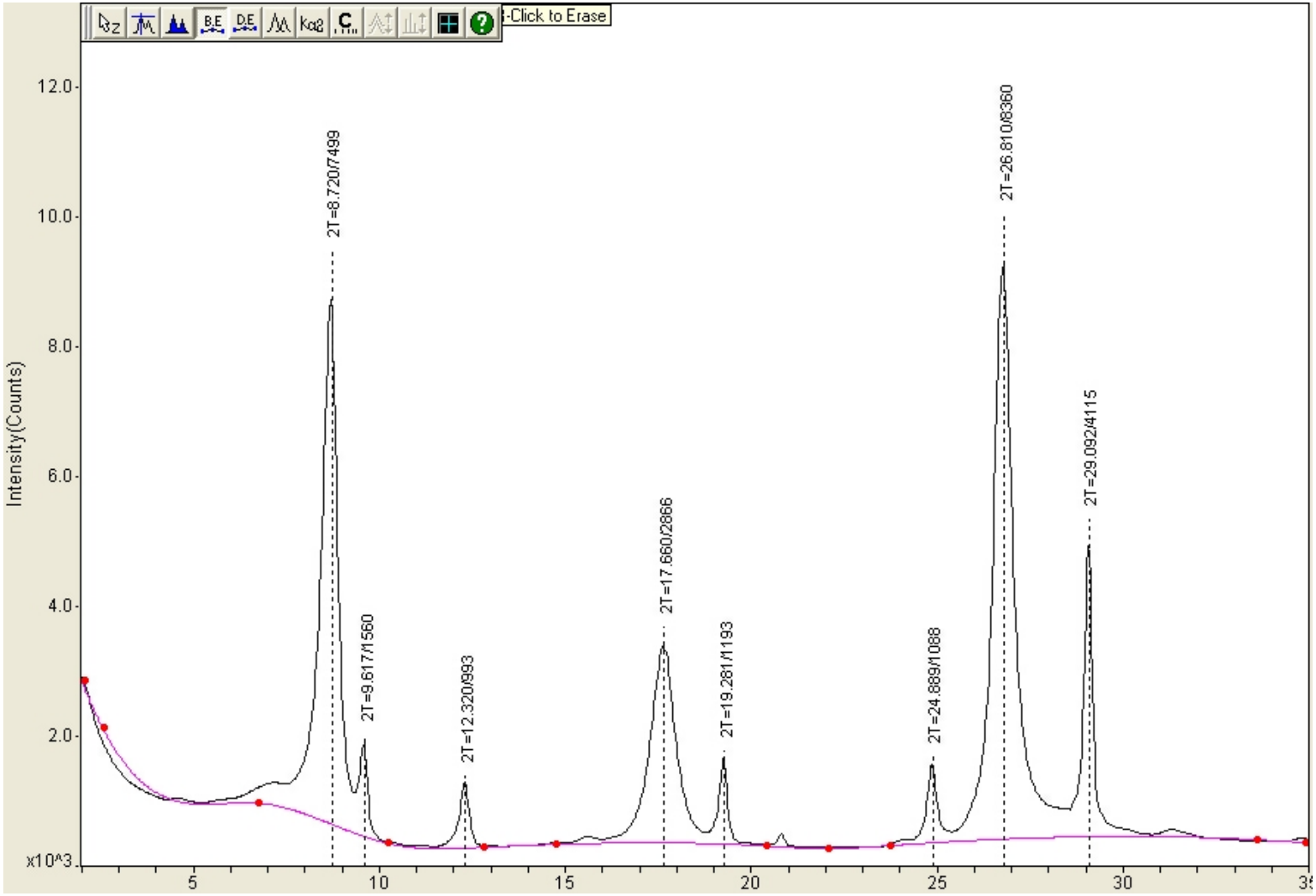
Click to Erase
Intensity(Counts)
x10^3
12.0
10.0
8.0
6.0
4.0
2.0
5
10
15
20
25
30
2T=8.720/7499
2T=9.617/1560
2T=12.320/993
2T=17.660/2866
2T=19.281/1193
2T=24.889/1088
2T=26.810/8360
2T=29.092/4115

SWH-GJG-0014

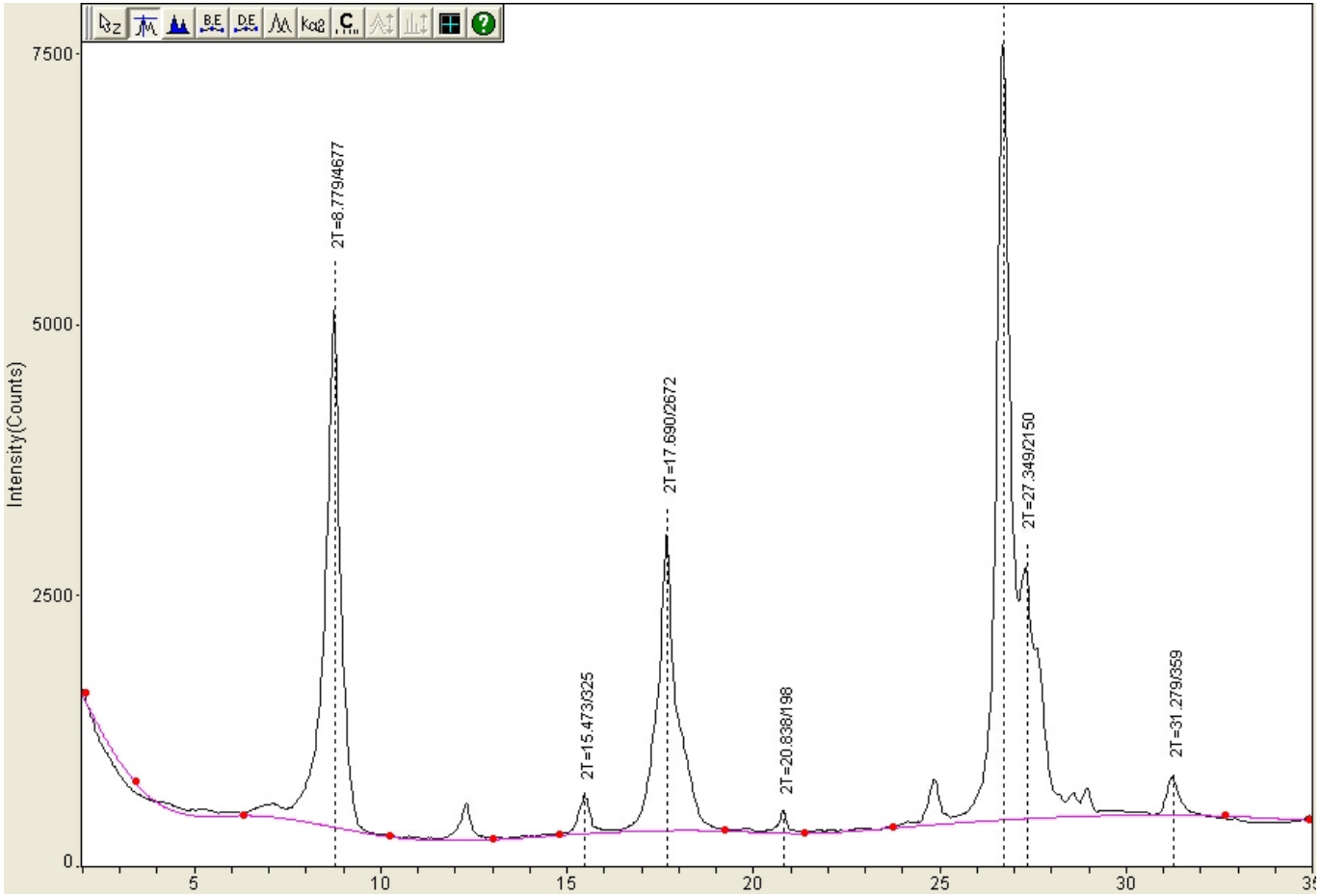
Intensity(Counts)
7500
5000
2500
0
5
10
15
20
25
30
2T=8.779/4677
2T=15.473/325
2T=17.690/2672
2T=20.838/198
2T=27.349/2150
2T=31.279/359

SWH-GJG-0015

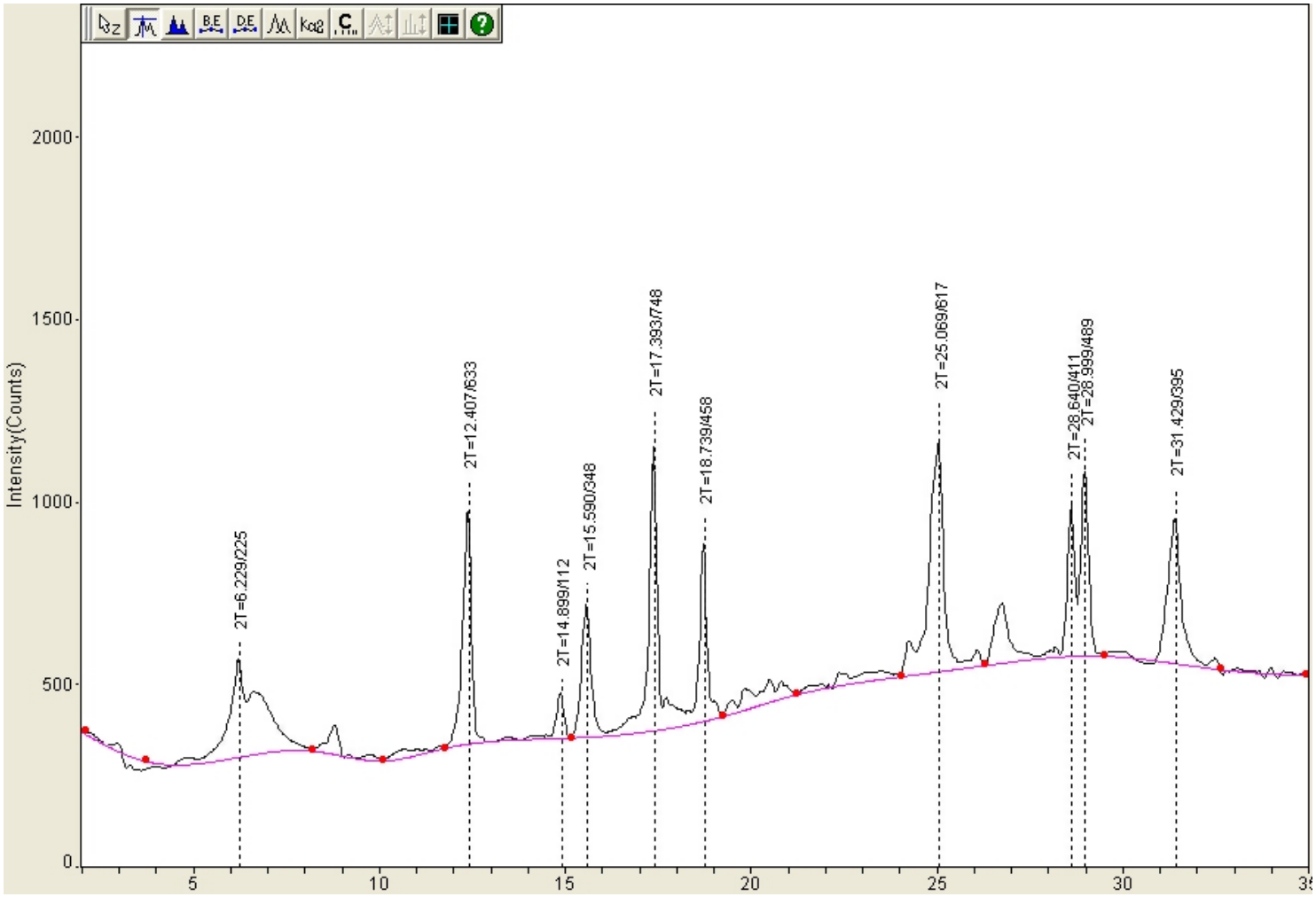
Intensity(Counts)
2000
1500
1000
500
0
5
10
15
20
25
30
2T=6.229/225
2T=12.407/633
2T=14.899/112
2T=15.590/348
2T=17.393/748
2T=18.739/458
2T=25.069/617
2T=28.640/411
2T=28.999/489
2T=31.429/395

Upper Southwest Hansen Profile

SWH-GJG-0020

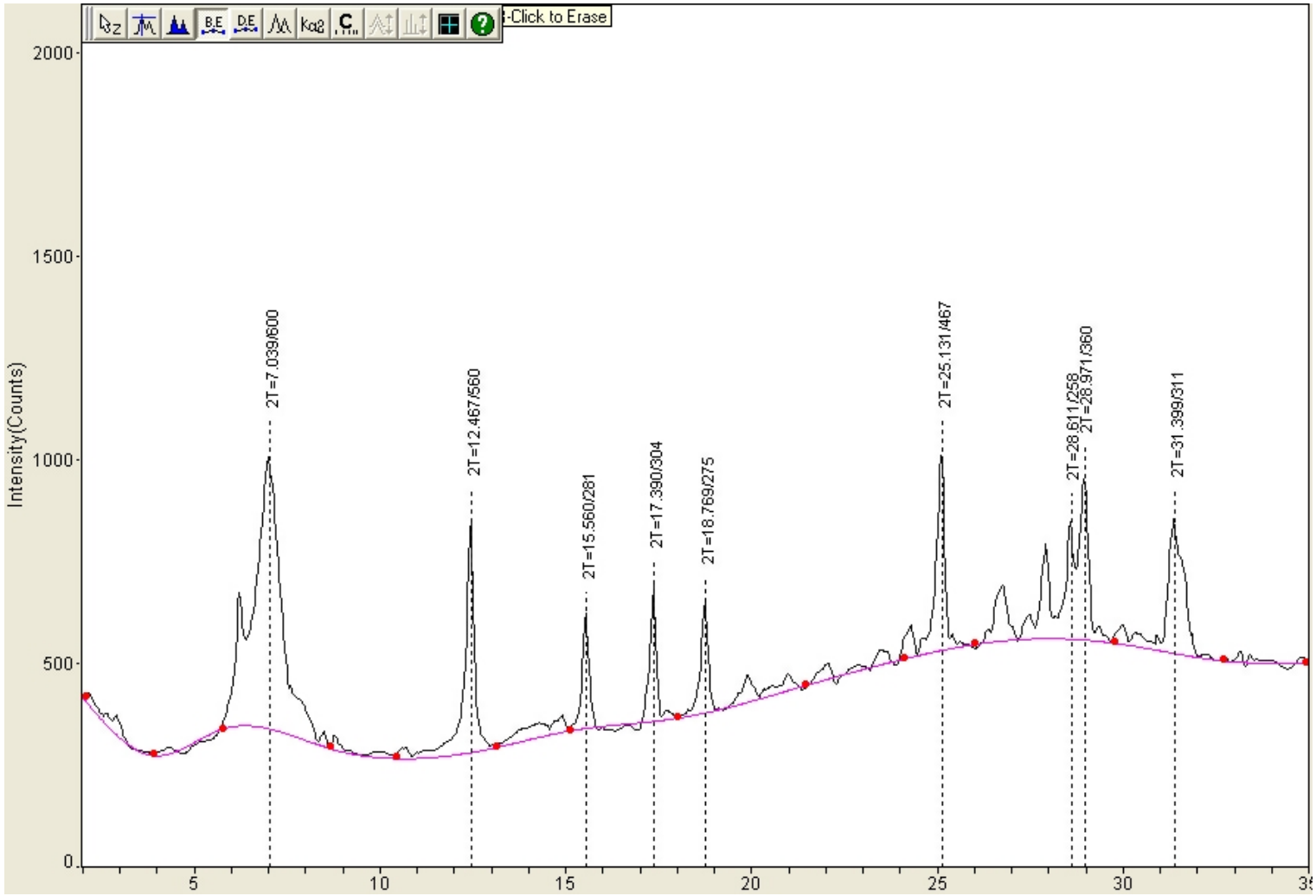

SWH-GJG-0020-20

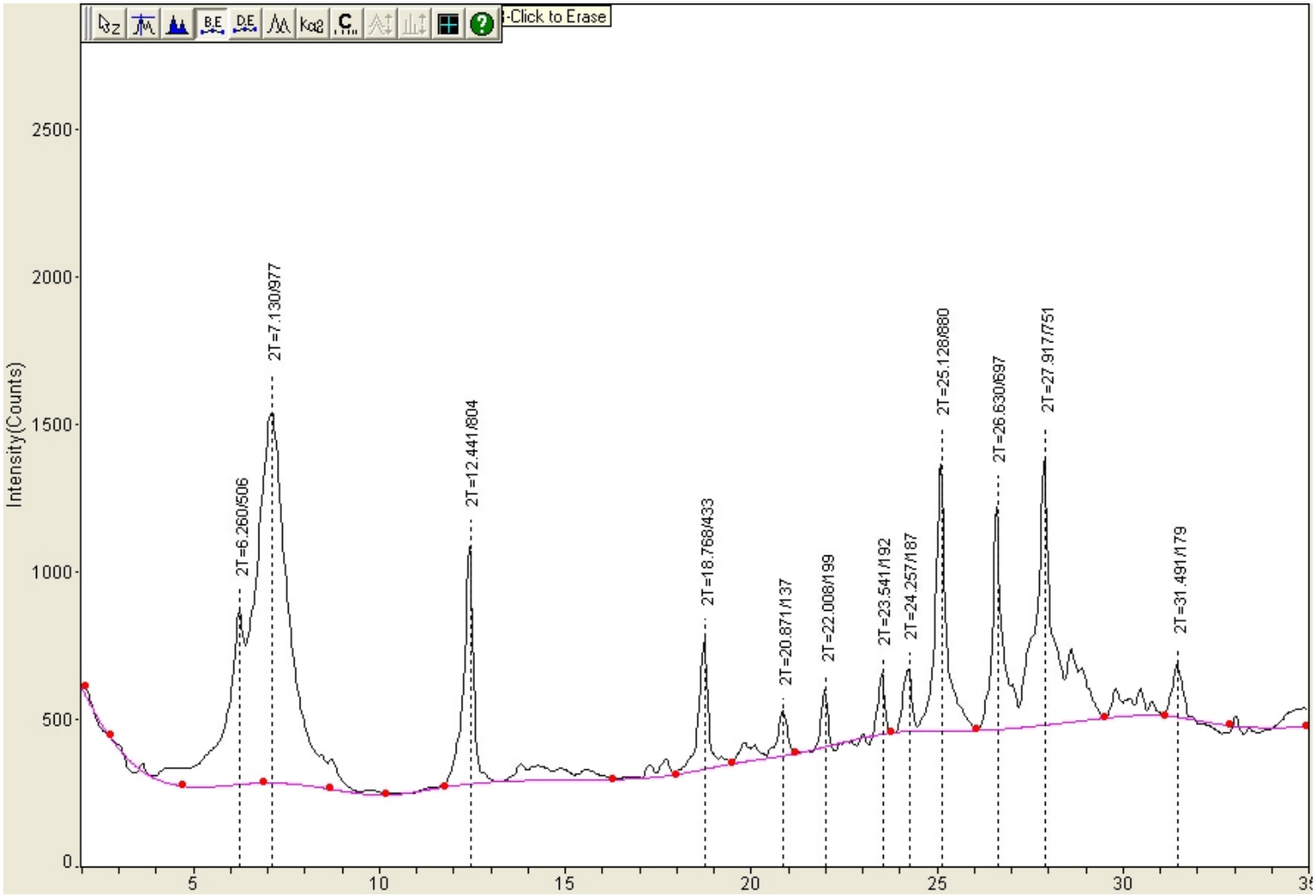

SWH-GJG-0021

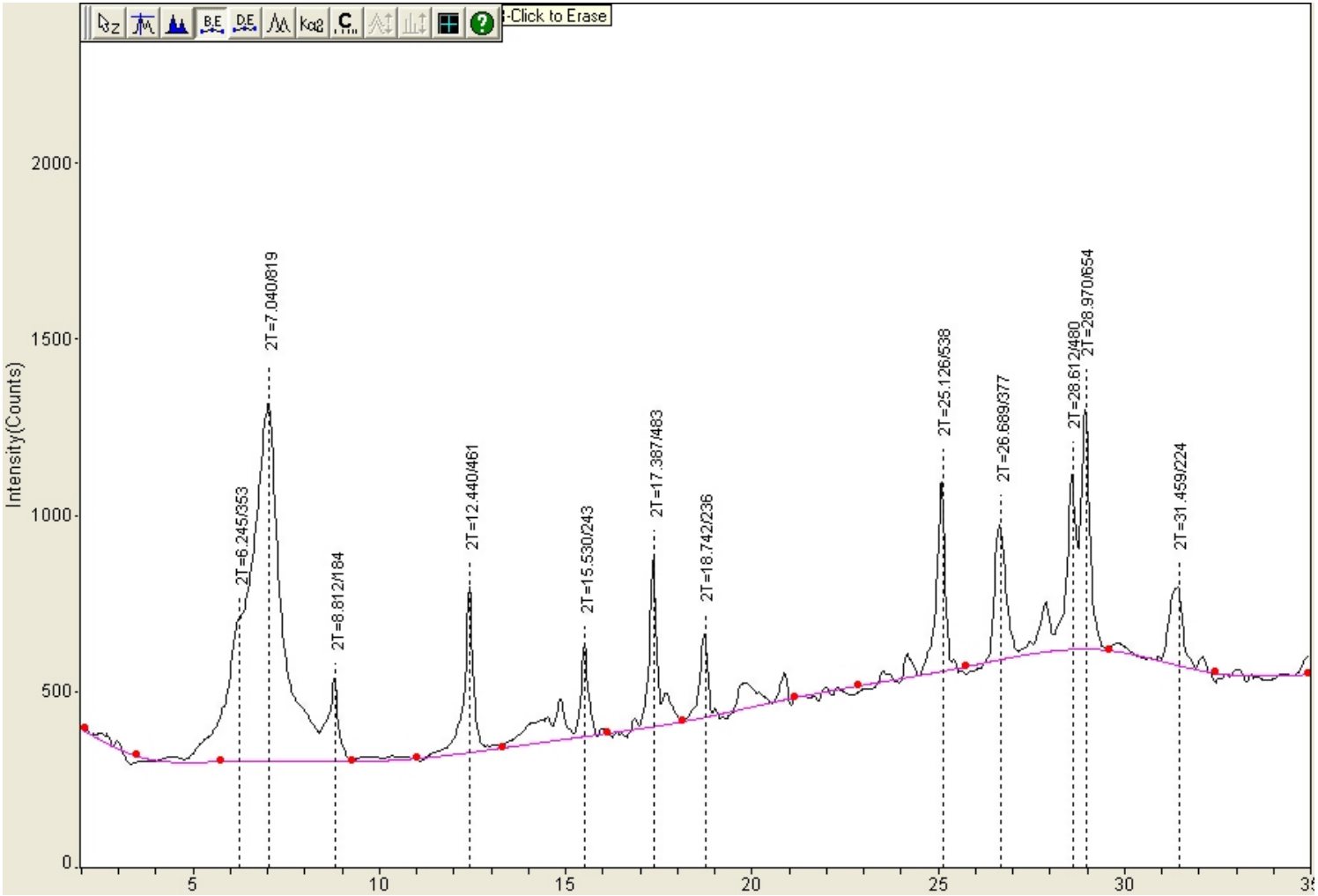
Click to Erase
Intensity(Counts)
2000
1500
1000
500
0
5
10
15
20
25
30
2T=6.245/353
2T=7.040/619
2T=8.812/184
2T=12.440/461
2T=15.530/243
2T=17.387/483
2T=18.742/236
2T=25.126/538
2T=26.689/377
2T=28.612/480
2T=28.970/654
2T=31.459/224

SWH-GJG-0022

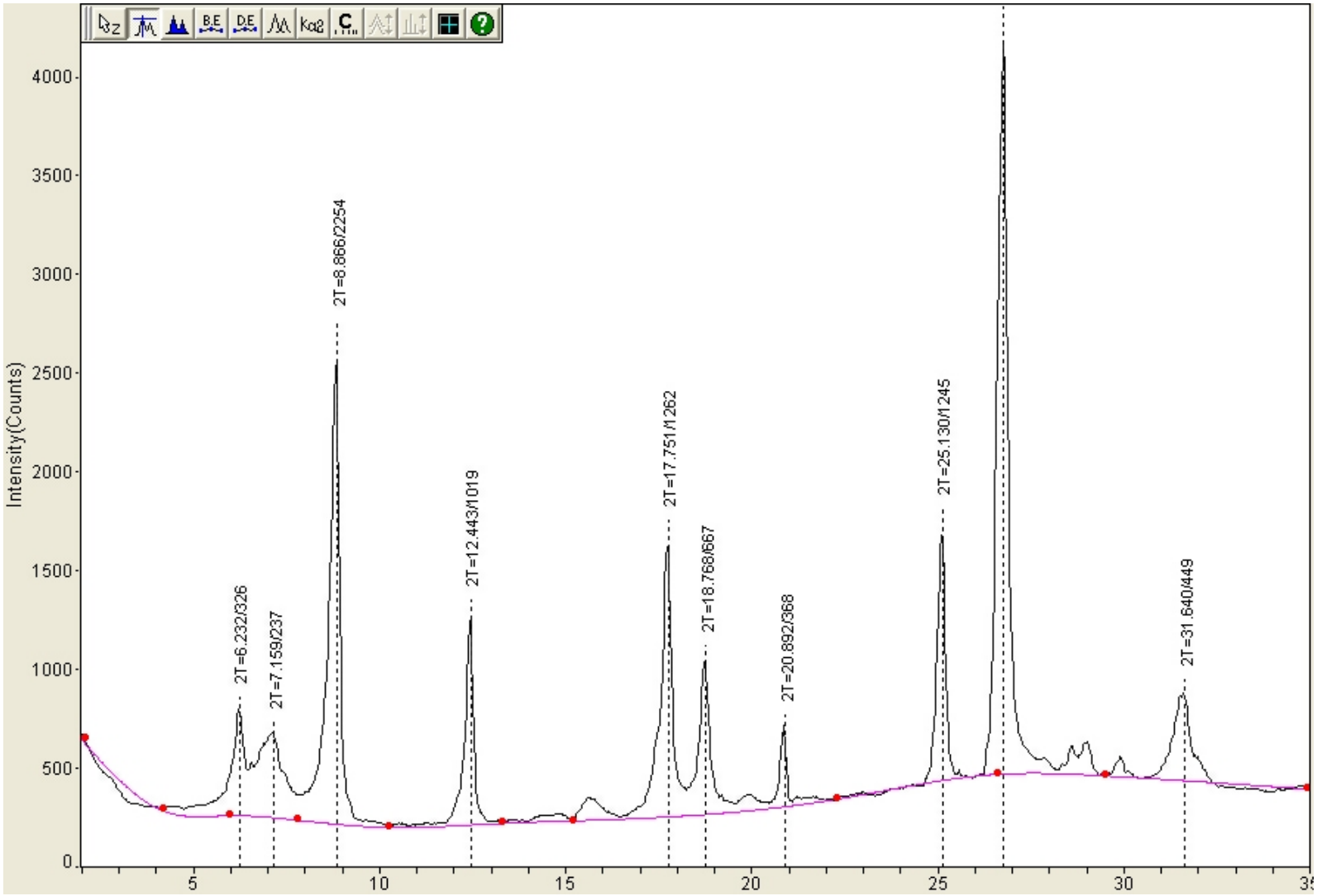
Intensity(Counts)
4000
3500
3000
2500
2000
1500
1000
500
0
5
10
15
20
25
30
2T=6.232/326
2T=7.159/237
2T=8.866/2254
2T=12.443/1019
2T=17.751/1262
2T=18.768/667
2T=20.892/368
2T=25.130/1245
2T=31.640/449

SWH-GJG-0023

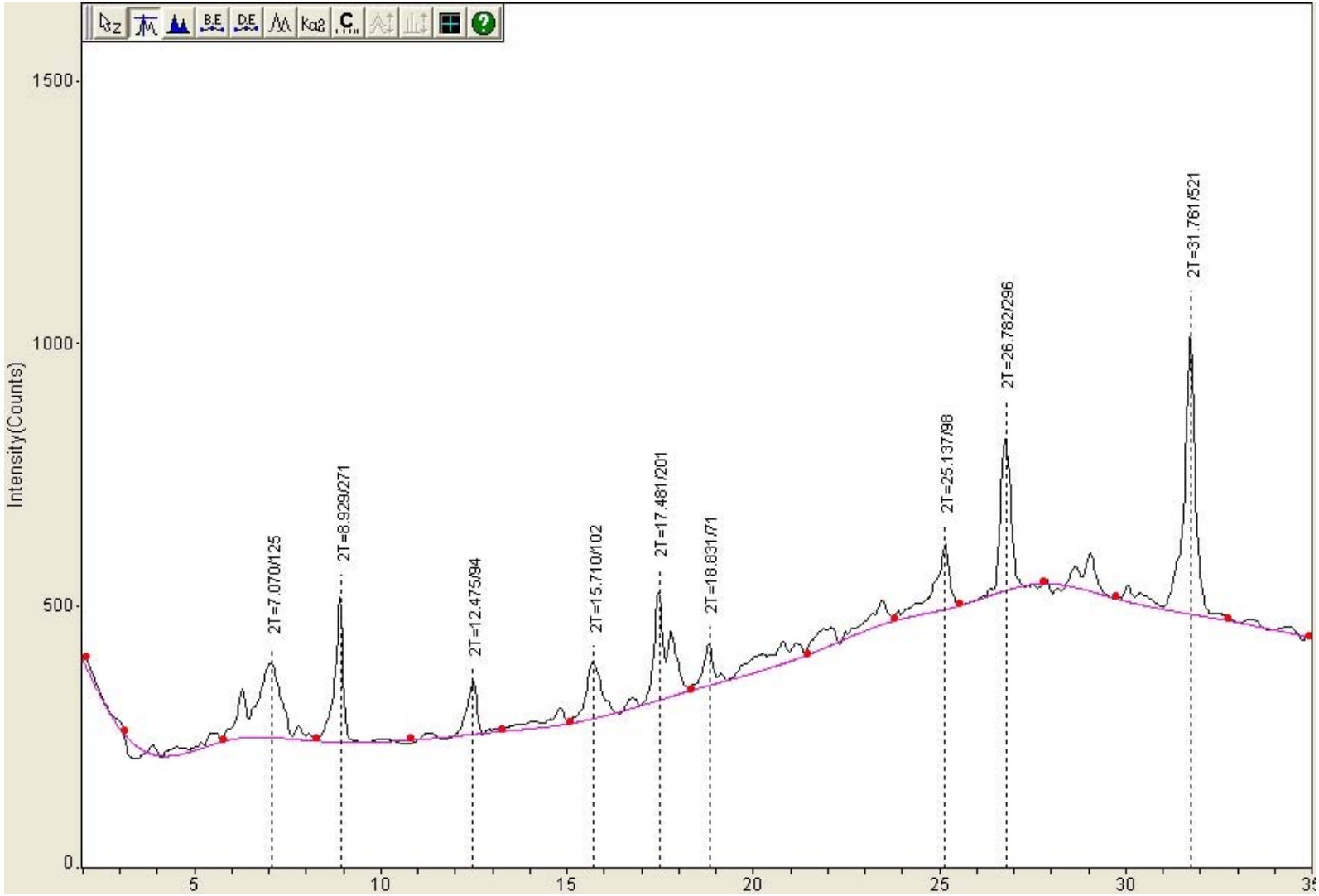
Intensity(Counts)
1500
1000
500
0
5
10
15
20
25
30
2T=7.070/125
2T=8.929/271
2T=12.475/94
2T=15.710/102
2T=17.481/201
2T=18.831/71
2T=25.137/98
2T=26.782/296
2T=31.761/521

APPENDIX E. In-situ profile sample pictures

Lower Southwest Hansen Profile

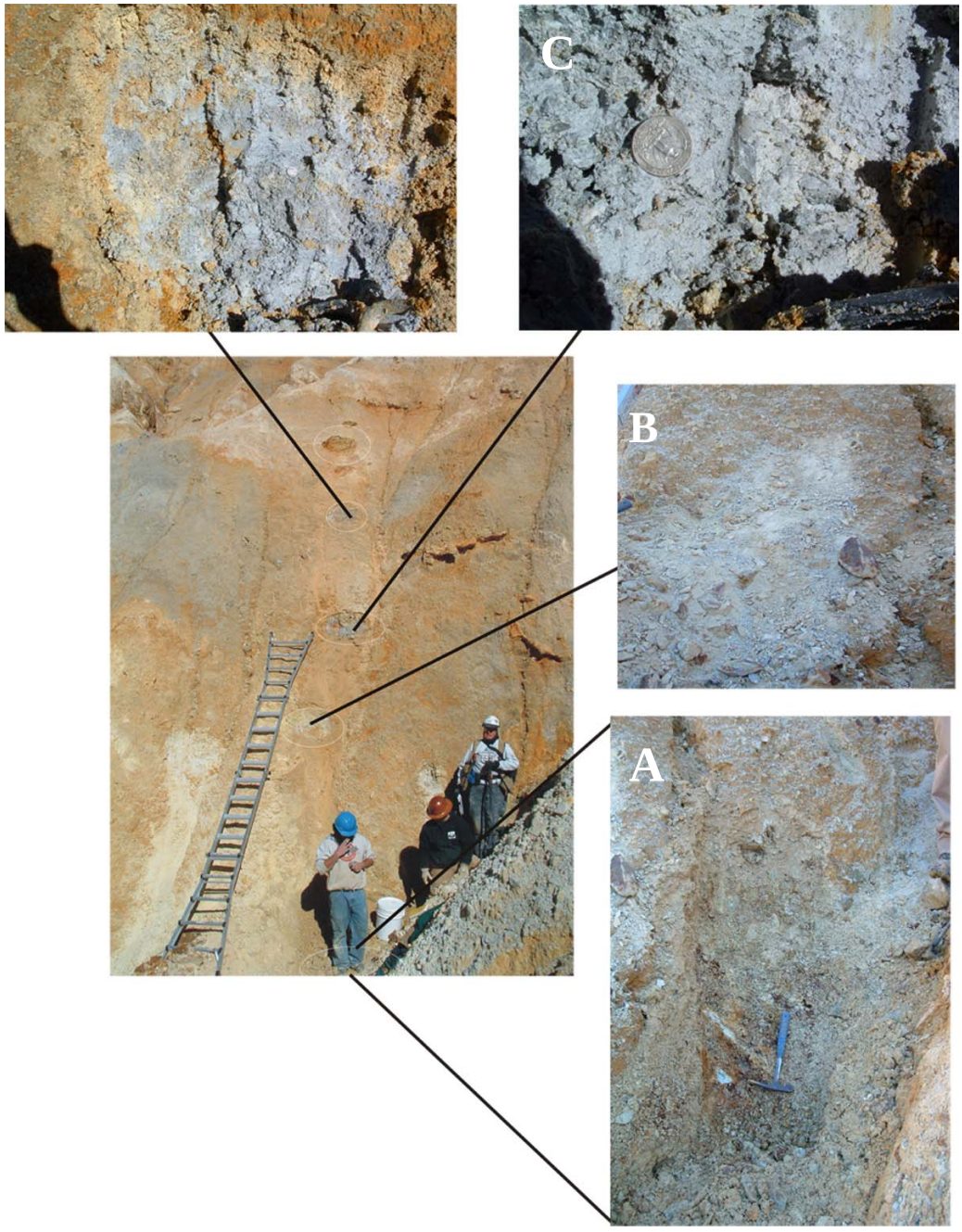

A) (SWH-GJG-0008-11) quartz latite porphyry bedrock at base of profile, notice gray clay vein near hammer. **B)** (SWH-GJG-0012) Mid profile sample location; note grayish color and large rock fragments. **C)** (SWH-GJG-0013) "gray clay" layer near the top of profile; note large gypsum crystal near right corner. **D)** (SWH-GJG-0014) another "gray clay" layer near top of profile. No picture available for top of profile (SWH-GJG-0015

Upper Southwest Hansen Profile

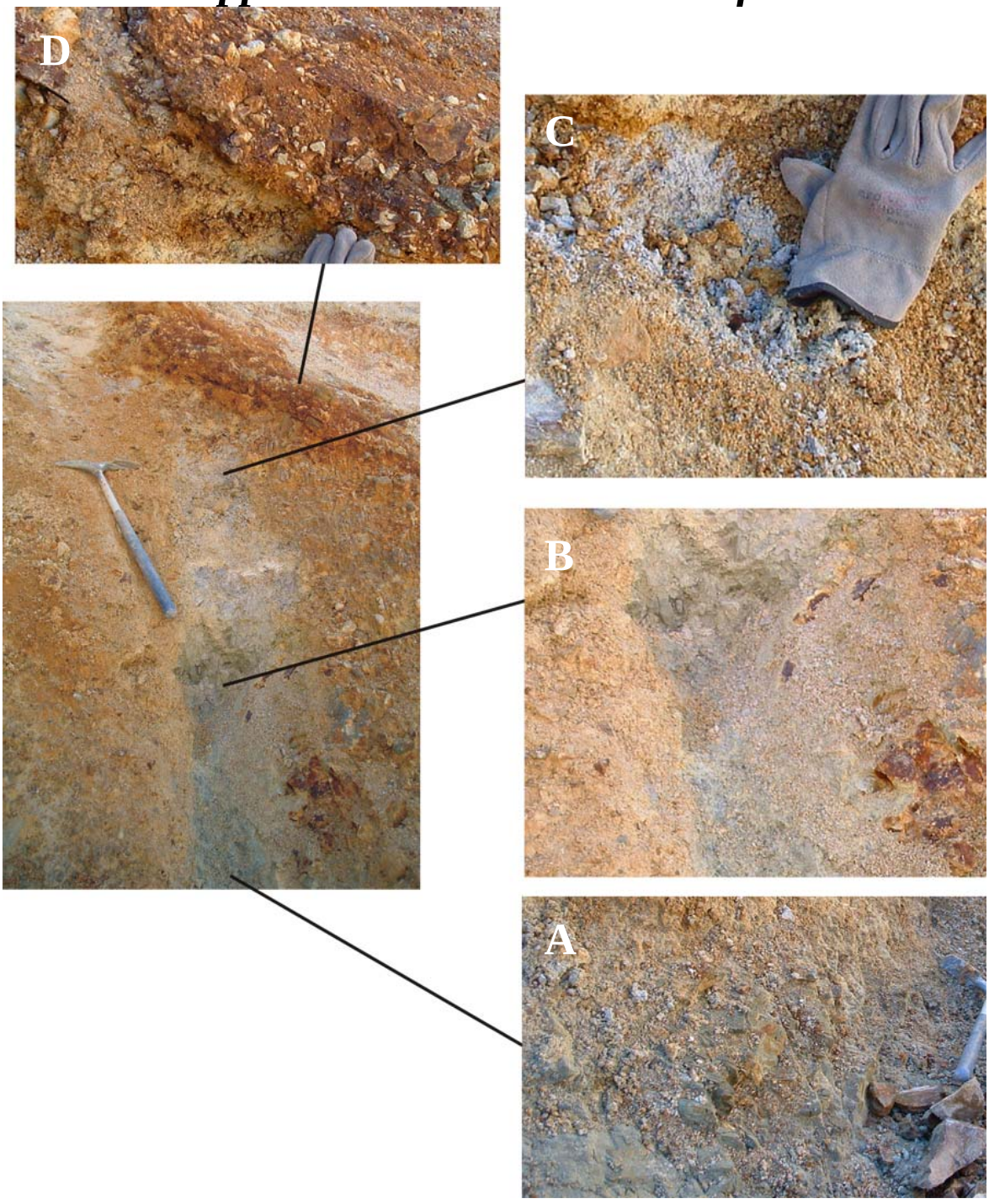

A) (SWH-GJG-0020) Highly fractured andesite bedrock at base of profile; B**)** (SWH-GJG-0021) fractured in-situ bedrock near base of profile; notice large clasts still in place; C**)** (SWH-GJG-0023) fine-grained “gray clay” layer near top of profile; D**)** **(**SWH-GJG-0023) ferricrete capping the top of profile

Hansen Profile

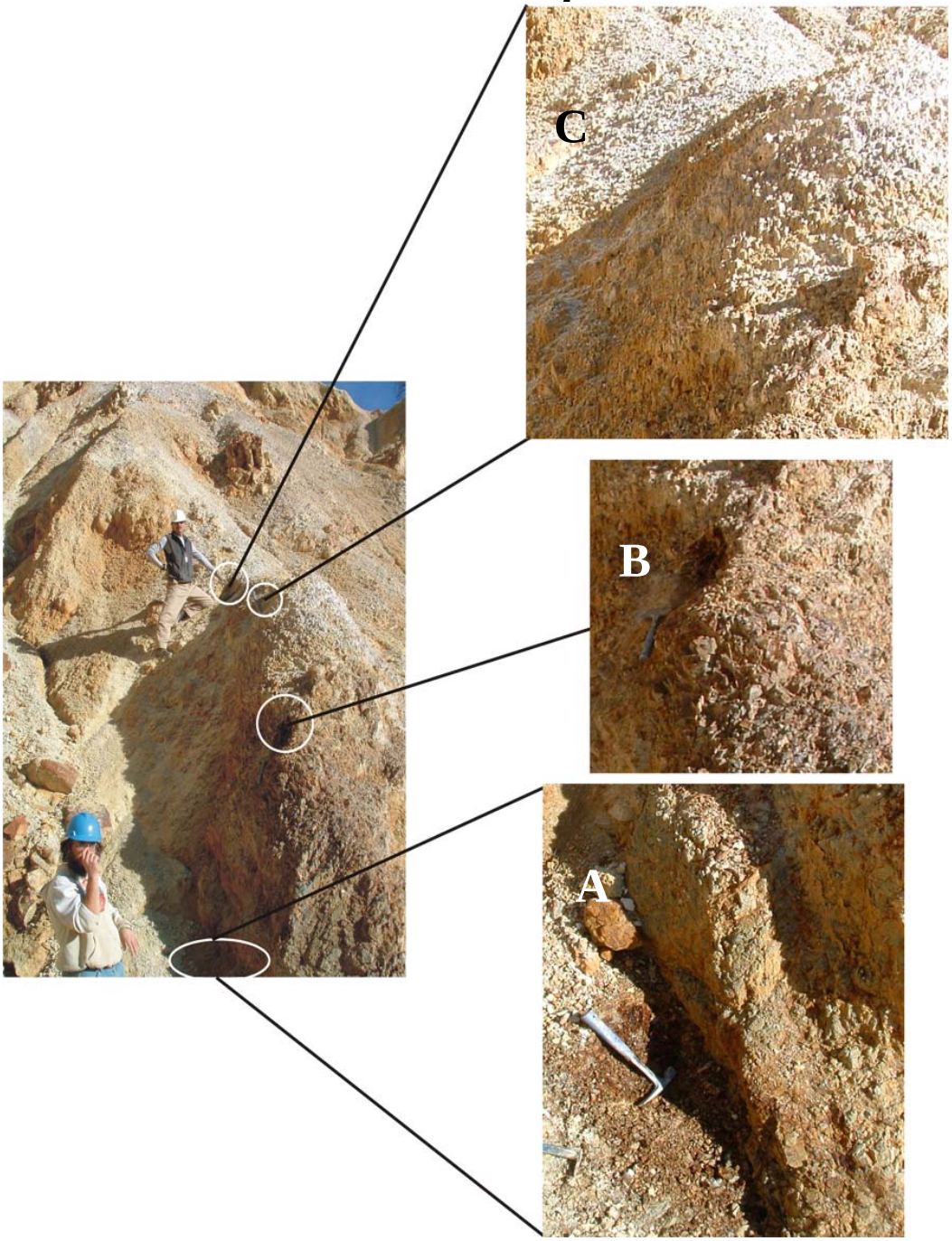

A) (HAS-GJG-0006-7) andesite bedrock at and near the base of profile; notice the intense fracturing; **B)** (HAS-GJG-0008) mid-profile weathered andesite bedrock, notice the intense fracturing and fe-oxide staining of sample location; **C) (**HAS-GJG-0009-10) “gray clay” layers near top of profile; notice the whitish-gray color change from three sample near the base.